Hydrodynamics and Growth of Colloidal Silica in Geothermal Reinjection

Shuying Chen

Department of Mechanical Engineering
University of Canterbury

This thesis is submitted in partial fulfilment of
the requirements for the degree of
Doctor of Philosophy

October 2019

I dedicate this to my mother, Zhu Jimin.

Acknowledgement

I would like to firstly thank my senior supervisor and mentor, Prof. Mark Jermy, for his continuous support, professional guidance, endless patience, and immense knowledge. The time he invested and the efforts he made are priceless and beyond measure. Also, I am sincerely grateful for the valuable opportunity to study towards PhD he offered. I had not ever imagined that I could possibly be awarded the highest academic degree one day. I still can and will always remember the thrilling moment when my application for the doctoral program was approved.

I would like to appreciate the advisor, Prof. Kevin Brown, for his continuous interests and supports, guidance in chemistry, valuable expertise in the field of silica scaling, and time invested in this thesis. Without his guidance, the contributions to the real world can be extremely limited.

I would like to acknowledge my supervisor, Prof. Mathieu Sellier, for his support to my PhD program. Also, I am grateful to him for introducing the world of computational fluid dynamics to me. Thanks to this, my interest in the field of computational science develops.

I am also grateful to the staff in the department who helped and supported me in past four years, including but not limited to Associate Prof. Sid Becker, Associate Prof. Catherine Bishop, Prof. Milo Kral, Prof. Susan Krumdieck, Linda Forbes, Annie Homewood, Kenneth Brown, Eric Cox, Dr. Natalia Kabaliuk, Paul Southward, and Kevin Stobbs.

I would also like to express my gratitude to Department of Mechanical Engineering, College of Engineering, University of Canterbury, for the resources provided for supporting my PhD program including but not limited to the departmental scholarship, the College of Engineering fees only scholarship, the expenses for supporting me in attending conferences, and the access to the learning materials.

A big thank you for the insightful comments and suggestions from the examiners, Dr John Burnell and Dr Oleh Weres.

Special thanks to my fellow postgraduates and friends studying and working in Christchurch, New Zealand, including but not limited to Simo Sun, Michael Leung, Dr Dan Liu, Kokwai Fung, Yicun Huang, Wenwang Pang, etc. who made my time of both studying and after hours enjoyable.

Lastly, but not least, I would like to thank my mother for her emotional and financial support and endless encouragement from the very beginning when I began to have the idea of pursuing the higher education to present: I owe it all to you.

Shuying Chen
October 2019

All models are wrong, but some are useful.

- George E. P. Box.

Abstract

In geothermal energy production from hot aquifers, the cooled and condensed geothermal brine may be reinjected into the water-bearing strata to maintain reservoir pressure and sequester toxic minerals. The solubility of amorphous silica reduces due to loss of heat, and the concentration may increase due to loss of water. Deposition (scaling) of silica may result, narrowing the fluid pathways in the reservoir and reducing the injectivity and the economic lifetime of the well.

In the present work, a comprehensive model is developed, to predict the injectivity as a function of time under the effects of reactive transport of relevant chemical species (e.g. silica, calcite, anhydrite, etc.), using a finite volume Eulerian approach. The fluid pathways in the geothermal reservoir are modelled as parallel flat plates. 2D unsteady transport partial differential equations are solved to model the heat and mass transfer. The consumption of the reactants and the formation of the products are implemented using sink and source terms respectively. The surface chemical reactions are modelled using semiempirical formulas developed from experimental results reported by other workers, with care taken to select data taken under conditions close to those in geothermal reservoirs where possible. The decrease in reservoir porosity due to accumulated scale is modelled by applying the porosity-permeability correlation proposed by Verma and Pruess (1988). The increase in porosity due to reservoir stimulation processes is also modelled.

Since the reinjected fluids (i.e. injectate) are supersaturated with respect with amorphous silica, silica can deposit directly (i.e. molecular deposition) but also can polymerise, nucleate, and form nanoparticles. A validated semiempirical method is proposed to model the growth and Ostwald Ripening of silica nanoparticles. The interactions between colloidal silica are found to differ from those predicted by the classic DLVO theory. These interactions are found to be better described by the soft particle model (Ohshima 2015). Therefore, a semi-theoretical model of silica polymerisation developed by Weres et al. (1981) and the soft particle model proposed by Ohshima (2015) are integrated to quantitively model the amorphous silica deposition where the dissolved silica is actively polymerising. The parameter describing the thickness of the soft shell of silicate chains, which was not quantified in previous studies of the soft-shell model, is estimated by fitting to colloidal growth data to complete the model.

The model outputs are validated by comparing to experimental results and real-world experience at laboratory and full scale (Huminicki and Rimstidt 2007; Tamura et al. 2018; Carroll et al. 1998; Mroczek et al. 2017; Van den Heuvel et al. 2018; Xu et al. 2004): the thermal and chemical sub-models are validated independently, as well as validating the code as a whole against injectivity measurements. The validation results suggest that the model can be useful in predicting the lifetime of geothermal injection under varying conditions.

A sensitivity study is carried out to rank processes which may be effective in extending the injection lifetime. The results suggest that., of the six analysed inputs (injection temperature, mass flow rate, pH, critical porosity and power exponent (used to estimated permeability based on porosity), feedzone thickness, and fracture aperture), injection temperature and pH appear to be more important than others.

Injection of chemical species that are expected to improve the geothermal injection (injection stimulation) is modelled. The model may be of use to estimate potential results of proposed stimulation plans. Several conceptual ideas to extend the injection lifetime are discussed, such as reservoir stimulation by acidizing, ageing and injection at low temperature, acidizing using weak acid, silica removal before injection, and reservoir recovery using hydrofluoric acid.

The developed holistic model is named as GEOREPR (GEOthermal Reinjection lifetime PRediction), which is offered as a free open-source code under the GNU (General Public License) since 2019, and may be developed further in the future. The potential users can use, modify, and redistribute the code for both commercial and non-commercial proposes. One can refer to https://github.com/MITHRILTech/GEOREPR for the latest version of GEOREPR.

Preface

The present thesis includes the contents published as the peer-reviewed conference proceedings as specified below. The manuscripts were written and the corresponding modelling were programmed and performed by the author of the thesis, Shuying Chen. The proceedings are co-authored with his supervisors. The inclusion of the contents from these papers in the present thesis is in accordance with the corresponding copyright policies of the publishers.

Silica particle growth model (Section 4.1.2)

Chen, S., Brown, K., and Jermy, M. (2018). Modelling of in situ silica particle growth and deposition under geothermal conditions. In *Proceedings 40th New Zealand Geothermal Workshop*. Taupo, New Zealand.

Silica stability model (Section 4.2.2)

Chen, S., Brown, K., and Jermy, M. (2018). An explanation for the unexpected interactions of silica nanoparticles using the soft particle model. In *Proceedings 40th New Zealand Geothermal Workshop.* Taupo, New Zealand.

Holistic model (Chapter 6, Section 8.5)

Chen, S., Brown, K., and Jermy, M. (2018). Predictions of average silica particle size over time under geothermal conditions. In *Proceedings 40th New Zealand Geothermal Workshop*. Taupo, New Zealand.

Conceptual ideas of the holistic model (Chapter 6, Section 8.7)

Chen, S., Brown, K., and Jermy, M. (2017). A model of silica colloid growth, stability and transport used to predict geothermal reinjection lifetime. In *Proceedings 39th New Zealand Geothermal Workshop*. Rotorua, New Zealand.

Conference presentations

Modelling of silica scaling during geothermal reinjection. At *Fluids in New Zealand*, Feb 2019. University of Otago, Otago, New Zealand.

Silica particle deposition under geothermal conditions. At *40th New Zealand Geothermal Workshop*, Nov 2018. Taupo, New Zealand.

Growth of colloidal silica. At *40th New Zealand Geothermal Workshop*, Nov 2018. Taupo, New Zealand.

Interactions of silica nanoparticles. At *40th New Zealand Geothermal Workshop*, Nov 2018. Taupo, New Zealand.

A simple model of silica colloid deposition in geothermal energy extraction systems. At *Fluids in New Zealand*, Feb 2018. University of Auckland, Auckland, New Zealand.

A model of silica colloid growth, stability and transport used to predict geothermal reinjection lifetime. At *39th New Zealand Geothermal Workshop*, Nov 2017. Rotorua, New Zealand.

Two models of silica colloid stability and their effect on the transport of silica in geothermal reservoirs. At *Fluids in New Zealand*, Feb 2017. University of Canterbury, Christchurch, New Zealand.

Contents

Chapter 1

Introduction

It is well-known that world energy demand has steadily increased since the industrial revolution. According to 2017 Key World Energy Statistics, published by the IEA (International Energy Agency), the world total energy consumption in 2015 was almost 9 500 Mtoe (million tonnes of oil equivalent), which is more than twice as high as 40 years ago (IEA 2017), as shown in Figure 1.1 below.

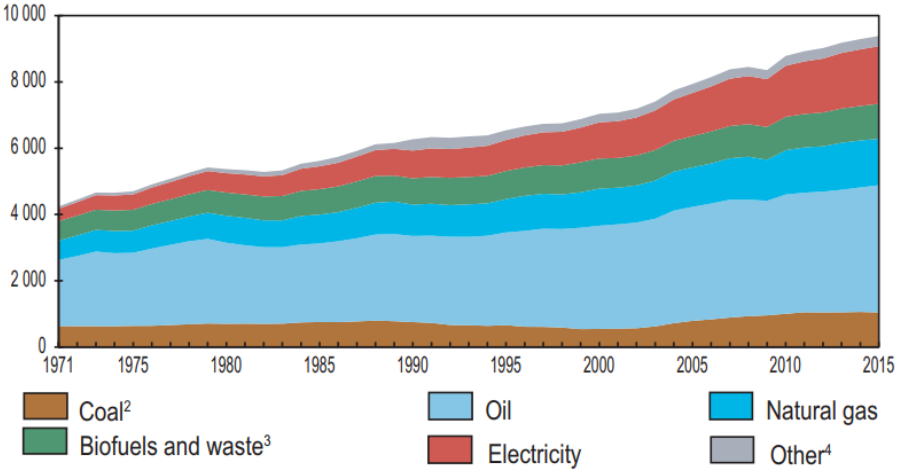

Figure 1.1: World total final energy consumption (TFEC) by fuel from 1971 to 2015, where 2: peat and oil shale are counted in *Coal*; 3: data for biofuels and waste final consumption was estimated for several countries; 4: heat, solar thermal, and geothermal are counted in *Other*, reproduced from IEA 2017.

On the other hand, the energy supply has spare capacity, since the total energy available for utilisation was about 13647 Mtoe, which was about 4000 Mtoe higher than 2015 consumption (IEA 2017), as shown in Figure 1.2 (a) below.

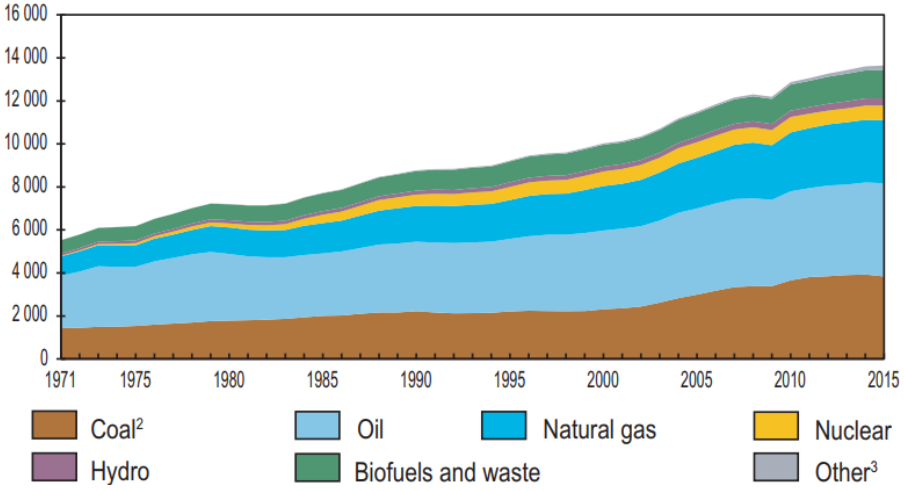

(a)

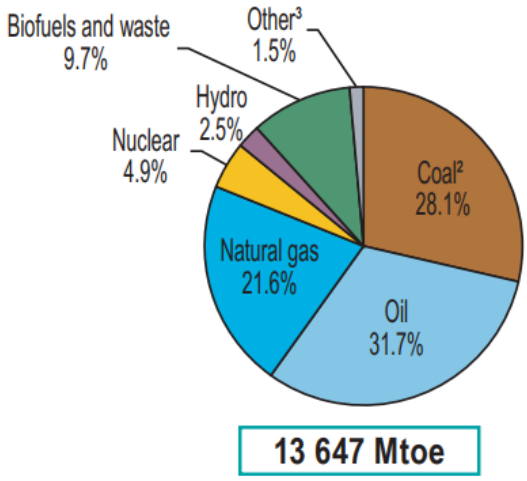

2015

(b)

Figure 1.2: (a) World total primary energy supply (TPES) by fuel from 1971 to 2015, (b) Fuel shares of TPES in 2015, where 2: peat and oil shale are counted in *Coal*; 3: heat, solar thermal, and geothermal are counted in *Other*, reproduced from IEA 2017.

Fossil fuels (including peat and oil shale, coal, oil, and natural gas) made up 81.4% in TPES (total primary energy supply) of 2015. Regardless of the problems of air pollution and the release of greenhouse gases due to fossil fuel consumption, investigations such as that carried out by El-Ashry (2010) suggested that oil, coal and gas reserves would be diminished to zero approximately within 35, 107 and 37 years, respectively. Although there have been recent promising developments in resource extraction techniques, for example, shale gas production using hydraulic fracturing, which may ease the urgency of the energy crisis, the limited fuel share of renewable energy is still one of the most urgent problems that require particular attention from human civilisation.

A few countries have already made remarkable progress in reducing their dependence on fossil fuels, as shown in Figure 1.3 below.

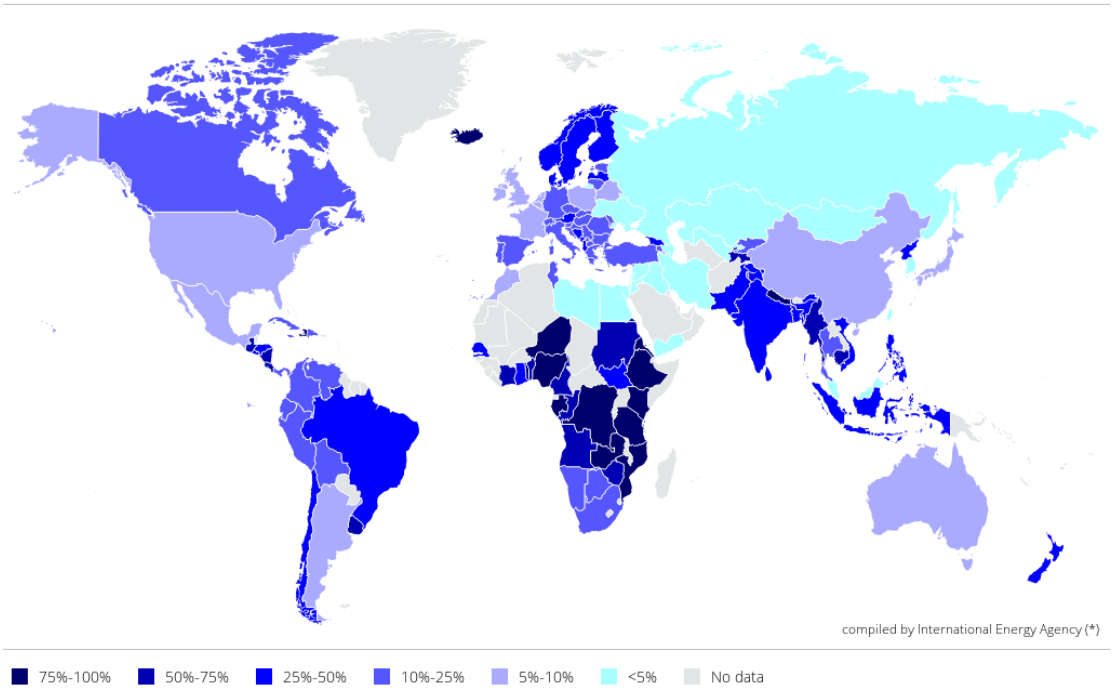

Figure 1.3: Share of the primary energy supply from renewable resources, by country. Reproduced from IEA 2017.

Of developed countries, New Zealand (NZ) has one of the highest proportions of renewable energy production. According to the Ministry of Business, Innovation and Employment (MBIE) of New Zealand, renewable resources contributed 84.8% of NZ's electricity supply (a 35-year high), and 40.2% of NZ's total primary energy supply (TPES) in 2016 (MBIE 2017). Statistical data from 2014 shows that geothermal energy (including geothermal electricity and heat) accounts for 56% of NZ's TPES generated from renewables, as shown in Figure 1.4 below:

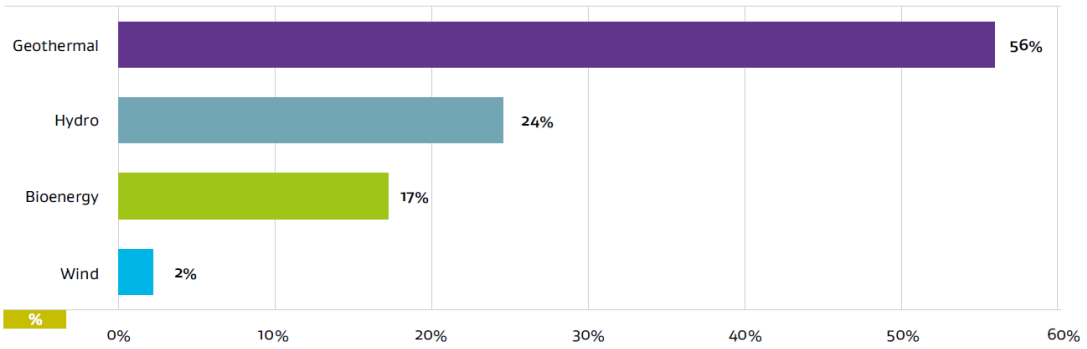

Figure 1.4: Percentages of New Zealand renewable primary energy supplies in 2014, reproduced from MBIE 2015. These figures are for energy release, not electricity production. Note that the unlikely high percentage of geothermal comparing to others is due to the relatively low efficiency of conversion of geothermal energy to electricity.

Geothermal energy has been used by humans in practical ways since the first half of the 19th century. A chemical plant, located in Larderello, Italy, was developed to extract boric acid from geothermal water, and boreholes were drilled to enhance the upwelling of the hot water (Dickson and Fanelli 2004), as shown in Figure 1.5 (a). At the same geothermal field, the earliest attempts to generate electricity from geothermal energy took place in 1904, as shown in Figure 1.5 (b).

(a) **(b)**

Figure 1.5: (a) One of the earliest attempts of applying geothermal resources – the "cover lagoon" used to extract boric acid; (b) the first engine powered by geothermal steam and its inventor, Prince Piero Ginori Conti, reproduced from Dickson and Fanelli 2004.

Since then, government and commercial companies have put tremendous efforts into the development of geothermal industries, drilling deeper wells, using technology developed in the oil industry. The significant rapid growth of geothermal power production has been observed. By 2015, Zarrouk and Moon (2014) estimated an approximate 73% increase in installed capacity within only 5 years to 18500 MWe (Bertani 2010).

The heat from low-enthalpy geothermal resources may be used directly for purposes such as domestic heating and horticulture, and heat from high-enthalpy resources may be used to generate electricity.

Geothermal power stations are similar to other Rankine cycle thermal power plants. By using a heat engine, such as a turboexpander, heat can be converted to mechanical energy and eventually to electricity. There are currently three major types of geothermal power stations in service: dry steam, flash steam, and binary cycle power plant. Dry steam power stations are the oldest and simplest type and make use of geothermal steam at sufficient enthalpy that can expand without forming liquid droplets. Flash steam plant extracts hot water (usually above 180℃ (Kashpura and Potapov 2000)) which is fed into tanks at low pressure so that the hot water boils and partially flashes into dry steam. The steam is separated from the water to generate electricity. The remaining water is often called the separated geothermal water (SGW). A binary cycle power station transfers heat from the geothermal fluid, through a heat exchanger, to a lower boiling point fluid (e.g. pentane) which boils and becomes gas to generate electricity once it gains enough heat. The binary cycle is the most recent development and may become the most common in the near future (Kashpura and Potapov 2000) as it is designed to utilise cooler geothermal reservoirs, such as a plant in Alaska (Chena hot springs) is utilising the underground water at approximately 57 ℃ for power production.

Gupta et al. (2007) suggested that it is very likely that the installed capacity of worldwide geothermal electricity production could go up by ten times without significant development in technology. However, the global development of geothermal industries still faces certain challenges.

First, the availability of the geothermal reservoirs, which are at depths that are economic to drill, are unevenly distributed around the world, which naturally leads to the unbalanced utilization

of geothermal energy around the world. Second, since capital and time investments for developing geothermal stations can be significant and collateral impacts must be considered (e.g. effects on groundwater levels, and concerns about hydraulic fracturing), political will may be necessary. This could be augmented by the potentially urgent need to replace non-renewable energy sources. Third, the challenges come from the development of other energy resources, such as the recent progress of shale gas production, the rapid increment of installed capacity of solar photovoltaic (PV) plants, possible future breakthroughs in controlled nuclear fusion, etc.

The efficiency of energy conversion from the enthalpy of geothermal fluids into electricity can vary from 1% in the Chena Hot Springs geothermal power plant, US (Holdmann and List 2007; Aneke et al. 2011) to 20.7% in the Darajat geothermal power plant, Indonesia (Ibrahim et al. 2005; Kaya et al. 2011). The efficiency is determined principally by the pressure and the temperature of the geothermal fluids. These efficiencies are lower than that of many other common kinds of power plants, principally due to the low temperature. Zarrouk and Moon (2014) plotted the comparison of the average efficiencies among the different types of power plants, reproduced in Figure 1.6 below:

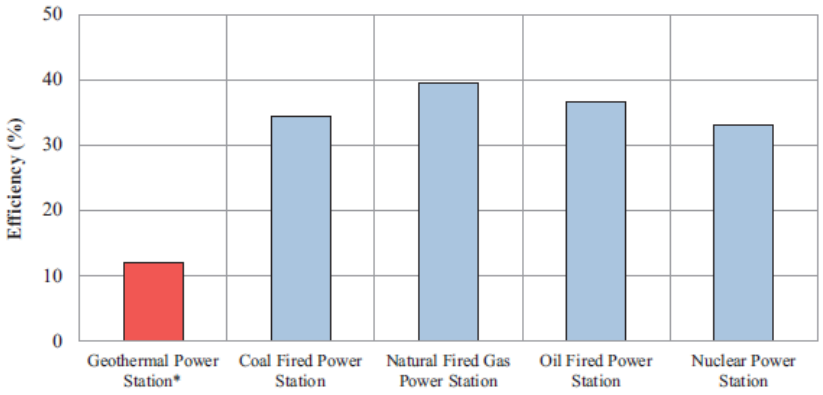

Figure 1.6: Comparison of energy convention efficiency among different types of thermal power plants, reproduced from Zarrouk and Moon 2014.

Therefore, although impressive progress has been made in the past decades, there is perhaps still a long way to go to make geothermal power production competitive. To achieve this, many limitations need to overcome.

One of the most pressing physical problems that limit the development of geothermal energy production is silica scaling (Brown 2011) i.e. the deposition of amorphous silica as shown in Figure 1.7 below, due to a reduction in solubility (see Section 2.2.2 for the estimation of silica solubility). This is expected to be more common in above-ground plants and reinjection wells (where the fluid is pumped back into the geothermal aquifer), and those parts of the aquifer near the reinjection wells, if no technique is applied to inhibit silica scaling.

Figure 1.7: Silica scale in a reinjection pipe, reproduced from Zarrouk and Moon 2014.

Like the example shown in Figure 1.7, the scale can block the pipelines transporting the geothermal brines and finally can lead to a power station shut-down in order to remove it or replace the scaled equipment.

Kashpura and Potapov (2000) commented that scale "…not only decreases the amount of extracted energy, but leads to the loss of power generation due to shutdowns and additional expenses for solid/deposits removal and disposal." Effectively inhibiting or even preventing the formation of scale would significantly increase the efficiency of geothermal power stations (Brown 2011; Zarrouk and Moon 2014).

Techniques like acidification using sulphuric acid can effectively inhibit the nucleation of amorphous silica, and therefore minimise silica scaling. However, some of the inhibition techniques may still require attention: in the case of acidification, when the fluid is being reinjected back to geothermal reservoirs, pH may rise again due to the dissolution of carbonate minerals, e.g. calcite, allowing precipitation of silica, and the inhibiting effects could be reduced or negated due to this.

This thesis attempts to contribute to an understanding of the silica scaling process at a fundamental level, in the hope that such understanding can be used to control scaling and hence reduce the costs of operation and/or extend the life of geothermal wells and plant.

Chapter 2

Literature review

2.1 Background research

The knowledge of fluid mechanics and the finite volume method used in the present work can be found in White 2003; Mott 2006; Versteeg and Malalasekera 2007. The conceptual ideas of particle deposition modelling are inspired by Elimelech et al. 2013.

The fundamental knowledge regarding amorphous silica is studied based on Iler 1979, which systematically demonstrates nearly every aspect of the chemistry of silica that is related to this project such as, the solubility of quartz and amorphous silica, the polymerization of silica, the formation of colloidal particles, the surface chemistry of silica, the discrepancy between the expectations of the traditional DLVO theory and the observations, the synthesising methods of silica gels, etc.

2.2 Chemistry of silica

2.2.1 Introduction

In the Earth's crust, silica is one of the most common components. Although this study is concerned with the formation, transport, and deposition of amorphous silica, it is worth knowing the structure of crystalline silica prior to understanding the surface of amorphous silica.

Silica, or silicon dioxide, naturally exists in several forms, such as quartz (stable below 870 ℃), tridymite (stable below 1470 ℃), cristobalite (stable below 1710 ℃)), amorphous silica and others (Brown 2011). At room temperature and atmospheric pressure, both quartz and amorphous silica are stable, but quartz is the most common and densest form, and the other two (tridymite and cristobalite) will not exist permanently but morph to quartz over time.

The silicon-oxygen tetrahedron ($[SiO_4]^{4-}$) is the main structural unit in silica. There is one silicon atom at the centroid (named the tetrahedral hole (Gould 1957)) bonded to four oxygen atoms as shown in Figure 2.1 below.

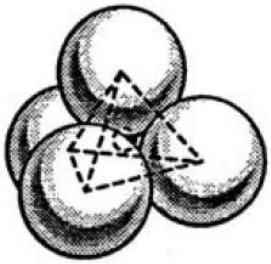

Figure 2.1: Space-filling model of a silicon-oxygen tetrahedron, reproduced from Breck 1974.

The length of a siloxane bond ($Si-O$) is about 0.162 nm, which is smaller than the sum of the radii of one silicon and one oxygen atoms (Unger 1979). This is related to the high stability of the bond. The formation of silicates is achieved by sharing oxygen atoms among silicon-oxygen tetrahedrons. A chain, sheet, or network of silica will form by sharing two, three, or four oxygen atoms per tetrahedron respectively (Gould 1957). If the bond angles are random and nonperiodic, amorphous silica forms, as shown in the left-hand diagram in Figure 2.2 below.

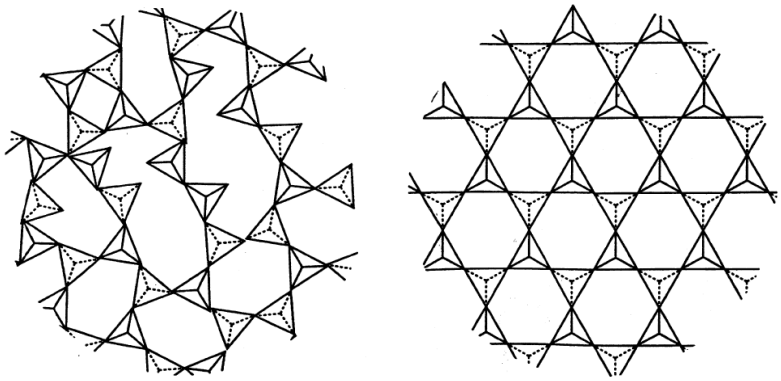

Figure 2.2: Schematic of 2D structures of amorphous (left) and crystalline (right) silica, reproduced from Pauling 1960.

Different structures result in different density for crystalline and amorphous silica, as shown in Table 2.1.

Table 2.1: Comparison of the densities for crystalline and amorphous silica, reproduced from Unger 1979.

Form	**Density (g cm^{-3} at 273 K)**
Amorphous silica	2.20
β-Cristobalite	2.21
β-Tridymite	2.26
β-Quartz	2.53
α-Cristobalite	2.65
Coesite	3.01

Assuming that the density of a given solid object ρ is a constant, the mass of the object m is usually proportional to the characteristic length r cubed, as shown in Equation 2.1 below.

$$m \propto r^3 \tag{2.1}$$

For instance, the mass of a solid sphere and a solid cube can be defined as $m = 4/3\ \rho\pi r^3$ and $m = \rho r^3$, where the characteristic length r physically means the radius of the sphere and the edge length of the cube respectively.

However, when aggregates of colloids are considered, the relationship between mass and size is different.

Mandelbrot (1989) developed the concept of fractal geometry in the 1980s, which has been adopted as an intriguing (Rarity 1989) approach to study colloid systems. Lin et al. (1989) published observations regarding the aggregates of colloidal gold, polystyrene, and silica (reproduced in Figure 2.3 below), and concluded that the theory of fractal geometry may be a possible explanation for the universality in the geometric form of aggregates of colloids.

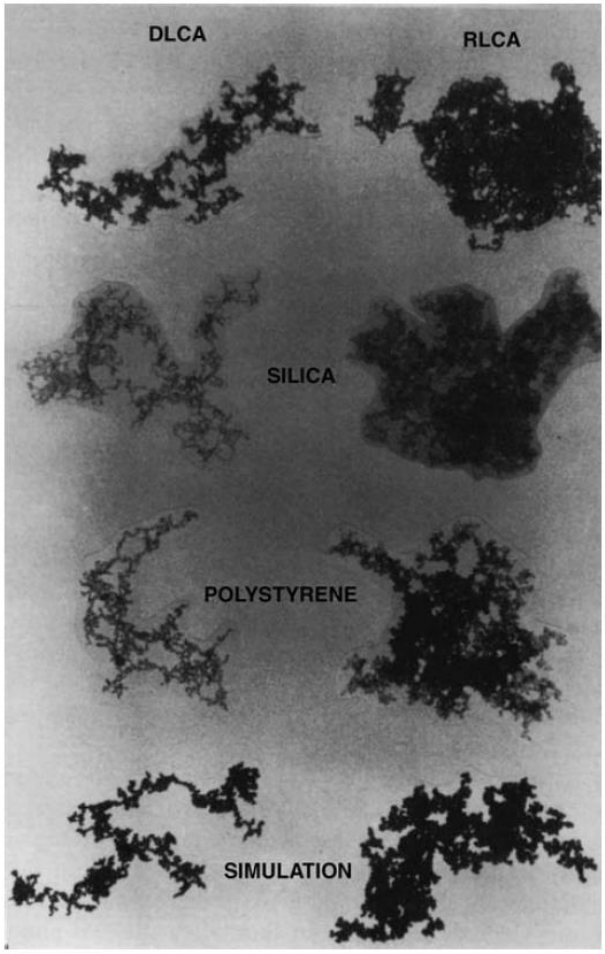

Figure 2.3: Diffusion-limited (DL) and reaction-limited (RL) aggregates of colloidal gold, polystyrene, silica, which were observed by using the transmission electron microscope, and computer simulation, reproduced from Lin et al. 1989.

Fractal geometry theory proposes that the correlation between the mass m and the characteristic length of a fractal object r can be expressed as:

$$m \propto r^{D_f} \tag{2.2}$$

where D_f is known as the mass fractal dimension of the object. It would be equal to the spatial dimension D, if the object of interest is non-fractal (Euclidean), say $D = 3$ for a sphere (as the volume of a sphere is propotional to the cubed diamater). For a fractal geometry, D_f shall be

smaller than D. One typical example for this correlation would be a tree (Brinker and Scherer 1990).

Similar to Equation 2.2 above, the correlation between the surface area and the characteristic length of a fractal object can be represented by:

$$s \propto r^{D_s} \tag{2.3}$$

where D_s is the surface fractal dimension, $(D-1) < D_s < D$. For a three-dimensional object, the surface fractal dimension should between 3 and 2. One interesting example would be a ball made crumpled from a piece of paper (Brinker and Scherer 1990), which is a surface fractal but not a mass fractal.

Auber and Cannell (1986) investigated the aggregation of colloidal silica (Ludox AS-40) by adding NaCl or HCl to the system to adjust pH. They estimated the fractal dimension for reaction-limited (RL) and diffusion-limited (DL) aggregation and reported that $D_f = 2.08 \pm 0.05$ for RL and $D_f = 2.08 \pm 0.05$ or $D_f = 1.75 \pm 0.05$ for DL, subject to pH and concentration of silica particles. Interestingly, clusters with the lower fractal dimension were always found to restructure and yield $D_f = 2.08 \pm 0.05$ after a period of time. The time for restructuring was fitted to $0.37[\mathrm{H^+}]^{-0.48}$ in seconds.

For the present study, the reason for studying the chemistry of silica is to model the natural formation of colloidal silica from monomeric silica (i.e. $\mathrm{Si(OH)_4}$) in cooled geothermal fluid, to find the in situ particle size and estimate the stability of silica nanoparticles under geothermal conditions, so that the deposition rate and the volume of silica scale can be predicted. Therefore, it is necessary to quantitatively understand the whole processes of silica polymerisation, nucleation, growth due to precipitate, and aggregation.

2.2.2 Solubility of silica

As mentioned before, quartz is the most common form of silica in nature. Brown (2011) suggested that quartz exists in the rock matrix of most geothermal reservoirs, which dissolves in hot geothermal water shown in Equation 2.4 below.

$$\mathrm{SiO_2(s, quartz) + 2H_2O \rightarrow Si(OH)_4(aq, silicic\ acid)} \tag{2.4}$$

The formed $\mathrm{Si(OH)_4}$ is named as silicic acid, or conventionally called dissolved silica, or monomeric silica.

Fournier (1986) proposed a formula describing the correlation between the temperature T (℃) in a range from 20 to 330 ℃ and the concentration of dissolved silica $C_{\mathrm{e,quartz}}$ in equilibrium with respect to quartz at saturated water vapour pressure in pure water, as shown in Equation 2.5 below:

$$\begin{aligned} T = {} & 3.1665 \times 10^{-7} C_{\mathrm{e,quartz}}^3 - 3.6685 \times 10^{-4} C_{\mathrm{e,quartz}}^2 + 0.28831 C_{\mathrm{e,quartz}} \\ & + 77.034 \log C_{\mathrm{e,quartz}} - 42.196 \end{aligned} \tag{2.5}$$

Before the geothermal water is extracted, it is in equilibrium with quartz. However, the silica usually deposits in the form of amorphous silica, which is more soluble than quartz in water under the same conditions due to lack of crystalline structure (Brown 2011). The solubility of amorphous silica at saturated water vapour pressure in pure water C_{e}^0 from 0 to 250 ℃ is given by Fournier and Rowe (1977):

$$\log C_e^0 = -\frac{731}{T} + 4.52 \tag{2.6}$$

where T is the absolute temperature. Note that the maximum valid temperature of Equation 2.6 is lower than the maximum temperature of interest in the geothermal reinjection modelling, such as the initial reservoir temperature of 260 ℃ in Xu et al. (2004); whereas, practically, no plant injects separated geothermal water at temperatures greater than 250 ℃, which would be too much of a waste of energy. Hence, it can be safe to apply Equation 2.6 in the present work. If the user does need to estimate the solubility at the temperatures up to 340 ℃, one can follow Equation 2.9-2.12 introduced in the present section below.

The comparison of solubility between quartz and amorphous silica is shown in Figure 2.4 below:

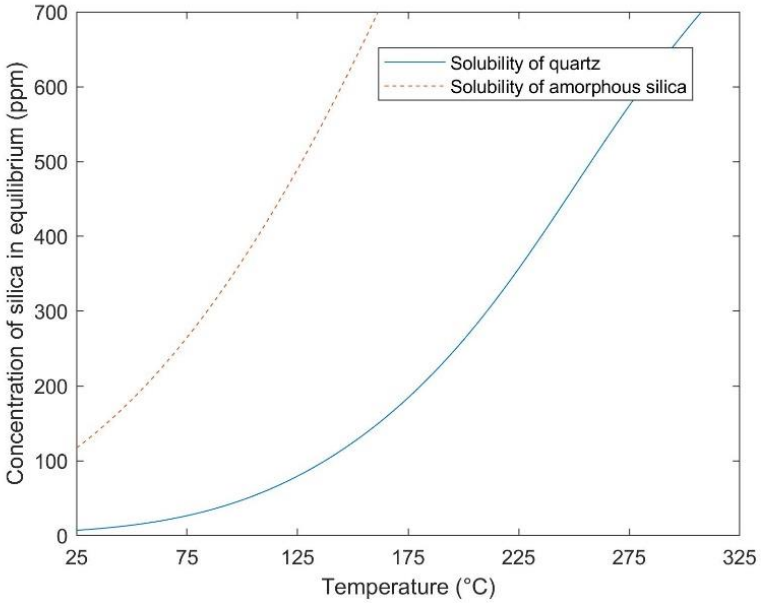

Figure 2.4: Comparison of estimated solubility between quartz and amorphous silica in pure water at saturated water vapour pressure.

Brown (2011) suggested that the solubility difference shown in Figure 2.4 theoretically allows a significant drop of temperature till the geothermal water becomes saturated with amorphous silica.

In practice, there are other salts such as sodium chloride dissolved in geothermal water and pH may not be neutral. Generally, the increasing concentration of other salts and the lowering pH will decrease the solubility of both quartz and amorphous silica.

To take the effects of pH into account, Brown (2011) suggested to use Equation 2.7 shown below, which considered the dissociation of silicic acid:

$$C_e = \left[1 + \frac{10^{\mathrm{pH}} K_{1,\mathrm{Si(OH)_4}}}{\gamma_{\mathrm{H_3SiO_4^-}}}\right] C_e^0 \tag{2.7}$$

where C_e is the solubility of amorphous silica when varying ionic strength and pH are considered, C_e^0 is defined in Equation 2.6, $\gamma_{\mathrm{H_3SiO_4^-}}$ is the activity coefficient of $\mathrm{H_3SiO_4^-}$ ion, which depends on temperature and dissolved salt concentration and can be found using the Debye-Hückel equation addressed in Appendix 1: Activity coefficients of Chapter 5, $K_{1,\mathrm{Si(OH)_4}}$ is the dissociation constant of silicic acid, given by:

$$\log K_1 = -\frac{2549}{T} - 15.36 \cdot 10^{-6}\, T^2 \tag{2.8}$$

where T is the absolute temperature.

To correct for salt content, Equation 2.9 below was proposed by Fournier and Marshall (1983), to find the molal solubility of amorphous silica in brines m_{e} at temperatures from 100 to 340 ℃ and pressures from vapour pressure to 1000 bar:

$$\log m_{\mathrm{e}} = -n \log \rho_s F + n \log \rho^0(\mathrm{v.p.}) + \log m^0(\mathrm{v.p.}) \tag{2.9}$$

where ρ_s is the density of the brine, $\rho^0(\mathrm{v.p.})$ is the density of pure water at the given temperature and the vapour pressure, F is the weight fraction of water in the brine, $m^0(\mathrm{v.p.})$ is the molal solubility of amorphous silica in pure water at given temperature T and vapour pressure v. p., and n is given by:

$$n = \frac{\log m^0(1000\ \mathrm{bar}) - \log m^0(\mathrm{v.p.})}{\log \rho^0(1000\ \mathrm{bar}) - \log \rho^0(\mathrm{v.p.})} \tag{2.10}$$

where $\rho^0(1000\ \mathrm{bar})$ and $m^0(1000\ \mathrm{bar})$ are the density of pure water and the molal solubility of amorphous silica at 1000 bar. $m^0(\mathrm{v.p.})$ and $m^0(1000\ \mathrm{bar})$ can be found by following the work of Fournier and Marshall (1983):

At vapour pressure:

$$\begin{aligned} \log m^0(\mathrm{v.p.}) = {} & -6.116 + 0.01625T - 1.758 \times 10^{-5}T^2 \\ & + 5.257 \times 10^{-9}T^3 \end{aligned} \tag{2.11}$$

At 1000 bar:

$$\begin{aligned} \log m^0(1000\ \mathrm{bar}) & \\ = {} & -7.010 + 0.02285T - 3.262 \times 10^{-5}T^2 \\ & + 1.730 \times 10^{-8}T^3 \end{aligned} \tag{2.12}$$

where T is the absolute temperature.

At this stage, the solubility of amorphous silica under relatively complex conditions can be reasonably predicted.

To conveniently express the degree of supersaturation, a variable called silica supersaturation index (SSI) is defined below:

$$SSI = C_{\mathrm{ds}}/C_{\mathrm{e}} \tag{2.13}$$

where C_{ds} is the concentration of dissolved silica. Hence, SSI>1, SSI=1, and SSI<1 physically means that the brines are oversaturated (or supersaturated, which means a solution is oversaturated, but does not crystallise or deposit), saturated, unsaturated with amorphous silica, respectively.

2.2.3 Formation of colloidal silica

The concept of colloidal silica includes gels and powders (obtained from dried sols, gels, or coacervates) as these are essentially colloids (1 to 1000 nm in diameter particles). However, in this study, as in (Bergna 2003), the term “colloidal silica” is used only to mean discrete, dense particles of amorphous silica smaller than 1.5 μm in diameter dispersed in water. A system of

dispersed unaggregated colloids is conventionally named a sol. For particles in water, it is called an aquasol or hydrosol.

Since the polymerisation process of silica is of great interest in geothermal industries, Weres et al. (1980) extensively studied the polymerisation of dissolved silica in water under varying silica concentration, temperature, pH, and ionic strength. By fitting the experimental data with the Lothe-Pound formalism, Weres el al. (1980) managed to develop a model that can reasonably predict the decreasing concentration of dissolved silica over time due to silica polymerisation in water at the temperature from 23 to 150 ℃ and pH less than 8. Based on the validation study conducted by the thesis author shown in Section4.1.1, this model can also be used to estimate the precipitation rate of dissolved silica under varying conditions as well. Therefore, it is integrated directly into this study for estimating the in situ concentration of dissolved silica and polymerised silica.

2.2.4 Silica surface

The chemistry and structure of the surface of colloidal silica determine many basic properties of the nanoparticles. Significant progress in understanding the surface properties of silica colloids has been made since the 1960s by applying techniques such as IR spectroscopy.

Hofman (1934) hypothesised that there may be silanol groups ($\equiv Si - OH$) on the surface of colloidal silica. Later, with the help of progressing experimental techniques, the hypothesis with respect to the surface groups was proved and broadened to more forms of structures, such as siloxane bridges and rings and the groups hydrogen-bonded with water. All hypothesised groups are covered in the following passages. NMR (nuclear magnetic resonance) Q^n terminology is used to represent that there are n ($n < 4$) oxygen atoms in one tetrahedral unit bonded to the core of the colloidal particle.

Silanol groups

In the case of a solution supersaturated with respect to amorphous silica, silanol groups usually form on the colloid surface due to the polymerisation of $Si(OH)_4$. Such groups may be separated into single, geminal, hydrogen-bonded vicinal (single or geminal), and internal silanol groups.

(a) Single silanol groups

Single silanol groups are also named isolated or free silanol groups. These groups are separated from each other far enough (no closer than 3.3 Å, or 0.33 nm) that hydrogen bonding does not form. NMR Q^n terminology for a single silanol group is Q^3, i.e. there are 3 oxygen atoms from one silica tetrahedron unit bounded to the colloid core, as shown in Figure 2.5 below.

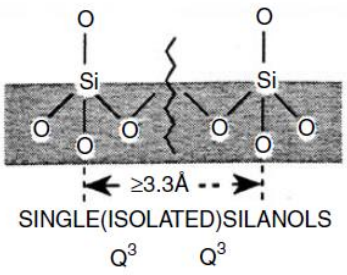

Figure 2.5: Schematic sketch for single silanol groups, reproduced from Bergna 2003.

(b) Geminal silanol groups (or silanediol groups)

Geminal silanol groups differ from the groups described above, mainly because there are two oxygen atoms from one silicate unit anchored on the particle core, as shown in Figure 2.6 below. Therefore, NMR Q^n terminology for a geminal silanol group is Q^2. This type of silica surface groups was hypothesised by Peri and Hensley (Peri and Hensley 1968) and was not observed until solid-state ^{29}Si CP (cross-polarisation) MAS (magic angle spinning) NMR spectroscopy became available.

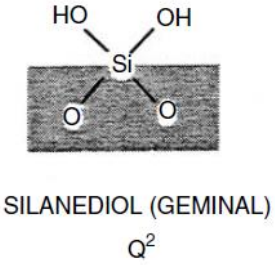

Figure 2.6: Schematic sketch for geminal silanol groups, reproduced from Bergna 2003.

(c) Silanetriols

Silanetriol groups were hypothesised by (Bergna 2003) but have not been experimentally identified yet. If this type of groups exists, NMR Q^n terminology should be Q^1, i.e. there is only one oxygen atom bounded to the colloid core, as shown in Figure 2.7 below.

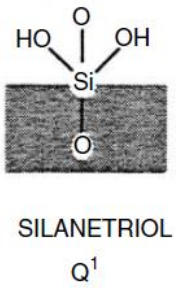

Figure 2.7: Schematic sketch for silanetriols groups, reproduced form Bergna 2003.

(d) Hydrogen-bonded vicinal silanol groups

Opposite to single silanol groups, hydrogen-bonded vicinal silanol groups are the surface silicone groups that are closer than 3.3 Å, or 0.33 nm, the maximum distance allowing hydrogen-bounding to occur, as shown in Figure 2.8 below.

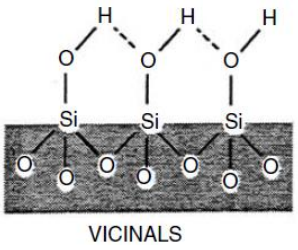

Figure 2.8: Schematic sketch for hydrogen-bonded vicinal silanol groups, reproduced form Bergna 2003.

Based on experimental observations, Hoffman and Knozinger (1987) found that there is another form of hydrogen-bonded silanol group: hydrogen-bonding happens between single and geminal silanol groups as well, as shown in Figure 2.9 below:

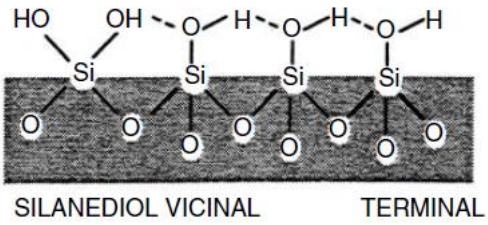

Figure 2.9: Schematic sketch for hydrogen-bonded vicinal silanol groups, reproduced form Bergna 2003.

(e) Internal silanol groups

Silanol groups are believed to exist not only on the particle surface, but also inside the particle. There would be structurally bounded water enclosed by the internal silanol groups as well, shown in Figure 2.10 below.

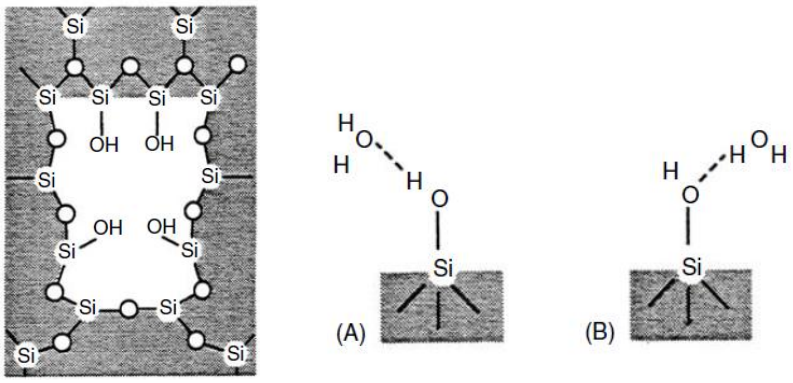

Figure 2.10: Schematic sketch for internal silanol groups (left) and two forms of hydrogen-bounded internal silanol groups with water, reproduced form Bergna 2003.

Similarly, impurities like salt ions that can be adsorbed by hydroxy groups ($-OH$, or dissociated $-O^-$) could be also packed within the silica colloids.

(f) Siloxane bridges

Two $\equiv Si-OH$ groups can lose a water molecule and form a siloxane group ($\equiv Si-O-Si\equiv$, shown in Figure 2.11 below), which is known as condensation. By applying heat treatment at a temperature less than about 500 ℃ (commonly in air), the induced condensation forms a strained siloxane group. This change is fully reversible in water (i.e. capable of rehydroxylation); at higher temperatures, stable siloxane groups form (Unger 1979). Their formation is also reversible, but at a significantly slower rate. It was reported (Zhuravlev 1993) that 5 years were needed to allow a 900 ℃ calcined amorphous silica sample to be fully rehydroxylated in water.

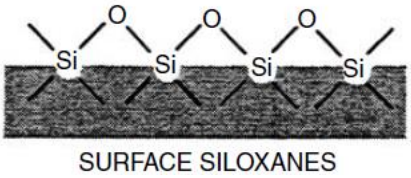

Figure 2.11: Schematic sketch for surface siloxane bridges, reproduced form Bergna 2003.

Based on the knowledge above, it is expected that there would be plenty of hydroxy groups ($-\mathrm{OH}$, or dissociated $-\mathrm{O}^-$) existing on the surface of naturally formed colloidal silica in water. Zhdanov and Kierlev (1957) suggested that the number concentration of hydroxyl groups on the surface of fully hydroxylated silica nanoparticles should be a constant. The silanol number, α_{OH} (number per nm^2), is conventionally used to refer to the constant. Varying α_{OH} has been reported (as shown in Figure 2.12 below), but it is widely accepted that α_{OH} is higher for silica particles formed by precipitation than synthesised pyrogenic silica.

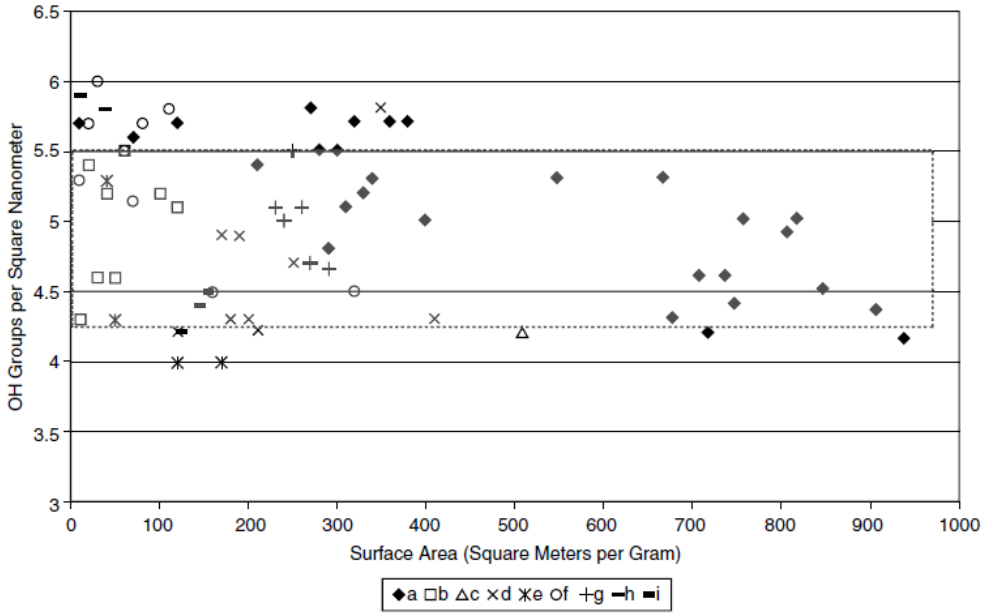

Figure 2.12: Measured surface hydroxyl group concentration over the surface area for one hundred silica samples of nine types (see Zhuravlev 1992), and the averaged α_{OH} is 4.6 per nm^2, reproduced from Zhuravlev 1992.

2.2.5 Aggregation of colloidal silica

Iler (1979) separated the aggregation into four types – gelling, coagulation, flocculation, and coacervation:

(a) Gelling: in a concentrated silica sol, colloidal particles attach to each other and form silica particle chains uniformly spreading the entire volume, i.e. no macroscopically concentrated silica. Since the silica network encloses water, the sol soon becomes viscous, then solidifies.

(b) Coagulation: in a dilute silica sol, particles attach to each other and form silica clusters, which will increase the local silica concentration. The clusters will eventually settle out due to gravity.

(c) Flocculation: in a dilute silica sol, silica particles become linked to the particles of introduced flocculation agents (e.g. hydrolysed aluminium).

(d) Coacervation: particles aggregate and separate out by becoming more hydrophobic. This occurs when the particle surface is enclosed by a layer of matter, which does not directly link the particles like flocculation agents.

If silica nanoparticles do not aggregate or settle at a significant rate, the sol is stable.

In this study, only the aggregation due to silica-silica particle interactions in dilute sols, i.e. coagulation, is of interest.

2.3 Colloidal deposition mechanism

For the purposes of this study, the deposition process of colloidal silica may be separated into two steps: particle transport and attachment.

2.3.1 Particle transport

When studying particle transport, there are two fundamental viewpoints which may be taken: Eulerian and Lagrangian.

The Eulerian method makes observations from fixed points, and describes the particle dynamics in terms of changes in the local concentration at these points. The Lagrangian method takes the viewpoint of a particle or particles moving through the system, and describes the dynamics in terms of the changes in location of that particle(s).

Regardless of which method is chosen, there are always two basic particle transport mechanisms involved in silica scaling: diffusion and convection (Levich 1962).

Diffusion can be classified as either Brownian motion or molecular diffusion.

Brownian motion

Brownian motion, or Brownian diffusion, shown in Figure 2.13, which is the random movement of a single particle. It is a result of collisions between the suspended particle and other moving particles or molecules in the same system. For this mechanism, the interactions among the particles of interest may not necessarily need to be considered.

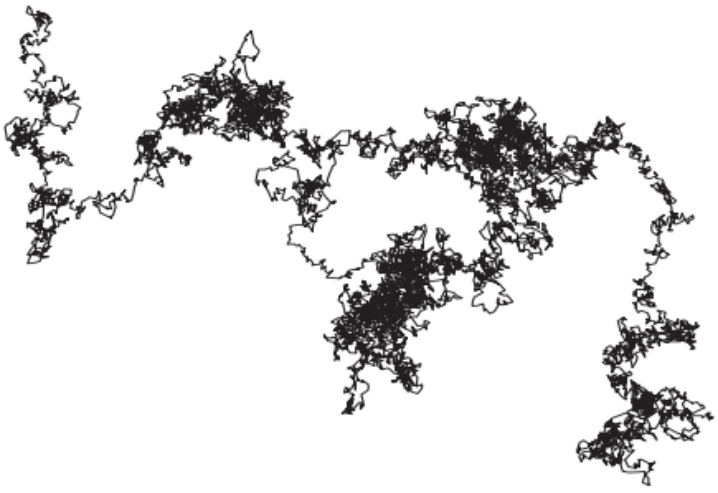

Figure 2.13: Planar Brownian motion of a particle, reproduced from Mörters and Peres 2008.

Molecular diffusion

Molecular diffusion, or diffusion, is the thermal movement of particles in any system with a temperature above absolute zero. The movements are determined by temperature, viscosity of fluid, and the size/mass of particles. Molecular diffusion describes a net flux of particles along a concentration gradient (from high to low). When the concentration gradient becomes zero, the molecules are still moving (Brownian motion), but the net transport due to molecular diffusion ends.

The result of molecular diffusion is that, unless some organizing influence acts on them, the particles of interest will eventually be distributed homogenously, shown in Figure 2.14.

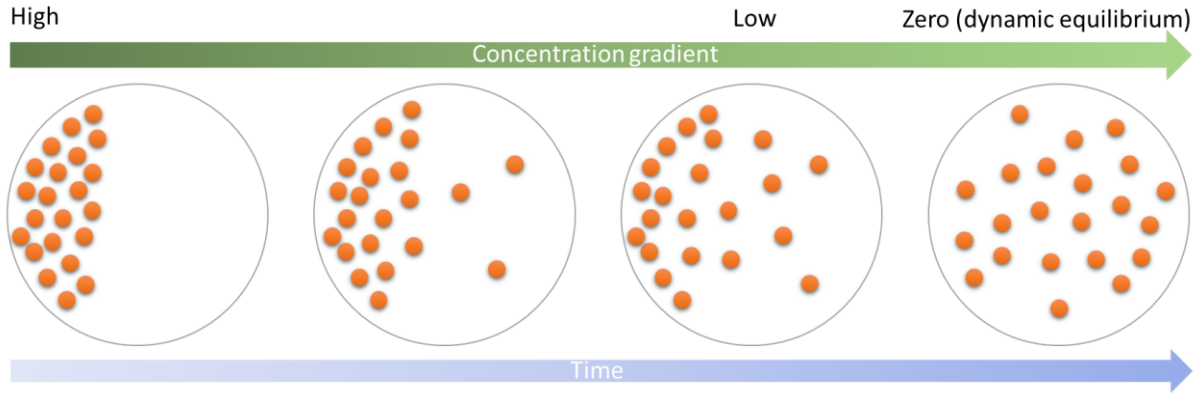

Figure 2.14: Molecular diffusion process.

Convection can be classified as turbophoresis, inertial, or external-force-induced transport.

Turbophoresis

Turbophoresis, shown in Figure 2.15 below, is a tendency of particles to move towards regions of less turbulence. This phenomenon can be explained in the terms of the particles being 'rolled' out from places with high turbulence to places with lower turbulence. It may be explained due to the eddies in low turbulence regions having insufficient momentum, that they cannot impart enough momentum to the particles for them to travel to regions of high turbulence. The result is a net flux of particles moving contrary to the gradient in the fluctuating component of velocity (Schwarzkopf et al. 2011) i.e. from regions of high fluctuation to quiet regions.

Particles with different Stokes numbers behave differently in turbulent flows. Stokes number, named after George Gabriel Stokes, is a dimensionless value describing the performance of particles suspended in a fluid flow, expressed in the following equation:

$$\mathrm{St} = \frac{t_0 u_0}{l_0} \tag{2.14}$$

where, t_0 is the relaxation time of the particles, u_0 is the fluid velocity far away from the obstacle, and l_0 is the characteristic dimension of the obstacle. A particle with a low Stokes number (i.e. St << 1) moves by approximately following fluid streamlines, while another particle with a large Stokes number (i.e. St >> 1) moves in a direction determined by its inertia and tends to continue along its original trajectory, as shown in Figure 2.15.

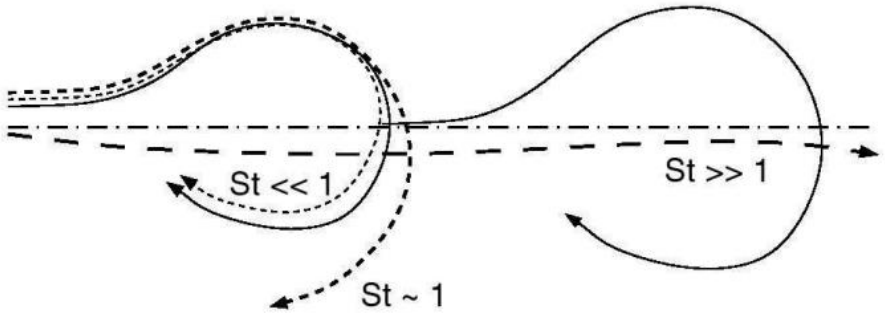

Figure 2.15: Turbophoresis transport of particles with different Stokes number (St): 1. St << 1: particles respond to the eddies of the flow at once; the turbulent particle diffusion is the same as for the fluid; 2. St >> 1: particles are not affected by the turbulence and will retain their previous velocity; the turbulent diffusion is approximately zero; 3. St ~ 1: particles will filter high frequency turbulence fluctuations and will be centrifuged to the peripheries of the turbulent structures. Reproduced from Schwarzkopf et al. 2011.

Inertial transport

In inertial transport, particles travel through a region of fluid with a different velocity without completely equilibrating their velocity with the fluid, as there is insufficient time for the drag forces to achieve this equilibration. A particle with a moderate or high Stokes number (i.e. St ~ 1 or St >> 1) experiencing turbophoresis transport will typically experience inertial transport as well.

External force induced transport

There are five important forces experienced by a single suspended silica nanoparticle: gravity, buoyancy, London-van der Waals force, electrostatic force, and Saffman lift force, as shown in Figure 2.16 below:

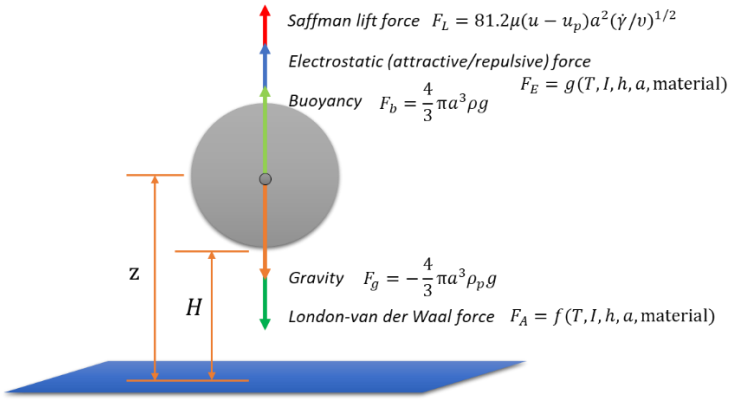

Figure 2.16: five external forces of interest applied on the colloidal silica particle.

London-van der Waals and electrostatic forces are pair interaction forces, exerted by one colloid on another. London-van der Waals force exists between all objects, and electrostatic force appears due to the accumulation of ions in the fluid near the colloid's surface (the electric double layer).

Saffman lift, named after Philip Geoffrey Saffman (Saffman 1965), describes a lift force perpendicular to the flow direction acting on a spherical particle due to the velocity gradient, the viscosity, and kinematic viscosity of the fluid. Saffman showed that, for large tube Reynolds numbers and very small particles, a particle with a velocity (u_{p1}) slower than the flow velocity (u_f) will move towards the axis of the pipe, however particles moving faster than the fluid will transport away from the axis (Saffman 1965), as shown in Figure 2.17.

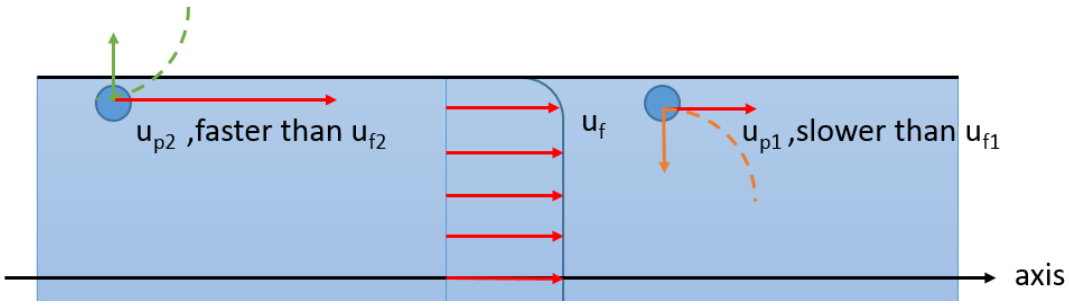

Figure 2.17: The effect of Saffman lift.

2.3.2 Particle attachment

When silica particles reach the surface (the collector) of a pore or fracture in the reservoir formation, it can bind to the surface permanently or temporarily, or keep suspending in the fluids. What can happen may strongly depend on the surface properties of the colloidal silica and the collector.

This is discussed further in Section 3.2 and 6.6.3.

2.4 Observations of silica deposition in geothermal brines

Yanagase et al. (1970) and Rothbaum et al. (1979) carried out several field experiments in Wairakei and Broadlands, New Zealand, respectively, to study the relationship between scaling time and silica scaling. In the experiment, the geothermal liquid was acidified. The scaling samples and rates were analysed and determined. The chemical composition and extrinsic features varied considerably.

Yanagase et al. (1970) found that allowing the silica to polymerise before handling (i.e. ageing) could limit the rate of silica scaling. Hence, they suggested that the ageing process could be a satisfactory method to inhibit silica deposition. However, Rothbaum et al. (1979) had a contrary conclusion: the ageing process could only have limited effects on silica deposition, and it may not be an effective method. Rothbaum et al. (1979) also reported that higher rates of silica deposition were observed in aerated geothermal water, and less silica scaling problems occurred at lower pH.

Weres and Tsao (1981) conducted a silica scaling experiment by using artificial geothermal brines, containing a known amount of hydrochloric acid and other dissolved species to simulate the geothermal liquid in Cerro Prieto, Mexico. At 95 ℃ and pH ~7.35 The deposition rate was observed to decrease from about 1.50×10^{-5} kg m^{-2} s^{-1} to 8.33×10^{-8} kg m^{-2} s^{-1} along the flow direction. Under these conditions, it was suggested that molecular deposition is the dominant deposition mechanism and only a modest fraction of amorphous silica forms colloids and deposit; and a moderate decrease of pH could reduce the silica deposition rates: an approximate three fourths decrement of silica deposition rate was reported when the pH was lowered from 7.35 to 6.5.

Weres et al. (1981) theoretically and experimentally investigated the kinetics of silica polymerisation based on the experiments conducted in the ranges of 0.5 to 1.2 g/L dissolved silica, 50 to 100 ℃, pH 2.5 to 8, 0 to 1 M sodium chloride, and up to 20 ppm fluoride. Weres et al. (1981) considered silica polymerisation as a two-step process: the formation of colloidal silica by homogeneous nucleation, and the silica particle growth due to the deposition of dissolved silica from the ambient solutions to the formed particle surface. By recording the decrease of dissolved silica concentration as a function of time, a semi-empirical model was successfully fitted and developed, which can reasonably predict the polymerisation process and, more importantly, silica molecular deposition rate in a relatively wide range of physical and chemical conditions.

It is suggested (Iler 1979; Weres et al. 1981) that a relatively low pH can limit the silica scaling rate by suppressing the polymerisation of silica. Acidification (i.e. lowering the pH of geothermal brines by adding acid) has been successfully applied in geothermal power plants such as the Hatchobaru power station, Japan (Kiyota et al. 2000), and as a result, the silica deposition rate was observed to decrease and the lifetime of reinjection was expected to be extended.

Mroczek and McDowell (1990) conducted a silica scaling experiment in 6-inch nominal diameter packed gravel beds and 1-inch diameter pipes at the flow rates of 3 and 30 L/min and the temperatures from 120 to 180 ℃. In the temperature range of 160 to 180 ℃, where the polymerisation rate of silica is limited, the silica deposition rate was reported to be a constant through the pipe, which was about 60 mg cm^{-2} $year^{-1}$ (i.e. 1.90×10^{-8} kg m^{-2} s^{-1} or 0.3 mm $year^{-1}$); whereas, in the temperature range of 120 to 140 ℃, where the polymerisation rate of silica is significant, the silica deposition rate was observed to decrease from 150 to 12 mg cm^{-2} $year^{-1}$ (i.e. 1.90×10^{-8} kg m^{-2} s^{-1} or 0.3 mm $year^{-1}$) along the flow direction in the pipe (i.e. from 4.76×10^{-8} to 3.81×10^{-9} kg m^{-2} s^{-1}). Varying the flow rate, it was reported that no significant difference in deposition rate was observed in the pipe. At the higher temperature range (160-180 ℃), the observations in the gravel bed experiments were similar to that in the pipe experiments. However, the silica scale in the gravel beds behaves differently at the lower temperature range: a soft porous silica scale formed near the inlet and rapidly blocked the beds at the flow rate of 30 L/min, but little silica scale was found in the beds at 3 L/min.

Mroczek and McDowell (1990) concluded that the silica deposition rate in pipe was mainly related to the concentration of dissolved silica, and the combination of a higher rock to fluid volume ratio and turbulence could lead to a notable difference in colloidal silica deposition rate when flow rate is varied.

To understand the effects of colloidal silica on silica deposition, Mroczek and Reeves (1994) undertook a silica scaling experiment in the Ohaaki geothermal field by mixing fresh geothermal fluid dissolved with unpolymerized silica and aged geothermal brine suspended with high concentration of colloidal silica and passing the mixed brines through 9 mm diameter X 600 mm long stainless steel tubes at the flow rate of 1 L/min. Mroczek and Reeves (1994) concluded that the silica deposition rate was determined by the concentration of dissolved silica; the deposition rate reached its maximum when the concentration ratio of monomeric to colloidal silica was 4; the morphologies of the silica scale were observed to be soft and porous in all cases; and particle size of silica particles may play a less critical role in silica scaling compared to the concentration of dissolved silica.

Carroll et al. (1998) measured the precipitation rate of amorphous silica in ~0.1 M sodium chloride aqueous solution and in geothermal water samples from Wairakei, New Zealand under

the conditions of pH 3.0-8.7 and 80-120 ℃ in laboratory experiments, and in the field under the conditions of pH ~7-8 and 60-117 ℃. The silica precipitation rates were of order 10^{-12} mol m^{-2} s^{-1} in the lab, and 10^{-10} mol m^{-2} s^{-1} in the field. These experimental results are reproduced in Section 6.4, and model predictions compared to them.

Garibaldi and Freeston (1981) experimentally investigated the effects of hydrodynamics on the silica deposition. A stainless flat plate and a cylinder were tested in a waste geothermal water tank at Wairakei, New Zealand. After a relatively slow scaling process lasting for about a week, a sudden increment of silica deposition rate was observed. On the stainless plate where the Reynolds number is approximately 5000-6000, it was reported that there was no deposition from the leading edge to 10 mm of the plate along the downstream direction; in the next 150 mm, the fibrous scale was observed; and on the rest of the plate, the periodically varying scale was found. On the cylinder, silica deposition was observed to be rapid where the fluid velocity was low, e.g. the stagnation point of a cylinder, but slow where the fluid velocity is high, e.g. the sides parallel to the flow direction. According to these phenomena, Garibaldi and Freeston (1981) suggested that diffusion was the dominant particle transport mechanism; the fibrous scale formed under the effects of the laminar boundary layer, whereas the pulsing deposition formed under the effects of a turbulent boundary layer.

To study the hydrodynamic effects on silica scaling, Dunstall and Brown (1998) developed an experiment apparatus where the flow rate and silica particle size could be controlled, at Wairakei, New Zealand, as shown in Figure 2.18 below:

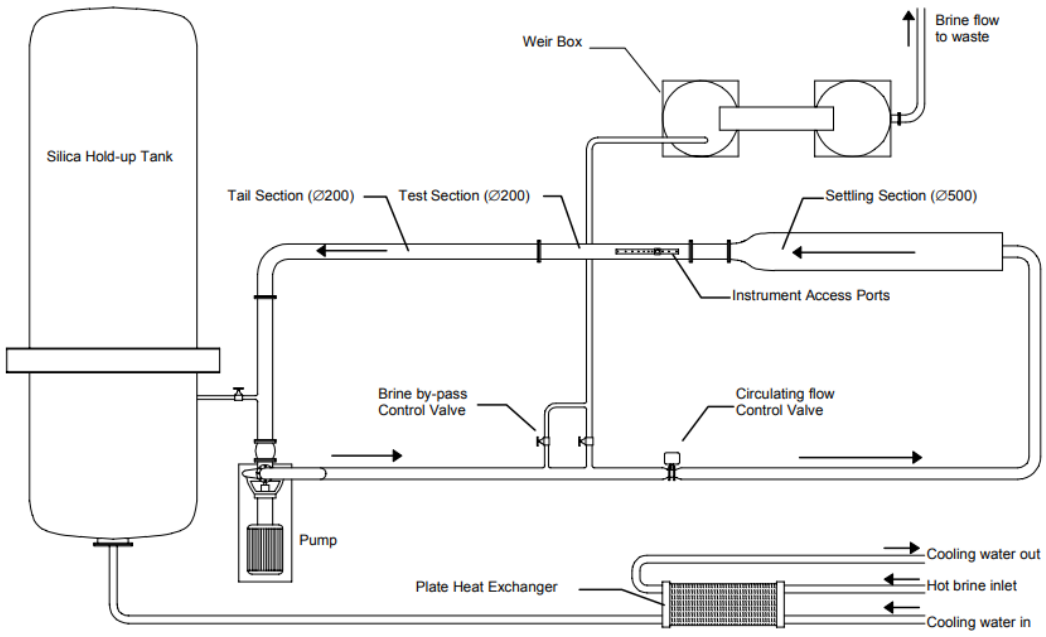

Figure 2.18: The test rig to study the hydrodynamic effects on silica scaling, reproduced from Dunstall and Brown 1998.

Dunstall and Brown (1998) selected a flat plate or a vertical cylinder to place in the test section of the water tunnel as the silica scale collector, as the flow conditions of these two geometries are well known. The test rig was capable of varying the flow velocity from 0.5 to 3 m/s, the temperature from 55 to 75 ℃ based on flow rate, and the silica particle size in diameter from 10 to 150 nm by controlling the ageing time and temperature.

Dunstall et al. (2000) applied this apparatus to investigate the silica scaling on the external surfaces of six 25 mm diameter mild steel pipe (16% tunnel blockage ratio) under the effects of

varying pressure around the cylinder. The flow velocity varied from 1 to 2 m/s and the silica particle size ranged from 25 to 125 nm. Another additional pipe with a tripping wire was used to study the effects of local turbulence, where the silica particle size was fixed to be 75 nm. Dunstall et al. (2000) concluded that the silica deposition occurred rapidly at locations where wall shear stress was high, i.e. the thin boundary layer allowed more particles that have enough momentum to penetrate through a relatively short distance to deposit on the surfaces; the inertia of silica particles played an important role in the deposition mechanism under the effects of turbulence.

Brown and Dunstall (2000) confirmed the existence of hydrodynamic effects on silica scaling but also observed contradictory results compared to Garibaldi and Freeston 1981: no deposition occurred near the stagnation point, whereas Garibaldi and Freeston (1981) reported high deposition rates at the same location. Brown and Dunstall (2000) also suggested that bacteria colonised in geothermal systems by air transfer (Cady et al. 1998) and could have effects on silica deposition, which can be enhanced by the presence of zinc.

Gunnarsson et al. (2010) reported a treatment to reduce silica deposition by ageing and diluting the separated geothermal water using steam condensate, successfully applied in Nesjavellir and Hellisheiði geothermal power plants, Iceland.

The injectivity index II (t hr^{-1} bar^{-1}) quantifies the ease of reinjection, defined by Equation 2.15 below:

$$II = \frac{\text{Mass flow rate}}{P_{\text{inj}} - P_{\text{res}}} \tag{2.15}$$

where P_{inj} is the pressure of the injected fluid and P_{res} is the initial pressure of the reservoir.

Mroczek et al. (2013; 2017) experimentally studied the silica scaling potential of cooled geothermal water saturated with amorphous silica at the Wairakei and Ohaaki fields, New Zealand. Small-scale field experiments at the Wairakei field, had shown a low silica scaling rate after brine (containing 730 ppm silica) was cooled to 30 ℃ and aged for several days before reinjection. Due to this success, the first major large-scale injection of cold (30 ℃) geothermal water in New Zealand was carried out at the Wairakei field. Mroczek et al. (2017) reported that, after a 10-month trial, there was no evidence of any loss of injectivity due to silica scaling. Following the trial at Wairakei, the injectate processed by the same method and ~42% dilution using steam condensate has been successfully reinjected at the Te Mihi Power Station since 2013 (Mroczek et al. 2017). However, in a similar small-scale field investigation at Ohaaki, silica deposition was observed in the rapidly cooled and briefly aged (30 min at 80 ℃) brine containing 840 ppm dissolved and polymerised silica and no other significant difference in brine chemistry. Hence no large-scale field trial at Ohaaki was proposed. Mroczek et al. (2017) suggested the silica scaling at Ohaaki was controlled by the deposition of the dissolved silica near the inlet and the deposition of colloidal silica was accelerated by a corrosion product such as iron ions.

Supercritical geothermal systems have gained more and more interest recently as they are capable of providing more energy to extract than conventional ones. Due to the high temperature and pressure (usually exceeding 400 ℃ and 100 bar) in this case, the geothermal fluid usually contains gaseous silica, which will precipitate once the pressure is lowered. Chauhan et al. (2018) suggested that the solubility of amorphous silica and quartz at such high temperatures and pressures can be predicted using the thermodynamic model proposed in

Karsek et al. 2013. Sigurdur et al. (2015) reported that, in the case of the hottest well around the world, IDDP-1 in Krafla, Iceland, the gaseous silica precipitated and became solid silica once the pressure dropped to less than 80 bar. Another major limitation comes from hydrogen chloride gas in the superheated steam, which becomes highly corrosive when it is condensed or mixed with geothermal brines (usually low enthalpy as well) from the shallower reservoir formation while extracting along the well. Also, when the steam becomes sub-critical and condenses, the hydrogen chloride gas dissolves in the condensed water to form hydrochloric acid. Sigurdur et al. (2015) recommended that the combined method of web scrubbing using simple acid/base chemistry and a controlled pressure drop can be applied to remove silica; to avoid formation of hydrochloride acid and corrosion due to this, deep casings can be used to prevent the mixing of hydrogen chloride gas and the low enthalpy geothermal water, or it is also applicable to inject alkaline separator water below the production zone to condense the steam and neutralise the formed acid. It was concluded (Sigurdur et al. 2015) that the future for utilisation of the supercritical steam can be very promising.

2.5 Simulations of silica deposition

Pott et al. (1996) simulated silica scaling on a flat plate using PHOENICS software, a computational fluid dynamics software package capable of numerically modelling heat and reactive mass transfer in single or multiphase flow. GENTRA is a subroutine of PHOENICS, which uses the Particle-Source-In-Cell method (Crowe 1977) to model the trajectories of particles. Pott et al. (1996) only considered the behaviours of colloidal silica in the early stage (i.e. the interactions between suspended and deposited silica particles were ignored) and modelled the trajectory of only one particle (i.e. the interactions between suspended particles were ignored as well). The driving force due to a concentration gradient, induced by the advection near the plate, was treated as a fictitious force -- the concentration force; apart from the drag force, the gravitational force, and pressure gradient, other variables that may have effects on the particle trajectory, such as London-van der Waals force, electrostatic force, Saffman lift force, were omitted. The modelling results suggested that the silica deposition rate was at its maximum at the leading edge of the plate and decreased along the flow direction, as shown in Figure 2.19 below; and the deposition rate depended on the particle size: smaller particles deposit faster than larger particles. Pott et al. (1996) also predicted that the high deposition rate near the leading edge could result in a scale bump, which could lead to an earlier transition from laminar to turbulent flow and accelerate the colloidal deposition.

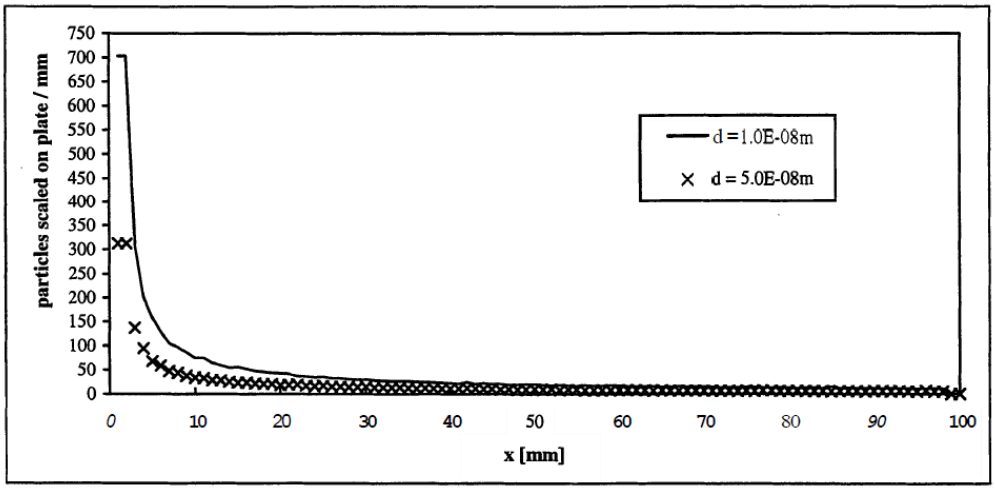

Figure 2.19: Predicted quantity of silica particles deposited per millimetre on the flat plate after 1/500 second, representing the formation of silica scale at the very early stage, where the solid line and the crosses represent the counts of deposited silica colloids of diameters of 1.0×10^{-8} m and 5.0×10^{-8} m respectively. Reproduced from Pott et al. 1996.

Based on an integrated finite difference method to model the fluid flow in porous media proposed by Narasimhan and Witherspoon (1976), Pruess et al. (1999) developed a numerical model, TOUGH2, to simulate the fluid transport in geologic media. Xu et al. (1998; 2001; 2012) introduced TOUGHREACT by integrating the subroutine of chemical reaction modelling to TOUGH2 using a sequential iterative approach (i.e. solving the transport and the reaction equations independently and sequentially in each iteration). It was shown (Xu et al. 2003; Wong et al. 2016) that TOUGHREACT was capable of reproducing the real-world experience of silica scaling in a geothermal reservoir due to reinjection, using empirical silica deposition rates. This can be accurate, but the empirical reaction rate must be estimated for each new set of conditions. A model that predicts it a priori is desired.

By considering the effects of Brownian and turbulent diffusion, turbophoresis, thermophoresis, Saffman lift force, and drag on the motion of silica particles, Chauhan et al. (2018) modelled the transport and deposition of silica under supercritical geothermal conditions using OpenFOAM, an open-source CFD package. The model was applied to simulate the silica deposition from superheated steam. The modelling results (Chauhan et al. 2018) suggested that rapid silica deposition occurs when the relaxation time of silica particles is small (i.e. particle size is small) under the effects of thermophoretic force (i.e. temperature gradient).

Chapter 3

Overview of methodology

This study concentrates on simulation of geothermal injection, using a-priori models where possible, and empirical models where required to make the computational expense practical or where a-priori models of the physics or chemistry are not available yet. The reactive transport of the injectate in an idealised fracture network is comprehensively studied and modelled.

The goal of this study is to build a holistic model that can be useful in predicting the geothermal reinjection lifetime limited by the silica scaling under varying controlling conditions. The aim is to develop a model which can allow users to gain insight into practical problems encountered in geothermal well operation.

Commercial packages like TOUGHREACT (Xu 2008) have been used to model the effects of scale deposition numerically (Xu et al. 2004, Wong et al. 2016), using an empirical method to predict the silica deposition rate (see Chapter 5, Equation 5.11 for details). This can be accurate for one-dimensional problems as it reasonably reflects the surface reaction based on experimental results. However, for two or three-dimensional problems, the deposition is limited by both the mass transfer and the surface reaction rate. Unless tuned to each new problem, the empirical method is no longer applicable in such cases, since experimental results may not cover the range of chemical and hydrodynamic conditions experienced in the well and the fractures, and localised deposition of a small mass of silica (e.g. at well exits) can have an enormous impact on injectivity (defined by Equation 2.15). Hence, a newly developed model may be necessary.

The methodology and the major novelty for this present study are briefly described in the following sections.

3.1 Conceptual ideas for the geothermal reinjection modelling

As mentioned before, the injectivity index is commonly used to reflect the performance of injection wells. Since the hydraulic fracturing is beyond the author's scope, the only reason for the injectivity change is considered to be the dissolution and precipitation due to the reaction (i.e. reactive mass transfer) between the injectate and the reservoir formation, since the hydraulic conductivity (or the permeability) may be respectively increased or decreased depending on which of the mechanisms is dominant. Therefore, the reactive transport modelling of the injectate is of the most interest.

3.2 Transport of heat and mass in the surrounding geothermal reservoirs

In the present work, the transport problem of heat and mass is modelled using the Eulerian method. Based on the law of conservation, a 2D transient convection-diffusion transport equation is defined as the governing equation. The processes that are not or difficult to include in the governing equation, such as the mass created or destroyed in chemical reactions, are separately defined as source or sink terms. One can refer to Section 6.5 for details.

When developing the model, there are a few aspects that should be comprehensively and carefully considered:

1. Geometry

The geometry set up is the cornerstone for the simulations in this work.

The cooled and condensed geothermal fluid is reinjected through the wellbore (Figure 3.1, blue cylinder) and is assumed to only spread along horizontal fracture networks, which are homogeneously distributed in the vertical direction. The geometry is thus axis-symmetric with radial distance from the wellbore represented by R. The reservoir is assumed vertically homogenous, i.e. rock properties are constant over a certain range of depths, and the porous reservoir rock lies between impermeable basement and cap rocks. The model is clearly much simpler than real geothermal reservoirs, but serves to demonstrate the evolution of the silica.

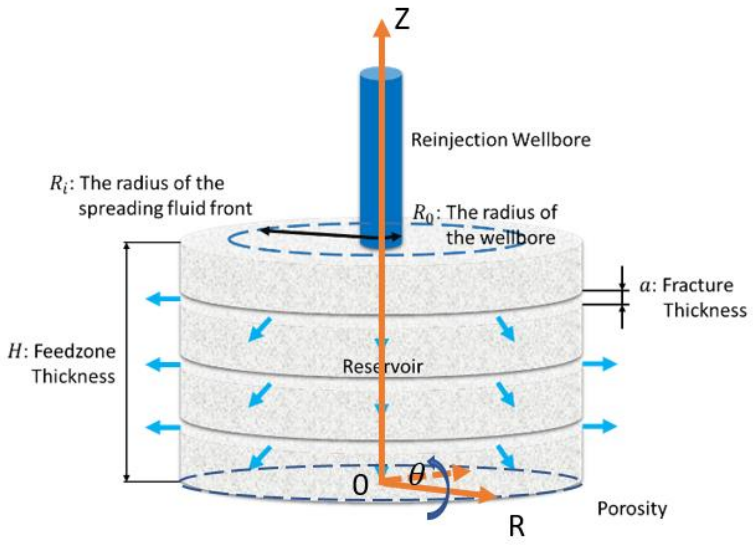

Figure 3.1: Simplified geometry consisting of an injection wellbore and geothermal reservoir.

In a fracture network, there may be preferential flow paths, which make a large contribution to the permeability despite forming a small fraction of the whole porosity. No vertical fracture is considered as the flow path in the following content, representing the non-permeability of caprocks. In the scale of interest, a parallel flat plate model, shown in Figure 3.2, is adopted as the geometric model of the fracture since the radial distance R is bigger than the aperture a by orders of magnitude. Tortuosity of the fractures is neglected.

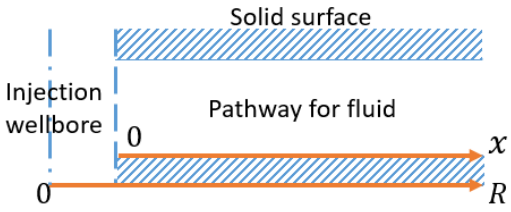

Figure 3.2: Parallel flat plate model showing the radial distance R and the (fluid) spreading distance $x = R - R_0$.

A more detailed description and the corresponding numerical mesh are presented in Section 6.2.

2. Hydrodynamics

Since the fracture is simplified to a set of smooth parallel plates, the hydrodynamics aspect is relatively simple to present. The only problem is that, due to the dissolution and precipitation of minerals, the geometry may vary with time and the injected fluids could be accelerated. Therefore, this could be considered to be a moving boundary problem. The geometry change due to the fluid-rock interaction may be ignored in the present work, considering that the moving boundary can significantly complicate the simulation and the available models such as the formulas shown in Section 6.1.2 have been developed and recognised to be capable of describing the problem.

Future works on this problem may be required. This will be briefly discussed in Chapter 10.

The hydrodynamics model outputs the fluid velocity to heat and mass transport model and estimates whether the effects of turbulence can be ignored.

3. Heat transfer

As the reinjected, cooled geothermal wastewater spreads in the geothermal reservoir. It may eventually arrive the production well, and if the injected fluids have not gained enough heat, the enthalpy of the fluids will be decreased. This phenomenon is called thermal breakthrough and is deleterious to energy extraction. Apart from that, in the reinjection modelling, the temperature plays a critical role in both the kinetics and the thermodynamics of every involved reactive problem. Therefore, the heat transfer in the reservoir due to reinjection is of great interest.

In the present work, four major heat transfer processes are modelled: (1) the heat advection induced by the injected fluids spreading along the radial direction; (2) the heat conduction between the injectate and the reservoir formation; (3) the heat conduction between the injectate and the original reservoir fluids before reinjection; (4) the heat conduction between the reinjection well and the reservoir formation (if the well casing is not heat insulated). The heating from the magma to the reservoir can also be included in the modelling.

Another problem to be addressed is thermophoresis, which is a phenomenon of particle transport due to temperature gradient. Chauhan et al. (2018) modelled particle transport in superheated dry steam where thermophoresis is considered, and suggested that the temperature gradient can accelerate the deposition especially for smaller particles. However, in the case of geothermal reinjection, the modelling results of heat transfer (such as shown in Section 8.1 and Bödvarsson and Tsang 1982) suggest that the temperature gradient near the fluid-rock interface can last for a very short period of time compared to the time scale of interest. Even, in the aspect of heat transfer, according to the modelling results shown in Bödvarsson and Tsang 1982, it

may be reasonable to simplify the problem from two-dimensional to one-dimensional due to this (no temperature gradient in the vertical direction), given the time scale of interest is sufficiently long. One can refer to Section 8.1 for details. Therefore, for simplification, thermophoresis should have least effects in the present work is not considered in the present work, but can be quantified in the future works for greater accuracy.

The heat transfer model outputs the temperature to the chemistry model.

4. Reactive mass transfer (silica transport excluded)

Regarding the reactive mass transfer, the problem is relatively complex. As described before, the term "reactive" physically means that species are creating and destroying due to reactions while transporting through the fluid pathways, i.e. the fractures. The transport is covered by the governing equation, and the reactions are represented using the source or the sink terms, which can be given by modelling the kinetics of each reaction.

While the dissolution and precipitation reactions are occurring, there shall be dissociation and association reactions happening simultaneously. Since the reaction rates of dissolution and precipitation are of most interest in the present work, and these are usually far lower than that of dissociation and association, a global assumption has to be made: the dissociations and associations of the all dissociable and associable chemical species mentioned in the thesis will be treated as instantaneous processes. Therefore, before and at the end of the dissolution and precipitation reactions within one time step, all dissolved species should at their dissociation equilibrium, which is guaranteed by solving coupled formulas derived from the equilibrium constants.

In different geothermal fields, the pressure can vary. Theoretically, the varying of pressure leads to the change of reaction rate. However, in practice, this usually can be considered as negligible for the reactions occurring in solid or liquid phase. In the present work, the injectate is assumed to be in liquid phase only, and therefore, it may be feasible to assume that all reactive processes of interest are independent of pressure.

To conveniently understand how the author develops the chemistry model, the workflow is summarised in Figure 5.25 at the end of this section.

There are a few key chemical species that require attention.

(1) Sodium chloride

The concentration of dissolved chloride in geothermal water essentially determines the ionic strength, which is a very important variable that has effects on the kinetics of almost every considered reaction at different levels.

In the present work, to simply the problem, sodium chloride (or its dissociation product: sodium and chloride ions) is assumed to be chemically inert in the present simulation. This physically means that (1) it will not chemically participate in any modelled reaction, and (2) it will not be created and destroyed during the reactive mass transfer. Therefore, all dissolved species that are not modelled are treated as sodium chloride. The ionic strengths of the two cases are defined to be equal, which can give a pseudo concentration of sodium chloride.

Omitting consideration of multivalent ions such as Al^{3+} is a major simplification. In many cases, at low levels of supersaturation, particles of Al-silicate composition seed formation of silica particles, and Al-silicate will itself form deposits from brine undersaturated in respect to amorphous silica (Newton et al. 2018). Therefore, this is not a safe assumption and can be one

of the drawbacks of the present work, considering a few species such as Al^{3+} can have unique effects, which may not be covered in the applied variables like ionic strength.

(2) Hydrogen ion

Acidification is commonly applied in the geothermal industries to inhibit the formation of colloidal silica (see Chapter 4 for details). It has been proved (Rothbaum et al. 1979; Gallup 1997; Brown 2011; Addison et al. 2015) to be one of the most effective techniques to minimise the silica scaling during the geothermal energy production. More detailed descriptions can be found in Chapter 5.

However, unlike sodium chloride, the concentration of hydrogen ion can be directly varied by the following seven reactions considered in the present work, which are shown in Equation 3.1-3.7 below:

$$H_2SO_4 \leftrightarrow H^+ + HSO_4^- \tag{3.1}$$

$$HSO_4^- \leftrightarrow H^+ + SO_4^{2-} \tag{3.2}$$

$$H^+ + CaCO_3(s) \leftrightarrow Ca^{2+} + HCO_3^- \tag{3.3}$$

$$CO_2(aq) + H_2O \leftrightarrow H^+ + HCO_3^- \tag{3.4}$$

$$HCO_3^- \leftrightarrow H^+ + CO_3^{2-} \tag{3.5}$$

$$CH_3COOH \leftrightarrow H^+ + CH_3COO^- \tag{3.6}$$

$$HF \leftrightarrow H^+ + F^- \tag{3.7}$$

The kinetics of the reactions shown in Equation 3.1-3.7 above is described in Chapter 5. There can be other reactions that can consume hydrogen ion, such as the dissociation of silicic acid ($Si(OH)_4$) and the silanol groups on the surface of silica particles ($\equiv Si - OH$). In practical, this may be negligible as the dissociation of silicic acid is very weak. For instance, at 25 ℃, the dissociation constant of silicic acid is approximately 1.22×10^{-10}, whereas that of acetic acid is about 1.75×10^{-5}. While other conditions are fixed, it is assumed that the concentration of hydrogen ion can only be varied by the reactions shown in Equation 3.1-3.7. Therefore, the in situ concentration of hydrogen ion and pH over time can be found by modelling the reactions above. For simplicity, it should be noted that all pH values referred in the present work are converted to the equivalent pH at the room temperature.

(3) Calcite and carbonate equilibria

Carbonate minerals (most commonly, calcite $CaCO_3$ (Browne 1978)) are common in geothermal reservoir formations. The dissolution of calcite can play a crucial role during the application of acidification. The reaction of the acid with carbonate minerals may rapidly neutralise hydrogen ion and cancel the inhibition effects. Apart from the subsequent silica polymerisation, clogging may occur due to the transport of fragments released from the rock matrix by this dissolution. This is disregarded in the present work as it is strongly dependent on the local rock properties. There are three reactions occur simultaneously: Equation 5.1, and Equation 3.8 and 3.9 shown below:

$$H_2CO_3 + CaCO_3(s) \leftrightarrow Ca^{2+} + 2HCO_3^- \tag{3.8}$$

$$H_2O + CaCO_3(s) \leftrightarrow Ca^{2+} + HCO_3^- + OH^- \tag{3.9}$$

The generated bicarbonate can undergo further reactions:

$$H^+ + HCO_3^- \leftrightarrow CO_2(aq) + H_2O \quad (3.10)$$

$$HCO_3^- \leftrightarrow H^+ + CO_3^{2-} \quad (3.11)$$

Under geothermal conditions (i.e. high pressure), carbon dioxide is always treated as a solute in the system. According to the equations above, it is very important to know the in situ distribution of carbonate species, as these species are the reactants and the products of the calcite dissolution and therefore have significant effects on the dissolution rate. pH (i.e. the concentration of hydrogen ion) will decide the distribution of carbonate species, as the preliminary modelling results shown in Figure 3.3 below.

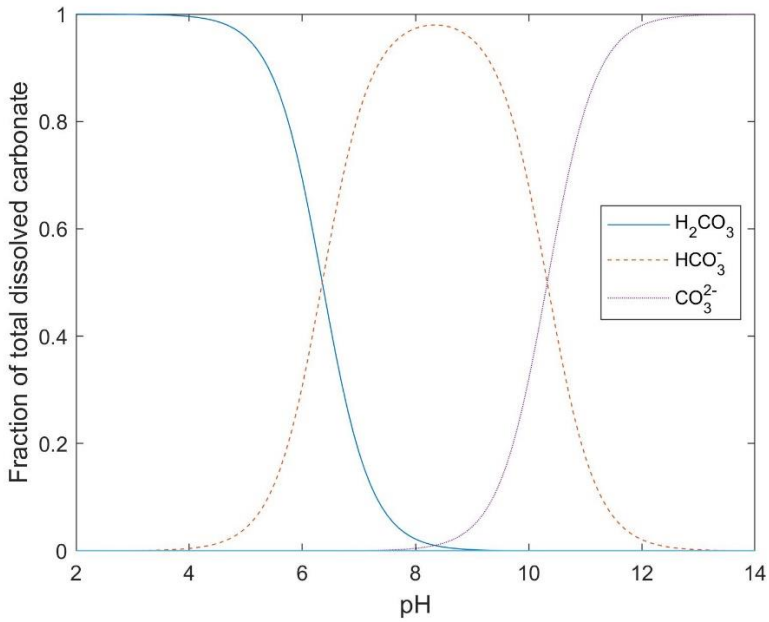

Figure 3.3: Carbonate species distribution as a function of pH.

(4) Calcium sulphate

As mentioned previously, sulphuric acid (H_2SO_4) is commonly used to acidify the injectate, which will increase the risk of $CaSO_4$ precipitation. To estimate the possibility of $CaSO_4$ deposition, the thermodynamics and the kinetics of anhydrite precipitation are studied and modelled, and the estimated concentration of dissolved $CaSO_4$ is constantly monitored while modelling.

(5) Weak acid

As discussed in Section 5.4, weak acids could be a better option than strong acids to inhibit silica scaling in the geothermal industry. The relative effects on silica deposition and reinjection lifetime are modelled to compare the difference between applying strong acid and weak acid.

(6) Hydrofluoric acid

Hydrofluoric acid HF is widely used to dissolve siliceous formations, such as deposited amorphous silica to increase the permeability of the porous media. It may be the only effective chemical method for silica scale removing. The kinetics of silica dissolution in hydrofluoric acid is described in Section 5.5.

To summarise the idea of the chemistry model, the workflow of what is described in this section is briefly shown below:

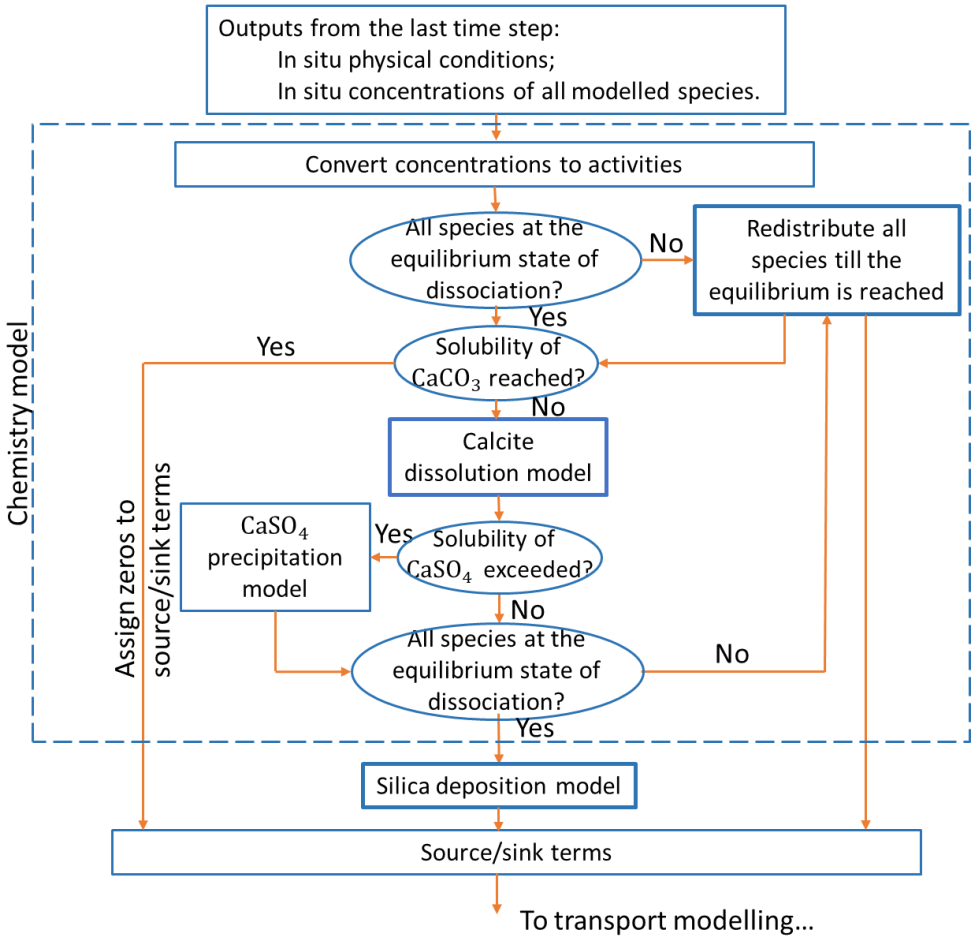

Figure 3.4: Workflow of the chemistry model.

The chemistry model outputs the chemical conditions to the silica transport and deposition model.

4. Silica transport and deposition

The deposition of amorphous silica on rock surfaces involves not only the direct precipitation of dissolved monomeric silica (deposited as single SiO_2 units) but also the deposition of colloidal silica (deposited as particles). When the state is far from equilibrium (i.e. the silica supersaturation index is relatively high, SSI $>$ 1; SSI $\cong$ 1 for the equilibrium), the dissolved silica always tends to polymerise, nucleate, and form silica nanoparticles. The kinetics of silica polymerisation is modelled by following the work of Weres et al. (1980), SILNUC, which is discussed in detail in Section 4.1.1. Given the in situ physical and chemical conditions, the model can estimate (1) the molecular deposition rate and (2) the concentration decrement and increment of dissolved and colloidal silica due to polymerisation respectively.

Depending on the conditions such as the degree of silica supersaturation and ageing time, there may be a preliminary deposition that the "clean" surface (i.e. no silica scale formed on the surface yet) would be covered up by silica and a thin silica layer could form. If molecular deposition dominates, the silica layer is expected to be dense; if colloidal deposition dominates, the silica layer is expected to be porous or "soft". If the former case is favoured, it would be expected that the silica scale may eventually occupy all accessible surfaces; however, if the latter is favoured, it may be more likely that discrete islands or colonies of scale eventually form on the collectors, surrounded by exposed native minerals. This preliminary deposition is assumed to be instantaneous and will be discussed further in Chapter 2.

Depending on whether molecular deposition dominates in the preliminary deposition, colloidal silica deposition in the later stage is considered to comprise two different mechanisms: (1) attachment between the suspended and the deposited silica particles (i.e. particle to particle); (2) attachment between the suspended silica particles and the dense silica layer (particle to plate). These two mechanisms can give different colloidal deposition rate. Theoretically, higher deposition rates are expected in the latter case if all other conditions are the same in both cases. The attachment in the later stage is similar in nature to the aggregation of free-moving colloids in the fluids. The biggest difference is that one object (the particle or the plate) is fixed.

The silica deposition mechanisms will be discussed more detailly in Section 6.6.3.

5. Computation of injectivity

The power model (Verma and Pruess 1988) described in Section 6.1.2 is used to compute the injectivity, as it takes fracture throats into account. The throats of the fluid paths can be one of the drawbacks as those are not included in the proposed geometry. Therefore, it is worth including functions that allow users to estimate the effect of fracture throats where the aperture is narrower. As the fracture throats are essentially the nozzles, the injectate will be accelerated and the corresponding effects are worth being investigated in future works.

3.3 Original work in this thesis

The following contents briefly summarise the novel ideas completed by the thesis author. Further investigations are still required on some topics, which will be discussed in Chapter 8.

1. Silica particle growth model

As described in Section 3.2, the interactions between silica particles (or particle and wall) determine the colloidal deposition rate. Knowing the size of silica particles is the starting point for estimating the total interaction potential, which comprises the attractive potential due to the London-van der Waals force and the repulsive potential due to the electrostatic force. The author proposes a semi-empirical model based on the LSW theory (Lifshitz and Slyozov 1961, Wagner 1961) of Ostwald ripening, used to predict silica particle growth over time under typical geothermal conditions. This is described in Section 4.1.2.

2. Stability model of colloidal silica

It has been shown that the DLVO theory can quantitatively describe the interactions of colloids for certain chemical compositions with reasonable accuracy. However, amorphous silica is an exception. The author adopts the soft particle model developed by Ohshima (2015) attempting to explain the exception and predict the interactions a priori. The soft particle model is a general model to quantify the electrostatic interactions caused by ion-penetrable surface layers of polyelectrolytes. The resulting model provides an explanation of the non-DLVO behaviour of silica particles, which is applied to predict the colloidal deposition rate. This is described in Section 4.2.2.

3. Model of reactive interactions between fluid and rock

Species other than silica are also considered in the present work (shown in Section 3.2). An algorithm to simulate the surface reactions of interest are developed based on experimental data directly. Specifically, the first-hand observations and expressions are revisited and summarised; reference data recorded under geothermal conditions are preferred; extrapolation formulas are developed if the conditions are out of the geothermal range; species that can accelerate or

suppress the reaction rate but are also involved in other reactions are taken into account a priori, such as the effects of dissolved carbon dioxide on the dissolution of calcite. This is described in Chapter 4 and Chapter 5.

4. Two-dimensional coupled heat and mass reactive transfer

Before developing the model to estimate the rate of silica deposition, it is necessary to know the in situ physical and chemical conditions. The author developed a two-dimensional transport model to simulate the heat and mass transfer, coupled with source and sink terms representing the effects of reactions on the mass transfer. This is described in Chapter 4.

5. Prediction of silica deposition rate

As described in Section 3.2, the author proposes a two-stage deposition model. In each stage, depending on many factors such as the degree of silica supersaturation, different mechanisms may determine the deposition rate. The molecular deposition rate is estimated by following the work of Weres et al. (1980); and the colloidal deposition rate is predicted by applying the soft particle model. This is described in Chapter 4.

6. Development of a holistic geothermal reinjection model—*GEOREPR*

All models developed in the present work are integrated and compiled to a holistic model using MATLAB. A finite volume solver is developed to solve the transient convection-diffusion equations. Also, an open sourced object-oriented finite volume MATLAB toolbox, FVTool (https://github.com/simulkade/FVTool), is adopted to reduce code maintenance time. This is described in Chapter 7.

7. Discussions of silica scaling inhibition methodologies based on *GEOREPR*

Concepts for injection stimulation are investigated and discussed with preliminary modelling results using the holistic model. Injectivity may be raised, with actions which affect the reservoir, the formation of scale, or the deposited mass. The discussion of the potential techniques in Chapter 9 includes the dissolution of calcite, control of silica polymerisation and particle formation, removal of silica from injectate, and dissolution of deposited silica.

3.4 Conceptual ideas for the geothermal simulation programme – *GEOREPR*

For simplicity, the code developed, as part of this work, to compute the geothermal reinjection lifetime prediction is named *GEOREPR*. The workflow of *GEOREPR* is shown in Figure 3.5 below.

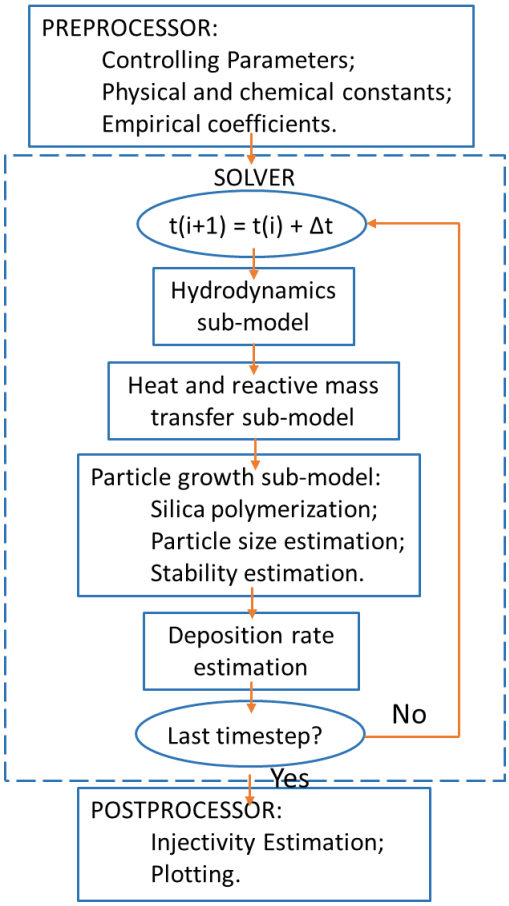

Figure 3.5: Workflow of *GEOREPR*.

The pre-processor is used to pre-process the "raw" inputs so that temporal or spatial parameters can be fed into the sub-models later. The geometry and time are discretised in this module as well, with the spatial mesh forming a series of control volumes in which transport quantities can be computed.

The solver computes in-situ temperature and concentrations of chemical species of interest within a for-loop. It consists of several sub-models. In each control volume, the hydrodynamics model solves the Navier-Stokes equations to find the fluid velocity; the mass and heat transfer models solve transient convection-diffusion equations to find the temperature and the concentration of chemical species; the particle growth model is used to find the stability of colloidal silica by modelling the polymerisation, nucleation, particle growth due to polymerisation, and aggregation. The deposition rate is then estimated by combining the computed results from the mass transfer model and the particle growth model. Finally, the solver records and sums the volume of scale in each time step. Output data for the current time step becomes input data for the next, to allow the time evolution of the system to be simulated.

After all desired time steps are completed, the post-processor receives a two-dimensional matrix representing the volumes of the scale along the fracture with respect to the time steps. Therefore, the injectivity index as a function of time can be estimated and the geothermal reinjection lifetime can be predicted.

Predictions are compared to real-world data to check the validity of the method.

Chapter 4

Chemistry of colloidal silica

Carmen (1940) was the earliest to comprehensively describe the formation of discrete colloidal silica from monomeric silica (silicic acid, $Si(OH)_4$) due to polymerisation. Essentially, the mechanism for silica polymerisation is the repetition of the following reaction:

$$-SiOH + HOSi- \rightarrow -SiOSi- + H_2O \quad (4.1)$$

i.e. the linkage of two $-SiOH$ groups and the formation of one $-SiOSi-$ bond, which is known as condensation.

Iler (1979) represented the formation of colloidal silica in water in terms of the following four steps, under certain physical and chemical conditions without any impurity or pre-existing silica particle that silicic acid can precipitate on (i.e. homogenous nucleation):

1. Polymerisation at the early stage

After a possible induction time during which no decrease of the concentration of dissolved silica can be observed, polymerisation happens especially when the aqueous system is supersaturated with respect to amorphous silica. The linkage of two single silicic acid molecules (i.e. the monomer or monomeric silica) due to polymerisation gives a dimer, and the linkage of more than two silicic acid molecules form oligomers.

2. Nucleation

Since there is a strong tendency among silicic acid to minimise the amount of $-SiOH$ groups but to maximise the quantity of $-SiOSi-$ bonds, ring structures will quickly generate at the early stage of polymerisation and there will be monomeric silica precipitating on the structures simultaneously. This leads to a spherical silica particle having condensed $-SiOSi-$ bonds internally and $-SiOH$ groups externally.

3. Ostwald Ripening

Due to thermal fluctuations, there will be particles formed from the previous step in different sizes. As smaller particles have higher surface energy and are more soluble, since the tendency of any system is to minimise its overall energy, particles above a critical size (usually can be estimated using the Gibbs-Kelvin equation (Gibbs 1961), Equation 4.18) will keep growing and smaller particles will dissolve, resulting in an increasing averaged particle size but a decreasing number concentration of particles.

4. Possible aggregation or gelling

Under proper conditions (relatively low pH and high ionic strength, in general), the rate of the attachment between suspended particles is significantly high. In dilute silica sols, this will result in discrete larger particles or aggregates, which may settle out; whereas in condensed silica sols, this will lead to a three-dimensional silica chained particle network uniformly expanded throughout the whole system, i.e. a gel. Silica gels, comprised of interlinked chains of $-Si(OH)_2-$ groups, form at low pH. Higher pH favors formation of compact, relatively dense particles which will in the presence of salts tend to weakly adhere, coagulate and settle out.

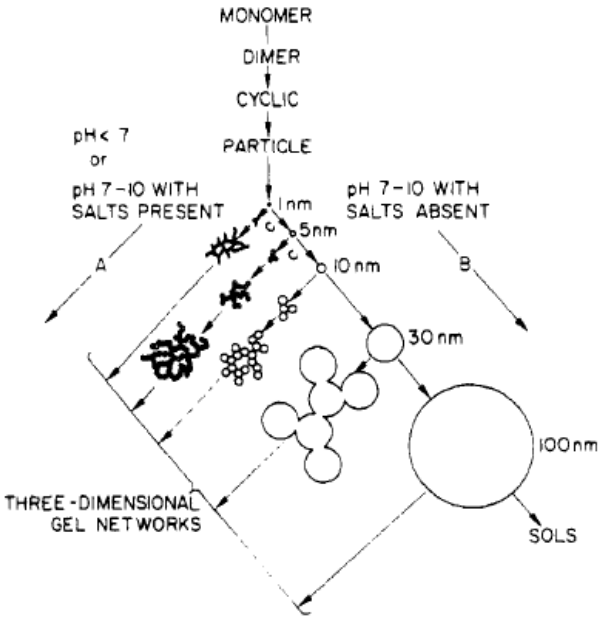

Figure 4.1: Formation of discrete and chained colloidal silica particles, reproduced from Iler 1979.

4.1 Silica polymerisation, nucleation, and particle growth due to precipitation

4.1.1 Kinetics of silica polymerisation

Weres et al. (1980) extensively studied the polymerisation of dissolved silica in water under varying silica concentration, temperature, pH, and ionic strength. By fitting the experimental data with the Lothe-Pound formalism, Weres el al. (1980) managed to develop a semi-empirical model, SILNUC, that can reasonably predict the decreasing concentration of dissolved silica over time due to silica polymerisation in water at the temperature from 23 to 150 ℃ and pH less than 8. However, limitations of the model as originally developed and incorporated in SILNUC are reflected in the present work: notably, the contribution of heterogeneous nucleation, for example in the presence of Al^{3+} in the brine, is not reproduced. Also, ability of the model to depict dissolution of silica particles and therefore also Ostwald Ripening is limited at best; perhaps adequate a $I \approx 0.08$ M, but clearly defective at I = 0.5 and 1.0 M (Figure 13 in Weres et al. 1980. Ionic strengths > 0.5 are rare in New Zealand). These limitations should be kept in mind using the model developed by Weres et al. (1980) and embodied in the SILNUC program.

The model, SILNUC, quantitatively describes two processes: the homogenous nucleation of silica and the subsequent growth due to the molecular deposition of silica on to the surfaces of

the formed particles. At the end of the present time step $\mathrm{d}t$, the concentration of dissolved silica C_{ds} can be represented by:

$$C_{\mathrm{ds}} = C_{\mathrm{ds},0} + \Delta C_{\mathrm{ds}} \tag{4.2}$$

where $C_{\mathrm{ds},0}$ is the concentration of dissolved silica at the end of the last time step, and ΔC_{ds} is the change in the concentration of dissolved silica in the present time step. As the decrement of the dissolved silica concentration over time is determined by the molecular deposition due to the significant large surface areas, ΔC_{ds} can be given by:

$$\Delta C_{\mathrm{ds}} = -j_{\mathrm{md}}\, A_{\mathrm{total}}\, \mathrm{d}t \tag{4.3}$$

where j_{md} is the silica molecular deposition rate, A_{total} is the total surface area of the formed colloidal silica, and the negative sign represents the dissolved silica is being consumed by the molecular deposition.

The silica molecular deposition rate (kg SiO_2 m^{-2} s^{-1}) is given by:

$$j_{\mathrm{md}} = \frac{1}{6}\, F\, k_{\mathrm{OH}}\, f_{\mathrm{f}}\, (1 - SSI^{-1}) \tag{4.4}$$

where the constant 1/6 is added by the author of the thesis to convert the unit used in Weres et al. 1980 (g SiO_2 cm^{-2} min^{-1}) to the SI unit (kg SiO_2 m^{-2} s^{-1}), F is a function of pH and ionic strength I representing the effects of the two variables on j_{md}, k_{OH} is the deposition rate constant and dependent on temperature T only, f_{f} is a fitted function assumed to be proportional to the deposition rate, representing the effects of dissolved silica concentration on j_{md}, and $(1 - SSI^{-1})$ is the term representing the redissolution of deposited silica occurring simultaneously with deposition.

The variable F is defined by:

$$F = h f'_{\mathrm{pH}} + (1 - h) f'_{\mathrm{pHnom}} \tag{4.5}$$

where $h = 0.45$ is a fitted parameter based on the experimental results, and f'_{pH} and f'_{pHnom} are given by:

$$f'_{\mathrm{pH}} = f_{\mathrm{pH}} / 0.118913 \tag{4.6}$$

$$f'_{\mathrm{pHnom}} = f_{\mathrm{pHnom}} / 0.118913 \tag{4.7}$$

$$\log f_{\mathrm{pH}} = f_0 / (1 + 6.2 f_0) \tag{4.8}$$

$$\log f_{\mathrm{pHnom}} = f_{0,\mathrm{nom}} / (1 + 6.2 f_{0,\mathrm{nom}}) \tag{4.9}$$

$$\log f_0 = \mathrm{pH} - 7.6 \tag{4.10}$$

$$\log f_{0,\mathrm{nom}} = \mathrm{pH}_{\mathrm{nom}} - 7.6 \tag{4.11}$$

where $\mathrm{pH}_{\mathrm{nom}}$ is called nominal pH (Weres et al. 1980). It represents contribution of ionised surface silanols which have Na^+ bonded to them, which effectively increases their acid strength. $\mathrm{pH}_{\mathrm{nom}}$ is given by:

$$\mathrm{pH}_{\mathrm{nom}} = \mathrm{pH} + \log([\mathrm{Na}^+] / 0.069) \tag{4.12}$$

where $[Na^+]$ is the activity of sodium ion. At this stage, the variable F can be found.

The variable k_{OH} is defined by:

$$\log k_{\mathrm{OH}} = 3.1171 - 4296.6/T \tag{4.13}$$

where T is the absolute temperature.

The variable f_{f} is defined by:

$$f_{\mathrm{f}} = SSI^5 \quad SSI < SSI_{\mathrm{t}} \tag{4.14}$$

$$f_{\mathrm{f}} = SSI_{\mathrm{t}}^5 + 5SSI_{\mathrm{t}}^4(SSI - SSI_{\mathrm{t}}) \quad SSI > SSI_{\mathrm{t}} \tag{4.15}$$

where SSI_{t} physically represents a "threshold" of SSI (Weres et al. 1980), given by:

$$\log SSI_{\mathrm{t}} = 0.0977 + 75.84/T \tag{4.16}$$

where T is the absolute temperature. At this stage, one can estimate the silica molecular deposition rate j_{md} using Equation 4.5.

By following Abraham 1974, the steady state homogenous nucleation rate ($\mathrm{m^{-3}\ H_2O\ s^{-1}}$) is defined by:

$$I_{\mathrm{N}} = Q_{\mathrm{LP}}\, Z\, j_{\mathrm{md}}\, \rho_{\mathrm{n}}/\rho_{\mathrm{SiO_2}}\, \rho_{\mathrm{H_2O}}\, A^* \exp(-\Delta F^*) \tag{4.17}$$

where, $Q_{\mathrm{LP}} = 3.34 \times 10^{25}\ \mathrm{kg^{-1}\ H_2O}$ is the Lothe-Pound factor, Z is the Zeldovich factor representing the possibility of polymerised silica with critical nucleation size r_{crit} (see Equation 4.18) to form a nucleus and continue to grow, ρ_{n} is the number density of $\mathrm{SiO_2}$ units in the solid phase, $A^* = 4\pi R_{\mathrm{crit}}^2$ is the surface area of the critical nucleus, ΔF^* is the free energy barrier.

The critical nucleation size $R_{crit,0}$ can be found using the Gibbs-Kelvin equation (Gibbs 1961):

$$R_{crit,0} = \frac{2\gamma}{\rho_n k_B T \ln \mathrm{SSI}} \tag{4.18}$$

where γ is the interfacial free energy (i.e. the surface tension, given in Equation 4.20 below), T is the absolute temperature.

The Zeldovich factor is given by:

$$Z = \frac{2}{3}\left(\frac{3}{4\pi\rho_{\mathrm{n}} n^{*2}}\right)^{\frac{1}{3}}\left(\frac{\gamma}{k_{\mathrm{B}}T}\right)^{\frac{1}{2}} \tag{4.19}$$

where $n^* = 4/3\ \pi r_{\mathrm{crit}}^3\, \rho_{\mathrm{n}}$ is the quantity of $\mathrm{SiO_2}$ in one critical nucleus, and γ is the surface tension in $\mathrm{J\ m^{-2}}$, given by:

$$\gamma = [63.68 - (0.049 + 0.2174\ I)\ T]\ 10^4 \tag{4.20}$$

Where the constant 10^4 is used for converting the unit from ergs $\mathrm{cm^{-2}}$ to ergs $\mathrm{m^{-2}}$, T is the absolute temperature, and I represents the effects of pH and sodium ions on the surface tension and is empirically defined by following Equation 4.21-4.23:

$$I = 0.45\ i_{\mathrm{pH}} + 0.55\ i_{\mathrm{pHnom}} \tag{4.21}$$

$$\log i_{\mathrm{pH}} = -0.75924\ +\ 0.58993\ (\mathrm{pH} - 7.6)\ - 0.11292\ (\mathrm{pH} - 7.6)^2 \tag{4.22}$$

$$\log i_{\mathrm{pHnom}} = -0.75924\ +\ 0.58993\ (\mathrm{pH_{nom}} - 7.6) - 0.11292\ (\mathrm{pH_{nom}} - 7.6)^2 \tag{4.23}$$

The free energy barrier can be estimated using:

$$\Delta F^* = \frac{\gamma A^*}{3k_B T} \tag{4.24}$$

where k_B is the Boltzmann constant in J K^{-1}. At this stage, one can use Equation 4.17 to find the nucleation rate.

Within each timestep dt, the total surface area of formed silica particles A_{total} can be described by:

$$A_{total} = A_{total,0} + \Delta A_{total} \tag{4.25}$$

where $A_{total,0}$ is the total surface area at the end of last time step, and ΔA_{total} is the change of the total surface area in the present time step dt. Hence, ΔA_{total} can be defined by:

$$\Delta A_{total} = A^* I_N \, dt \tag{4.26}$$

At this stage, one can eventually estimate the concentration of the dissolved silica due to silica polymerisation over time by iterating Equation 4.2.

The computer code of the model described above, SILNUC, was originally written using MNF4 FORTRAN (Weres et al. 1980), which the author of the thesis is unfamiliar with. Therefore, SILNUC was reproduced in MATLAB by following the formulas presented above. For convenience, a MATLAB app was developed as well, which includes a user interface to ease the modelling, as shown in Figure 4.2 below.

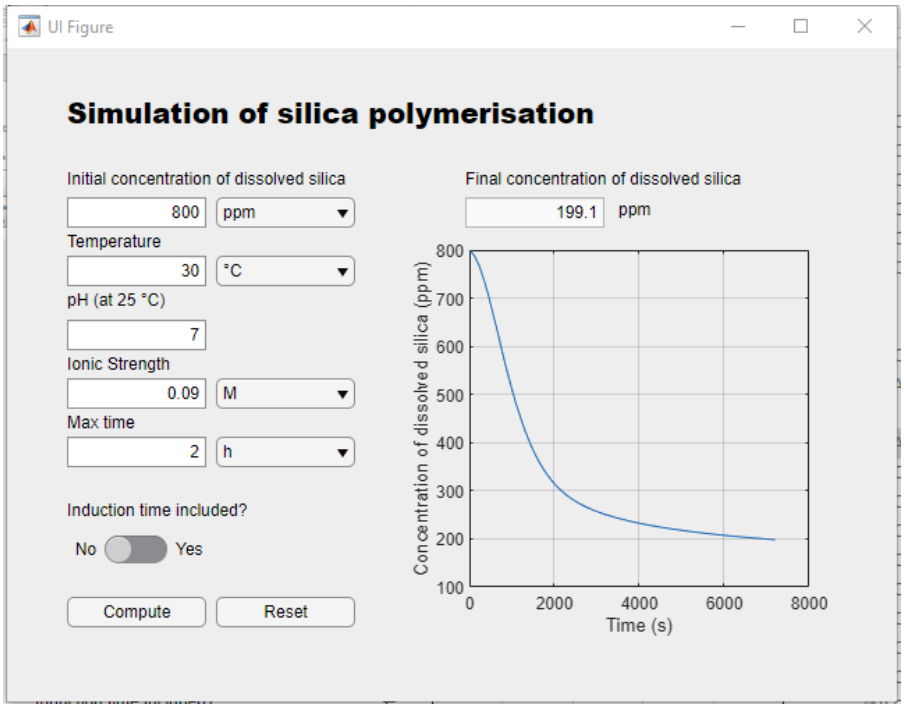

Figure 4.2: The user interface of the reproduced SILNUC in the form of MATLAB app.

To verify that the model was reproduced correctly, the experimental results of silica polymerisation in Weres et al. 1980 were used to compare with the predictions made by the reproduced SILNUC in MATLAB. For simplicity, only one comparison is shown in Figure 4.3 below. The corresponding experimental conditions were that the initial concentration of dissolved silica $C_{ds,i}$ was about 1000 ppm, pH was about 6.23, the total concentration of the introduced sodium ion C_{Na^+} was about 0.09 M, and the temperature was 50 ℃.

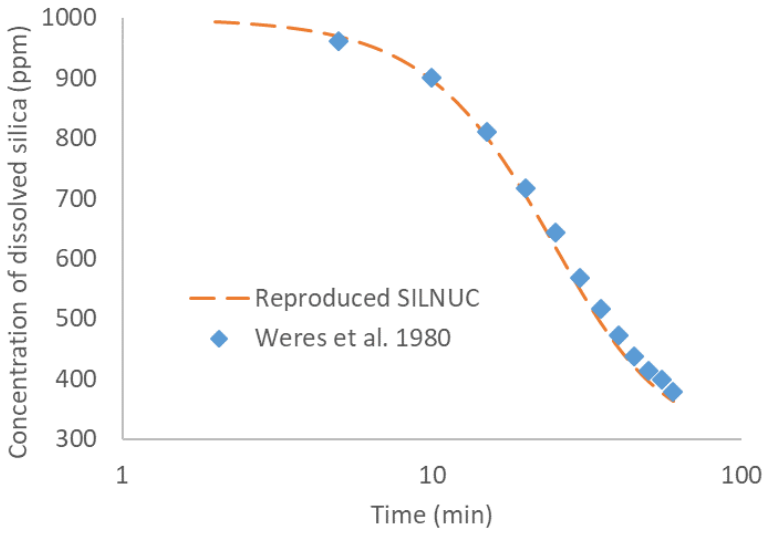

Figure 4.3: Comparison between the prediction made from the reproduced SILNUC in MATLAB and the observation under conditions $C_{ds,i} = 1000$ ppm, pH $= 6.23$, $C_{Na^+} = 0.09$ M, and $T = 50$ ℃ reported in Weres et al. 1980.

Another validation is conducted against Tobler and Benning (2013). The comparison can be seen in Figure 4.4 below:

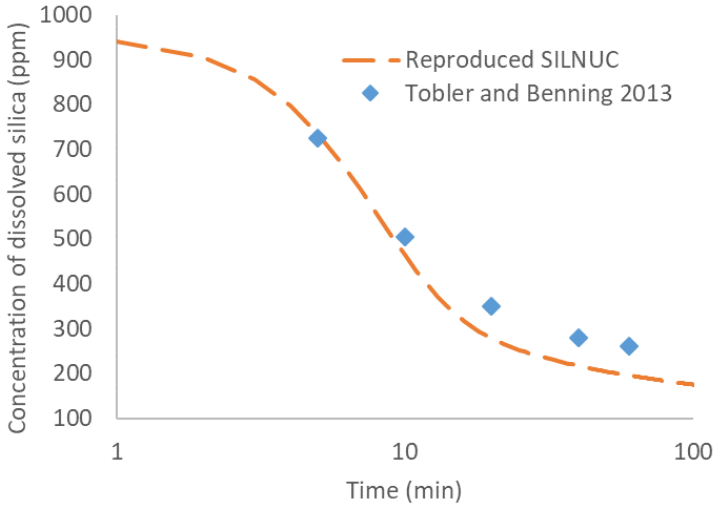

Figure 4.4: Comparison between the prediction made from the reproduced SILNUC in MATLAB and the observation under conditions $C_{ds,i} = 960$ ppm, pH $= 7$, $C_{Na^+} = 0.06$ M, and $T = 30$ ℃ reported in Tobler and Benning 2013.

Hence, the concentration decrement of dissolved silica in the case of geothermal reinjection can be reliably predicted with acceptable accuracy. This is further discussed in Chapter 8.

4.1.2 Particle growth

In most high enthalpy geothermal fields, homogeneous nucleation is suggested (Weres et al. 1981) to be the dominant mechanism of initial silica particle formation. Molecular deposition of monomeric silica to the particle surface should also be taken into account. Iler (1979) showed that, at pH above 6-7, polymerisation and nucleation happen rapidly as the degree of ionisation

is relatively high. Small silica particles of 1-2 nm diameter can form in minutes. It is suggested (Vysotskii and Strazhesko 1974) that there are two fundamental mechanisms of silica particle growth in water after nucleation:

1. Growth due to the precipitation of that silicic acid which is already in the solution, onto nuclei surfaces;

2. Growth of larger particles due to the dissolution of smaller particles, i.e. Ostwald Ripening.

At later times, Ostwald ripening and aggregation may be the main mechanisms of particle growth, since the first mechanism becomes slower than the second when the degree of silica supersaturation is reduced by polymerisation.

An in-situ particle size measurement experiment (Tobler et al. 2009, Tobler and Benning 2013) showed that colloidal silica particles first appear at a size very close to the critical nucleation size, then rapidly grow, then the growth rate reduces, and eventually the average particle size may converge to a certain definite value (i.e. asymptotically approaching a definite size), as shown in Figure 4.5 below. This is suggested to be a consequence of limited supply of silica, and further growth can occur when new silica is added to the solution, but nucleation cannot (i.e. no new nuclei are produced, Weres et al. 1980; Brown 2011).

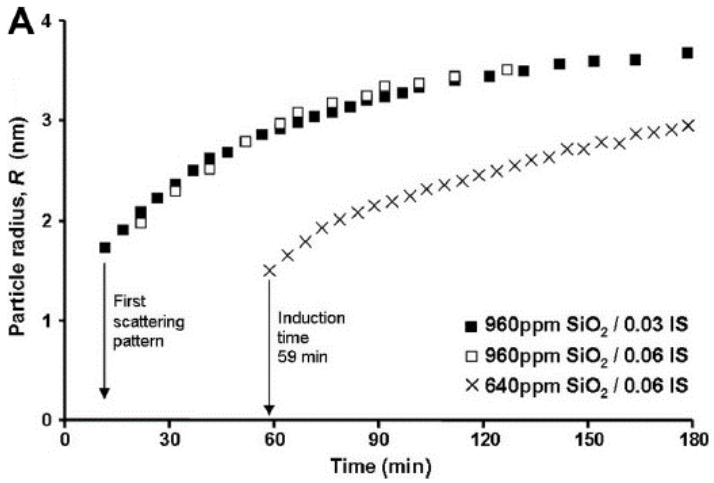

Figure 4.5: Particle radius as a function of time, observed by rapid cooling 230 ℃ solutions dissolved with 640 or 960 ppm silica and 0.03 or 0.06 M sodium chloride to 30 – 60 ℃, reproduced from Tobler and Benning 2013.

Iler (1979) conducted an experiment by heating silicic acid solutions at 100 ℃ for 48 hours at a constant initial SiO_2: Na_2O ratio of 190:1. The following observations were reported:

Table 4.1: Effects of varying silica concentrations on the final particle diameter at a constant SiO_2: Na_2O ratio, reproduced from Iler 1979.

% SiO_2	Initial pH	Final pH	Particle Diameter (nm)
7.75	8.59	9.9	13.5
3.0	8.91	9.9	13.4
1.0	9.26	9.66	12.5
0.3	9.63	9.25	13.1

According to the experimental results, when silica particle growth ceased, it was found (Iler 1979) that, when the initial SiO_2: Na_2O ratio was a constant, the final average particle size was independent of the initial silica concentration; and the final average particle size might be dependent on temperature only. The SiO_2: Na_2O ratio was used as a metric by Iler (1979) as, when synthesising the colloidal silica samples, to trigger the nucleation, sodium oxide (Na_2O) was usually added to silicic acid solutions. Hence, sodium hydroxide (NaOH) was produced so that pH could be increased. At high pH, where most of the surface silanol groups are ionised, the ratio of NaOH to SiO_2 in the sol determines the surface to volume ratio of the particles and therefore their size. The behaviour will differ at lower pH values, where only a fraction is ionised.

This conclusion was supported by the observations reported by Alexander and McWhorter (1976) and Broge and Iler (1971), who studied silica particle growth in aqueous solutions at high temperatures and superatmospheric pressures. The results are reproduced in Table 4.2 below:

Table 4.2: Experimental results obtained by heating 4% silicic acid at pH 8-10, reproduced from (Alexander and McWhorter 1976; Broge and Iler 1971). Note: limited by the experimental technique at that time, the particle size could only be indirectly obtained based on parameters like specific surface area

Mole Ratio SiO_2: Na_2O	Time	Temperature (°C)	Specific Surface Area ($m^2 g^{-1}$)	Estimated Particle Diameter ($m\mu$)
100	1 hr	80	600	5
64	6 hr	85	510	6
100	5 hr	95	420	7
78	6 hr	98	406	7
80	30 min	100	350	8
85	3 hr	160	200	15
85	3.25 min	270	200	15
85	0.9 min	250	225	15
90	3.1 min	200	271	10
85	10 min	200	228	12
85	10 min	295	78	36
85	30 min	295	—	64
Very high[a]	3 hr	340	—	88
Very high[a]	6 hr	340	—	105
Very high[a]	3 hr	350	20	150

[a] Traces of sodium ions remaining in the starting particles after deionization of the sol before autoclaving resulted in a pH of about 8 in the final sol.

It was observed that the final particle size increases with rising temperature when the initial SiO_2: Na_2O ratio is fixed. Further investigations by Iler (1979) showed the effect of temperature on final silica particle size even more clearly (see Figure 4.6 and Figure 4.7 below).

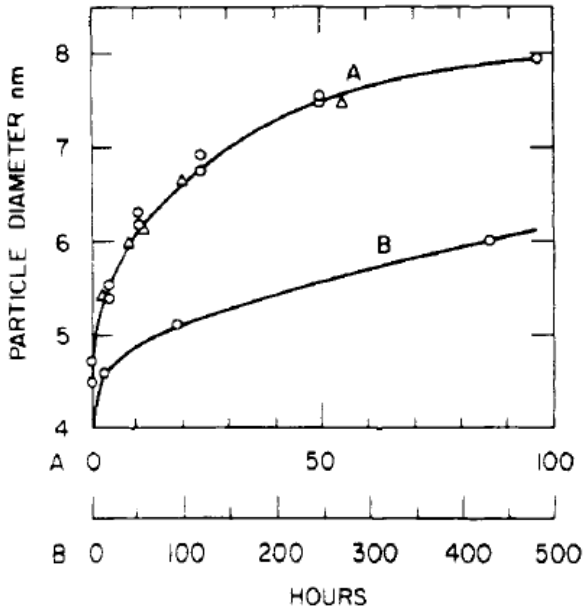

Figure 4.6: Silica particle growth over time in 3% SiO_2 aqueous solution where initial SiO_2: Na_2O and pH are fixed to 102 and 8.5 respectively, at 90 ℃ (A) and 50 ℃ (B), reproduced from (Iler 1979).

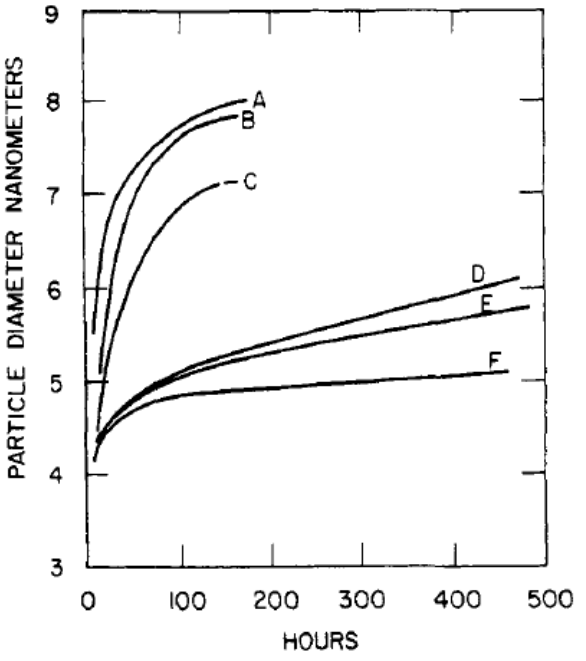

Figure 4.7: Particle growth of pre-existing 3.5 nm silica particles over time at varying SiO_2: Na_2O ratios and other conditions shown in Table 4.3.

Table 4.3: Conditions for the experimental results shown in Figure 4.7

Curve	Temperature (°C)	SiO_2: Na_2O	pH
A	90	97	8.8–9.7
B	90	186	7.9–9.7
C	90	470	7.1–8.1
D	50	97	8.8–9.0
E	50	186	7.9–8.4
F	50	470	7.1–7.5

It is clear from the above mentioned studies that when the initial SiO_2: Na_2O ratio is fixed, the final particle size rises with temperature, at least when the ratio is in the range 64 – 470 as used in those studies. However, under typical geothermal conditions, the ratio can be significantly higher than 470. For instance, for an ideal injectate dissolved with 1000 ppm silica and 0.09 M sodium chloride only at pH 8 and the room temperature (i.e. $[OH^-] \approx 10^{-6}$ M), the initial SiO_2: Na_2O ratio is about 5202.

If the finding that final particle size is determined by temperature still holds to be true under geothermal conditions, it would be of interest in the present study as it may be feasible to assume the initial SiO_2: Na_2O ratio in the injectate is fixed: if the temperature of the injectate is lowered by cooling before reinjection, smaller particles may form as nucleation is faster due to the greater degree of supersaturation, creating many more particles, which are expected to be more colloidally stable than the larger particles generated in higher temperatures under same chemical conditions, due to the lower attractive potential for the smaller particles.

Although one cannot simply predict that the deposition rate will be decreased due to the higher stability of the smaller particles, as their number concentration will be higher, there may be a noticeable difference in morphology of the silica scale.

More recently, in-situ and time-resolved observations of silica particle growth were made by Tobler et al. (2009; 2013). At room temperature, to trigger the formation of silica particles, acid was added to the solutions of 640 or 1600 ppm silica and 0.02, 0.05, 0.11, or 0.22 M sodium chloride to adjust pH from 12 to neutral in (i.e. pH-induced growth) Tobler et al. (2009); rapid cooling of the solutions of 640 or 960 ppm silica and 0.03 or 0.06 M sodium chloride from 230 ℃ to 30 – 60 ℃ (i.e. temperature induced growth) was used to trigger particle formation in Tobler and Benning (2013),. Both of the experiments were monitored using synchrotron-based small angle X-ray scattering (SAXS) and dynamic light scattering (DLS). After comparing with both the pH-induced and T-induced experiments, Tobler and Benning (2013) concluded that the final particle size depends on temperature but may not depend on concentration of silica, nor on ionic strength, nor on the methods that induce the silica particle formation, but the induction time and the growth rate may depend on these parameters.

4.1.2.1 Kinetics of particle growth

Nielsen (1964) proposed three mechanisms to describe the processes of colloidal particle growth after nucleation: diffusion controlled, mononuclear, and polynuclear growth.

For diffusion limited spherical particle growth, Nielson (1964) suggested that the growth rate can be expressed by:

$$\frac{dR}{dt} = \frac{D(c_b - c_s)\bar{v}_n}{R} \tag{4.27}$$

where R is the radius of the particle, t is time; for the precipitating species, D is its diffusion coefficient, c_b is its concentration in the bulk solution at time t, c_s is its concentration on the particle surface, and $\bar{v}_n$ is its molar volume, which is about 0.027 m^3 per 1000 mol for amorphous silica (Rumble and CHEMnetBASE 2017). Since the particle surface is recognised as the interphase boundary, it may be feasible to assume that, for the diffusion-controlled mechanism, c_s is equal to the solubility of the precipitating material c_e. Then, Equation 4.27 becomes:

$$\frac{dR}{dt} = \frac{D(c_b - c_e)\bar{v}_n}{R} \tag{4.28}$$

For surface controlled spherical particle growth (the diffusion is relatively rapid when compared to the surface reaction rate, i.e. $c_b \approx c_s$), two mechanisms are involved: mononuclear and polynuclear. Mononuclear growth physically represents the mechanism of a layer-by-layer precipitating process, i.e. a subsequent layer begins to form only when the formation of its previous layer is complete. The growth rate following the mononuclear growth mechanism can be described by:

$$\frac{dR}{dt} = k_m c_b^m R^2 \tag{4.29}$$

where, for the mononuclear surface reaction, k_m is its rate constant, and m is its reaction order.

Whereas, for polynuclear growth, the subsequent layer can start to grow before the growth of the previous layer is completed. The growth rate dominated by the polynuclear growth mechanism can be defined by:

$$\frac{dR}{dt} = k_p c_b^p \tag{4.30}$$

where, for the mononuclear surface reaction, k_p is its surface reaction rate constant, and p is its reaction order.

Williams et al. (1985) suggested that all three of these mechanisms may be involved in the growth of colloidal particles. For the initially formed nucleus, mononuclear growth may be important; polynuclear growth could be dominant when the nanoparticles grow bigger; in the later stage, diffusion limited growth should be critical. In practice, the mononuclear growth mechanism is usually not considered as it is expected to have effects only in the very early stage (Nishimori et al. 1996).

Chronomal analysis

As suggested by (Nishimori et al. 1996), the present work will only consider two particle growth mechanisms that may have significant effects on the silica particle growth after nucleation: polynuclear and diffusion-controlled. To identify which of the two mechanisms dominates, Nielsen's chronomal analysis (Nielsen 1964) can be used.

The reaction degree α is defined by the amount of a certain species reacting at time t, over the total quantity of the species that can participate in the reaction:

$$\alpha = \frac{c_0 - c_b}{c_0 - c_e} \tag{4.31}$$

where c_0 is the initial concentration of the precipitating species.

An approximation was proposed by Nielson (1964) to correlate the reaction degree α and the particle radius R at time t:

$$\alpha = \left(\frac{R}{R_e}\right)^3 \tag{4.32}$$

where R_e is the final particle radius.

For the diffusion-controlled mechanism, by combining Equation 4.28, 4.31, and 4.32, the time t can be described using the chronomal I_d:

$$t = \frac{R_e^2}{3\bar{v}_n(c_0 - c_e)} I_d \tag{4.33}$$

And the chronomal I_d, which may be physically understood as a dimensionless time, is defined by:

$$I_d = \int_0^a x^{-\frac{1}{3}} (1-x)^{-1}\, dx \tag{4.34}$$

The chronomal I_d can be solved using standard methods (LaMer and Dinegar 1950):

$$I_d = \frac{1}{2}\ln\frac{1-\alpha}{(1-\alpha^{1/3})^3} - \sqrt{3}\tan^{-1}\frac{\sqrt{3}}{1+2\alpha^{-1/3}} \tag{4.35}$$

Similarly, for the polynuclear mechanisms, the time t can be expressed using the corresponding chronomal I_p:

$$t = \frac{R_e}{3\bar{v}_n c_0^p k_p} I_p \tag{4.36}$$

In this case the chronomal I_p is defined by:

$$I_p = \int_0^a x^{-\frac{2}{3}} (1-x)^{-p}\, dx \tag{4.37}$$

Although the solution to Equation 4.37 may not be easy to express explicitly like Equation 4.35, one can still find it numerically.

To identify whether the particle growth after the nucleation is fully diffusion limited, one can use Equation 4.33 to predict the degree of reaction α over time, and then compare it with experimental observations. Similarly, by substituting experimental results, i.e. the particle size, or the degree of reaction, as a function of time, into Equation 4.36 and 4.37, one may obtain a set of fitted parameters: the reaction rate constant k_p and the reaction order p. By considering the fitted values in the light of the physics of the known growth mechanisms, one can conclude whether the particle growth is following the surface reaction-controlled or the diffusion-controlled mechanism.

JMAK model

Alternatively, the Johnson-Mehl-Avrami-Kolmogorov (JMAK) theory (Avrami 1939) may be used to model the phase transformation as well. It is based on the following assumptions: (1) the nucleation process is macroscopically homogenous but microscopically random, (2) the growth rate is independent of the fraction of phase transformation (i.e. what proportion of the material has experienced a phase transformation), and (3) the growth is isotropic, i.e. growing

in all directions at the same rate. The Avrami equation (Avrami 1939) was derived to describe the fraction of transformed species α:

$$\alpha = 1 - \exp[-k_a(t - t_0)^n] \tag{4.38}$$

where k_a is the reaction constant, and the exponent n was suggested by Hulbert to be dependent on the mechanisms of nucleation and growth and the growth dimensionality. For the case of spherical particles formed by the surface reaction-controlled mechanism, n should be equal to 4 for the stage of homogenous nucleation and equal to 3 for the stage of subsequent particle growth (Hulbert 1969).

The Avrami equation can be expressed in logarithmic form:

$$\ln(-\ln[1 - \alpha]) = \ln k_a + n \ln(t - t_0) \tag{4.39}$$

If an experimental observation follows the JMAK kinetic model, a straight line should be obtained in a plot of $\ln(-\ln[1 - \alpha])$ over $\ln(t)$, which is conventionally named the Avrami plot.

By assuming that the silica particle growth is limited by surface reaction (i.e. polynuclear growth mechanism), Tobler et al. (2009) fitted their experimental results with both the chronomal and JMAK models, as shown in Figure 4.8 and Table 4.4.

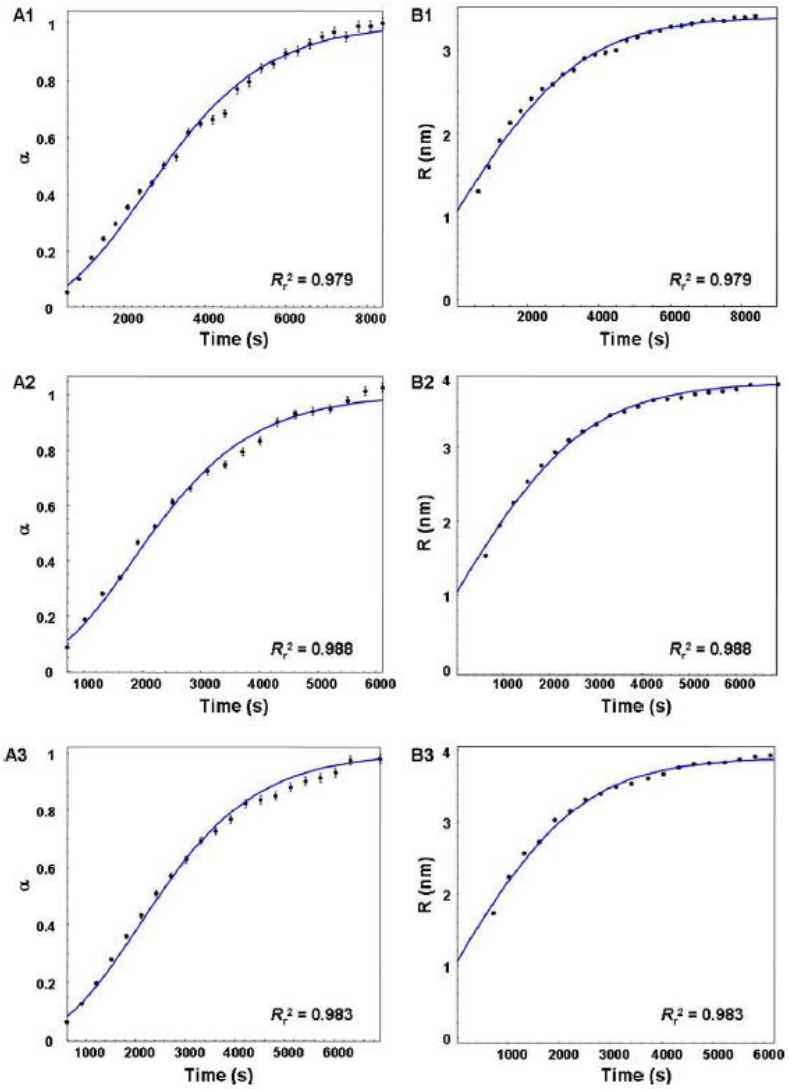

Figure 4.8: The reaction degree α (A1-3) and the silica particle radius R (B1-3) over time, fitted with the chronomal model. A1 and B1, A2 and B2, and A3 and B3 were observed in aqueous solutions oversaturated with 640 ppm silicic acid at the room temperature, neutral pH, atmospheric pressure, and 0.02, 0.11, and 0.22 M ionic strength respectively, reproduced from Tobler et al. 2009.

Table 4.4: Summary of the parameters obtained by postprocessing experimental results, reproduced from Tobler et al. 2009: the initial particle growth rate G_0 and the reaction constant k_p were fitted with the chronomal model; the estimated radius of nuclei R_0^+ and R_0 was respectively obtained by using the theoretical expression Equation 4.18 (assuming the surface tension is fixed at 77.9 ± 3.4 erg cm^{-2}, which is reproduced from Tobler et al. 2009; other resources such as Weres et al. 1980 estimated this mostly in the range $40 - 45$ erg cm^{-2} under similar conditions) and extrapolating the fitted chronomal model curve to $t = 0$; the reaction constant k_a was fitted with the JMAK model.

	Initial [SiO_2] (ppm)	Induction time (min)	Ionic strength (M)	R_0^+ (nm)	Chronomal Analysis				JMAK model		Aggregation observed (by DLS)?
					R_0 (nm)	G_0 (10^{-3} s^{-1})	k_p (10^{-4} s^{-1})	p	k_a (10^{-4} s^{-1})	n (averaged)	
pH induced (adjusting pH from 12 to 7)	**640**	**< 10**	**0.02**	**1.07**	**1.09**	**0.70**	**5.13**	**1**	**2.77**	**1.7 ± 0.1**	**No**
		< 10	0.11	1.06	1.00	1.09	7.75	1	3.34	1.7 ± 0.1	No
		< 10	0.22	1.04	1.05	1.20	8.22	1	3.61	1.7 ± 0.1	No
	1600	< 10	0.05	0.68	-	-	-	-	-	-	No
		< 10	0.22	0.67	-	-	-	-	-	-	Yes, at t = 30 min
T induced (rapid cooling from 230 ℃ to 30-60 ℃)	**640**	**~60**	**0.06**	**1.07**	**-**	**-**	**<1.46**	**1**	**-**	**-**	**No**
	960	< 10	0.03	0.85	1.47	-	1.46	1	-	-	No

As shown in the fitting results above, one can see that the fitted power component p in the chronomal analysis, the variable of Equation 4.30 as well, was always one. Therefore, Tobler et al. (2009 and 2013) concluded that silica particle growth is dominated by the first-order surface reaction and argued that the JMAK model was not valid due to the power component n being far less than 3. Surprisingly, the observed value of n=1.7 is quite close to the reported mass fractal dimension D_f for reaction-limited (RL) silica aggregations induced by adding salts, which was estimated to be 1.75 ± 0.05 (Aubert and Cannell 1986). This was not mentioned by Tobler et al. However, they did analyse the particle shapes, and confirmed that the silica nanoparticles formed did indeed have fractal structures, especially in the early stage. The estimated mass fractal dimension was reported to be a function of time, increasing from ~1 to 2.3-2.4, as shown in Figure 4.9:

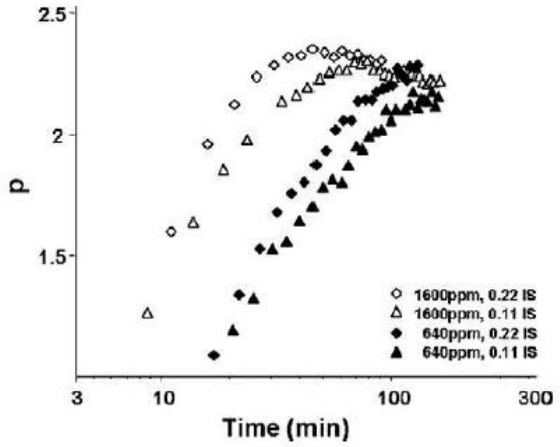

Figure 4.9: Estimated mass fractal dimension vs. time, where the mass fractal dimension D_f was represented by p in the plot, reproduced from Tobler et al. 2009.

Moreover, the theory of hydrous and porous structures for amorphous silica colloids is supported by the conclusions from Iler (1979) and Perry and Keeling-Tucker (2000), and the particle sizes were reported to be slightly smaller when observed using SAXS and TEM compared to those measured using conventional DLS (Tobler et al. 2009), where dehydration and vacuum shall eliminate the open structures.

Iler (1979), Perry and Keeling-Tucker (2000), and Tobler et al. (2009) all concluded that laboratory-grown amorphous silica colloids have hydrous (i.e. not all inner silica chains completely polymerised to crosslink particles) or porous structures. Naturally formed silica colloids under geothermal conditions may have fractal geometries as well. Therefore, unless it is specified otherwise, the thesis author will only consider the hydrodynamic radius (the radius of an equivalent hard sphere having the same mass diffusivity, which can be measured using dynamic light scattering) or diameter and its subsequent effects in the coming sections.

According to Table 4.4, apart from the observed induction time, there is a large discrepancy between two of Tobler et al.'s data points with respect to the surface reaction rate k_p between temperature and pH induced experiments under similar conditions (marked in bold). Tobler et al. (2009) suggested that this may be caused by the time needed to reach a certain degree of supersaturation (instantaneous vs. 2-3 minutes).

4.1.2.2 Particle growth in the late stages

It is widely accepted that Ostwald ripening (OR) is one of the crucial mechanisms in the late stages of silica particle growth (Iler 1979, Perry and Keeling-Tucker 2000, Tobler et al. 2009, Tobler and Benning 2013).

Although the phenomenon of Ostwald Ripening was discovered and described in 1896 by Wilhelm Ostwald, it was not successfully modelled until 1958 by Lifshitz and Slyozov, and 1961 by Wagner, who independently concluded the same results by adopting different approaches. Combined, these works are known as the Lifshitz-Slyozov-Wagner (LSW) theory of Ostwald Ripening.

When the diffusion of monomers limits the particle growth, the average particle size $\bar{R}$ can be estimated using Lifshitz and Slyozov 1961:

$$\bar{R}^3 = \frac{4}{9} D\alpha\nu t \tag{4.40}$$

where D is the diffusion coefficient of the monomers, t is time since Ostwald Ripening begins, and the parameter α_{OR} is a function of surface tension γ, temperature T, and the solubility of the monomers C_∞:

$$\alpha = \frac{2\gamma\nu C_\infty}{R_g T} \tag{4.41}$$

where the constants ν and R_g are the molar volume of the precipitating material and the ideal gas constant, respectively.

More conveniently, if particle growth follows the model derived by Lifshitz and Slyozov (1961), under certain conditions, one will observe the average particle size increase as a function of $t^{1/3}$, i.e.

$$\bar{R} \propto t^{1/3} \tag{4.42}$$

When the surface reaction (i.e. the precipitation of monomers, assumed to be a first order reaction) dominates the particle growth, the average particle size $\bar{R}$ may be predicted using:

$$\bar{R}^2 = \frac{32}{81} \alpha k_s \nu t \tag{4.43}$$

where k_s is the net precipitation rate of monomers.

If particle growth follows the model shown in Equation 4.43, one would see the average particle size increase as a function of $t^{1/2}$, i.e.

$$\bar{R} \propto t^{1/2} \tag{4.44}$$

Depending on whether the particle growth obeys either Equation 4.42 or 4.44, one could easily determine whether the sol development is dominated by Ostwald Ripening or whether other mechanisms should be considered. After fitting their pH induced observations with the LSW theory, and observing when the radius was proportional to $t^{1/2}$ and when to $t^{1/3}$, Tobler et al. (2009) concluded that Ostwald ripening may dominate the silica particle growth only in the late stages, and the Ostwald ripening mechanism is not valid to model the entire silica particle growth process, as shown in Figure 4.10 below:

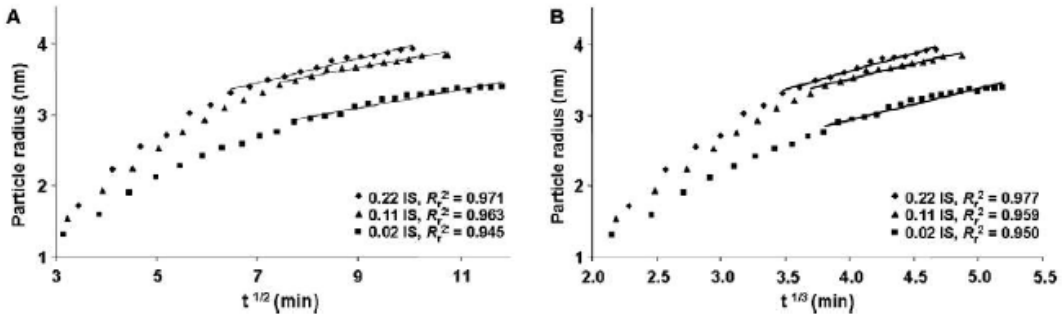

Figure 4.10: Particle radius as functions of the square root of time (diffusion controlled OR) and the cube root of time (surface reaction controlled OR), reproduced from Tobler et al. 2009.

In their later investigations (Tobler and Benning 2013), i.e. the temperature induced experiments, the authors stated that any attempt for fitting the observations with Ostwald ripening model may be impractical due to the particle growth being incompletely recorded, i.e. experiments were stopped once the final particle size was reached. To further study the problem and reveal possible intrinsic correlations, the experimental results were replotted in a logarithmic scale as shown in Figure 4.11 below:

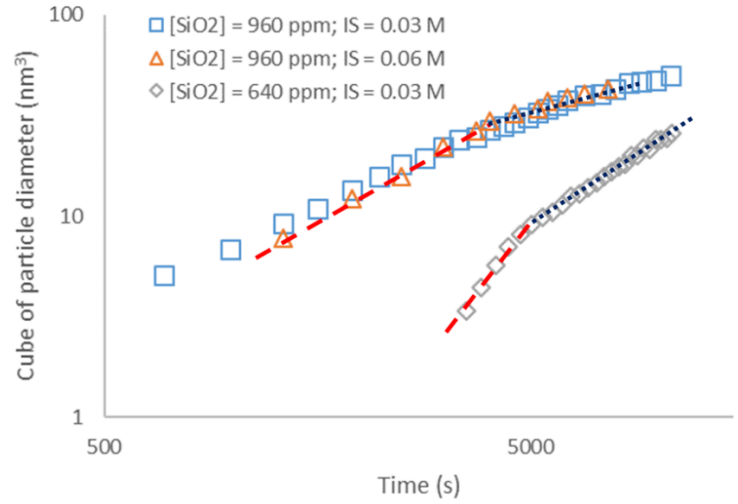

(a)

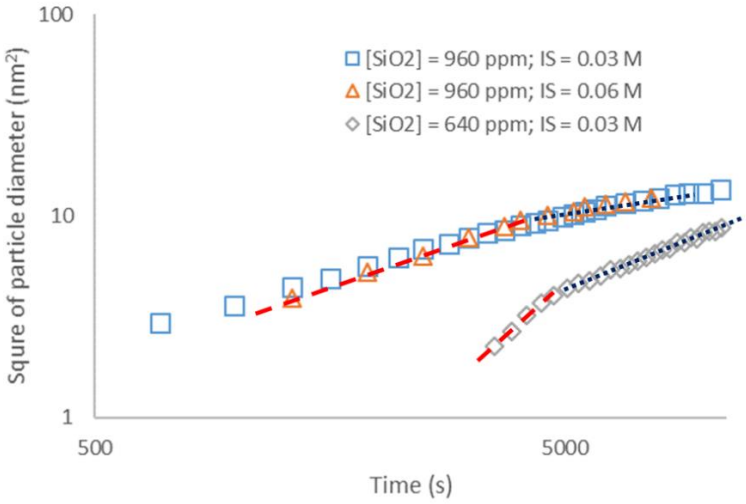

(b)

Figure 4.11: (a) Cube of particle radius and (b) square of particle radius over time. Only two cases in each plot are shown in straight lines for clarity, where one can see an apparent slope change between two lines in each case. Observations are reproduced from Tobler and Benning 2013.

Compared to the fitting results shown in Figure 4.10, Figure 4.10 suggested to the thesis author that Ostwald ripening may not be valid for describing the whole particle growth process but could have a $t^{1/3}$ period and a $t^{1/2}$ period that can be mathematically fitted with the LSW Ostwald Ripening model separately. However, extra caution is needed when interpreting the

fitted model. All of the various particle growth models summarised before are simple approximations to the process which may be accurately applicable to some systems, but do not reliably describe the complex behavior of silica sols.

4.1.2.3 Hypothesis of silica particle growth

We propose that, leaving aside aggregation for the moment and assuming that the nucleation process is instantaneous, homogenous silica nucleation and the subsequent particle growth can be modelled as a three-stage process, as shown in Figure 4.12 below.

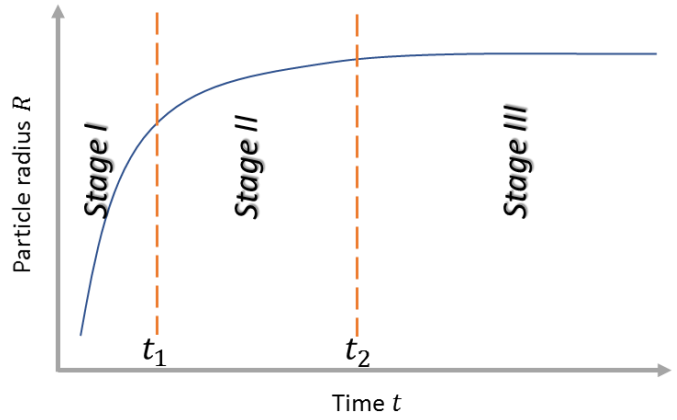

Figure 4.12: Qualitative plot of 3-stage particle growth, where t_1 and t_2 represent the end of Stage I and II respectively.

1. Stage I: initial pseudo surface reaction-controlled particle growth

The first stage may be rapid as the degree of supersaturation (quantitatively described by the silica supersaturation index, SSI) is relatively large in the early stage. When the concentration of dissolved silica along with silica saturation index SSI drops due to the formation of silica particles, the particle growth rate dR/dt decreases and the diffusion-controlled mechanism may become more important (Makrides, Turner, and Slaughter 1979). One may notice that Stage I and Stage II, III below are interpreted as pseudo processes as the thesis author is unable to fully justify whether this is physically correct but only tends to apply simple models with possible explanations.

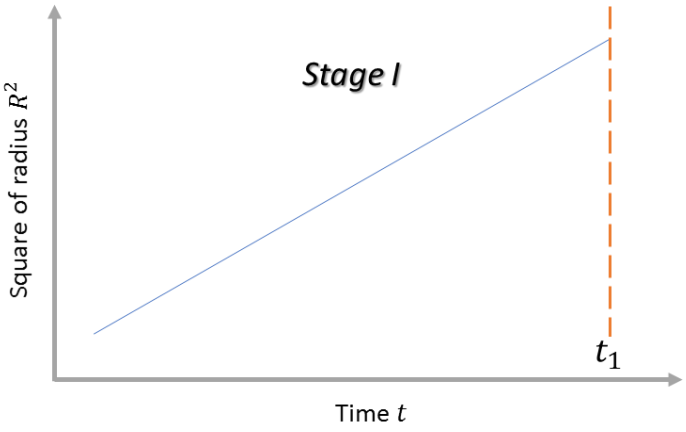

Figure 4.13: Qualitative plot of Stage I: initial particle growth

Hence, in Stage I, the square of average silica particle radius $\bar{R}^2$ is proportional to the time t, i.e.:

$$\bar{R}^2 = k_1 t + b_1 \quad \text{for} \quad t < t_1 \tag{4.45}$$

Since Stage I is proposed to be a pseudo surface reaction-controlled process, similar to the precipitation rate of monomeric silica determined by temperature, pH, ionic strength, and the degree of silica supersaturation, the slope k_1 is expected to depend on all these factors as well.

Theoretically, the intercept b_1 should not be less than the square of the initial critical nucleation radius (i.e. $b_1 \geq R_{crit,0}^2$ to reasonably predict the particle size at the beginning of the whole process (i.e. $t = 0$). For simplicity, it may be feasible to let $b_1 = R_{crit,0}^2$.

This stage ends when the final particle size in Stage I $R_{max,1}$ is reached at t_1.

2. Stage II: subsequent growth due to pseudo diffusion-controlled Ostwald ripening until the surface silica concentration reaches equilibrium, i.e. $dR/dt = 0$ due to $c_b = c_e$.

In the second stage, the diffusion-controlled mechanism is assumed to become dominant. This stage may last longer than Stage I, and has slower particle growth than the previous stage. It ends when the equilibrium is reached (i.e. the particle stops growing and becomes stable). Based on the observations reported by (Tobler et al. 2009, Tobler and Benning 2013, Mroczek et al. 2017), when the equilibrium mentioned above is reached, it may not be necessary for SSI to be equal to one. In practice, during polymerisation, the measured "final" concentration of monomeric silica is greater than the theoretical solubility.

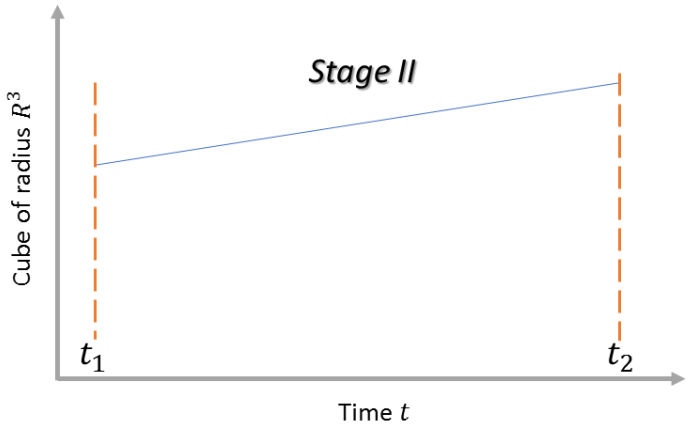

Figure 4.14: Qualitative plot of Stage II: subsequent particle growth.

Hence, in stage II, the cube of the average silica particle radius $\bar{R}^3$ is proportional to the time t, i.e.:

$$\bar{R}^3 = k_2(t - t_1) + b_2 \quad \text{for} \quad t_1 \leq t < t_2 \tag{4.46}$$

As Stage II is assumed to be a diffusion-limited process, the slope k_2 is expected to be mainly dependent on temperature, and pH, ionic strength, and the degree of silica supersaturation may play roles as well.

b_2 shall be equal to the cube of the particle size at $t = t_1$, which is the maximum particle size in Stage I:

$$b_2 = R_{max,1}^3 \quad \text{when} \quad t = t_1 \tag{4.47}$$

This stage ends when the final particle size R_{max} is reached at t_2.

3. Stage III: pseudo steady state where particles stop growing

If the conditions do not favour aggregation, silica particles suspended in water can exist for years or even decades without noticeable variation in size (Iler 1979).

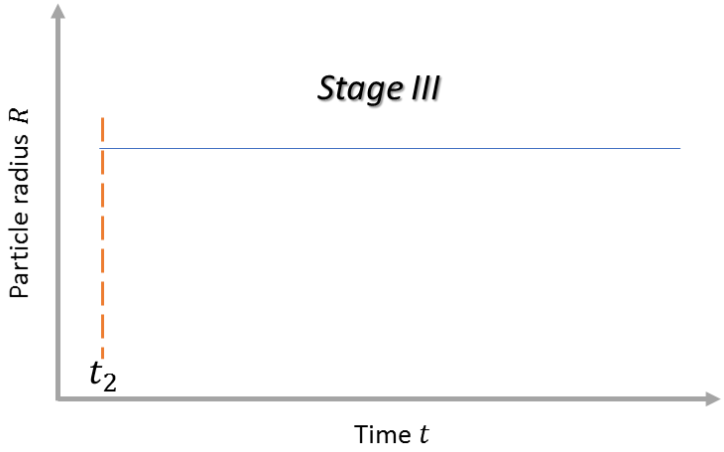

Figure 4.15: Qualitative plot of Stage III: steady state.

Hence, in stage III, if the temperature is constant, the average particle size is expected to be fixed at the final size R_{max}, i.e.:

$$\bar{R} = R_{max} \quad \text{for} \quad t \geq t_2 \tag{4.48}$$

4.1.2.4 Fitting results and discussion

Since there are few published time-resolved silica particle growth observations where silica polymerisation is actively happening, only the experimental results reported by (Tobler et al. 2009) are used to find k_1, $R_{max,1}$(i.e. $b_2^{1/3}$) for Stage I and k_2 for Stage II. The observations in Tobler and Benning 2013 are used for validation.

As shown in Figure 4.12, a critical time t_1 separates Stage I and II. After the maximum particle size in Stage I $R_{max,1}$ is reached at t_1, one can observe an obvious change in slope that marks the end of Stage I, as shown in Figure 4.16 below.

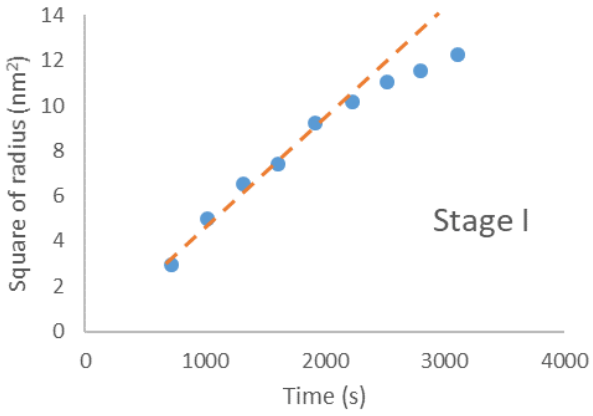

Figure 4.16: Square of particle radius over time, fitted with a linear correlation (dash line). The observations (dots) are reproduced from Tobler et al. 2009: the pH-induced

experiment in the 0.22 M ionic strength solution initially dissolved with 640 ppm monomeric silica at pH = 12 and room temperature. Note that the last three points are offset from the fitted line.

Therefore, the first point that has the obvious offset is recognised as the maximum particle size in Stage I $R_{max,1}$. According to all available particle growth history data, it is found that the ratio of $R_{max,1}$ to the final particle size R_{max} (i.e. $R_{max,1}/R_{max}$) is about 0.80. Therefore, for simplicity, $R_{max,1}$ is empirically defined by:

$$R_{max,1} = 0.80\, R_{max} \tag{4.49}$$

The experiment in (Tobler et al. 2009) was done at 25℃, neutral pH, ionic strength (I) 0.02, 0.05, 0.11, 0.22 M, and *SSI* ~5.46 and ~13.64. By plotting the candidate points (i.e. observed particle size history) on axes of time and radius squared or cubed (for Stage I and II respectively) as in Figure 4.16, one can easily find the slope $k_1$and k_2 for Equation 4.45 and 4.46 separately.

For each experiment under certain conditions (ionic strength and *SSI*), there is a pair of $k_1$and k_2 (six pairs under six sets of conditions in total). By treating the two conditions as free parameters, the following correlations can be fitted:

for $0 \leq \mathrm{t} < t_1$ (i.e. Stage I)

$$k_1 = 0.0019 + 9.2 \times 10^{-5}\mathrm{SSI} + 0.020I - 7.0 \times 10^{-4}\mathrm{SSI} \cdot I - 0.033I^2 \tag{4.50}$$

for $\mathrm{t} \geq t_2$ (i.e. Stage II)

$$k_2 = -3.5 \times 10^{-4} + 9.6 \times 10^{-4}\mathrm{SSI} + 0.026I - 0.0048\mathrm{SSI} \cdot I - 0.031I^2 \tag{4.51}$$

R^2 (the coefficient of determination, indicating the viability of the fitted function) for Equation 4.50 and 4.51 are > 0.99. Note that the variables: pH, temperature, and initial concentration of amorphous silica, are embedded in the variable *SSI*. Due to a lack of available experimental data at different pH, the model is expected to be less sensitive to pH than it should. Considering typical pH in geothermal reinjection is close to neutral or slightly alkaline (usually less than 9), the insensitivity is considered to have the least effects on the modelling results.

The reported final particle sizes (Alexander and McWhorter 1976; Broge and Iler 1971; Tobler et al. 2009; Tobler and Benning 2013) can be plotted in Figure 4.17 below:

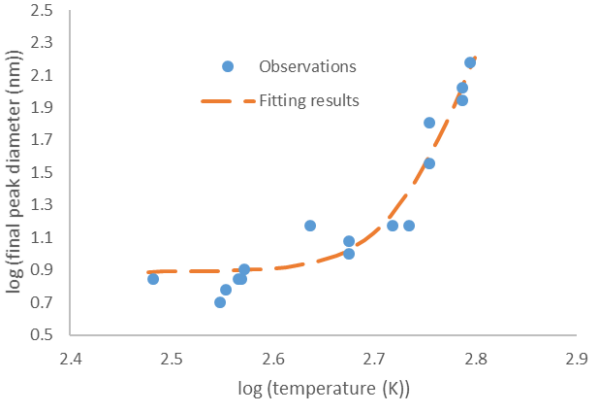

Figure 4.17: Reported final particle diameter as a function of temperature in a logarithmic scale.

These observations were reported under the conditions of SiO_2: Na_2O mole ratio from very high (due to very low salt concentration) to about 0.1, *SSI* from about 163 to 5.46, ionic strength from 0.22 to very low, pH around neutral, and temperature from room temperature to 350 ℃.

It can be seen that the final particle size is sensitive principally to temperature, increasing exponentially, and is much less sensitive to other parameters. Thus, the final silica particle diameter D_{max} in the temperature range from 298 to 623 K (i.e. $25 - 350$ ℃) may be empirically expressed by:

$$D_{max} = 1.7 \times 10^{-5} \exp(0.025T) + 7.7 \tag{4.52}$$

where D_{max} is in nm. The R^2 for Equation 4.52 is > 0.90. The predictions made from Equation 4.52 are plotted as the orange dashed curve in Figure 4.17.

Since the temperature and *SSI* of the available data lie outside typical geothermal conditions (e.g. in the case of geothermal reinjection in New Zealand fields: $T = \sim 160$ ℃, $I = \sim 0.09$ M, $\text{SSI} = \sim 1.5$, and pH close to neutral if not acidified, as shown in Figure 4.18 below), extrapolations have to be made.

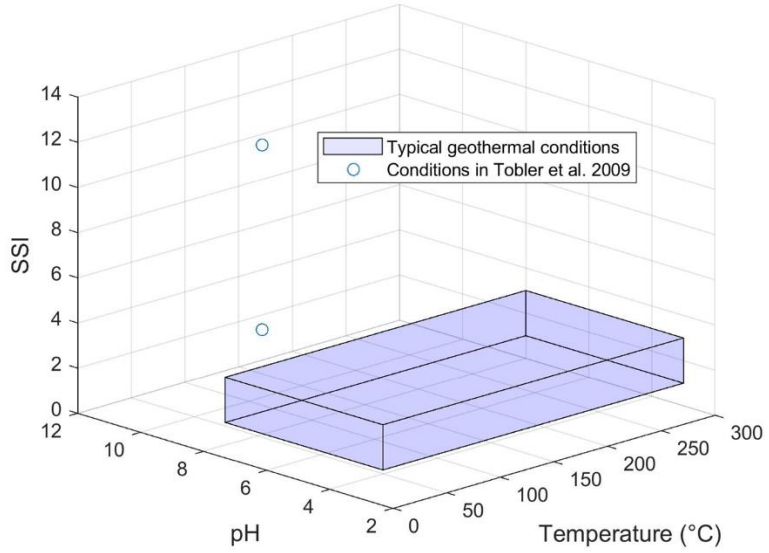

Figure 4.18: Comparison between typical geothermal conditions (blue cube) and the conditions in Tobler et al. 2009 (dots). Note that the blue cube covers the possible cases of acidification (low pH) and reinjection at room temperature (low temperature); the variable ionic strength is not shown for clearness, as the values used in Tobler et al. 2009 are in the range of typical geothermal conditions.

In Stage I, the surface reaction limits the silica particle growth. Based on the LSW theory and the proposed three-stage silica particle growth model (Equation 4.43 and 4.45), k_1 is seen to be proportional to $\frac{64}{81}\frac{\gamma \nu C_\infty}{R_g T} k_s$.

As the temperature *T* varies, the surface tension γ can be predicted by following (Weres et al. 1980); the solubility C_∞ change is well-known (Iler 1979, Gunnarsson and Arnórsson 2000); k_s is essentially the rate of the reaction between silicic acid and amorphous silica surfaces. (Fleming 1986) suggested that this reaction showed an Arrhenius temperature dependence with an activation energy of 13.1 ± 0.9 kcal mol^{-1}in the temperature range of $25 - 100$ ℃. We

assume this relationship can be extrapolated to typical geothermal conditions. Hence, k_s can be represented by:

$$k_s = k_s^{298K} \exp\left[-\frac{E}{R_g}\left(\frac{1}{T} - \frac{1}{298.15}\right)\right] \tag{4.53}$$

where k_s^{298K} is the reaction rate at 298 K, and E is the activation energy.

Therefore, k_1 can be re-expressed by:

$$k_1 = \frac{\gamma C_\infty}{T} \frac{298.15}{\gamma^{298K} C_\infty^{298K}} \frac{k_s}{k_s^{298K}}\ k_1^{298K} \tag{4.54}$$

where γ^{298K} and C_∞^{298K} are the surface tension and the solubility at 298 K, and k_1^{298K} is equivalent to k_1 predicted in Equation 4.50.

By combining Equation 4.53 and 4.54:

$$k_1 = \frac{\gamma C_\infty}{T} \frac{298.15}{\gamma^{298K} C_\infty^{298K}} \exp\left[-\frac{E}{R_g}\left(\frac{1}{T} - \frac{1}{298.15}\right)\right]\ k_1^{298K} \tag{4.55}$$

The SSI in the data used is also out of the range of typical geothermal conditions. However, the coefficients preceding SSI in Equation 4.50 are quite small compared to those of ionic strength, suggesting that the effects of SSI on k_1 are limited. It is assumed that Equation 4.50 and 4.55 can be used in a wider SSI range than $\sim 5.46 - \sim 13.64$ as the introduced errors may only have very limited effects on k_1.

In stage II, the diffusion of monomeric silica limits the silica particle growth. According to the LSW theory and the proposed three-stage silica particle growth model (Equation 4.40 and 4.46), k_2 may be considered to be proportional to $\frac{4}{9} D \frac{\gamma \nu C_\infty}{R_g T} \nu$.

Given that temperature is changing, the diffusion coefficient for monomeric silica D may be calculated from the Einstein-Stokes equation (Rebreanu et al. 2008):

$$D = \frac{k_B T}{6\pi\mu r} \tag{4.56}$$

where μ is the dynamic viscosity of the solution, and r is the radius of the silicic acid molecule. Since $k_B/6\pi r$ is independent of temperature, D is proportional to T/μ. By assuming the dynamic viscosity of the solution is equal to that of water at the same temperature, μ as a function of temperature can be easily found in (Keenan 1978). Other parameters, such as γ, C_∞, and SSI, are handled similarly.

Therefore, k_2 can be re-expressed by:

$$k_2 = \frac{T}{\mu} \frac{\gamma C_\infty}{T} \frac{\mu^{298K}}{298.15} \frac{298.15}{\gamma^{298K} C_\infty^{298K}}\ k_2^{298K} \tag{4.57}$$

where k_2^{298K} is equivalent to k_2 predicted in Equation 4.51.

By rearranging:

$$k_2 = \frac{\gamma C_\infty}{\mu} \frac{\mu^{298\mathrm{K}}}{\gamma^{298K} C_\infty^{298K}}\ k_2^{298K} \tag{4.58}$$

To validate the performance of the model, two examples are used: one is the pH-induced observations in (Tobler et al. 2009) at 25℃, neutral pH, I = 0.22 M, and SSI = ~5.46, the other is the T-induced experimental results from (Tobler and Benning 2013) at 30℃, neutral pH, I = 0.06 M, and SSI = ~5.46.

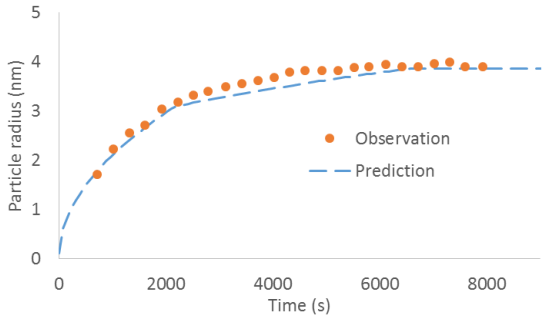

(a)

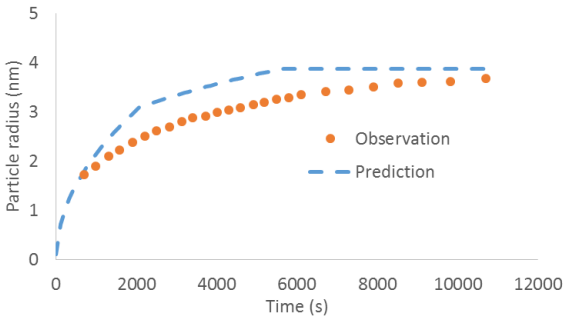

(b)

Figure 4.19: Comparison between observations and predictions at (a) 25℃, neutral pH, I = 0.22 M, and SSI = ~5.46 and (b) 30℃, neutral pH, I = 0.06 M, and SSI = ~5.46; observations reproduced from Tobler et al. 2009; Tobler and Benning 2013.

It can be seen that the three-stage particle growth model might be useful to predict the silica particle size as a function of time if the polymerisation is pH induced, but a discrepancy exists when the polymerisation is temperature induced. Tobler and Benning (2013) considered this as the consequence of the supersaturation differences at the early stage. In the pH-induced experiment (Tobler et al. 2009), the supersaturation is established within 30 s by adjusting pH from 12 to 7 (i.e. a sudden *SSI* jump); in the temperature-induced experiment (Tobler and Benning 2013), the supersaturation is reached by cooling the solution from 230 to 30 ℃ in about 3 min (i.e. a gradual *SSI* increase). Therefore, the discrepancy suggests that the model is more suitable to predict the silica particle growth in conditions where the silica polymerisation is triggered instantaneously.

On the other hand, one may note that, despite the discrepancy at the early stage, good agreement is obtained for the final particle size R_{max}. Mroczek et al. (2017) reported a field observation that silica nanoparticles with an average diameter of 8-9 nm at about 80 ℃. By following Equation 4.52, it is predicted that the final particle size D_{max} is about 7.8 nm under the same conditions. This suggests the model might be feasible to predict the final silica particle size some geothermal brines. Further validations in a wider range of conditions can be very useful.

SILNUC (described in Section 4.1.1) models polymerisation of silica and the evolution of a silica sol by representing the continuous distribution of sizes actually present in terms of a discrete "classes" of particles nucleated at different times and characterised by different sizes. However, it might be difficult to apply this to reproduce the experimental data, such as the observations shown in Tobler et al. 2009 and 2013.

The silica particle growth model proposed in Section 4.1.2 describes the evolution of the sol in terms of a single parameter, the average particle size $\bar{R}$. When implementing this to the holistic model, it is assumed that, in each control volume, the particle size distribution is strictly homogenous, i.e. all particles have the same size $\bar{R}$; on the other hand, moving from cell to cell along the flow direction, due to the increasing residence time in different control volumes, the particle size $\bar{R}$ is expected to increase. This approach eases the later modelling of the interactions between silica particles in each cell.

4.2 Aggregation and stability of silica colloids

4.2.1 Aggregation of silica particles

In this section, the aggregation of silica nanoparticles is considered. As described before (see Section 2.2.5), Iler (1979) classified the aggregation into four types – gelling, coagulation, flocculation, and coacervation. Only coagulation is of interest for this study.

4.2.1.1 Approach of silica particles

Aggregation requires contact between particles. Van der Waals force is the main attractive force driving the close approach of colloidal particles, however the electrostatic force repels them. Apart from that, Iler (1979) suggested the hydrogen bonded water molecules on the surface of a silica particle act against the aggregation as well, which may be responsible for the abnormal observed stability, discussed later. However, this presumed effect somehow "disappears" for the larger particles: at low pH (say 2) and negligible ionic strength, the surface charge for a silica nanoparticle should be at minimum, and therefore rapid coagulation is expected to occur, however, this is true only for relatively large particles (say 50-100 nm or above in diameter), i.e. small silica particles are unexpectedly stable in water at low pH.

4.2.1.2 Linkage of silica particles

If the attractive force is stronger than the repulsive force, silica particles will tend to approach and contact each other. Aggregation happens when one particle successfully captures the other and bonding occurs. Particles can be attached due to adhesion, however, condensation may be more common, which is essentially the polymerisation of the surface silanol groups from different particles with the release of a water molecule. This will form siloxane ($-\mathrm{Si}-\mathrm{O}-\mathrm{Si}-$) bonds, which are strong (Iler 1979), as shown in Figure 4.20 below.

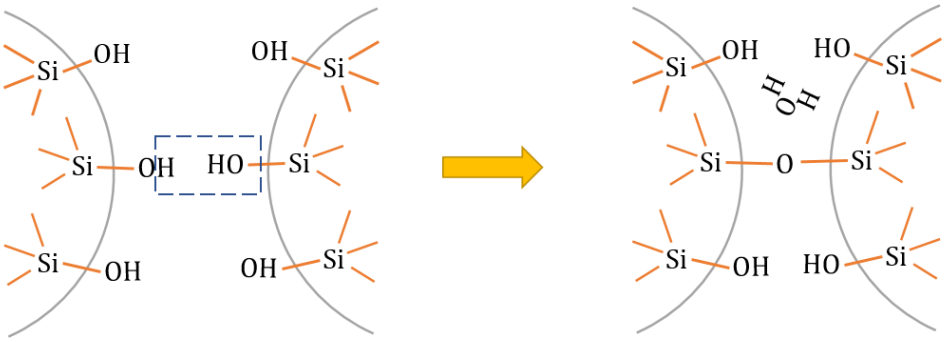

Figure 4.20: Polymerisation mechanism: $-Si-O-Si-$ bonds form due to the polymerisation of surface silanol groups from different particles.

Once two silica particles aggregate, a dimer particle will form. Since the solubility of amorphous silica depends on the particle curvature and there is a negative curvature at the linkage point, molecular silica deposition will happen near this point, which gradually changes the morphology of the aggregate and consolidate the linkage, as shown in Figure 4.21 below.

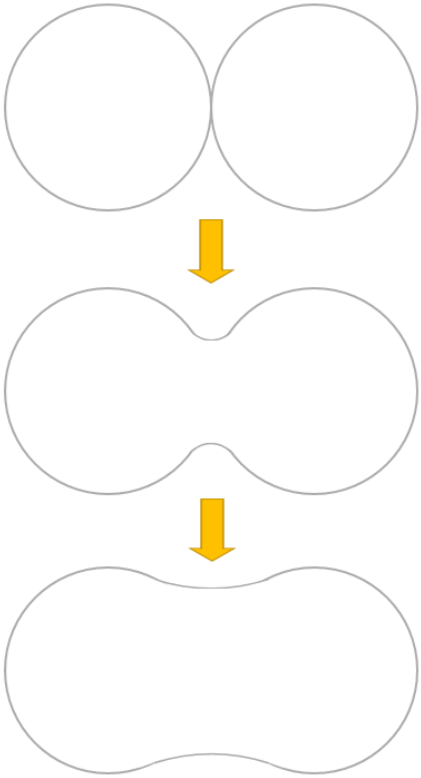

Figure 4.21: Molecular deposition occurs instantaneously at the linkage point of two silica particles

Before the "actual" linkage, i.e. the formation of siloxane ($-Si-O-Si-$) bonds between colliding particles, there are several other mechanisms proposed.

1. "Dehydration" mechanism

Allen and Matijevic (1969) proposed that silica particles will become less soluble due to the exchange of salt ions and the protons on a particle surface, which will "dehydrate" the surface as the hydrogen bonded water on the surface will be released along with the exchanged protons, as shown in Figure 4.22 below. They suggested that the effects of "dehydration" only depend

on the quantity of the exchanged salt ion but not the valence of the ion, i.e. regardless of the valence, one cation will only occupy one silanol site.

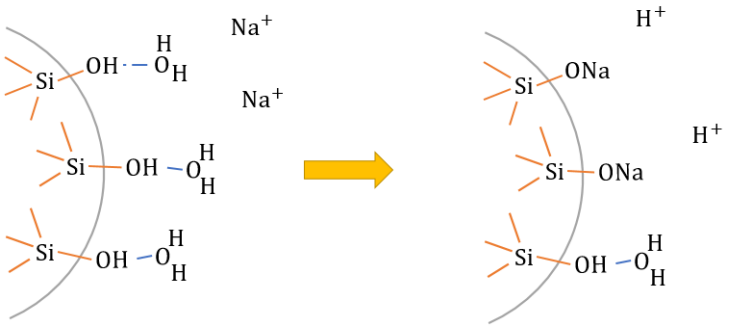

Figure 4.22: "Dehydration" mechanism: the hydrogen boned water molecules are released due to ion exchange, and the "dehydrated" silica particles become less soluble.

2. "Interparticle" bonding mechanism

Depasse and Watillon (1970) suggested that the "interparticle" acid-base bonds form among silica particles at pH 7-11, as shown in Figure 4.23 below.

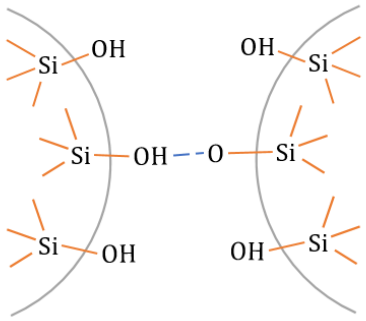

Figure 4.23: "Interparticle" bonding mechanism: silica particles are initially attached by acid-base bonds at relatively higher pH.

3. Cation bridging mechanism

Iler (1979) proposed that the hydrated salt ions may act like bridging agents in the early stage of aggregation. As shown in Figure 4.24 below, a sodium ion Na^+, the simple and the most common example, is usually hydrated in water and surrounded by six water molecules; attracted by the electrostatic force, the hydrated ion will then lose one water molecule and attach to an ionised silanol surface group to form a neutral complex; and eventually the initial linkage occurs as the water molecules on the neutral complex will form hydrogen bonds with the surface silanol groups from other silica particles.

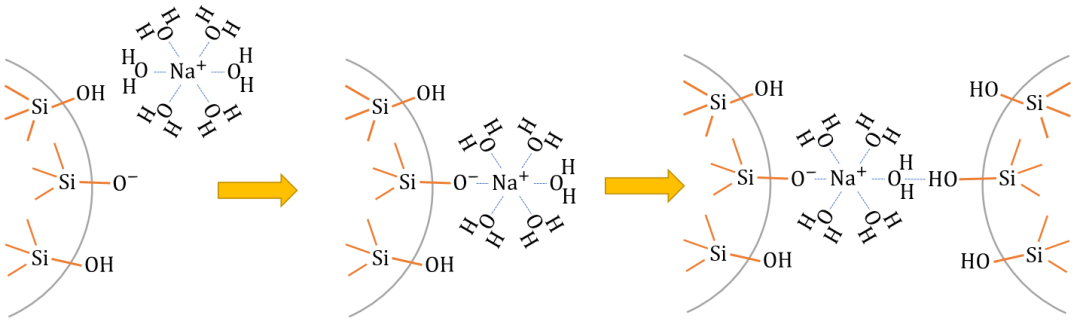

Figure 4.24: Particle bridging due to the hydrated salt ions.

Also, aggregation is much faster with divalent cations and even faster with trivalent cations – can be three orders of magnitude more efficient with trivalent than with monovalent cations.

4.2.1.3 Formation of aggregates and agglomerates

The aggregation rate of colloidal silica will affect the morphology of the scale. It was suggested (Hunter 1993) that rapid coagulations will result in scale deposits with open structures but, for slow coagulations, denser scales will form. Therefore, based on the morphology of silica scale samples formed under varying conditions, one can infer which conditions caused rapid silica scaling.

When conditions favour coagulation, discrete silica nanoparticles (primary particles, normally in the range of dozens of nanometres) will start to be loosely linked and form aggregates (usually in the range of hundreds of nanometres). In the later stages, these aggregates may grow further by monomeric deposition and become denser by dissolution from areas of high positive surface curvature and redeposition in low or negative curvature to form denser structures, which are often called agglomerates (often in the range of thousands of nanometres), as shown in Figure 4.25 below.

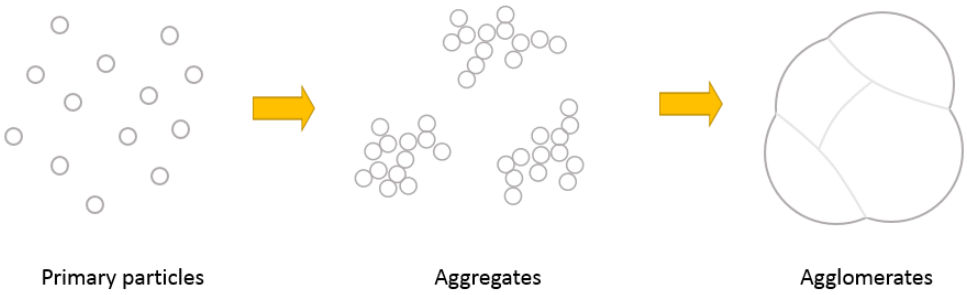

Figure 4.25: Aggregation of nanoparticles

4.2.2 Stability of colloidal silica

Under typical geothermal conditions, silica scaling is usually (Brown 2011) mainly dominated by the deposition of colloidal silica. For the present work, it is hypothesized that the deposition process can be described as follows: monomeric silica may firstly polymerise to form nuclei which grow to become colloidal particles, which would coat the fracture surfaces (to at least one particle thick) in a time much less than the lifetime of the well. Hence, one can treat the

wall as having the electrochemical properties of silica, regardless of rock mineral content, i.e. the deposition is recognised as the interaction between deposited and suspended particles.

The interaction behaviours of silica nanoparticles under geothermal conditions decide the attachment (aggregation) rate, which consequently determines the deposition rate. Therefore, a quantitative description of the interaction of colloidal silica is of great value to the geothermal industries in predicting the rate of formation of silica scale.

4.2.2.1 DLVO theory and discrepancy with observations

DLVO theory (Derjaguin and Landau 1941, Verwey and Overbeek 1955), is commonly used to quantitatively describe the interaction between colloids. The theory describes the total interaction potential between colloidal silica particles V_T as the sum of the attractive potential V_A due to the van der Waals force and the repulsive potential V_E due to the electrostatic force:

$$V_T = V_A + V_E \tag{4.59}$$

For simplicity, the case of two identical colloidal particles is considered below. The attractive potential between the two colloids with the same radius a can be represented by (Hamaker 1937):

$$V_A = -\frac{A}{6}\left(\frac{2}{u^2+4u} + \frac{2}{(u+2)^2} + \ln\left[\frac{u^2+4u}{(u+2)^2}\right]\right) \tag{4.60}$$

where, $u = H/a$ is the dimensionless surface-to-surface distance between particles, H is the separation distance (i.e. dimensional surface-to-surface distance), and A is the Hamaker constant, represented by Equation 4.61 below (Hamaker 1937, London 1937):

$$A = 0.75k_BT(1+2\kappa H)e^{-2\kappa H} + \frac{3\hbar\omega}{16\sqrt{2}}\frac{(n_1^2-n_3^2)^2}{(n_1^2+n_3^2)^{3/2}}\left[1+\left(\frac{H}{\lambda}\right)^q\right]^{-1/q} \tag{4.61}$$

where, k_B is the Boltzmann constant, T is the absolute temperature, $\kappa = \sqrt{\frac{2e^2N_Ac_iz^2}{\varepsilon k_BT}}$ is the Debye-Huckel parameter, e is the electron charge, N_A is Avogadro's number, c_i is the concentration of the background electrolyte, z is the valence of the electrolyte, ε is the permittivity, $\hbar$ is the Planck constant divided by 2π, $\lambda = \frac{c}{\pi^2\omega}\sqrt{\frac{2}{n_3^2(n_1^2+n_3^2)}}$ is the characteristic wavelength of the retardation effect, c is the speed of light, $\omega = 3.3\times10^{15}$ is the characteristic frequency of the retardation effect, $n_1 = 1.43$ and $n_2 = 1.33$ are the refractive index of silica and medium (water) respectively, and $q = 1.185$ is a fitting factor (Škvarla 2013).

The electrostatic repulsion between two similar colloids is due to the surface charge φ_0. In the case of amorphous silica, the silanol group may either dissociate a proton to the solution or obtain a proton from the solution depending on the pH. Hence, the surface of a silica particle will be either negatively or positively charged unless the pH is at the "point of zero charge" where these effects are balanced.

Ions from the background electrolyte are adsorbed to the charged surface to form a charged layer, called the Stern layer or the first layer. Due to the existence of the first layer, ions with opposite charge are attracted and electrically mask the first layer. These ions form another charged layer, called the second layer or the diffuse layer since it is loosely organized. The assembly comprising the two charged layers is named the "double layer" or "electrical double layer", shown in Figure 4.26:

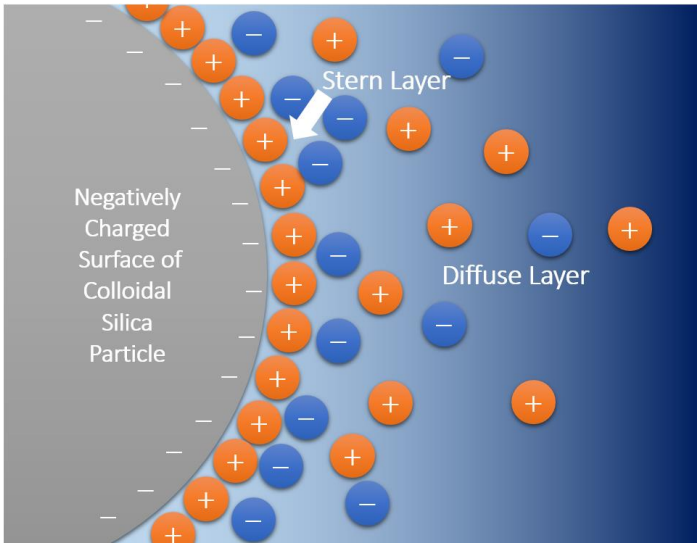

Figure 4.26: Schematic of the double layer. Note that only cations are present in the Stern layer, and cations predominate in the diffuse layer; there is no " layer" where anions predominate. The sum of the cations in the Stern layer and the cations along with the anions in the diffuse layer is equal to the absolute value of the negative surface charge.

By assuming the surface potential is maintained to be constant (Derjaguin 1940), the electrostatic repulsion potential can be expressed as (Equation 4.62):

$$V_E = 2\pi\varepsilon\varphi_0{}^2 r \ln[1 + \exp(-\kappa h)] \tag{4.62}$$

In practice, another parameter – the zeta-potential (or ζ-potential) is usually substituted in place of surface potential φ_0 in Equation 4.62, which may be smaller in magnitude than φ_0 but is easier to estimate by measuring the electrical mobility of the sols.

Theoretically, since homogenous silica nucleation is favoured under geothermal conditions (Weres et al. 1981), given sufficient time, an oversaturated silicic acid solution will become a monodisperse colloidal silica suspension. The diffusion limited or "fast" aggregation rate constant k_{fast}, is defined by:

$$k_{fast} = \frac{8k_B T}{3\mu} \tag{4.63}$$

where, k_B is the Boltzmann constant, and μ is the dynamic viscosity of water. k_{fast} reveals the fastest aggregation process as no repulsive effect is considered, i.e. particles aggregate once they collide due to Brownian motion.

The reaction limited, or "slow" aggregation rate constant, k_{slow}, can be considered as k_{fast} divided by the stability ratio W. W can be treated as the inverse of the probability of aggregation. In this case, repulsive effects are taken into account. Therefore, the stability ratio of colloidal silica, W, is defined by (Fuchs 1934):

$$W = \frac{k_{fast}}{k_{slow}} = 2\int_0^{\infty} \frac{\beta(u)}{(u+2)^2} exp(\frac{V_T(u)}{k_B T})\, du \tag{4.64}$$

where, $\beta(u)$ is the hydrodynamic correction factor, defined by Equation 4.66 below. W quantifies the difficulty of colloidal aggregation. As the silica deposition process on the fracture

surface is dominated by the bonding (aggregation) of suspended and deposited silica particles, higher stability can lead to a lower deposition rate.

The hydrodynamic correction factor is initially applied to correct the diffusion coefficient due to the effects of viscous drag:

$$D(u) = D_0/\beta(u) \tag{4.65}$$

where, D_0 is the diffusion coefficient of a particle in an infinitely dilute solution. Therefore, β converges to 1 when the intersphere surface separation approaches infinity, i.e. $H \gg a$.

The expression for the hydrodynamic correction factor in the case of two spherical colloids having the same size is given by (Honig et al. 1971):

$$\beta = \frac{4}{3}\sinh(\alpha)\sum_{n=1}^{\infty}\frac{u(u+1)}{(2u-1)(2u+3)} \cdot \left[\frac{4\cosh^2(u+\frac{1}{2})\alpha + (2u+1)^2\sinh^2(\alpha)}{2\sinh(2u+1)\alpha - (2u+1)\sinh(2\alpha)} - 1\right] \tag{4.66}$$

where α is defined by:

$$\cosh(\alpha) = \frac{u}{2} + 1 \tag{4.67}$$

The factor can then be numerically approximated to a rational function (Honig, et al. 1971):

$$\beta(u) \approx \frac{6u^2 + 13u + 2}{6u^2 + 4u} \tag{4.68}$$

At this point, the interaction potential V_T can be predicted by the DLVO theory described previously, the expected stability ratio W can then be computed.

The sequence in which the variables required to quantify the stability are combined is summarised in Figure 4.27:

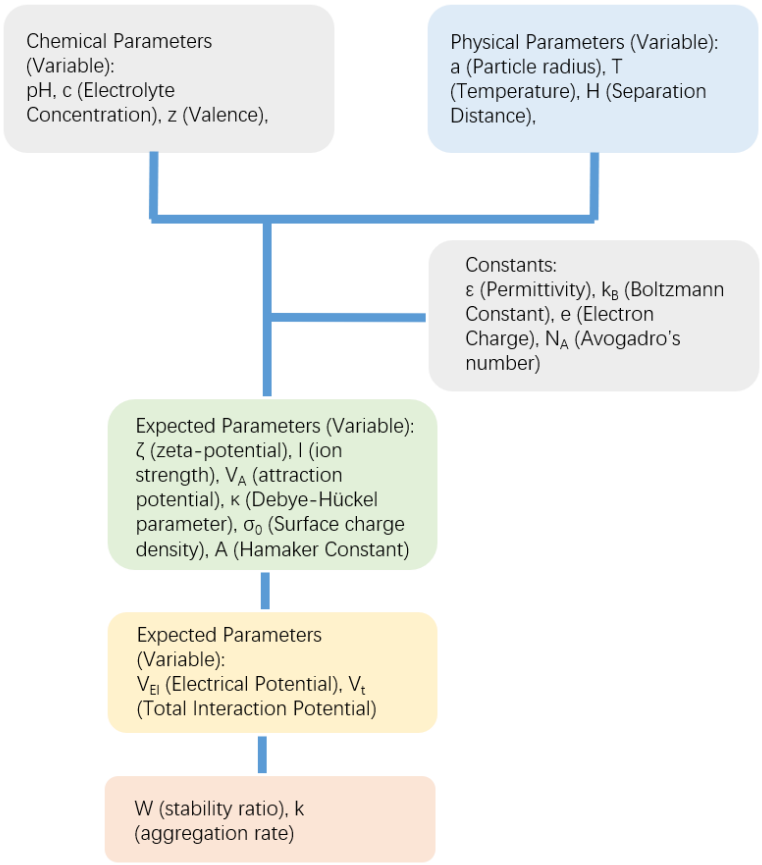

Figure 4.27: Sequence of calculation resulting in stability values.

It has been shown that DLVO theory can predict the stability of colloids of a range of chemical compositions with reasonable accuracy (Adamczyk and Weroński 1999). However, amorphous silica is an exception (Iler 1979, De Gennes 1987, Healy 1994, Kobayashi et al. 2005), as shown in Figure 4.28.

The solid line represents the experimentally obtained stability ratio. Only pH is discussed below as a parameter, although positive ions (i.e. metallic ions) of the background electrolyte solution are expected to have similar effects on the stability ratio as the hydrogen ion, and other related parameters (e.g. temperature, particle size, etc.) may not qualitatively affect the curve. The pH range of interest here is only from 0 to around 10, as amorphous silica begins to dissolve and form silicates when pH > 10.

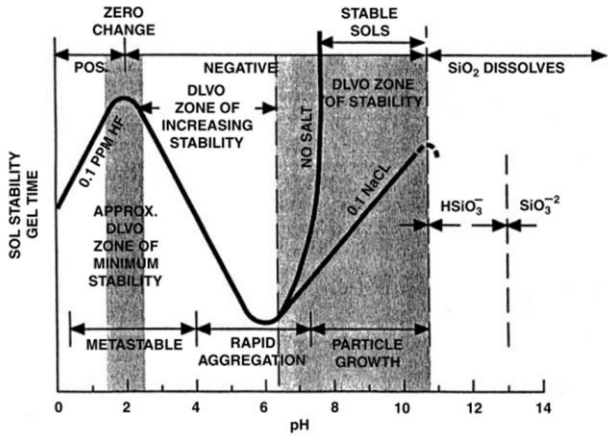

(a)

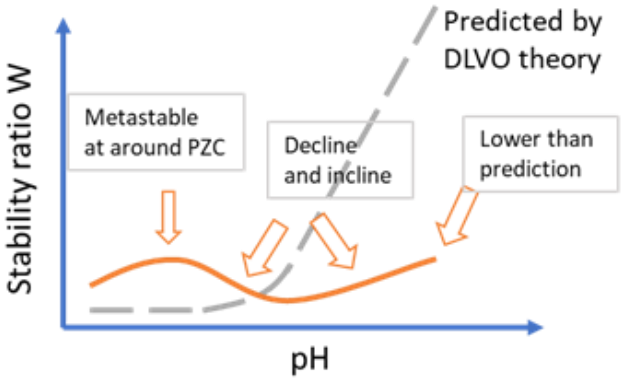

(b)

Figure 4.28: Qualitative comparison with the predictions using the DLVO theory.

According to (Iler 1979), the discrepancy is often defined by the following four observations:

1) The point of zero charge (pzc) is usually defined as the pH value at which a particle submerged in a background electrolyte solution shows zero charge on the surface. According to experimental results, the pzc is close to pH = 2, at which the colloidal silica particle is expected to be unstable based on DLVO theory due to the absence of repulsive electrostatic potential. However, in reality, silica sols are known to be stable between pH 0 and pH 4.

2) While the concentration of hydrogen ions is decreasing within the range of pH = ~2 to pH = ~6, the degree of surface charge, usually evaluated by surface charge density or zeta-potential, is theoretically predicted and experimentally verified to be increasing. Hence, according to DLVO theory, the stability ratio is expected to be growing, which is in contrast with the reality that it is declining.

3) Although silica colloids show qualitatively DLVO-like behaviour at 6 < pH < 10, the observed stabilities are lower than the predictions by many orders of magnitude.

4) According to DLVO theory, the stability ratio of colloidal silica continuously increases as pH increases from acid to alkaline due to the decreasing concentration of hydrogen ions causing the rise of repulsive electrostatic potential. The difference (the unexpected peak and drop) between the prediction and observations reveals the existence of additional effects not accounted for in DLVO theory.

De Gennes (1987) proposed that these unexpected interaction behaviours are due to a gel or hairy layer, which consists of silicone polymers anchored on the surface of silica particles, as illustrated in Figure 4.29.

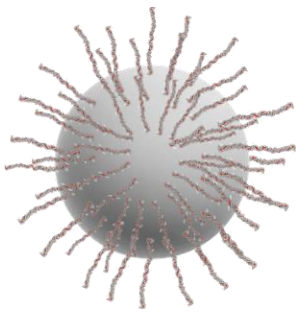

Figure 4.29: A sketch of a colloidal particle with a hairy layer, the "hairs" being polymer chains of silicone.

Some researchers (De Gennes 1987, Healy 1994) suggested that the major effect of the hairy layer is the extra steric barrier, i.e. the energy barrier caused by overlapping electron clouds. This significantly increases the total energy barrier that must be overcome by the colloids to aggregate, as shown in Figure 4.30 below.

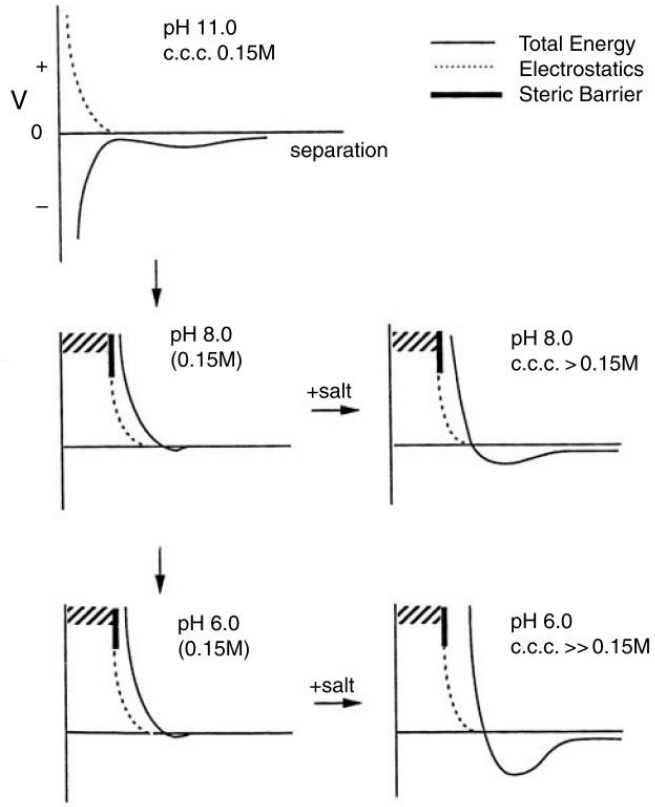

Figure 4.30: Total interaction energy between two colloidal silica particles as a function of distance, starting at pH=11 and 0.15M symmetrical electrolyte (binary electrolytes such as KCl and NaCl), and then varying the pH and the concentration of the background electrolyte, reproduced from De Gennes 1987.

De Gennes (1987) published his theory regarding the interaction of particles covered with the hairy layers and assumed that, after the contact of the hairy layers, the polymers compress against each other but do not interdigitate, and concluded that the abnormal stability of colloidal silica could be due to the steric interaction.

However, the extra steric barrier will only shift the predicted stability curve above the traditional curve based on the DLVO theory, i.e. it can only predict higher stability than DLVO theory. Experimental observations show the silica colloids also might be less stable than the DLVO predictions at some conditions (Figure 4.28).

Ohshima (2015) extended De Gennes' model by considering how charged hairy layers would affect the interactions. He suggested (Ohshima 2015) that the particles having charged hairy layers have very different electrostatic behaviours when compared to the particles having no such structures on their surface. Ohshima defined a class of colloid "soft" particles, which are coated by ion-penetrable surface layers of polyelectrolytes.

Ohshima described the compression of the hairy layer, leading to a two-stage soft particle model at the beginning (approach and compression), but soon extended this to include interdigitation of the hairy layer, hence the three-stage soft particle model (Figure 4.31). This proved useful in

explaining physical problems such as bacterial adhesion, red blood cell aggregation, etc. (Pribush et al. 2007, Hori and Matsumoto 2010).

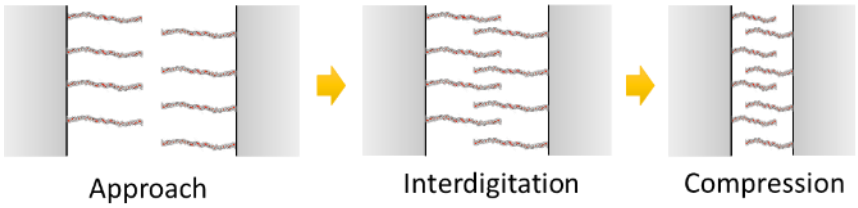

Figure 4.31: Schematic of (a) the two-stage soft particle model which assumes the brushes compress but do not interdigitate; (b) the three-stage soft particle model which assumes the brushes interdigitate and compress when $h \leq h_c$.

To this author's knowledge, Škvarla (2013) is the first researcher who applied the soft particle model attempting to describe the interactions between colloidal silica. This is very inspirational to the thesis author. However, there were two drawbacks: (1) the model (Ohshima 2011) applied in Škvarla 2013 is the older version of the soft particle model which only discussed how particles interact when approaching; and (2) there was a typo in the concluding formula (equivalent to Equation 4.104) in Ohshima 2011, independently found by the thesis author but not by Škvarla (2013). Ohshima confirmed the latter when contacted by the thesis author. In fact, before that, Ohshima had already corrected the error in his recent work (Ohshima 2015), and more importantly, the soft particle model was also extended to be more comprehensive, including the interaction behaviour of soft particles after first approach. Therefore, Škvarla (2013) was partially successful in explaining the experimentally observed stability curve by adopting Ohshima's soft-particle model published in 2011, but the discrepancy could not be completely explained. Later, Škvarla and Škvarla (2017) measured the thickness of gel layer by atomic force microscopy (AFM). The experimental results supported the application of the soft particle model, where d = ~150 nm, neutral pH, c_{KCl} = 0.001 – 0.1, d_0 = 13.9 – 0.9 nm.

The present work considers whether Ohshima's model may be applied to the case of silica colloids by adopting the most recently developed and corrected soft particle model and following the methodology of Škvarla 2013.

The experimental results used in the present work are reproduced from (Škvarla 2013). Observations were made by measuring the absorbance (at 380, 540, and 800 nm) of a silica-water-KCl suspension system as a function of time under varying chemical conditions (pH = 2.6, 4, 6, and 8; ionic strength = 0.001 to 1 M), revealing the progressing aggregation process. The (50, 150, and 320 nm SEM diameters) silica samples are homogenous nonporous silica having natural hydroxyl silanol groups on the surface, suspended in KCl brines, produced by Bangs Laboratories Inc. (Škvarla 2013).

4.2.2.2 Ohshima's three-stage soft particle model

In this section, the interaction potentials of two soft particles are derived by reproducing the work of Ohshima (2015), for each of the three stages. The mathematical scheme of Ohshima's model may be complicated. However, after understanding how the model is developed (the contents shown in the present section), it may be possible to reduce the model to one variable remaining uncertain, the thickness of the ion-penetrable hairy layer d_0. In Section 4.2.2.3, it is proposed that a universal expression for it can be found, thus completing the soft particle model and allowing stability of silica sols to be predicted and explained.

1. Stage I: Approach

To model the electrostatic interaction, it is necessary to solve the Poisson-Boltzmann equations in ranges both inside and outside the hairy layer. For simplicity, one can initially consider two parallel plates 1 and 2 with ion-penetrable hairy layers on the surface, i.e. soft plates. The thicknesses of the layers 1 and 2 are d_1 and d_2 respectively. The two soft plates are separated by a distance H and immersed in a brine having N different ionic species with valence z_i and number density n_i,. The layers 1 and 2 are assumed to be charged at the uniform charge densities ρ_{fix1} and ρ_{fix2} separately, which is defined by $\rho_{fixi} = Z_i e N_i$ where Z_i and N_i are the valence and the number density of the dissociated groups respectively. The coordinate set up is shown in Figure 4.32.

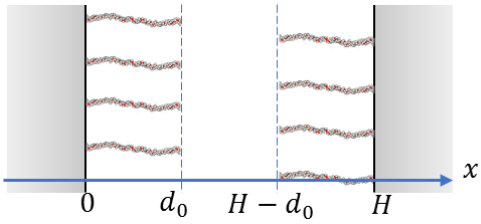

Figure 4.32: Parallel soft plates showing the different regions: hairy layer 1 ($0< x < d_0$), solution ($d_0 < x < H - d_0$) separation distance H.

It is assumed that the electric potential distribution ψ over x can be described using the one-dimensional planar Poisson-Boltzmann equations:

for $0 < x < d_0$:

$$\frac{d^2\psi(x)}{dx^2} = -\frac{1}{\varepsilon_r \varepsilon_0}\sum_{i=1}^{N} z_i e n_i \exp\left(-\frac{z_i e\psi(x)}{k_B T}\right) - \frac{\rho_{fix1}}{\varepsilon_r \varepsilon_0} \tag{4.69}$$

for $d_0 < x < H - d_0$:

$$\frac{d^2\psi(x)}{dx^2} = -\frac{1}{\varepsilon_r \varepsilon_0}\sum_{i=1}^{N} z_i e n_i \exp\left(-\frac{z_i e\psi(x)}{k_B T}\right) \tag{4.70}$$

for $H - d_0 < x < H$:

$$\frac{d^2\psi(x)}{dx^2} = -\frac{1}{\varepsilon_r \varepsilon_0}\sum_{i=1}^{N} z_i e n_i \exp\left(-\frac{z_i e\psi(x)}{k_B T}\right) - \frac{\rho_{fix2}}{\varepsilon_r \varepsilon_0} \tag{4.71}$$

However, for simplicity, one can replace the parameters by using a scaled (i.e. non-dimensionalised) forms:

for $d_0 < x < H - d_0$:

$$\frac{d^2y(x)}{dx^2} = \kappa^2 \sinh y \tag{4.72}$$

for $0 < x < d_0$ and $H - d_0 < x < H$:

$$\frac{d^2y(x)}{dx^2} = \kappa^2(\sinh y - \sinh y_{DON1}) \tag{4.73}$$

where the scaled electric potential is defined by $y(x) = \frac{ze\psi(x)}{k_BT}$, and the scaled Donnan potential, which is the electric potential due to the distribution of ion species caused by the charged hairy layers, is $y_{DON1} = \frac{ze\psi_{DON1}}{k_BT} = \text{arcsinh}(\frac{ZN_0}{2zn})$.

The following boundary conditions with respect to the left plate are:

$$\left.\frac{d\psi(x)}{dx}\right|_{x=h/2} = 0 \tag{4.74}$$

$$\left.\frac{d\psi(x)}{dx}\right|_{x=d_0^-} = \left.\frac{d\psi(x)}{dx}\right|_{x=d_0^+} \tag{4.75}$$

$$\psi(x = d_0^-) = \psi(x = d_0^+) \tag{4.76}$$

$$\left.\frac{d\psi(x)}{dx}\right|_{x=0^+} = 0 \tag{4.77}$$

Alternatively, in the form of the scaled parameters:

$$\left.\frac{dy}{dx}\right|_{x=h/2} = 0 \tag{4.78}$$

$$\left.\frac{dy}{dx}\right|_{x=d_0^-} = \left.\frac{dy}{dx}\right|_{x=d_0^+} \tag{4.79}$$

$$y(x = d_0^-) = y(x = d_0^+) \tag{4.80}$$

$$\left.\frac{dy}{dx}\right|_{x=0^+} = 0 \tag{4.81}$$

The first boundary condition is due to symmetry, the second is a consequence of assuming the permittivity of the hairy layer and the solution are equal, the combination of the second and third shows that the potential and its gradient are continuous near the layer edge, and the final boundary condition assumes the surface of the particle core is uncharged, i.e. all dissociation sites have been occupied by the polyelectrolyte brushes.

The interaction force per unit area can be computed by integrating the excess osmotic pressure and the Maxwell stress ΔΠ(x) and T(x) over arbitrary closed surfaces x' and x'' encasing any plate of interest, say $x' = H/2$ and $x'' = -\infty$ for convenience.

The excess osmotic pressure and the Maxwell stress are respectively defined by:

$$\Delta\Pi(x) = [n_+(x) + n_-(x)]k_BT - 2nk_BT = nk_BT[e^{-y(x)} + e^{y(x)} - 2] \tag{4.82}$$

$$T(x) = -\frac{1}{2}\varepsilon_r\varepsilon_0\left(\frac{d\psi(x)}{dx}\right)^2 \tag{4.83}$$

where $n_+(x)$ and $n_-(x)$ are the number concentration of positive and negative ions at x respectively. Hence, the interaction force per unit area can be represented by using ΔΠ(x) and T(x):

$$P_{pl}(H) = [\Delta\Pi(x') + T(x')] - [\Delta\Pi(x'') + T(x'')] \tag{4.84}$$

As $\left.\frac{dy}{dx}\right|_{x=-\infty,H/2} = 0$, one can find $\Delta\Pi(-\infty) = 0$ and $T(-\infty) = T(H/2) = 0$. By substituting the known values:

$$P_{pl}(H) = \Delta\Pi(H/2) = 4nk_BT\sinh^2\left(\frac{y\left(\frac{H}{2}\right)}{2}\right) \text{ for } H \geq 2d_0 \tag{4.85}$$

Based on the linear superposition approximation (LSA, Derjaguin & Landau 1941; Verwey & Overbeek 1948), the scaled potential $y\left(\frac{H}{2}\right)$ is approximately equal to $2y_0\left(\frac{H}{2}\right)$, where y_s is the local undisturbed electric potential, i.e. the potential of one soft plate in the absence of the other soft plate. Considering the boundary condition $y(x = \infty) = 0$, y_s can be easily derived by integrating Equation 4.72 and 4.73:

$$y_s(x) = 4\,\text{arctanh}[\tanh\left(\frac{y_0}{4}\right)\exp(-\kappa(x - d_0))] \tag{4.86}$$

where $y_0 = \frac{ze}{k_BT}\psi(0) = y_{DON1} - \tanh(y_{DON1}/2)$.

Therefore, the electrostatic force per unit is for $\kappa(H - 2d_0) \geq 1$ and $H \geq 2d_0$ can be found by substituting Equation 4.86 to 4.85:

for $H \geq 2d_0$:

$$P_{pl}(H) = 64nk_BT\tanh^2(y_0/4)\exp[-\kappa(H - 2d_0)] \tag{4.87}$$

By integrating $P_{pl}(H)$, the electrostatic potential per unit area $V_{pl}(H)$ can be found:

$$\begin{aligned} V_{pl}(H) &= \int_H^\infty P_{pl}(H)\,dH \\ &= \frac{1}{4\varepsilon_r\varepsilon_0\kappa^3}\{\left[\rho_{fix1}\sinh(\kappa d_1)\right. \\ &\quad \left.+ \rho_{fix2}\sinh(\kappa d_2)\right]^2\left[\coth\left(\frac{\kappa(H + d_1 + d_2)}{2}\right) - 1\right] \\ &\quad - \left[\rho_{fix1}\sinh(\kappa d_1) - \rho_{fix2}\sinh(\kappa d_2)\right]^2\left[1\right. \\ &\quad \left.- \tanh\left(\frac{\kappa(H + d_1 + d_2)}{2}\right)\right]\} \end{aligned} \tag{4.88}$$

In the case of an arbitrary potential, the LSA is used to find the electrostatic potential between the soft plates.

In the absence of one plate (say plate 2), the undisturbed electric potential distribution of the other plate (say plate 1) can be expressed by solving Equation 4.69-4.71:

$$\psi_1(x) = \frac{2k_BT}{ze}\ln\left(\frac{1 + \tanh\left(\frac{ze\psi_{o1}}{k_BT}\right)\exp(-\kappa x)}{1 - \tanh\left(\frac{ze\psi_{o1}}{k_BT}\right)\exp(-\kappa x)}\right) \tag{4.89}$$

$$\psi_2(x) = \frac{2k_BT}{ze}\ln\left(\frac{1+\tanh\left(\frac{ze\psi_{o2}}{k_BT}\right)\exp(-\kappa x)}{1-\tanh\left(\frac{ze\psi_{o2}}{k_BT}\right)\exp(-\kappa x)}\right) \tag{4.90}$$

where ψ_{o1} and ψ_{o2} are the undisturbed surface potentials of plate 1 and 2 respectively, which are related to the Donnan potential ψ_{DON1} and ψ_{DON2}:

$$\psi_{o1}(x) = \psi_{DON1} - \left(\frac{k_BT}{ze}\right)\tanh\left(\frac{ze\psi_{DON1}}{2k_BT}\right) \tag{4.91}$$

$$\psi_{o2}(x) = \psi_{DON2} - \left(\frac{k_BT}{ze}\right)\tanh\left(\frac{ze\psi_{DON2}}{2k_BT}\right) \tag{4.92}$$

And the Donnan potential is defined as:

$$\psi_{DON1} = \left(\frac{k_BT}{ze}\right)\text{arcsin h}\left(\frac{\rho_{fix1}}{2zen}\right) \tag{4.93}$$

$$\psi_{DON1} = \left(\frac{k_BT}{ze}\right)\text{arcsin h}\left(\frac{\rho_{fix2}}{2zen}\right) \tag{4.94}$$

At large separation distance, Equation 4.89 and 4.90 can be simplified to the asymptotic form:

$$\psi_1(x) = \psi_{\text{eff1}}\exp(-\kappa x) \tag{4.95}$$

$$\psi_2(x) = \psi_{\text{eff2}}\exp(-\kappa(H-x)) \tag{4.96}$$

where ψ_{eff1} and ψ_{eff2} are the effective surface potentials of plate 1 and 2 respectively and defined by:

$$\psi_{\text{eff1}}(x) = 4\tanh\left(\frac{ze\psi_{o1}}{4k_BT}\right) \tag{4.97}$$

$$\psi_{\text{eff2}}(x) = 4\tanh\left(\frac{ze\psi_{o2}}{4k_BT}\right) \tag{4.98}$$

Therefore, the electric potential distribution in the range of $0 < \text{x} < \text{H}$ can be found:

$$\psi(x) = \psi_1(x) + \psi_2(x) = \psi_{\text{eff1}}\exp(-\kappa x) + \psi_{\text{eff2}}\exp(-\kappa(H-x)) \tag{4.99}$$

Hence, by combining Equation 4.93-4.99, one can find:

$$P_{pl}(H) = 2\varepsilon_r\varepsilon_0\kappa^2\psi_{\text{eff1}}\psi_{\text{eff2}}\exp(-\kappa H) \tag{4.100}$$

By integrating $P_{pl}(H)$, the electrostatic potential per unit area $V_{pl}(H)$ can be found:

$$V_{pl}(H) = \int_H^\infty P_{pl}(H)\,dH = 2\varepsilon_r\varepsilon_0\kappa\psi_{\text{eff1}}\psi_{\text{eff2}}\exp(-\kappa H) \tag{4.101}$$

By integrating $V_{pl}(H)$, the electrostatic potential between two spherical colloids 1 and 2 $V_{sp}(H)$ can be found:

$$V_{sp}(H) = \frac{2\pi(a_1+d_1)(a_2+d_2)}{(a_1+d_1)+(a_2+d_2)}\int_H^\infty V_{pl}(H)\,dH \tag{4.102}$$

By substituting Equation 4.88 to 4.102 one can find:

$$V_{sp}(H) = \frac{1}{4\varepsilon_r\varepsilon_0\kappa^3}\frac{\pi(a_1+d_1)(a_2+d_2)}{a_1+d_1+a_2+d_2}\{[\rho_{fix1}\sinh(\kappa d_1) + \rho_{fix2}\sinh(\kappa d_2)]^2 \ln[\frac{1}{1-\exp(-\kappa(H+d_1+d_2))}] - [\rho_{fix1}\sinh(\kappa d_1) - \rho_{fix2}\sinh(\kappa d_2)]^2 \ln[1 + \exp(-\kappa(H+d_1+d_2)]\} \quad (4.103)$$

By substituting Equation 4.100 derived using the LSA to Equation 4.102, one can find a simpler expression:

$$V_{sp}(H) = \frac{4\pi(a_1+d_1)(a_2+d_2)}{a_1+d_1+a_2+d_2}\varepsilon_r\varepsilon_0\psi_{\text{eff1}}\psi_{\text{eff2}}\exp(-\kappa H) \quad (4.104)$$

2. Stage II: Interdigitation

Next, the case of interdigitation, as shown in Figure 4.33, is considered. The coordinate set up is shown below.

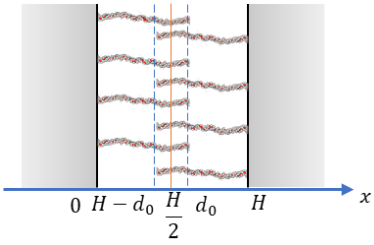

Figure 4.33: Parallel soft plates showing the different regions: hairy layer 1 ($0< x < H - d_0$), interdigitation zone ($H - d_0 < x < d_0$), and separation distance H.

As shown in Figure 4.33, the layers within the range $0 < \text{x} < \text{H} - d_0$ and $d_0 < x < H$ are undisturbed, and in $\text{H} - d_0 < x < d_0$ are interdigitating. For this case, the assumption of uniformly distributed dissociated groups remains. Therefore, the number density of ionised groups in $0 < \text{x} < \text{H} - d_0$ and $d_0 < x < H$ is still N_0, and in $\text{H} - d_0 < x < d_0$ shall be $2N_0$. It is assumed that the electric potential in the case of interdigitation follows the Poisson-Boltzmann equations below:

for $0 < x < H - d_0$ and $d_0 < x < H$:

$$\frac{d^2y(x)}{dx^2} = \kappa^2(\sinh y - \sinh y_{DON1}) \quad (4.105)$$

for $H - d_0 < x < d_0$:

$$\frac{d^2y(x)}{dx^2} = \kappa^2(\sinh y - \sinh y_{DON2}) \quad \text{for } H - d_0 < x < d_0 \quad (4.106)$$

where y_{DON1} and y_{DON2} are the scaled Donnan potentials in the regions of undisturbed and interdigitation respectively, which are defined by $\sinh y_{DON1} = \frac{ZN_0}{2zn}$, $\sinh y_{DON2} = \frac{ZN_0}{zn}$.

Consider the following expressions:

$$y(x) = y_{DON1} + \Delta y \quad \text{for } 0 < x < H - d_0 \text{ and } d_0 < x < H \quad (4.107)$$

$$y(x) = y_{DON2} + \Delta y \quad \text{for } H - d_0 < x < d_0 \quad (4.108)$$

Equation 4.105 and 4.106 can then be linearized to:

$$\frac{d^2\Delta y}{dx^2} = \kappa_1^2 \Delta y \quad \text{for } 0 < x < H - d_0 \text{ and } d_0 < x < H \tag{4.109}$$

$$\frac{d^2\Delta y}{dx^2} = \kappa_2^2 \Delta y \qquad \text{for } H - d_0 < x < d_0 \tag{4.110}$$

where $\kappa_1 = \kappa\sqrt{\cosh(y_{DON1})}$ and $\kappa_2 = \kappa\sqrt{\cosh(y_{DON2})}$ physically mean the Debye-Hückel parameters in the undisturbed and interdigitation regions respectively.

The following boundary conditions with respect to the left plate are:

$$\left.\frac{dy}{dx}\right|_{x=h/2} = 0 \tag{4.111}$$

$$\left.\frac{dy}{dx}\right|_{x=h-d_0^-} = \left.\frac{dy}{dx}\right|_{x=h-d_0^+} \tag{4.112}$$

$$y(x = h - d_0^-) = y(x = h - d_0^+) \tag{4.113}$$

$$\left.\frac{dy}{dx}\right|_{x=0^+} = 0 \tag{4.114}$$

With the boundary condition above (Equation 4.111-4.114), Equation 4.105 and 4.106 can be solved, and the electrostatic force per unit area can be found:

for $0 < x < H - d_0$

$$y(x) = y_{DON1} - \left(\frac{\kappa_1}{\kappa_2}\right)(y_{DON2} - y_{DON1})\frac{\sinh\left[\kappa_2\left(\frac{H}{2} - d_0\right)\right]}{G(H)}\cosh(\kappa_1 x) \tag{4.115}$$

for $H - d_0 < x < d_0$

$$y(x) = y_{DON2} - (y_{DON2} - y_{DON1})\frac{\sinh[\kappa_1(H - d_0)]}{G(H)}\cosh[\kappa_2(x - h/2)] \tag{4.116}$$

for $d_0 < x < H$

$$y(x) = y_{DON1} - \left(\frac{\kappa_1}{\kappa_2}\right)(y_{DON2} - y_{DON1})\frac{\sinh\left[\kappa_2\left(\frac{H}{2} - d_0\right)\right]}{G(H)}\cosh[\kappa_2(H - x)] \tag{4.117}$$

where $G(H)$ is defined by:

$$\begin{aligned} G(H) = {} & \sinh\big(\kappa_1(H - d_0)\big)\cosh\left[\kappa_2\left(\frac{H}{2} - d_0\right)\right] \\ & - \left(\frac{\kappa_2}{\kappa_1}\right)\cosh\big(\kappa_1(H - d_0)\big)\sinh\left[\kappa_2\left(\frac{H}{2} - d_0\right)\right] \end{aligned} \tag{4.118}$$

The electrostatic force per unit area can be found using the same approach, i.e. by considering the excess osmotic pressure and the Maxwell stress applied on the soft plate. The integral of the Poisson Boltzmann equation outside the hairy layers will give a constant $\Delta\Pi(x) + T(x)$, but this is not true within the layers due to the charges of the dissociated groups, i.e. $\Delta\Pi(x) + T(x)$ is varying over x. Therefore, one surface must be $x' = d_0$, the other is chosen to be $x'' = -\infty$ for convenience:

$$P_{pl}(H) = [\Delta\Pi(d_0) + T(d_0)] - [\Delta\Pi(-\infty) + T(-\infty)] \tag{4.119}$$

Similarly, based on the boundary conditions, one can find $\Delta\Pi(-\infty) = 0$ and $T(-\infty) = 0$:

$$P_{pl}(H) = [\Delta\Pi(d_0) + T(d_0)] \tag{4.120}$$

That is:

$$\begin{aligned} P_{pl}(H) = 4nk_BT \Bigg\{ & \sinh^2\left[\frac{y_{DON2}}{2}\right. \\ & \left. - \frac{y_{DON2} - y_{DON1}}{2G(H)} \sinh\left(\kappa_1(H - d_0)\right) \cosh\left[\kappa_2\left(\frac{H}{2} - d_0\right)\right]\right] \\ & - \frac{1}{4}\left(\frac{\kappa_2}{\kappa}\right)^2 \left(\frac{y_{DON2} - y_{DON1}}{G(H)}\right)^2 \sinh^2\left[\kappa_2\left(\frac{H}{2} - d_0\right)\right]\Bigg\} \\ & \text{for } d_0 < H < 2d_0 \end{aligned} \tag{4.121}$$

The electrostatic interaction potential between the spherical particles can be found by following the same method described in Equation 4.101-4.103, or by solving numerically.

3. Stage III: Compression

Now, consider the third stage for the two-stage model: after the hairy layers interdigitate to a distance H_c, the polymer chains start to compress, as shown in Figure 4.34 below.

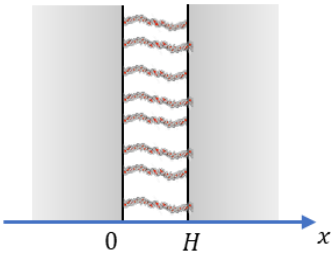

Figure 4.34: Parallel soft plates showing the compression stage.

For simplicity, only the case of full interdigitation is considered in this work, i.e. the compression stage starts when the brushes are completely interdigitated ($H_c = d_0$).

The separation distance can then be expressed by $\mathrm{H} = \mathrm{d} \leq d_0$.

Previously, it was assumed that the layer is uniformly charged and the charge density (ρ_{fix1} and ρ_{fix2}) is a constant. However, in this case, it is a function of H, i.e. increasing while compressing. The assumption of uniformly distributed charged groups remains. For simplicity, it is assumed that $N_1 = N_2 = 2N_0$, i.e. the subscript "0" means "undisturbed". Therefore, the number density of the ionised groups N' in this case can be related to the undisturbed number density $2N_0$:

$$N'\frac{\mathrm{H}}{2} = N_0 d_0 \tag{4.122}$$

Since the potential within the compressed layers is constant (both layers are uniformly charged) and depends on the separation distance H but not on the location x, it is assumed that the scaled electric potential $y(x) = ze\psi(x)/k_BT$ obeys the following Poisson-Boltzmann equation:

for $0 < x \leq 2d_0$:

$$\frac{d^2y(x)}{dx^2} = \kappa^2\left[\sinh y - \frac{ZN'}{2zn}\right] = 0 \tag{4.123}$$

i.e. the electric potential is equal to the Donnan potential $\psi_{DON}{}'(H)$ for this case everywhere. Therefore, the formula containing the scaled Donnan potential $y_{DON}{}'$ in this case can be derived:

$$\sinh[y_{DON}{}'(H)] = \frac{ZN'}{2zn} = \frac{ZN_0d_0}{znH} \tag{4.124}$$

By solving, one can find the electrostatic force per unit area:

for $0 < H \leq 2d_0$:

$$P_{pl}(H) = 2nk_BT\left[\sqrt{\left(\frac{ZN_0d_0}{2znH}\right)^2 + 1} - 1\right] \quad \text{for } 0 < H \leq d_0 \tag{4.125}$$

The related potential can be found by following the approach described previously (Equation 4.101-4.103).

4.2.2.3 Fitting results and discussion

The interaction between soft particles can be modelled using this three-stage approach. Compared to the classic model, the charged hairy layer with the finite thickness (d_0) can provide a stronger but not excessively repulsive potential, like the steric barrier.

When the two particles aggregate, the separation distance H is called the capture distance H_c. In the frame of DLVO theory, it is usually assumed to be 0, i.e. one particle captures the other once their separation distance becomes 0 ($H_c = 0$).

In contrast, different stages in the soft particle model can be considered by positing different capture distances. To find the stability, the integral in Equation 4.64 shall be performed from infinity to the assumed capture distance H_c instead of to 0. Therefore, there are three cases to be considered.

1. The capture distance is $2d_0$ (i.e. $H_c = 2d_0$). The two particles are attached once the hairy layers touch each other, i.e. only Stage I (approach) is taken into account;

2. The capture distance is between d_0 and $2d_0$ (i.e. $d_0 \leq H_c < 2d_0$). The two particles are attached till the hairy layers become interdigitated, i.e. both Stage I and II (approach and interdigitation) are considered;

3. The capture distance is less than d_0 ($H_c < d_0$). The two particles aggregate till the hairy layers are compressed, i.e. all three stages (approach, interdigitation, and compression) are applied.

Note that the thickness of hairy layers d_0 only limits the bounds of H_c for the three cases.

When the background chemical (pH and ionic strength) conditions are given, the surface charge can be found. The approach taken in this study is to adjust d_0 until the predicted stability matches the observation under the same conditions. If such a match can be found across a range of pH, it is inferred that the soft particle model better represents the physics of silica colloid interaction than does the DLVO theory. The fitting process is summarised in Figure 4.35 below:

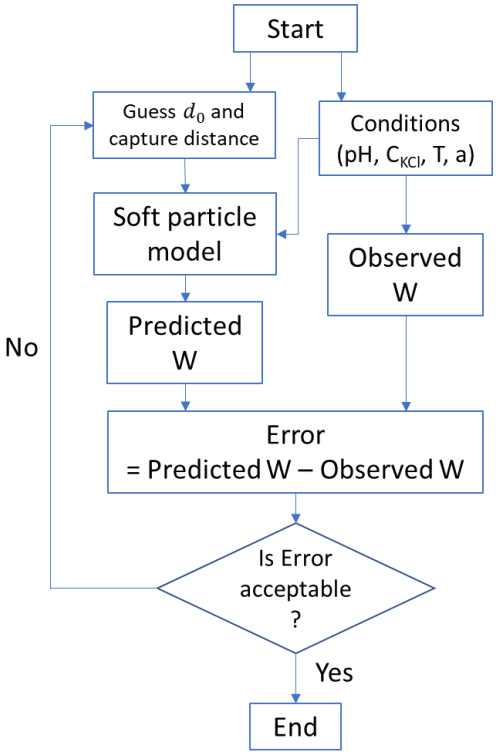

Figure 4.35: The workflow of the fitting process. d_0 is the only free parameter, and all other values are taken from the reported experimental conditions. The observed stability can be fitted almost exactly (All errors are less than 5% of observed W) by giving a separate value of d_0 for each experiment. Recall that a represents the radius of the particle (hairy layer excluded).

The complete set of inputs and fitting results is shown in Table 4.5 below.

Table 4.5: Stability fitting results: d_{lab} is the average diameter of silica particle samples; I is the ionic strength, which is equal to the concentration of KCl in this case; $-\sigma_0$ is the surface charge density reproduced from Škvarla 2013 and estimated by following Sonnefeld 1995 if the experimental data is not presented; W is the observed stability; W_{DLVO} is the estimated stability using the DLVO theory (missing data due to the absence of the corresponding zeta-potential); W' is the fitted stability using the soft particle model; d_0 is the fitted thickness of hairy layers.

pH = 4		d_{lab} = 50 nm				d_{lab} = 150 nm				d_{lab} = 320 nm			
I(M)	$-\sigma_0$ (mC m^{-2})	W	W_{DLVO}	W'	d_0(nm)	W	W_{DLVO}	W'	d_0(nm)	W	W_{DLVO}	W'	d_0(nm)
0.001	1.39	-				58.3	2.41E+03	58.12	22.29	220.0	8.10E+15	219.52	24.38
0.0025	1.42	-				49.6	5.83	49.84	12.09	100.0	2.26E+10	100.43	13.50
0.005	1.48	-				16.1	2.69E-05	16.04	7.69	22.0	0.08	22.03	8.71
0.007	1.51	-				20.0	1.16E-06	20.10	6.12	17.0	6.74E-05	17.08	7.00
0.01	1.57	8000.0	6.63E-08	7.91E+03	3.72	12.0	2.70E-07	11.93	4.87	12.0	1.13E-06	11.88	5.59
0.025	1.89	1010.0	5.48E-08	1.03E+03	2.08	11.0	1.77E-07	10.88	2.75	8.0	3.99E-07	7.98	3.20
0.05	2.43	110.0	5.59E-08	113.54	1.42	10.0	1.81E-07	10.17	1.86	5.1	4.08E-07	5.07	2.19
0.07	2.85	105.0	5.60E-08	102.86	1.19	18.0	1.81E-07	17.48	1.56	3.6	4.06E-07	3.53	1.85
0.1	3.49	110.0	5.70E-08	110.72	1.01	22.0	1.84E-07	22.85	1.31	5.4	4.14E-07	5.47	1.55
0.2	5.87	-				20.0		19.89	1.00	4.0		4.06	1.17
0.25	6.69	140.0		149.36	0.69	-				-			
0.5	12.02	500.0		541.76	0.54	38.0		38.16	0.69	5.1		5.27	0.81
0.7	16.28	600.0		626.80	0.48	-				9.5		9.77	0.71
1	22.67	700.0		731.57	0.43	25.0		23.52	0.55	-			

pH = 6		d_{lab} = 50 nm				d_{lab} = 150 nm				d_{lab} = 320 nm			
I(M)	$-\sigma_0$ (mC m^{-2})	W	W_{DLVO}	W'	d_0(nm)	W	W_{DLVO}	W'	d_0(nm)	W	W_{DLVO}	W'	d_0(nm)
0.001	6.53	-				161.3	1.10E+19	161.73	33.02	-			
0.0025	8.58	-				128.8	2.56E+13	128.38	19.80	-			
0.005	11.30	-				103.5	6.04E+09	104.15	13.69	230.0	4.99E+29	229.95	14.82
0.01	11.90	55000.0	3.34E-06	5.51E+04	7.63	88.2	0.31	88.74	8.985	100.0	5.25E+07	99.84	9.83
0.025	17.06	23000.0	3.38E-08	2.25E+04	4.65	35.9	0.0061	35.70	5.542	110.0	1.29E+04	109.99	6.06
0.05	20.80	20000.0	3.05E-08	2.00E+04	3.13	27.4	7.05E-05	26.90	3.769	80.0	0.9961	78.70	4.13
0.07	23.20	5000.0	3.05E-08	5.07E+03	2.61	16.4	6.75E-06	16.40	3.142	5.0	0.0063	5.11	3.49
0.1	26.50	300.0	3.05E-08	289.36	2.18	5.2	1.11E-06	5.26	2.612	4.5	9.93E-05	4.44	2.89
0.25	27.05	250.0		257.21	1.20	3.7		3.67	1.467	1.3		1.28	1.65
0.5	27.20	280.0		306.21	0.75	-				-			
0.7	27.21	300.0		326.44	0.60	-				-			
1	27.22	390.0		371.22	0.46	-				-			

pH = 8		d_{lab} = 50 nm				d_{lab} = 150 nm				d_{lab} = 320 nm			
I(M)	$-\sigma_0$ (mC m^{-2})	W	W_{DLVO}	W'	d_0(nm)	W	W_{DLVO}	W'	d_0(nm)	W	W_{DLVO}	W'	d_0(nm)
0.005	52.60	4.00E+05	5.61	3.99E+05	15.89	348.8	2.36E+18	347.39	17.90	205.0	1.16E+48	204.83	19.21
0.01	58.20	3.00E+05	5.00E-05	3.01E+05	10.68	187.5	1.33E+03	187.81	12.19	105.0	3.15E+15	105.09	13.14
0.025	71.60	1.95E+05	2.59E-06	1.96E+05	6.39	156.3	0.19	157.00	7.38	100.0	2.04E+07	99.26	7.99
0.05	82.50	2.50E+04	2.76E-07	2.56E+04	4.35	123.5	1.33E-04	122.61	5.03	90.0	3.93	89.37	5.46
0.07	88.20	1.40E+04	1.47E-07	1.39E+04	3.61	68.4	1.12E-05	69.13	4.18	60.0	0.02	61.12	4.54
0.1	95.20	8000.0	2.03E-07	8.27E+03	2.95	74.6	4.97E-05	77.77	3.43	18.0	0.54	18.25	3.75
0.25	103.92	1010.0		963.39	1.74	7.1		7.05	2.05	1.3		1.26	2.25
0.5	117.20	600.0		624.16	1.16	5.2		5.15	1.37	1.4		1.43	1.51
0.7	117.20	750.0		751.84	0.94	6.0		6.03	1.11	1.8		1.87	1.23
1	117.21	-				7.0		7.54	0.89	2.2		2.12	0.99

Note that the colloidal silica samples analysed above are not naturally formed in geothermal water but under ideal lab conditions.

The only free parameter is d_0, which is assumed to be a function of pH, c_{KCl}, and particle size a. The values of d_0 obtained are plotted in Figure 4.36.

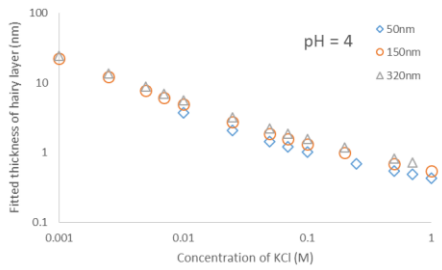

(a)

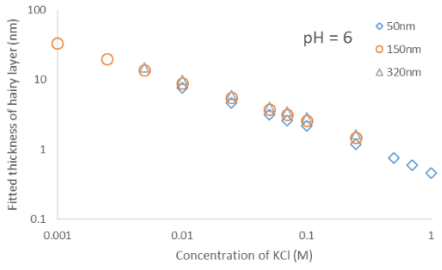

(b)

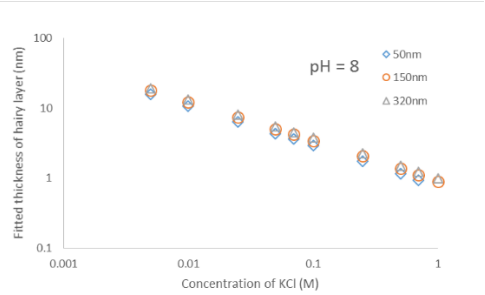

(c)

Figure 4.36: Fitted hairy layer thickness as a function of KCl concentration and pH in logarithmic scales.

A systematic variation of the fitted d_0 values with c_{KCl}, a and pH are seen, suggestive of a physical relationship. In logarithmic scales, d_0 is seen to be strongly dependent, and nearly linear with, c_{KCl}, only weakly dependent on particle size a, and modestly increasing as pH rises. Therefore, the following correlations may be proposed and fitted to describe the correlations between d_0 and c_{KCl} and pH.

When pH is a constant:

$$\log d_0 = a_{d_0} \log c_{\mathrm{KCl}} + b_{d_0} \tag{4.126}$$

Otherwise:

$$\log d_0 = c_{d_0}(d_{d_0}\mathrm{pH} + e_{d_0}) \log c_{\mathrm{KCl}} + (f_{d_0}\mathrm{pH} + \mathrm{g}_{d_0}) \tag{4.127}$$

where a_{d_0}, b_{d_0}, c_{d_0}, d_{d_0}, e_{d_0}, f_{d_0}, and g_{d_0} are fitting parameters.

By assuming that the capture distance is $2d_0$ (i.e. only Stage I is considered), which physically means that the particles are successfully linked once the hairy layers from two particles collide as shown in Figure 4.37 below, the fitting results are good enough to conclude that Ohshima's soft particle model is valid to explain the unexpected interactions between the colloidal silica at least in the range of pH = 4, 6, and 8, c_{KCl} = 0.001-1 M.

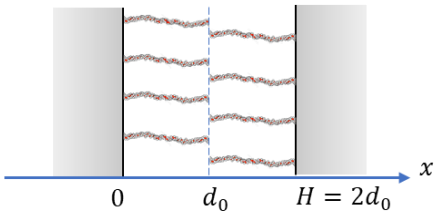

Figure 4.37: Two soft particles aggregate once two hairy layers collide. This is equivalent to Figure 4.32 when the separation distance H is equal to $2d_0$. At this moment, $H = H_c = 2d_0$.

4.2.2.4 Interpretation of the varying hairy layer thickness

According to Figure 4.36, it can be concluded that the variation in d_0 is dominated by pH and the concentration of KCl (or ionic strength of the background electrolyte when implementing the model). Particle size has minor effects as well. The results seem feasible, since the more favourable the conditions are to silica polymerisation (i.e. higher pH and lower ionic strength), the thicker the hairy layers are expected to be.

By ignoring the effects of particle size, a linear correlation between log d_0 and log c_{KCl} can be fitted:

at pH = 4 ($R^2 = 0.97$),

$$\log d_0 = -0.5535 \log c_{\mathrm{KCl}} - 0.3957 \tag{4.128}$$

at pH = 6 ($R^2 = 0.98$),

$$\log d_0 = -0.6032 \log c_{\mathrm{KCl}} - 0.2403 \tag{4.129}$$

at pH = 8 ($R^2 = 0.99$),

$$\log d_0 = -0.5698 \log c_{\mathrm{KCl}} - 0.1062 \tag{4.130}$$

Equation 4.128-4.130 may be safely applied to estimate the thickness of the hairy layers at pH = 4, 6, and 8 and $c_{\mathrm{KCl}} = 0.001 - 1\mathrm{M}$ at 25℃.

To conveniently apply Equation 4.128-4.130, a generalised form for pH is proposed below as well:

$$\log d_0 = -(0.00426\mathrm{pH} + 0.5455) \log c_{\mathrm{KCl}} + (0.08738\mathrm{pH} - 0.7475) \tag{4.131}$$

where $R^2 = 0.98$.

To allow this fitting results to be feasibly applied in the holistic model, c_{KCl} is replaced with the ionic strength I, which is in the range of 0.001-1 M as well, and this range of I may cover typical geothermal conditions (about 0.07 M in New Zealand fields, dominated by the concentration of sodium chloride). Considering potassium has the weakest coagulating effect among the common cations in geothermal brines, this major simplification could result in an overestimated stability and therefore an underestimated colloidal silica deposition rate.

As d_0 is fitted to match the observed stability, the observed stability behaviour is directly reproduced by reinputting the predicted d_0 using Equation 4.128-4.131 to this new model (Figure 4.38). Hairy layer thickness varies with pH, and thus so does repulsive electrostatic potential, which permits variations in stability that are not predicted by the classic DLVO theory.

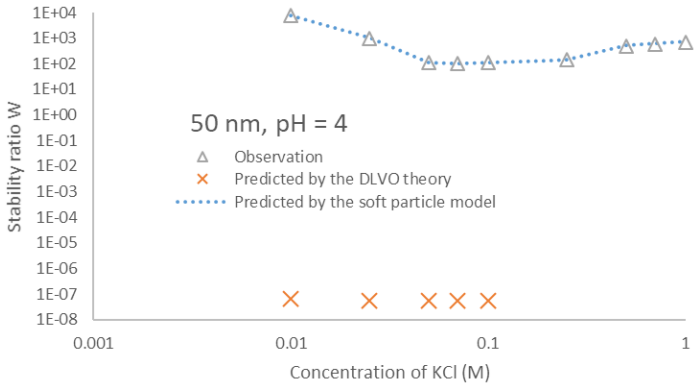

(a)

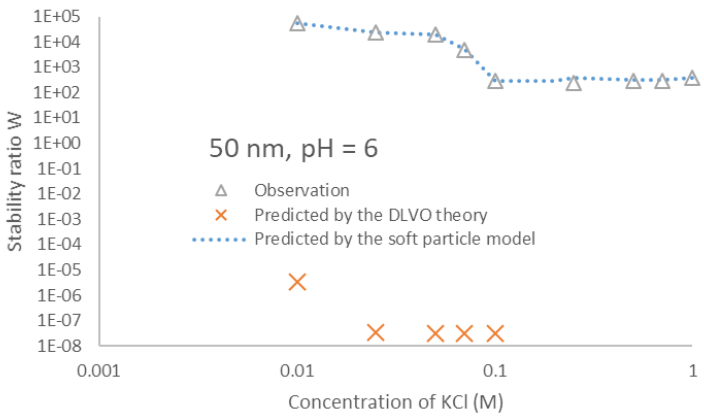
50 nm, pH = 6
Observation
Predicted by the DLVO theory
Predicted by the soft particle model
Stability ratio W
Concentration of KCl (M)
1E+05
1E+04
1E+03
1E+02
1E+01
1E+00
1E-01
1E-02
1E-03
1E-04
1E-05
1E-06
1E-07
1E-08
0.001
0.01
0.1
1

(b)

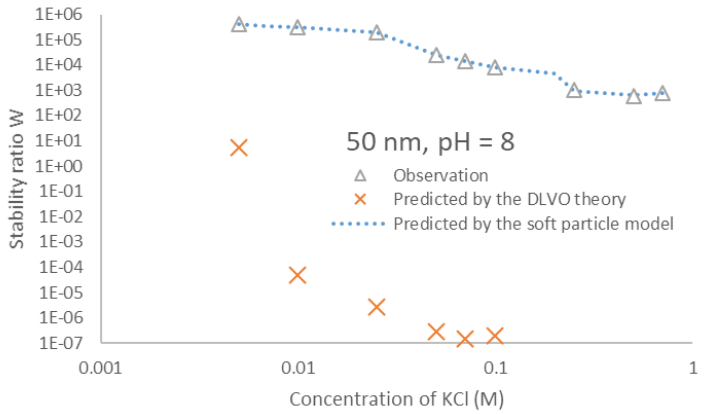
50 nm, pH = 8
Observation
Predicted by the DLVO theory
Predicted by the soft particle model
Stability ratio W
Concentration of KCl (M)
1E+06
1E+05
1E+04
1E+03
1E+02
1E+01
1E+00
1E-01
1E-02
1E-03
1E-04
1E-05
1E-06
1E-07
0.001
0.01
0.1
1

(c)

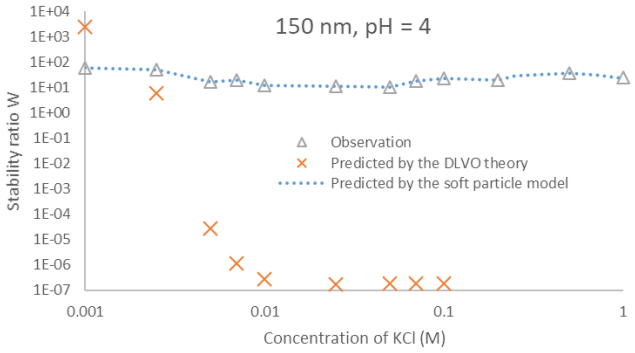
150 nm, pH = 4
Observation
Predicted by the DLVO theory
Predicted by the soft particle model
Stability ratio W
Concentration of KCl (M)
1E+04
1E+03
1E+02
1E+01
1E+00
1E-01
1E-02
1E-03
1E-04
1E-05
1E-06
1E-07
0.001
0.01
0.1
1

(e)

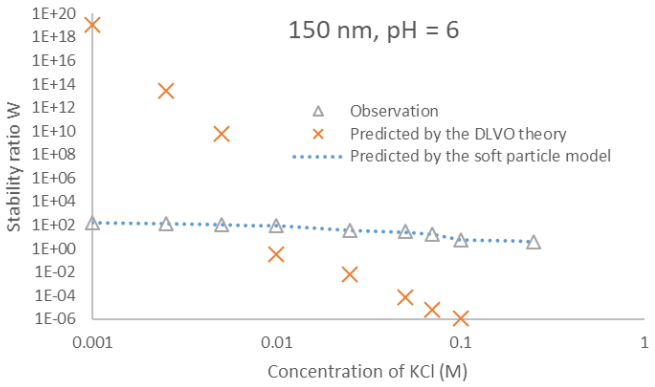
150 nm, pH = 6
Stability ratio W
1E+20
1E+18
1E+16
1E+14
1E+12
1E+10
1E+08
1E+06
1E+04
1E+02
1E+00
1E-02
1E-04
1E-06
0.001
0.01
0.1
1
Concentration of KCl (M)
Observation
Predicted by the DLVO theory
Predicted by the soft particle model

(f)

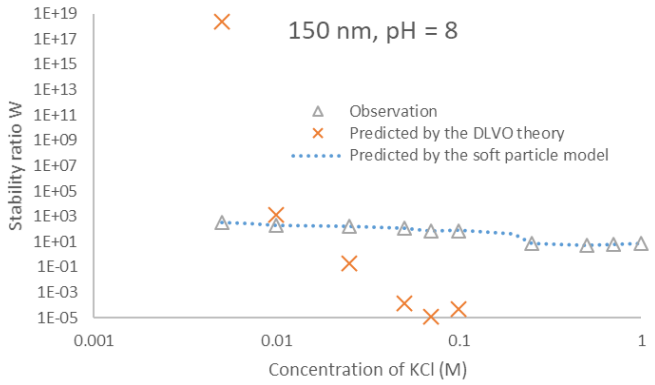
150 nm, pH = 8
Stability ratio W
1E+19
1E+17
1E+15
1E+13
1E+11
1E+09
1E+07
1E+05
1E+03
1E+01
1E-01
1E-03
1E-05
0.001
0.01
0.1
1
Concentration of KCl (M)
Observation
Predicted by the DLVO theory
Predicted by the soft particle model

(g)

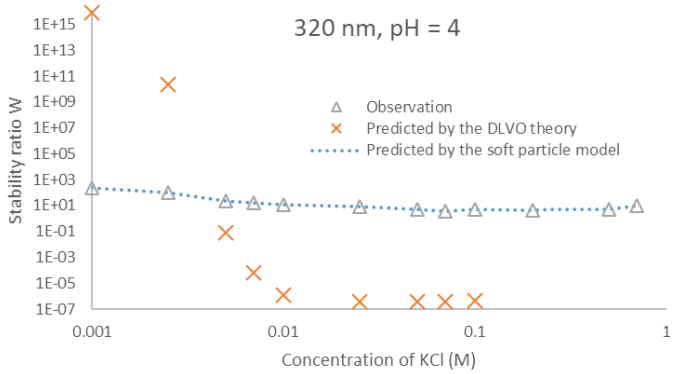
320 nm, pH = 4
Stability ratio W
1E+15
1E+13
1E+11
1E+09
1E+07
1E+05
1E+03
1E+01
1E-01
1E-03
1E-05
1E-07
0.001
0.01
0.1
1
Concentration of KCl (M)
Observation
Predicted by the DLVO theory
Predicted by the soft particle model

(h)

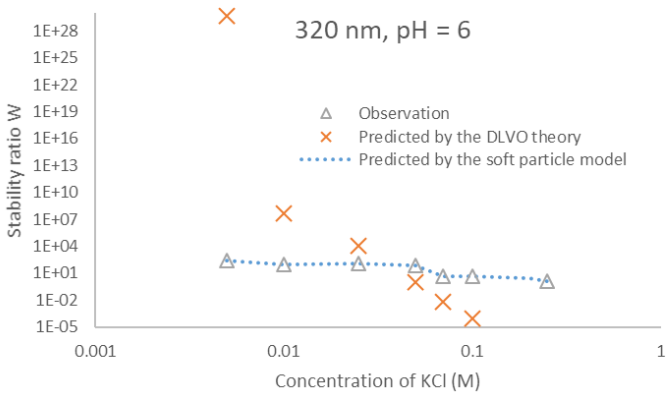

(i)

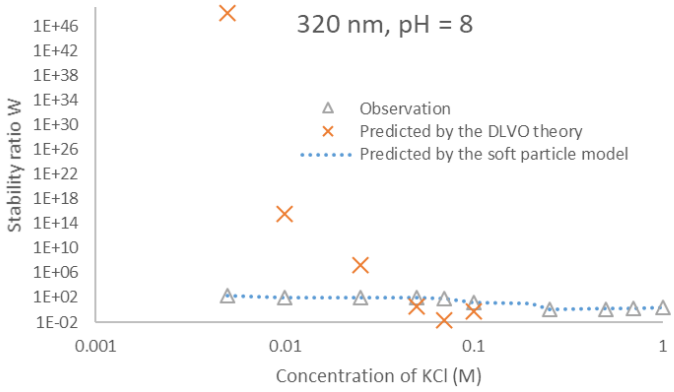

(j)

Figure 4.38: Comparison between the observed and the predicted (by the DLVO theory and the soft particle model) stability as a function of c_{KCl} for 50, 150, and 320 nm in diameter silica particles at pH = 4, 6 and 8, and 25 ℃.

As the classic DLVO theory fails to model the interactions of silica particles, it can be very difficult to precisely simulate colloidal silica deposition. Comparing to the work of Škvarla (2013), the thesis author adopts the most recent developed soft particle model (Ohshima 2015) and manages to apply the model to describe the interactions of colloidal silica under all available conditions. Ohshima's latest soft particle model (Ohshima 2015) is shown to explain the unexpected interaction behaviours at pH = 4, 6, and 8 and $c_{KCl} = 0.001 - 1M$ at 25℃, which may offer a better understanding of the mechanisms for silica particle attachment and silica scaling, at least at room temperature. Also, the new correlations to predict the thickness of hairy layers d_0 are proposed. Further experimental studies may be of interest to investigate the interactions between silica particles and silica coated plates at high temperature in the frame of the soft particle model.

Chapter 5

Acidification

Acidification is used (Rothbaum et al. 1979; Gallup 1997; Brown 2011; Addison et al. 2015) as a method to inhibit silica scaling, by limiting the kinetics of polymerisation of dissolved silica. pH 4.5 – 5.0 is often chosen as a compromise between maximising the desired effects and minimising corrosion of pipe (Brown 2011; Addison et al. 2015). Sulphuric acid (aqueous solution of H_2SO_4) is commonly used in geothermal energy production as it is the cheapest way of achieving the desired pH. In New Zealand, the technique has been successfully applied at the Ngatamariki station, the Nga Awa Purua Station, and the Kawerau Station (Addison et al. 2015).

Since carbonate minerals (most commonly, calcite $CaCO_3$ (Browne 1978)) are common in the formations hosting geothermal aquifers, the dissolution of calcite may play a crucial role during the application of acidification. Also, since the application of sulphuric acid will introduce additional sulphate ion (SO_4^{2-}), the risk of the problematic calcium sulphate ($CaSO_4$) precipitation can be significantly increased. In practice, before injecting sulphuric acid, the possibility of anhydrite precipitation will be estimated: if it is high, hydrogen chloride acid will be used instead. In this chapter, the potential consequences of acidification such as calcite dissolution and calcium sulphate precipitation are discussed.

There are three forms of calcium carbonate found in rocks: calcite, aragonite, and vaterite, of which calcite is the most common and stable near the Earth's surface (Reeder 1990). As calcite is a salt of carbonic acid, it will dissolve in any stronger acid. Bénézeth et al. (2013) suggested that prior to any such dissolution, at all temperatures and pH between neutral to alkaline, and in regions where calcite is present in the aquifer, most geothermal fluids are saturated with respect to calcite. Acidification will minimise the concentration of dissolved carbon dioxide $CO_2(aq)$ (including carbonic acid H_2CO_3), bicarbonate ion HCO_3^-, and carbonate ion CO_3^{2-} to a negligible level, however, after pH increases to neutral due to calcite dissolution, the concentrations of these species will increase again till the solution reaches equilibrium. Considering that the calcium carbonate has retrograde solubility i.e. its solubility product constantly decreases as the temperature increases (see Equation 5.21, 5.22, and Figure 5.5) and, in the case of geothermal reinjection, the injectate is heated by the reservoir rocks, the possibility of calcite precipitation far away from wellbore may be significant.

Thus, the deliberate dissolution of calcite, by acidification, and its corresponding reactive transport are of interest in many underground-resource extracting industries. Dissolution may

broaden the pores in the porous media or the aperture of the fracture networks, and therefore may increase the porosity, permeability, conductivity, and injectivity of the surrounding reservoir. However, the calcite neutralises the acid rapidly and cancels its inhibiting effects on silica nucleation. Qualitatively speaking, the fractures near the wellbore may be expanded, but the cost would be the formation of colloidal silica gradually plugging the fluid pathways further away. In oil extraction industries, similar problems of fast mineral dissolution near the wellbore are reported (Fredd and Fogler 1998) as well: a higher injection flow rate must be reached to stimulate the reservoir further away, which may require more expensive injection equipment.

In this chapter, to better understand the effects of calcite dissolution in the process of geothermal reinjection, the kinetics of the reactions are quantitatively described. In later chapters, the relevant processes will be modelled, and estimates of the consequences of acidification schemes made.

Consider a geothermal reservoir of interest in a cylindrical coordinate system, which will be comprehensively discussed further in Section 6.2, as shown below (Figure 5.1).

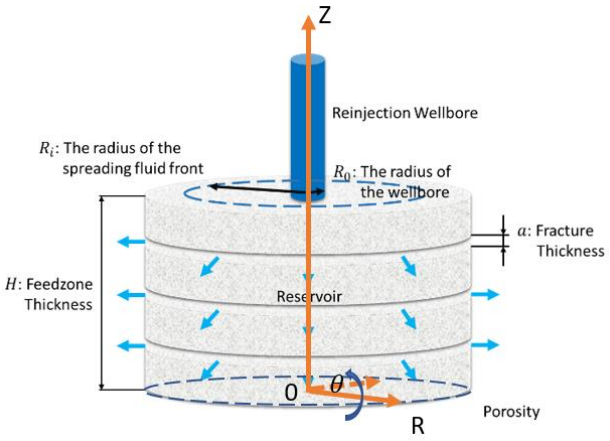

Figure 5.1: Simplified geometry consisting of an injection wellbore and geothermal reservoir.

As the rocks usually consist of many types of minerals heterogeneously distributed, to simplify the problem, it is assumed that the rocks are composed of only calcite and inert mineral (i.e. no chemical reaction occurs between the inert mineral and the injectate under any circumstance), which are homogenously distributed vertically and axially (with respect to the injection wellbore). Hence, the distribution of calcite is a function of the radial distance only, which can be defined by the user. To expose the potential consequence as much as possible, the default input is that 30% calcite and 70% inert mineral are homogenously distributed radially. In practice, the percentage of calcite would be extremely high. The typical value is usually a maximum of 5%.

The mass transfer of the reactants from the bulk flow to the rock surface will be discussed in Section 6.4.3. In this chapter, only the surface reaction is covered, and the goal is to find clear and simple methodologies that can reasonably predict the surface reaction rate under typical geothermal conditions.

When acid contacts a calcite surface, three surface reactions involved with solid calcite ($CaCO_3(s)$) occur simultaneously:

$$H^+ + CaCO_3(s) \leftrightarrow Ca^{2+} + HCO_3^- \tag{5.1}$$

$$H_2CO_3 + CaCO_3(s) \leftrightarrow Ca^{2+} + 2HCO_3^- \quad (5.2)$$

$$H_2O + CaCO_3(s) \leftrightarrow Ca^{2+} + HCO_3^- + OH^- \quad (5.3)$$

The product, bicarbonate ion (HCO_3^-), can undergo further reactions to form carbonic acid (H_2CO_3) or carbonate ion (CO_3^{2-}) depending on the pH.

Plummer et al. (1978) suggested the pH and the CO_2 partial pressure determines which of the reactions above limits the dissolution. Based on experimental investigations, Plummer et al. (1978) summarised that the reaction Equation 5.3 is always relevant in aqueous solutions, but more importantly, at 25 ℃, when pH is lower than 5 and CO_2 partial pressure is lower than 0.1 atm, the calcite dissolution mainly depends on reaction Equation 5.1; at CO_2 partial pressure greater than 0.1 atm or pH higher than about 5, reaction Equation 5.2 becomes important. However, in the case of geothermal reinjection, as the acidification excludes CO_2, the latter case (Equation 5.2) may be negligible at the early stage of injection.

Rotating disks are sometimes used to experimentally investigate the kinetics of the reactions between fluids and solid surfaces (Blake et al. 1968; Litt and Serad 1964), including the dissolution rate of calcite in acid. The apparatus is essentially a disk made of or mounted with solid reactant, installed on a rotating shaft and submerged in a solution where physical and chemical conditions, such as temperature, pressure, pH, etc., are controlled. By adjusting the external conditions and, more importantly, the rotational speed, the effects of the reactant transfer and the surface reaction on the dissolution rate can be differentiated. Newman (1966) derived the following formula to estimate the reactant mass flux J from the bulk solution to the rotating disk surface:

$$J = K_{MT}(C - C_i) = \left(\frac{0.62048\, Sc^{-\frac{2}{3}} \sqrt{\nu\omega}}{1 + 0.2980\, Sc^{-\frac{1}{3}} + 0.1451\, Sc^{-\frac{2}{3}}} \right)(C - C_i) \quad (5.4)$$

where K_{MT} represents the mass transfer coefficient, C and C_i are the concentrations of the reactant in the bulk solution and at the disk surface respectively, $Sc = \nu/D_e$ is the Schmidt number, ν is the kinematic viscosity of the solution, D_e is the effective diffusion coefficient of the reactant, and ω is the rotating speed of the disk. Unless specified otherwise, the unit of concentration mentioned in this chapter is molal (i.e. mol kg^{-1}). Under laminar conditions, where the Reynolds number obeys $Re = \omega R^2/\nu \leq 3 \times 10^5$ (Ellison 1969), the thickness of the boundary layer is a constant (i.e. independent of the radius of the disk R). Therefore, the estimated mass flux J can be used to represent both the local and the global mass transfer rate.

In the rotating disk experiment, when the mass transfer dominates the dissolution, the measured dissolution rate can be shown as a linear function in the square root of the rotational speed ω, and, once the rotational speed is fast enough that the system is well-stirred, it will gradually converge to a maximum (i.e. become independent of the square root of ω), when the surface reaction becomes the limiting step, as shown in Figure 5.2 below.

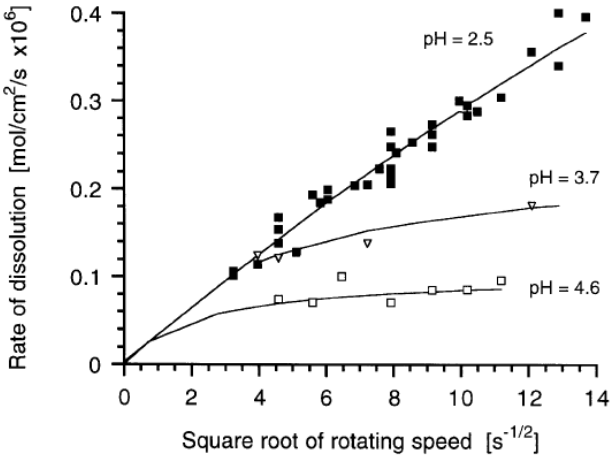

Figure 5.2: Dissolution rate as a function of the square root of rotating speed: different pH values were obtained by adding NaAc to 0.5 M HAc solutions, reproduced from Fredd and Fogler 1998.

As shown in Figure 5.2, when the pH of the HAc-NaAc (where Ac indicates acetate) system is 2.5, the mass transfer of reactants limits the reaction rate at all speeds; whereas, when pH is increased to 3.7 or greater, the surface reaction becomes the rate limiting step (at speeds satisfying $\sqrt{\omega} > 2\ s^{-1/2}$).

Sjöberg and Rickard (1983) measured the dissolution rate of calcite as a function of pH and temperature by carrying out rotating disk experiments between 1 and 62 °C at pH 2.7 to 8.4 in 0.1 and 0.7 M aqueous HCl-KCl-solutions under one atmospheric pressure. Their observations agreed with the three regimes mechanisms identified by Plummer et al. (1979): H^+-dependent, transitional, and H^+-independent as shown in Figure 5.3 below, where the abbreviation DBL means the diffusive boundary layer in which molecular diffusion is the dominant transport mechanism.

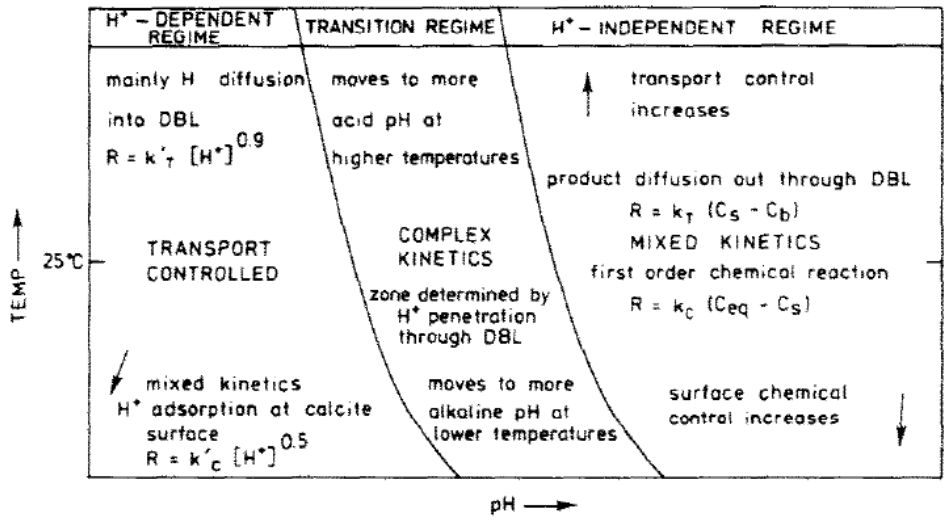

(a)

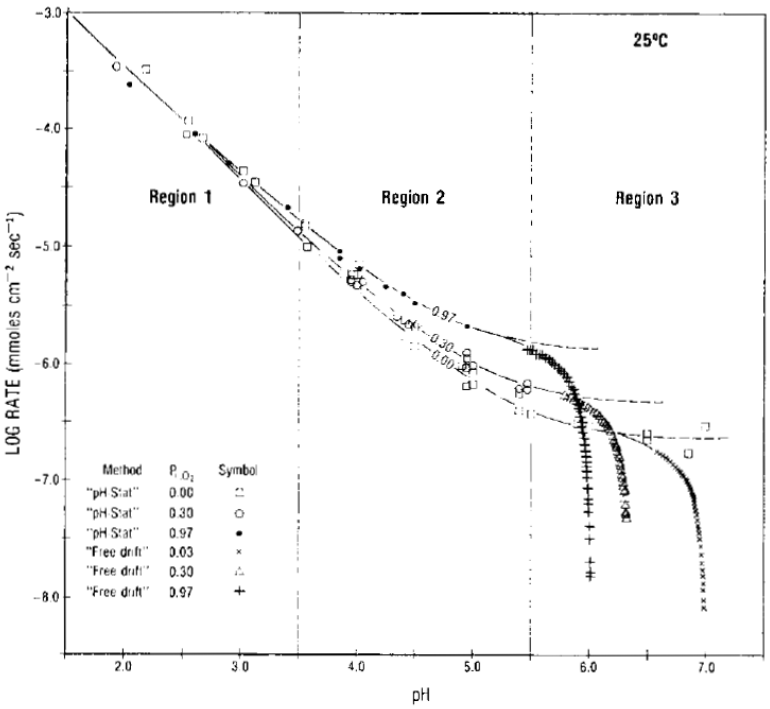

(b)

Figure 5.3: Summary of (a) the kinetics of calcite dissolution under varying temperature and pH, (b) calcite dissolution rates under varying pH and partial pressure of carbon dioxide, reproduced from Plummer et al. 1978; 1979.

In the H^+-dependent regime (Region I in Figure 5.3b), the dissolution rate is mainly dominated by the mass transport of hydrogen ions; in the H^+-independent regime (Region III in Figure 5.3b), a mixed kinetics determined by dissolution product diffusion (from the boundary layer to the bulk flow) and a first order surface reaction; and in the transition regime (Region II in Figure 5.3b), the kinetics is more complex. Fortunately, this regime covers a limited pH range. Sjöberg and Rickard (1983) reported that the boundaries separating the three regimes are approximately at pH 4.0 to 5.5 at 25 °C in 0.7 M aqueous KCl solutions, and will shift to lower pH when temperature is increased. As we are interested in the pH range from about 4.5 to 8.5 at geothermal temperature, it may be assumed that the calcite dissolution under geothermal conditions lie in the H^+-independent regime at all times. As the temperature increases, it may be expected that the mixed kinetics will be more and more influenced by the mass transfer of the reactants.

Despite the difficulties of modelling of a multicomponent system, at this stage, estimation of the calcite dissolution rate seems straightforward. However, it is worth noting that the published rates of calcite dissolution exhibit discrepancies larger than an order of magnitude, especially in the pH range of interest, as shown in Figure 5.4 below, in which the letter labels indicate results published by particular authors.

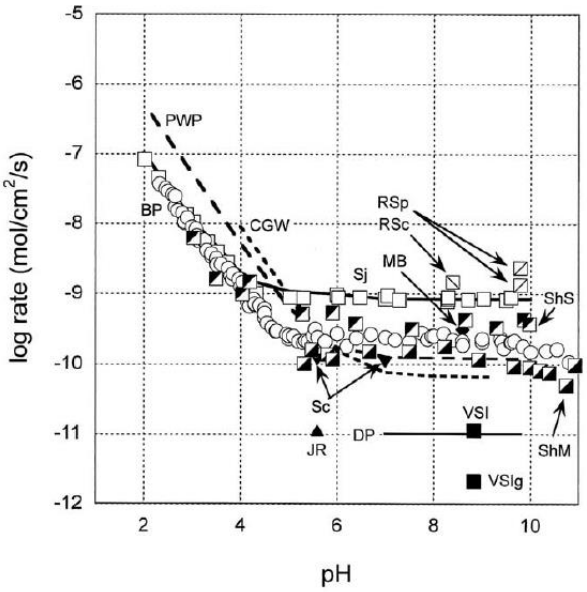

Figure 5.4: Summary of the published observations of calcite dissolution rates, reproduced from Arvidson et al. 2002.

Some discrepancies may be attributed to the varying experimental conditions (e.g. ionic strength, partial pressure of CO_2, etc.), however, Arvidson et al. (2002) suggested there could be important factors that are yet unreported or unanalysed, e.g. surface conditions (roughness, defects), impurities, grain size, etc. Therefore, the assumption of ignoring the possible reasons for the discrepancies must be made.

In the following sections, methods that can be used in the present work to reasonably model the kinetics of the surface reactions between the injectate and rocks are discussed and developed.

Currently, empirical methods like those reviewed and summarised by Palandri and Kharaka (2004); Xu et al. (2003) are widely applied to model reactive geochemical transport in geologic media.

For multiple mechanisms (mechanisms that multiple relevant reactions are occurring simultaneously), reaction rates can be semi-empirically computed by using the following formula (Lasaga et al. 1984; 1995; 1998):

$$\frac{dm}{dt} = -S \sum_j [A_j \exp\left(-\frac{E_{a,j}}{RT}\right) f_j \, g_j] \tag{5.5}$$

where $\frac{dm}{dt}$ is the rate of concentration change ($\frac{dm}{dt} > 0$ for dissolution, and $\frac{dm}{dt} < 0$ for precipitation), and S is the reactive surface area. For the jth reaction, A_j is the pre-exponential factor, $E_{a,j}$ is the observed activation energy, T is the absolute temperature, and R is the gas constant.

The dimensionless term f_j, a function of the activity of the ith species ($a_{i,j}$) for the jth reaction, is defined by:

$$f_j = \prod_j a_{i,j}^{n_{i,j}} \tag{5.6}$$

where $n_{i,j}$ is the reaction order of the ith species in the jth reaction.

The dimensionless term g_j, a function of the chemical affinity representing the slowing effect on the jth reaction rate when the equilibrium is being reached, may be defined by:

$$g_j = [1 - \Omega^{p_i}]^{q_i} \tag{5.7}$$

where $\Omega = \mathrm{Q/K}$ is the saturation index, Q is the product of the activity, K is the equilibrium constant, and p_i and q_i are the dimensionless empirical power components, which can be estimated based on transition state theory if the reaction mechanisms are clear (Lasaga 1995; 1998). Otherwise, $p_i = q_i = 1$ is assumed. Equation 5.5 and 5.7 show that the dissolution or precipitation rate strongly depends on the degree of saturation. Equilibrium is reached when $\Omega = 1$, i.e. $\mathrm{Q = K}$.

In the case of mineral precipitation, a critical saturation index Ω_c, usually >1, is commonly identified (Reddy 1986; Sibley et al. 1987; Steefel and Van Cappellen 1990; Schoonen and Barnes 1991b; Nordeng and Sibley 1994; Shiraki and Brantley 1995; Lebrón and Suárez 1996; Normand et al. 2002) but has not been quantified for most minerals (Palandri and Kharaka 2004). Precipitation may not occur until $\Omega > \Omega_c$. Xu et al. (2004) suggested that the critical saturation index Ω_c is dependent on temperature T.

By combining Equation 5.5-5.7, one can get the following expression:

$$\frac{dm}{dt} = -S \sum_j \left\{ A_j \exp\left(-\frac{E_{a,j}}{RT}\right) \prod_j a_{i,j}^{n_{i,j}} \left[1 - \left(\frac{Q}{K}\right)^{p_i}\right]^{q_i} \right\} \tag{5.8}$$

As most of the experimental results were obtained by varying pH and temperature, Equation 5.8 can be expressed in the form of three mechanisms (i.e. mechanisms of reaction in pure water, catalysed by hydrogen ions, and by hydroxide ions):

$$\begin{aligned} \frac{dm}{dt} = -S \Bigg\{ & k_{acid}^{298.15K} \exp\left[-\frac{E_{acid}}{R}\left(\frac{1}{T} - \frac{1}{298.15}\right)\right] a_{H^+}^{n_1} \left[1 - \left(\frac{Q}{K}\right)^{p_1}\right]^{q_1} \\ & + k_{neutral}^{298.15K} \exp\left[-\frac{E_{neutral}}{R}\left(\frac{1}{T} - \frac{1}{298.15}\right)\right] a_{H_2O}^{n_2} \left[1 - \left(\frac{Q}{K}\right)^{p_2}\right]^{q_2} \\ & + k_{base}^{298.15K} \exp\left[-\frac{E_{base}}{R}\left(\frac{1}{T} - \frac{1}{298.15}\right)\right] a_{H^+}^{n_3} \left[1 - \left(\frac{Q}{K}\right)^{p_3}\right]^{q_3} \Bigg\} \end{aligned} \tag{5.9}$$

where $k_j^{298.15K}$ is the rate constant with respect to the j mechanism at room temperature (i.e. 298.15K). The activity of $\mathrm{H^+}$ instead of $\mathrm{OH^-}$ is used for the base-catalysed mechanism for simplicity. Terms representing other known mechanisms (say the effects of $\mathrm{HCO_3^-}$ and the partial pressure of $\mathrm{CO_2}$ on the dissolution of carbonate minerals) may be included in Equation 5.9 as well.

For reactions far from equilibrium, the term for the chemical affinity $\left[1 - \left(\frac{Q}{K}\right)^{p_i}\right]^{q_i}$ is close to one. By normalising Equation 5.9 to the reaction surface area S, it can be simplified to:

$$\begin{aligned} \frac{dm}{Sdt} = -[& A_{acid} \exp\left(-\frac{E_{acid}}{RT}\right) a_{H^+}^{n_1} + A_{neutral} \exp\left(-\frac{E_{neutral}}{RT}\right) a_{H_2O}^{n_2} \\ & + A_{base} \exp\left(-\frac{E_{base}}{RT}\right) a_{H^+}^{n_3}] \end{aligned} \tag{5.10}$$

Based on the empirical method presented above, Palandri and Kharaka (2004) reviewed available observations and published a survey of the rate parameters in Equation 5.10 for common minerals. By substituting the values in (Palandri and Kharaka 2004), one can easily estimate dissolution rates of minerals at varying pH and temperature.

Palandri and Kharaka (2004) suggested that for most minerals, the precipitation rate cannot be directly measured, as corresponding metastable products may precipitate prior to the precipitation of the actual minerals. For example, anhydrite is the stable form of calcium sulphate precipitate when the temperature is above say 40 ℃, however it is difficult to observe the direct precipitation of anhydrite crystals even if the temperature is well above 60 ℃ and anhydrite seeds are added (Morales et al. 2012); in an aqueous solution supersaturated with respect to quartz, silica usually precipitates in the form of amorphous silica instead of quartz.

For minerals for which both dissolution and precipitation can be described by single reversible mechanisms, Palandri and Kharaka (2004) suggested that the precipitation rate $k_{\mathrm{precipitation}}$ can be estimated based on the observed dissolution rate $k_{\mathrm{dissolution}}$ and the equilibrium constant K_{eq} using the principle of microscopic reversibility (Tolman 1925; Lasaga 1998):

$$K_{\mathrm{eq}} = k_{\mathrm{dissolution}}/k_{\mathrm{precipitation}} \tag{5.11}$$

K_{eq} is equivalent to the solubility product K_{sp} defined in Equation 5.17. Note that microscopic reversibility only applies to individual reaction steps, not to entire sequences of steps.

Equation 5.11 can be very useful in the present work as, in some cases (e.g. precipitation of anhydrite), the dissolution or precipitation rate cannot be explicitly expressed, but the equilibrium constant and the rate of the opposite reaction may be well-known. Therefore, the dissolution or precipitation rate can be expressed using the following forms (Equation 5.12 and 5.13):

$$k_{\mathrm{precipitation}} = k_{\mathrm{dissolution}}/K_{\mathrm{eq}} \tag{5.12}$$

$$k_{\mathrm{dissolution}} = k_{\mathrm{precipitation}}K_{\mathrm{eq}} \tag{5.13}$$

The empirical method above can be used to simulate the geochemical reactions of interest with reasonable accuracy. Numerical simulation packages like TOUGHREACT (Xu et al. 2003) have successfully implemented this method to make useful predictions for the management of geothermal reservoirs.

However, some drawbacks are apparent:

It does not take mass transfers of reactants and products near the boundary layer into account, i.e. a mass transfer model must be coupled.

The ranges of varying conditions over which empirical data is available are limited, i.e. extrapolations are inevitable.

In the case of geothermal reinjection, it is most desired that experimental data are available under typical geothermal conditions (high pressure and temperature, varying pH, and low to moderate salinity), but few observations exist under these conditions yet as the experiments can be expensive and difficult to design and control.

The uncertainties from the experiments have been inherited.

Since there are factors that can affect the accuracy of the experimental data, the performance of the model strongly depends on the uncertainties of the observations. Therefore, the reference data must be carefully chosen.

The effects of dissolution and precipitation on the surface reaction area S are ignored.

Depending on the properties of the reactants and the products, molecules may not be homogenously released from or absorbed by the mineral surface. Therefore, the reaction surface area may change.

Since reactions involving calcium carbonate ($CaCO_3$) and calcium sulphate ($CaSO_4$) are of the most interest in geothermal operations, the rate parameters (Palandri and Kharaka 2004) for Equation 5.10 for these minerals are reproduced in Table 5.1 and Table 5.2 as a reference:

Table 5.1: Calcium carbonate dissolution rate parameters, reproduced from (Palandri and Kharaka 2004)

Mineral	Acid Mechanism			Neutral Mechanism		Carbonate Mechanism		
	$\log k^{298.15K}$	E_a	n	$\log k^{298.15K}$	E_a	$\log k^{298.15K}$	E_a	n
Calcite	-0.30	14.4	1.000	-5.81	23.5	-3.48	35.4	1.000

Table 5.2: Calcium sulphate dissolution rate parameters, reproduced from (Palandri and Kharaka 2004)

Mineral	Acid Mechanism			Neutral Mechanism	
	$\log k^{298.15K}$	E_a	n	$\log k^{298.15K}$	E_a
Anhydrite	--	--	--	-3.19	14.3
Gypsum	--	--	--	-2.79	0

where $k^{298.15K}$ is in mol m^{-2} s^{-1}, E_a is in kJ mol^{-1}, n under Acid Mechanism is for the activity of H^+, and n under Carbonate Mechanism is for the partial pressure of CO_2.

There are other relevant factors which may have effects on reaction rate, but are not straightforwardly included in Equation 5.10 such as the activity coefficients (see Equation 5.19). Therefore, unnecessary errors may be introduced when converting the activity to the concentration.

Therefore, in the present work, the semi-empirical method (Equation 5.10) will only be integrated as an optional sub-model, which can be enabled by users if needed. In the following sections, the default algorithm to simulate the surface reactions of interest are developed based on the experimental data directly. Specifically, the first-hand observations and expressions are revisited and summarised; reference data recorded under geothermal conditions are preferred; extrapolation formulas are developed if the conditions are out of the geothermal range; species that can accelerate or suppress the reaction rate but are also involved in other reactions are taken into account a priori, such as the effects of dissolved carbon dioxide on the dissolution of calcite.

Since the reaction, dissolution, and precipitation rates are of interest in the present work, and these are usually far greater than the dissociation and association rates, a global assumption has to be made: the dissociations and associations of the all dissociable and associable chemical species mentioned later will be treated as instantaneous processes.

5.1 Kinetics of calcite dissolution

The calcite dissolution process may be described as a sequence: mass transfer of reactants (e.g. the hydrogen ion) from the bulk solution to the solid-liquid interface, surface reaction, and release of the products. Overall, the calcite dissolution due to acid can be represented by:

$$2H^+ + CaCO_3(s) \leftrightarrow Ca^{2+} + CO_2(aq) + H_2O \tag{5.14}$$

The carbon dioxide generated may undergo further reactions to carbonate and bicarbonate ions:

$$CO_2(aq) + H_2O \leftrightarrow H^+ + HCO_3^- \tag{5.15}$$

$$HCO_3^- \leftrightarrow H^+ + CO_3^{2-} \tag{5.16}$$

It should be noted that under geothermal conditions (i.e. high pressure), carbon dioxide is always treated as a solute in the system. At a lower pressure (the order of 1 atm), CO_2 bubbles may form on the calcite surface and limit the surface available for reaction (Lund et al. 1974). Bubbles are not considered in the present work.

The solubility product constant of $CaCO_3$ $K_{sp,CaCO_3}$ is defined by:

$$K_{sp,CaCO_3} = a_{Ca^{2+}} a_{CO_3^{2-}} = \gamma_{Ca^{2+}}[Ca^{2+}]\,\gamma_{CO_3^{2-}}[CO_3^{2-}] \tag{5.17}$$

where $[Ca^{2+}]$ and $[{CO_3}^{2-}]$ are the concentration of calcium and carbonate ions respectively, γ is the activity coefficient. In the case of ideal solutions, the activity of a solute is equal to its concentration, i.e. $\gamma = 1$. Note that, unless specified otherwise, the units for solubility product constant are molal.

As the effects of electrolyte are of interest and not negligible, to physically estimate the concentrations of interested chemical species based on the calculated activities, the activity coefficients of the related chemical species have to be explicitly defined, which is covered in Appendix 1 at the end of the present chapter.

According to Equation 5.17, the pre-existing chemical species such as sulphate SO_4^{2-}, hydrogen ion H^+, and carbonic acid H_2CO_3 have direct effects on $[Ca^+]$ and $[{CO_3}^{2-}]$. The physical and chemical conditions play important roles as well. Specifically, the solubility product constantK_{sp} is determined by temperature (i.e. at a fixed temperature and equilibrium, the activity product of Ca^{2+} and CO_3^{2-} should always be a constant); and the ionic strength of background electrolytes and temperature are usually treated as two of the variables that determine the activity coefficient γ, i.e.:

$$K_{sp} = f_{Ksp}(T) \tag{5.18}$$

$$\gamma = f_\gamma(T, I, \dots) \tag{5.19}$$

Therefore, at a fixed temperature, the concentrations of Ca^{2+} and CO_3^{2-} can be shifted when the conditions (e.g. I) are varied.

In practice, some researchers often use the concentration product (i.e. $K'_{sp,CaCO_3} = [Ca^+]\left[{CO_3}^{2-}\right] = K_{sp,CaCO_3}/(\gamma_{Ca^+}\,\gamma_{CO_3^{2-}})$) at equilibrium to represent the solubility as well. For instance, if there is no pre-existing Ca^+ and ${CO_3}^{2-}$, at equilibrium, the concentration of dissolved calcite can be roughly equal to $K'^{\,0.5}_{sp,CaCO_3}$ (Note that this is only a simple example. In practice, the geothermal brines are usually dissolved with Ca^+ and ${CO_3}^{2-}$, and $[Ca^+]$ is usually much higher than $[{CO_3}^{2-}]$, therefore neither will be equal to $K'^{\,0.5}_{sp,CaCO_3}$) It should be noted that ${K_{sp,CaCO_3}}'$ is no longer a function of temperature only but other variables that determine the

activity coefficients such as ionic strength will become important. Hence, the expression for $K_{sp,\mathrm{CaCO_3}}{}'$ should explicitly include all parameters that have effects on the solubility, i.e.:

$$K_{sp}{}' = f_{Ksp'}(T, I, \dots) \tag{5.20}$$

The solubility constants of calcite at low temperatures (< 100 ℃) have been extensively investigated (Jacobson and Langmuir 1974; Berner 1976; Plummer and Busenberg 1982; Sass et al. 1983; Gledhill and Morse 2006).

Plummer and Busenberg (1982) experimentally investigated the $\mathrm{CaCO_3} - \mathrm{CO_2} - \mathrm{H_2O}$ system between 0 and 90 ℃. Based on the experimental results, Plummer and Busenberg (1982) proposed the following widely recognised expression (Equation 5.21) to predict the solubility constant $K_{sp,\mathrm{CaCO_3}}$ up to 90 ℃:

$$\log K_{sp,\mathrm{CaCO_3}} = -171.9065 - 0.077993T + \frac{2839.319}{T} + 71.595 \log T \tag{5.21}$$

where T is the absolute temperature.

However, few studies have been carried out at higher temperatures. Segnit et al. (1962) and Ellis (1963) measured the solubility constant up to 200 and 320 ℃ respectively; Arnórsson (1981) proposed the expression below (Equation 5.22) that reasonably agrees with the measurements of Segnit et al. (1962) and Ellis (1963) and can be used to find the solubility constant $K_{sp,c}$ up to 320 ℃:

$$\log K_{sp,\mathrm{CaCO_3}} = 10.22 - 0.0349T - \frac{2476}{T} \tag{5.22}$$

where T is the absolute temperature. Equation 5.21 and 5.22 agree reasonably well as shown in Figure 5.5 below:

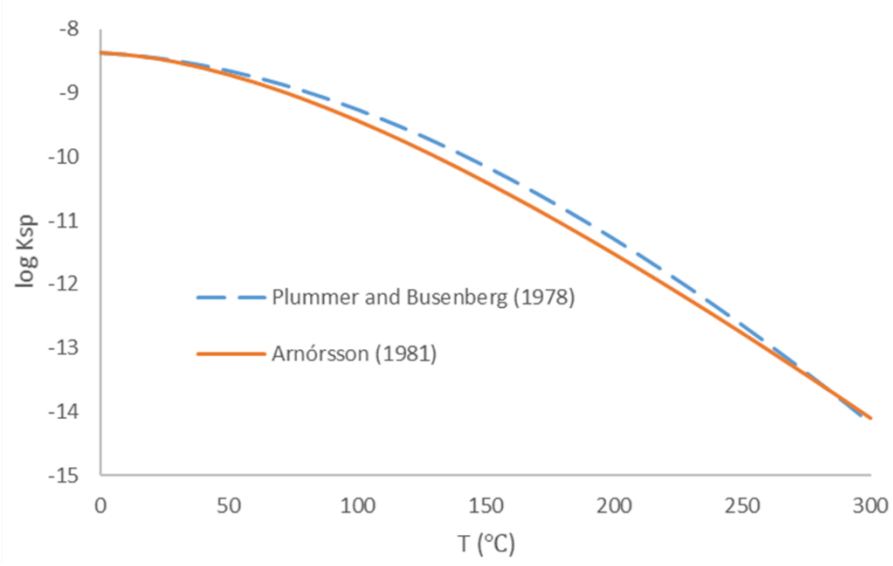

Figure 5.5: Comparison between Equation 5.21 (dash line) and 5.22 (solid line), proposed by Plummer and Busenberg (1982) and Arnórsson (1981) respectively. Note that Equation 5.21 is extrapolated when temperature is above than 90 ℃.

Equation 5.22, proposed by Arnórsson (1982), not only covers typical geothermal temperatures but is based on more recent experimental data than (Segnit et al. 1962) and (Ellis 1963). Therefore, Equation 5.22 is used in the present work to estimate $K_{sp,\mathrm{CaCO_3}}$.

The equilibrium constants for the dissociations shown in Equation 5.15 and 5.16 $K_{\mathrm{H_2CO_3}}$ and $K_{\mathrm{HCO_3^-}}$ are defined by:

$$K_{d,\mathrm{H_2CO_3}} = \frac{a_{\mathrm{H^+}} a_{\mathrm{HCO_3^-}}}{a_{\mathrm{CO_2(aq)}} a_{\mathrm{H_2O}}} = \frac{\gamma_{\mathrm{H^+}}[\mathrm{H^+}]\,\gamma_{\mathrm{CO_3^{2-}}}[\mathrm{HCO_3^-}]}{\gamma_{\mathrm{CO_2}(aq)}\,[\mathrm{CO_2}(aq)]} \tag{5.23}$$

$$K_{d,\mathrm{HCO_3^-}} = \frac{a_{\mathrm{H^+}}\, a_{\mathrm{CO_3^{2-}}}}{a_{\mathrm{HCO_3^-}}} = \frac{\gamma_{\mathrm{H^+}}[\mathrm{H^+}]\,\gamma_{\mathrm{CO_3^{2-}}}[\mathrm{CO_3^{2-}}]}{\gamma_{\mathrm{HCO_3^-}}\,[\mathrm{HCO_3^-}]} \tag{5.24}$$

Based on experimental investigations, the formulas for predicting the equilibrium constants $K_{d,\mathrm{H_2CO_3}}$ and $K_{d,\mathrm{HCO_3^-}}$ are proposed by Plummer and Busenberg (1982); Mehrbach et al., (1973), which can be applied to at least 250 ℃:

$$\log K_{\mathrm{H_2CO_3}} = -356.3094 - 0.06091964T + \frac{21834.37}{T} + 126.8339 \log T - 1684915/\mathrm{T}^2 \tag{5.25}$$

$$\log K_{\mathrm{HCO_3^-}} = -107.8871 - 0.03252849T + \frac{5151.79}{T} + 38.92561 \log T - 563713.9/T^2 \tag{5.26}$$

where T is the absolute temperature. The formulas above can be safely used at higher temperatures to at least 250 ℃ under the vapour pressures of water (Plummer and Busenberg 1982).

Plummer et al. (1978) comprehensively investigated the dissolution rate of Iceland Spar (a transparent variety of calcite) at temperatures from 5 to 60 ℃, partial pressures of $\mathrm{CO_2}$ from $10^{-3.5}$ to 1.0 atm, and pH from 2.0 to 7.7. By comparing the experimental results with the observations of Berner and Morse (1974), Plummer et al. (1978) identified the three regimes of different kinetics of calcite dissolution and proposed an empirical method to predict the dissolution rate using the Arrhenius equation:

$$k_i = A \exp(-\frac{E_a}{RT}) \tag{5.27}$$

where k_i is the reaction rate of species i. The physical meaning of the Arrhenius equation is that the fraction $\exp(-\frac{E_a}{RT})$ of molecules react at the collision frequency A, and the minimum activation energy at the temperature T for that reaction is E_a. The Arrhenius equation is often expressed in the following form:

$$\ln k_i = \ln A + \left(-\frac{E_a}{R}\right)\frac{1}{T} \tag{5.28}$$

Conventionally, the plot of $\ln k_i$ as a function of $1/T$ is often used to analyse the effects of temperature on the reaction rate, which is named an Arrhenius plot.

The net kinetic reaction coefficient of the forward and the backward reactions (Equation 5.1, 5.2, and 5.3), k, is defined by:

$$k_{d,\mathrm{CaCO_3}} = k_1 a_{\mathrm{H^+}} + k_2 a_{\mathrm{H_2CO_3}} + k_3 a_{\mathrm{H_2O}} - k_4 a_{\mathrm{Ca^{2+}}} a_{\mathrm{CO_3^{2-}}} \tag{5.29}$$

where k_1, k_2, and k_3 are the first order forward reaction rate constants for Equation 5.1, 5.2, and 5.3, k_4 is the backward reaction rate constant, and a is the activity of the species denoted

by the subscripts. Unless mentioned otherwise, all reaction rate constants mentioned in this chapter are in $\mathrm{cm/s}$.

k_1 represents the effects of the reaction Equation 5.1, i.e. the dissolution due to hydrogen ion attack:

$$\log k_1 = -2.802 - 444/T \tag{5.30}$$

where T is the absolute temperature. The corresponding Arrhenius activation energy is 2.0 $\mathrm{kcal/mol}$. k_1 physically means the transport rate constant of $\mathrm{H^+}$.

k_2 shows the effects of the reaction Equation 5.2, i.e. the dissolution due to carbonic acid:

$$\log k_2 = -0.16 - 2177/T \tag{5.31}$$

The corresponding Arrhenius activation energy is 10.0 $\mathrm{kcal/mol}$.

k_3 stands for the effects of the reaction Equation 5.3, i.e. the dissolution due to water (hydrolysis):

$$\log k_3 = -8.86 - 317/T \quad \text{for } T \leq 298 \tag{5.32}$$

$$\log k_3 = -4.10 - 1737/T \quad \text{for } T > 298 \tag{5.33}$$

The corresponding Arrhenius activation energies are 1.5 and 7.9 $\mathrm{kcal/mol}$ respectively.

The backward reaction rate constant k_4 is defined by:

$$k_4 = \frac{K_{\mathrm{HCO_3^-}}}{K_{\mathrm{CaCO_3^0}}}\{k_1' + \frac{1}{a_{\mathrm{H^+(s)}}}[k_2 a_{\mathrm{H_2CO_3(s)}} + k_3 a_{\mathrm{H_2O(s)}}]\} \tag{5.34}$$

where $K_{\mathrm{HCO_3^-}}$ and $K_{\mathrm{CaCO_3^0}}$ are the equilibrium constants for the dissociation of bicarbonate ion ($\mathrm{HCO_3^- \leftrightarrow H^+ + CO_3^{2-}}$) and the $\mathrm{CaCO_3^0}$ ion pair (the ion complex of positive and negative ions temporarily bonded due to the attractive electrostatic force) $\mathrm{CaCO_3^0 \leftrightarrow Ca^{2+} + CO_3^{2-}}$ respectively, and k_1' is the forward reaction rate for the reaction Equation 5.3, which could be approximately 10 to 20 times higher than k_1, and the subscript s means the corresponding activities at the adsorption layer.

For the dissociation of the ion pair $\mathrm{CaCO_3^0}$ ($\mathrm{CaCO_3^0 \leftrightarrow Ca^{2+} + CO_3^{2-}}$), $K_{\mathrm{CaCO_3^0}}$ is defined by:

$$K_{d,\mathrm{CaCO_3^0}} = \frac{a_{\mathrm{Ca^{2+}}} a_{\mathrm{CO_3{}^{2-}}}}{a_{\mathrm{CaCO_3^0}}} = \frac{\gamma_{\mathrm{Ca^{2+}}}[\mathrm{Ca^{2+}}]\,\gamma_{\mathrm{CO_3{}^{2-}}}[\mathrm{CO_3{}^{2-}}]}{\gamma_{\mathrm{CaCO_3^0}}[\mathrm{CaCO_3^0}]} \tag{5.35}$$

which is not to be confused with Equation 5.17. Equation 5.17 physically describes the equilibrium state of dissolution reaction (solid to dissolved species), while Equation 5.35 represents that of the dissociation reaction (dissolved neutral species to dissolved ionised species). Their mathematical correlation can be expressed as $K_{sp,\mathrm{CaCO_3}} = K_{d,\mathrm{CaCO_3^0}}\, a_{\mathrm{CaCO_3^0}} = a_{\mathrm{Ca^{2+}}} a_{\mathrm{CO_3{}^{2-}}}$.

The expression for estimating the association constant $K_{a,\mathrm{CaCO_3^0}}$ (i.e. the inverse of dissociation constant $1/K_c$) of $\mathrm{CaCO_3^0}$ between 5 and 80 ℃ is proposed by Plummer and Busenberg (1982):

$$\log K_{a,\mathrm{CaCO_3^0}} = -1228.732 - 0.299444T + \frac{35512.75}{T} + 485.818 \log T \tag{5.36}$$

$$K_{\mathrm{d,CaCO_3^0}} = 1/K_{a,\mathrm{CaCO_3^0}} \tag{5.37}$$

where T is the absolute temperature.

In the H^+-dependent regime, the first term on the left-hand side of Equation 5.29 limits the net dissolution rate constant k. In the transition regime, the first three terms on the left-hand side of Equation 5.29 dominate. In the H^+-independent regime, the backward reactions revealed by k_4 must be considered.

The transition state theory (TST) (Laidler and King 1983) suggests that the surface dissolution rate can be represented by:

$$J_{d,\mathrm{CaCO_3}} = k_{d,\mathrm{CaCO_3}}(1 - a_{Ca^{2+}}\, a_{CO_3^{2-}}/K_{sp,\mathrm{CaCO_3}}) \tag{5.38}$$

It should be noted that the kinetics of calcite dissolution described above are based on the experiments mostly at temperatures less than 373 K and 1 atm total pressure. To apply the model under typical geothermal conditions, it must be assumed that the data can be extrapolated.

Talman et al. (1990) compared the extrapolated results of Plummer et al.'s model (1978) with observations at relatively higher temperatures of 100, 150, and 210 ℃. The plot of comparisons is reproduced in Figure 5.6 below:

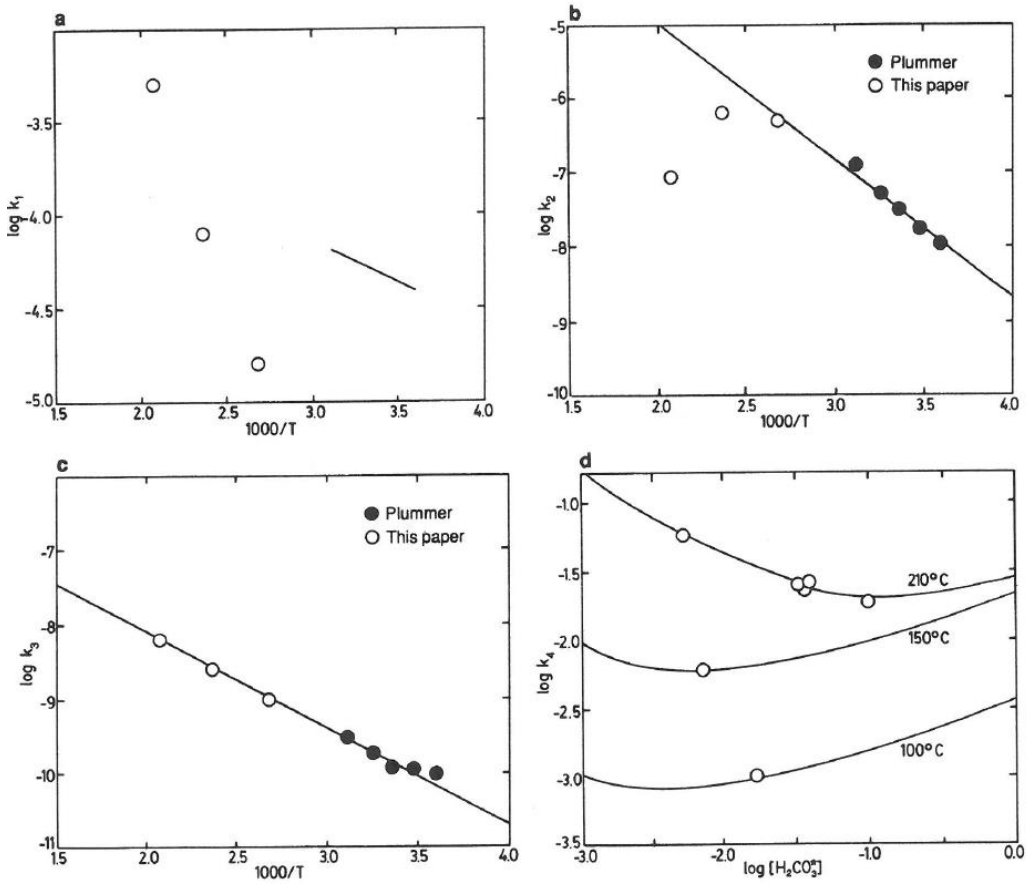

Figure 5.6: Comparison among the observed calcite dissolution rate constant at 100, 150, and 210 ℃ (hollow dots, Talman et al. 1990), that at lower temperatures (solid dots, Plummer et al. 1978), and the extrapolated Plummer et al.'s model (lines and curves) in Arrhenius polts. Figures a, b, c, and d show the reaction rate constant k_1, k_2, k_3, and k_4

respectively. Note that the horizontal axes are 1000/absolute temperature and the log of activity of H_2CO_3.

The extrapolation is acceptable for k_3 and k_4 (Figure 5.8 c and d), but discrepancies exist for k_1 at all higher temperatures and k_2 at temperatures above 100 ℃ (Figure 5.8 a and b). Talman et al. (1990) commented that: (1) as it was very difficult to conduct experiments at the higher temperatures in more acidic solutions, k_1 could hardly be precisely measured under such conditions (i.e. the observations may not be reliable or precise enough to refit to an expression); (2) despite what is mentioned in (1), the experiment to measure k_1 at 100 ℃ was believed (Talman et al. 1990) to be well constrained, and the discrepancy could be caused by the difference of surface area or crystal features; (3) the sudden drop of k_2 at 150, and 210 ℃ shown in Figure 5.8 b was suggested (Talman et al. 1990) to be the consequence of a change in the reaction mechanism, which still needs further investigation. To the knowledge of this thesis' author, the reasons behind the discrepancy shown in Figure 5.8 may still not be well explained. In the case of geothermal reinjection, the injection temperature would be very likely less than 210 ℃, and close to 150 ℃ or even lower, where the discrepancy may be modest (within one order of magnitude). Specifically, the comparison between the observed and extrapolated k_1 and k_2 at 100, 150, and 210 ℃ is reproduced below:

Table 5.3 Comparison between the observed and extrapolated k_1 and k_2 at higher temperatures, reproduced from Talman et al. 1990

Temperature (℃)	Observed $\log k_1$	Observed $\log k_2$	Extrapolated $\log k_1$	Extrapolated $\log k_2$
100	-4.8	-6.3	-4.0	-6.0
150	-4.1	-6.2	-3.9	-5.3
210	-3.3	-7.1	-3.7	-4.7

The thesis author chooses to use Plummer et al.'s model (1978) plus a refitted empirical expression for k_2 (Equation 5.39 below) to model calcite dissolution in the present work. Equation 5.39 is fitted by combining Plummer et al.'s model (1978) and Talman et al.'s measurements (1990) and is considered safe to extrapolate to at least 210 ℃. The assumption for safe extrapolation to higher temperatures has to be made.

$$\log k_2 = -685.5 - 0.2045T + 1.556 \times 10^4/T + 277.6 \log T \tag{5.39}$$

The comparison between Plummer et al.'s model (1978, including the extrapolation from 60 ℃), Talman et al.'s measurements (1990), and Equation 5.39 is shown in Figure 5.7 below.

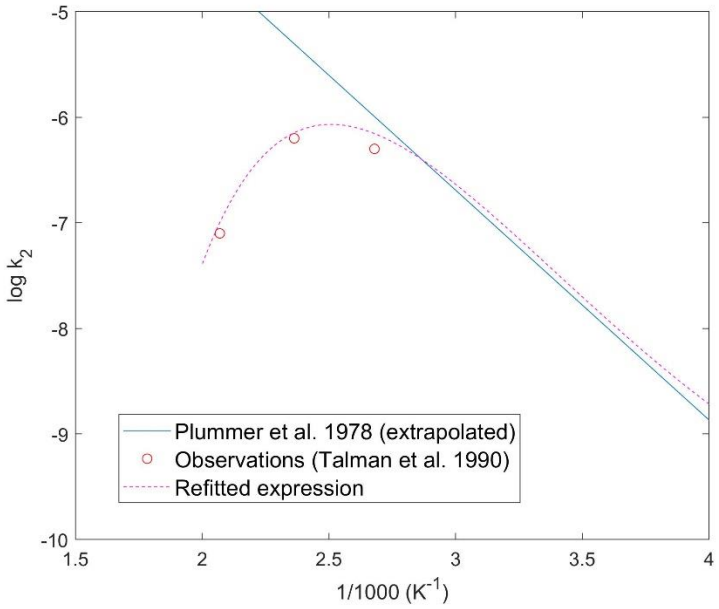

Figure 5.7: Comparison of Plummer et al.' s model (1978, including the extrapolation from 60 ℃, solid line), Talman et al.' s measurements (1990, hollow dots), and refitted Equation 5.39 (dash line).

At this stage, the kinetics of calcite dissolution can be modelled.

5.2 Effects on inhibiting silica scaling

As presented in Chapter 1, the model of the kinetics of silica polymerisation by Weres et al. (1980), (as coded into SILNUC), is reproduced and integrated into the present model.

To quantify the inhibiting effects of acidification on silica polymerisation, typical NZ geothermal reinjection conditions are input to this model. The input data are summarised in Table 5.4 below:

Table 5.4 Summary of input parameters representing typical NZ geothermal reinjection conditions

Notation	Value used	Explanation
T_{inj}	160 ℃	Initial temperature of injected fluid
c_{inj}^{SiO2}	1200 ppm	Initial concentration of monomeric silica in injected fluid
I_{inj}	0.09mol/kg	Initial ionic strength of injected fluid
pH_{inj}	7	Initial pH of injected fluid
pH'_{inj}	4.5	pH of injected fluid after acidification

The simulation results are plotted in Figure 5.8 below:

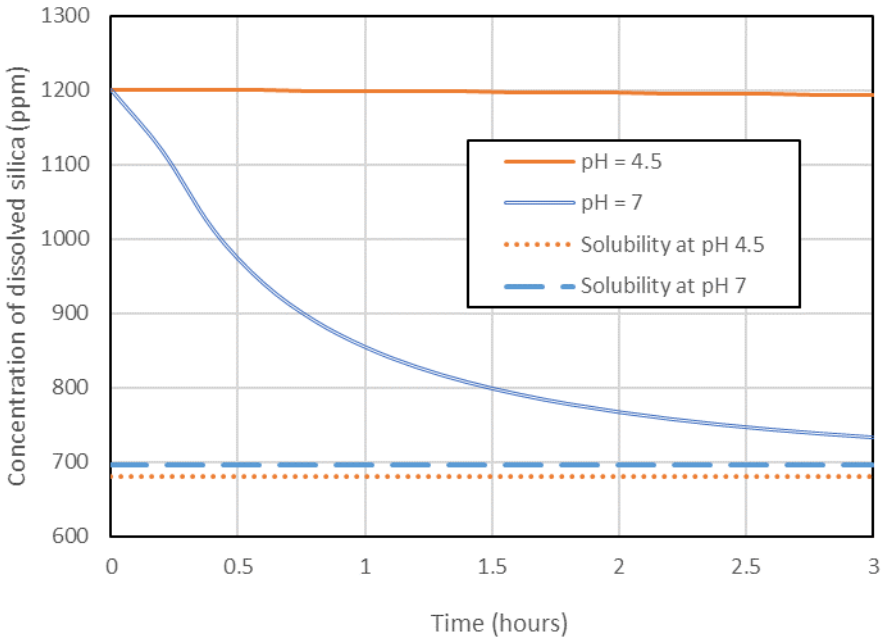

Figure 5.8: Comparison of the concentration decline of dissolved silica as a function of time at pH = 4.5 (orange solid curve) and 7 (blue solid curve), 160 ℃, and 0.09 M ionic strength, and the solubility of amorphous silica under the former (orange dotted line) and latter (blue dashed line) conditions.

Compared to pH 7, the inhibiting effects of acidification is clear. Despite the solubility of amorphous silica being slightly lower at pH 4.5, which should offer a slightly higher tendency for polymerisation (usually negligible as far as polymerisation rate is concerned), within 3 hours, a negligible amount of monomeric silica has polymerised to form colloidal silica. Ideally, if the added hydrogen ions remain in the injectate, no obvious silica polymerisation can be observed for days or even years depending on the initial degree of silica supersaturation (i.e. *SSI*). It should be noted that modifying pH can only affect the kinetics but not the thermodynamics of silica polymerisation. i.e. acidification can only delay the polymerisation which will eventually happen but after a longer time. By applying this technique, the silica scaling can be significantly delayed long enough to avoid silica scaling near the wellbore and allow the separated geothermal water to be injected further into in the reservoir formation. Therefore, the lifetime of reinjection can be extended.

5.3 Effects on surrounding rocks of a reinjection well

Singurindy and Berkowitz (2004) point out that some of the products of dissolution of calcite may be transported with the fluid, deposit at the far end of the fracture, and eventually clog the fluid pathway in the same way colloidal silica does. Therefore, when considering the effects of calcite dissolution on rock, it is better to treat the process as a coupled problem of dissolution and precipitation instead of only taking the fracture expansion due to dissolution into account.

5.3.1 Kinetics of calcite precipitation under geothermal conditions

Since heat transfer plays a crucial role in geothermal reinjection, and given the retrograde solubility of calcite, the possibility of calcite precipitation as the injectate heats up should be considered.

To determine whether calcite precipitation due to heat transfer is problematic, the kinetics of calcite precipitation is studied in this section. For simplicity, the detailed nucleation and crystal growth processes are not covered in the present work. The goal in this section is to find a method to reasonably estimate the "macroscopic" surface precipitation rate of calcite under varying conditions. In Chapter 6, the transport of the reactant from the bulk solution to the mineral surface will be considered in detail.

The process of calcite precipitation can be expressed by:

$$\mathrm{Ca^{2+}} + \mathrm{CO_3^{2-}} \rightarrow \mathrm{CaCO_3(s)} \tag{5.40}$$

The second-order rate law applied to model the kinetics of crystallization for pure $\mathrm{CaCO_3}$ (Nancollas and Reddy 1971) is:

$$-\frac{da_{\mathrm{Ca^{2+}}}}{dt} = -\frac{da_{\mathrm{CO_3^{2-}}}}{dt} = k_{p,\mathrm{CaCO_3}}(a_{\mathrm{Ca^{2+}}}a_{\mathrm{CO_3^{2-}}} - K_{sp,\mathrm{CaCO_3}}) \tag{5.41}$$

alternatively, by replacing activity with concentration:

$$-\frac{d[\mathrm{Ca^{2+}}]}{dt} = -\frac{d[\mathrm{CO_3^{2-}}]}{dt} = k'_{p,\mathrm{CaCO_3}}\{[\mathrm{Ca^{2+}}][\mathrm{CO_3^{2-}}] - K'_{sp,\mathrm{CaCO_3}}\} \tag{5.42}$$

where $k_{p,\mathrm{CaCO_3}}$ ($k'_{p,\mathrm{CaCO_3}}$) is the precipitation rate constant, $K'_{sp,\mathrm{CaCO_3}}$ is the concentration product of $\mathrm{Ca^{2+}}$ and $\mathrm{CO_3^{2-}}$ when the solution is saturated with respect to calcite, defined by:

$$K'_{sp,\mathrm{CaCO_3}} = ([\mathrm{Ca^{2+}}][\mathrm{CO_3^{2-}}])_{\mathrm{eq}} = \frac{K_{sp,\mathrm{CaCO_3}}}{\gamma_{\mathrm{Ca^+}}\,\gamma_{\mathrm{CO_3^{2-}}}} \tag{5.43}$$

The solubility product of calcite $K_{sp,\mathrm{CaCO_3}}$ is defined by Equation 5.17 and 5.21; and the correlation among the solubility product, the dissolution rate, and precipitation rate is shown in Equation 5.11; the dissolution rate constant $k_{d,\mathrm{CaCO_3}}$ is defined by Equation 5.29-5.34. Therefore, $k_{p,\mathrm{CaCO_3}}$ can be defined by:

$$k_{p,\mathrm{CaCO_3}} = k_{d,\mathrm{CaCO_3}}/K_{sp,\mathrm{CaCO_3}} \tag{5.44}$$

5.3.2 Kinetics of anhydrite precipitation under geothermal conditions

As mentioned previously, sulphuric acid ($\mathrm{H_2SO_4}$) is commonly used to acidify the injectate. Considering that the calcite dissolution will release calcium ion to the fluid, the risk of calcium sulphate ($\mathrm{CaSO_4}$) precipitation can be significantly increased. The related reaction can be expressed as:

$$\mathrm{Ca^{2+}} + \mathrm{SO_4^{2-}} \leftrightarrow \mathrm{CaSO_4(s)} \tag{5.45}$$

It should be noted that calcium sulphate scale may have three main forms: anhydrite ($\mathrm{CaSO_4}$, including "soluble" and "insoluble" sub-forms, i.e. hexagonal symmetry and orthorhombic), gypsum ($\mathrm{CaSO_4 \cdot 2H_2O}$), and hemihydrate ($\mathrm{2CaSO_4 \cdot H_2O}$). The latter two forms may be produced under their favoured conditions (say at lower temperature), and have larger molar volumes compared to $\mathrm{CaSO_4}$, requiring less precipitation to block a given pore. Provided the temperature is above about 40 ℃, the form with the lowest solubility in water is "insoluble" anhydrite (Figure 5.9) i.e. $\mathrm{CaSO_4}$ will precipitate in the form of anhydrite while it can still be soluble with respect to other forms such as gypsum.

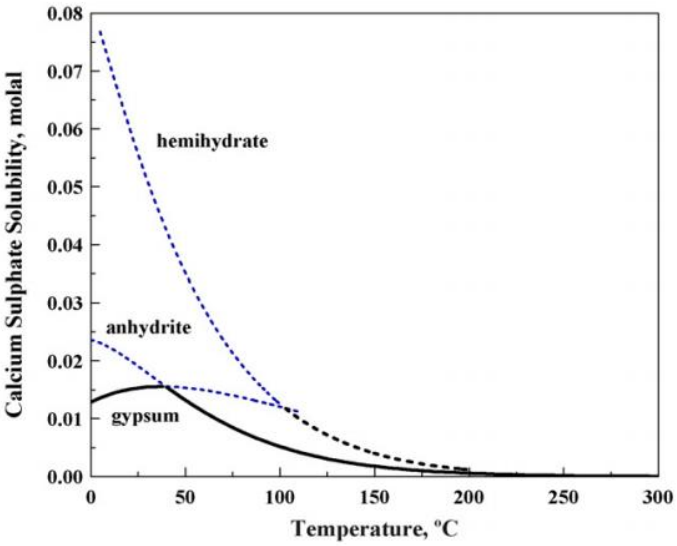

Figure 5.9: Solubility of calcium sulphate in pure water; reproduced from Azimi et al. 2007.

Therefore, to simplify the problem, under geothermal conditions where the temperature is usually above 30 ℃, it may be feasible to assume that calcium sulphate only precipitates in the form of insoluble anhydrite. In the case of geothermal reinjection, the acidification of injectate using sulphuric acid can suppress silica scaling, however, after the acid is neutralised, which cancels the inhibiting effects on silica nucleation, the possible deposition of calcium sulphate could make the scale problem even worse.

Singurindy and Berkowitz (2004) studied this problem experimentally by injecting HCl/H_2SO_4 solution with varied concentrations through calcareous sandstone samples containing different kinds of 0.8, 1.3, and 2.5 mm fractures (shown in Figure 3.10 below).

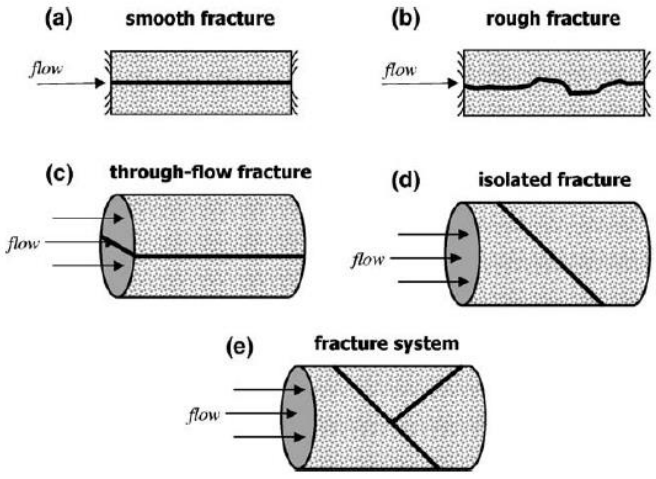

Figure 5.10: Rock samples used in the experiments of Singurindy and Berkowitz (2004), reproduced from Singurindy and Berkowitz 2004.

By comparing the hydraulic conductivity change for different rock samples, it was reported that the precipitation of gypsum may be negligible for a through-flow fracture, and fractures with rough surfaces generally clog faster than those with smooth surfaces. Some of the effects are summarised in Figure 5.11.

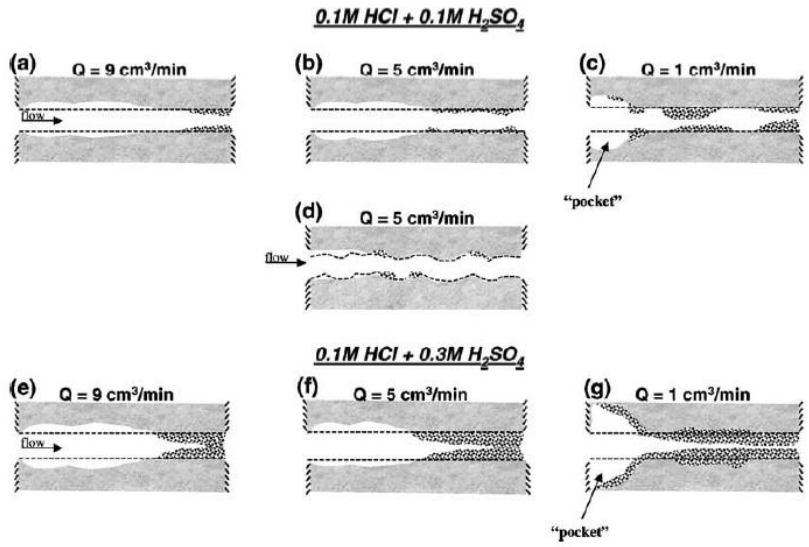

Figure 5.11: Schematic of the effects of the dissolved and precipitated solids on the smooth and rough fractures; reproduced from Singurindy and Berkowitz 2004.

Interestingly, temporal oscillations in the hydraulic conductivity (shown in Figure 5.12 below) were reported for almost all experiments. This was attributed to the variation of the concentration of Ca^{2+} due to coupled dissolution and precipitation processes. In particular, the hydraulic conductivity, the porosity, and the concentration of Ca^{2+} are increased by the initial dissolution of calcite, and gypsum ($CaSO_4 \cdot 2H_2O$) may form and deposit when Ca^{2+} accumulates and reaches the critical supersaturation index of gypsum, which could decrease the hydraulic conductivity and the porosity. As the deposition of gypsum decreases the concentration of Ca^{2+}, the effects of calcite dissolution will become dominant again.

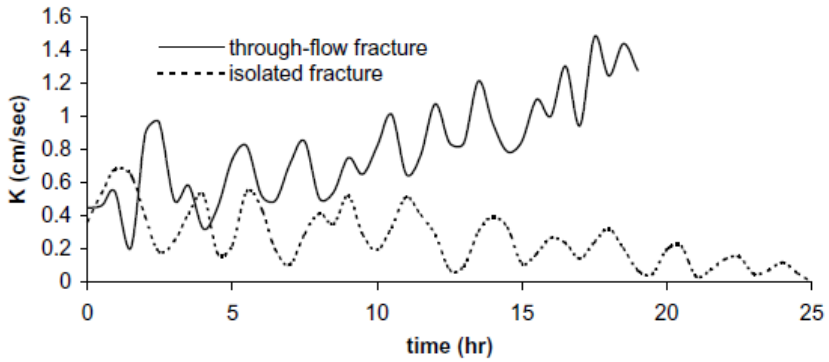

Figure 5.12: Oscillations in the hydraulic conductivity due to coupled dissolution and deposition, reproduced from Singurindy and Berkowitz 2004. It was reported that the higher the injecting flow rate, the longer the period of oscillation.

Singurindy and Berkowitz (2004) summarised their observations in Figure 5.13 below.

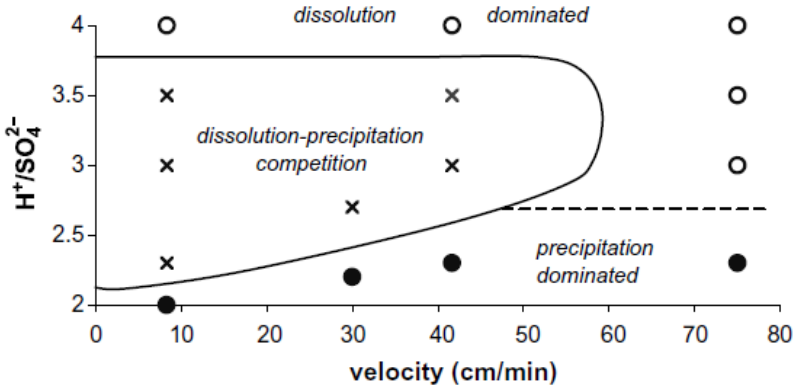

Figure 5.13: Summary of the observations as a function of the fluid velocity and the concentration ratio of H^+ to SO_4^{2-}, reproduced from Singurindy and Berkowitz 2004.

Although the conditions differ from typical geothermal conditions (room temperature and one atmospheric pressure versus the higher temperature and pressure e.g. 160 ℃ and 20 MPa), the results hold lessons for the geothermal case. The conditions in the experiments of Singurindy and Berkowitz (2004 were that the fluid velocity is in the range of 0 to 10 cm/min, and if sulphuric acid is the only source of protons and sulphate ions, $[H^+]/[SO_4^{2-}] \approx 2$. In natural geothermal fluids or undosed separated geothermal water, there would be naturally existing SO_4^{2-} dissolved from numerous minerals (such as anhydrite ($CaSO_4$) and thenardite (Na_2SO_4)) and the negligible amount of H^+ compared to SO_4^{2-} as the typical pH is usually close to 7-8, hence $[H^+]/[SO_4^{2-}]$would become less than 2 and hold but not far from 2. Although the molar volume of anhydrite (about 46 cm^3/mol) is lower than that of gypsum (about 75 cm^3/mol), it is still higher than that of calcite (about 37 cm^3/mol). Since, mole for mole, it occupies more volume, the deposition of anhydrite may cause scaling problems along with amorphous silica. To minimise the anhydrite problem, the experimental results shown in Figure 5.13 suggest that, theoretically, one could simply mix HCl and H_2SO_4 to obtain a relatively higher $[H^+]/[SO_4^{2-}]$ for acidification, instead of using sulphuric acid only. However, this method can be lack of practical utility as hydrogen chloride acid is too expensive for acidification. HCl is only used where an immediate anhydrite oversaturation is expected.

Since it was assumed previously that the calcium sulphate only exists in the form of anhydrite under geothermal conditions, the kinetic model for anhydrite deposition only is built below.

Calcium sulphate is one of the most common of the compounds that exhibit a retrograde solubility (decreases with increasing temperature), since its dissolution is exothermic. The solubility in pure water over temperature is plotted in Figure 5.9 below.

Blount and Dickson (1969) experimentally investigated the solubility of $CaSO_4$ in 0 – 6 mol/kg aqueous solutions of sodium chloride at temperatures from 100 to 450 ℃ and pressures from 1 to 1000 bars. Based on the observations, Blount and Dickson (1968) suggested that the solubility will be higher when pressure is increased, at any specific set of fixed conditions (i.e. temperature and concentration of NaCl are constant), shown in Figure 5.14 below:

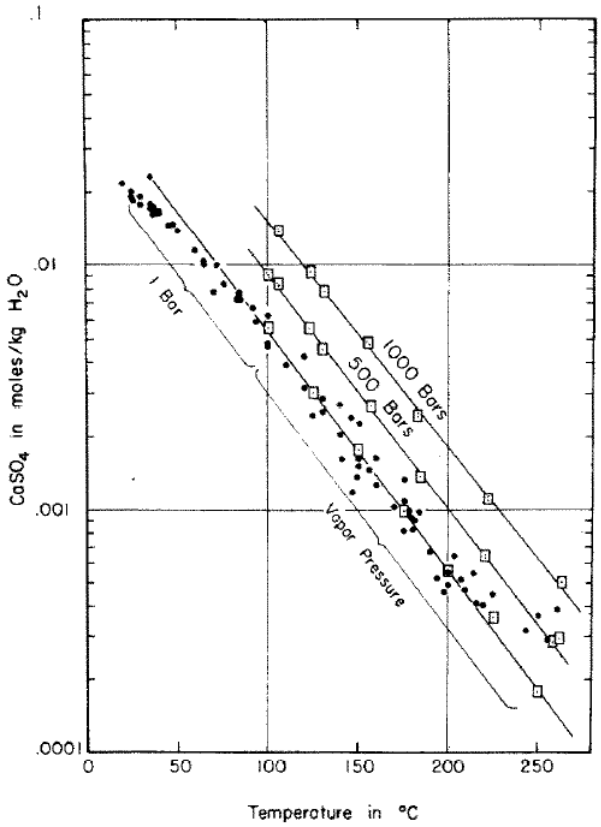

Figure 5.14: Summary of the observed solubility of calcium sulphate in pure water as a function of temperature and pressure; reproduced from Blount and Dickson 1969.

Based on the experimental results, the following expression was proposed (Blount and Dickson 1969) to predict the anhydrite solubility $C_{\mathrm{e,CaSO_4}}$ in pure water under the physical conditions in the range of 100 to 450 ℃ and 1 to 1000 bars, which includes typical geothermal conditions (e.g. 260 ℃ and 200 bars):

$$\ln C_{e,\mathrm{CaSO_4}} = -2.917 - 0.02314T + 0.001179P + 6.02 \times 10^{-9}PT^2 - 2.07 \times 10^{-7}P^2 \tag{5.46}$$

where T is the temperature in ℃, and P is the pressure in bars.

However, it becomes more complicated when varying temperatures and concentrations of NaCl are involved. The observations (Blount and Dickson 1968) are reproduced in Figure 5.15 below.

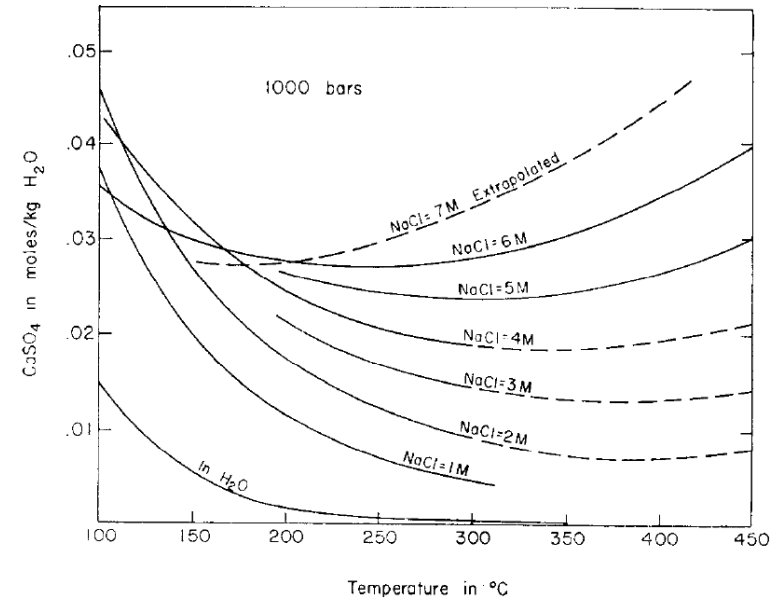

(a)

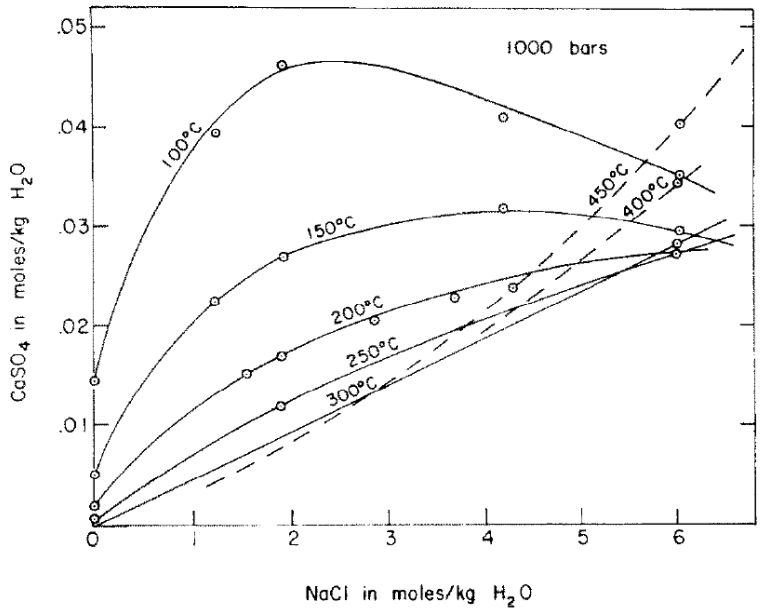

(b)

Figure 5.15: Solubility of calcium sulphate under the effects of (a) varying temperatures and (b) concentrations of NaCl; reproduced from Blount and Dickson 1968.

According to observed data shown in Figure 5.15 (a), when the concentration of NaCl is raised above 1 M, the solubility of $CaSO_4$ is no longer continuously decreased along the temperature but firstly decreased to a minimum and then increased. On the other hand, at a fixed temperature, there will be a maximum in solubility as the concentration of NaCl is increased, and the NaCl concentration where the maximum occurs is presumed to depend on the temperature. However, since the temperatures and the NaCl concentrations where extrema are found in Figure 5.15 lie outside typical geothermal conditions (e.g. [NaCl] < 1 M and T > 100 ℃), it may be concluded that under geothermal conditions, the solubility of anhydrite will be decreased by increasing temperature, but increased by increasing NaCl concentration.

Since the presence of hydrogen ions may lead to the formation of hydrogen sulphate (HSO_4^-), it is expected that varying pH will shift the solubility of anhydrite. The solubility of $CaSO_4$ in sulphuric acid has been measured by (Marshall et al. 1966; Zdanovskii et al. 1968; Dutrizac 2002; Ling and Demopoulos 2004) and summarised by (Azimi et al. 2007).

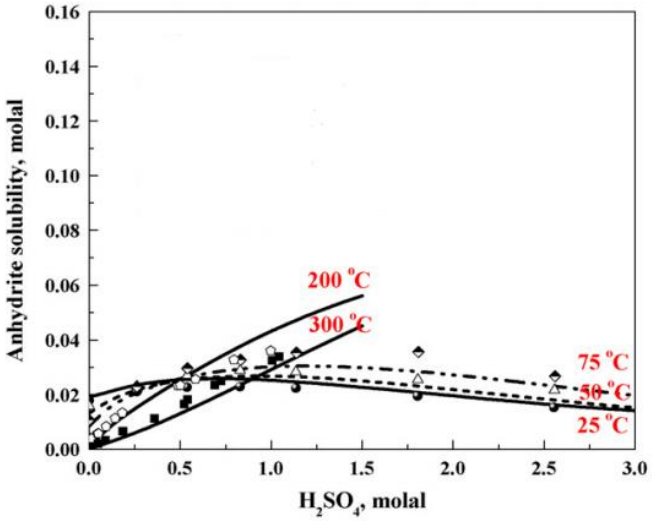

Figure 5.16: Solubility of calcium sulphate in H_2SO_4 solutions; reproduced from Azimi et al. 2007.

Based on the experimental data shown above, the solubility of $CaSO_4$ will be moderately increased by adding H_2SO_4 and decreased at very high H_2SO_4 concentrations, at low temperatures (25 to 60 ℃); at higher temperatures, the solubility of $CaSO_4$ over the amount of added H_2SO_4 will be strongly increased and decreased again. This increase-decrease phenomenon is due to the decline of the second dissociation constant of sulphuric acid as the temperature is increased. In practice, the lowest pH that is used in geothermal dosing is about 4.5. Thus, there will be approximately $10^{-4.5}$ molal hydrogen ions present, which will at the very low end of the diagram in Figure 5.16.

Thermodynamically, the solubility constant of $CaSO_4$ can be defined by:

$$K_{sp,CaSO_4} = a_{Ca^{2+}} a_{SO_4^{2-}} = \gamma_{Ca^{2+}}[Ca^{2+}]\,\gamma_{SO_4^{2-}}[SO_4^{2-}] \tag{5.47}$$

Haddon and Brown (1924) and Partridge and White (1928) reported the solubility of insoluble anhydrite in water from 20 to 220 ℃. The solubility constant $K_{sp,CaSO_4}$ based on these experimental data is fitted to this data (Figure 5.17 below):

$$\log K_{sp,CaSO_4} = 4.287 - 0.02092T - 423.7/T \tag{5.48}$$

where T is the absolute temperature. It should be noted that Equation 5.48 is based on the experimental data up to 220 ℃ which is a relatively high temperature but may not be high enough for some geothermal wells. Hence, it is assumed that Equation 5.48 can be safely extrapolated to at least 300 ℃.

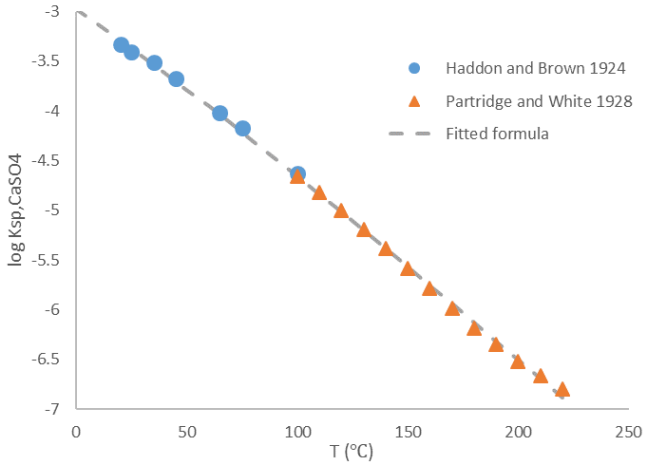

Figure 5.17: Comparison among the observed $\log K_{sp,\mathrm{CaSO_4}}$ by Haddon and Brown (1924) and Partridge and White (1928) and the formula used in the present work.

Marshall and Jones (1966) experimentally studied the $CaSO_4$-H_2SO_4-H_2O system from 25 to 350 °C and proposed the following formula (Equation 5.54) to estimate the concentration product of Ca^{2+} and SO_4^{2-} at equilibrium $K'_{sp,\mathrm{CaSO_4}}$ in aqueous electrolyte solutions:

$$\log K'_{sp,\mathrm{CaSO_4}} = \log([\mathrm{Ca^{2+}}][\mathrm{SO_4^{2-}}]) = \log K_{sp,\mathrm{CaSO_4}} + 8S_0 \frac{\sqrt{I}}{1 + A_{sp}\sqrt{I}} + B'I - C'I^2 \quad (5.49)$$

where S_0 is the Debye-Hückel limiting slope, which is equal to S when T ≤ 300 °C or $S/1.1$ when T > 300 °C and S is mentioned later and defined in Equation 5.55, A_{sp}, B', and C' are adjustable parameters. These parameters (S_0, A_{sp}, B', and C') may be treated as a function of temperature.

The dissociation of H_2SO_4 is commonly recognised as the following two steps:

$$\mathrm{H_2SO_4} \leftrightarrow \mathrm{H^+} + \mathrm{HSO_4^-} \quad (5.50)$$

$$\mathrm{HSO_4^-} \leftrightarrow \mathrm{H^+} + \mathrm{SO_4^{2-}} \quad (5.51)$$

The dissociation constants $K_{1,\mathrm{H_2SO_4}}$ and $K_{2,\mathrm{H_2SO_4}}$ are defined by:

$$K_{1,\mathrm{H_2SO_4}} = \frac{a_{\mathrm{H^+}} a_{\mathrm{HSO_4^-}}}{a_{\mathrm{H_2SO_4}}} = \frac{\gamma_{\mathrm{H^+}}[\mathrm{H^+}]\,\gamma_{\mathrm{HSO_4^-}}[\mathrm{HSO_4^-}]}{\gamma_{\mathrm{H_2SO_4}}[\mathrm{H_2SO_4}]} \quad (5.52)$$

$$K_{2,\mathrm{H_2SO_4}} = \frac{a_{\mathrm{H^+}} a_{\mathrm{SO_4^{2-}}}}{a_{\mathrm{HSO_4^-}}} = \frac{\gamma_{\mathrm{H^+}}[H^+]\,\gamma_{\mathrm{SO_4^{2-}}}[\mathrm{SO_4^{2-}}]}{\gamma_{\mathrm{HSO_4^-}}[\mathrm{HSO_4^-}]} \quad (5.53)$$

where $K_{1,\mathrm{H_2SO_4}}$ is usually treated as infinite, and $K_{1,\mathrm{H_2SO_4}} \gg K_{2,\mathrm{H_2SO_4}}$.

Based on the reported data, the following expression is fitted to conveniently estimate $K_{2,\mathrm{H_2SO_4}}$ from 25 to 350 °C:

$$\log K_{2,\mathrm{H_2SO_4}} = 4.793 - 0.01659T - 549.1/T \quad T \le 623\ \mathrm{K}\ (350\ °\mathrm{C}) \quad (5.54)$$

where T is the absolute temperature. The comparison is shown in Figure 5.18 below.

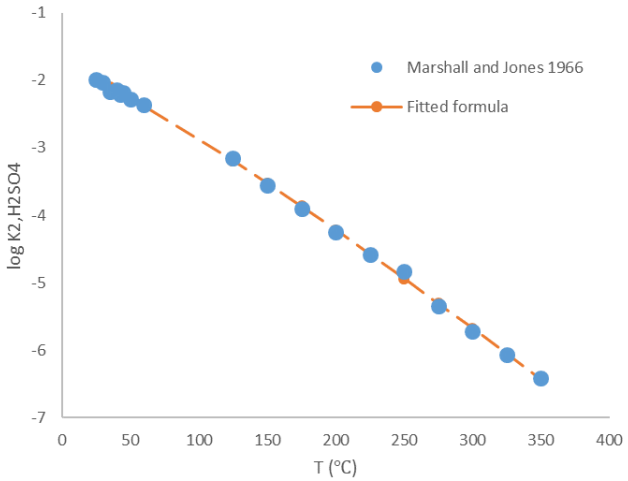

Figure 5.18: Comparison between the observed $\log K_{2,\mathrm{H_2SO_4}}$ by Marshall and Jones (1966) and the formula used in the present work.

Similar to $K'_{sp,\mathrm{CaSO_4}}$, Marshall and Jones (1966) proposed the following expression to predict the second dissociation constant of sulphuric acid:

$$\log K_{2,\mathrm{H_2SO_4}}{}' = \log\left(\frac{[\mathrm{H^+}][\mathrm{SO_4^{2-}}]}{[\mathrm{HSO_4^-}]}\right) = \log K_{2,\mathrm{H_2SO_4}} + 4S\frac{\sqrt{I}}{1 + A_k\sqrt{I}} \qquad (5.55)$$

where S is the Debye-Hückel limiting slope which is equal to S_0 in Equation 5.54 when T $\leq$ 300 ℃ and $1.1S_0$ when T $>$ 300 ℃, A_k is a fitting parameter, and B' and C' are not included in Equation 5.60 as these are negligible when $I < 0.5$ M.

The fitted parameters in Equation 5.49 and 5.60 are summarised in Table 5.5 below:

Table 5.5: Summary of fitted S, A_{sp}, B', and C', reproduced from (Marshall and Jones 1966)

T(℃)	S	A_{sp}	A_k	B'	C'
25	0.5080	1.49	0.94	0.0194	0.0134
30	0.5125	1.51	0.96	0.0124	0.0130
35	0.5176	1.52	0.98	0.0060	0.0124
40	0.5229	1.53	1.01	0.0022	0.0120
43	0.5262	1.53	1.02	0.00165	0.0117
45	0.5282	1.53	1.03	0.0011	0.0114
50	0.5337	1.54	1.07	0	0.0108
60	0.5449	1.55	1.12	0	0.0096
125	0.6422	1.60	1.42	0	0
150	0.6899	1.60	1.51	0	0
175	0.7451	1.60	1.58	0	0
200	0.8097	1.60	1.65	0	0
225	0.8880	1.60	1.71	0	0
250	0.9848	1.60	1.77	0	0
275	1.1120	1.60	1.77	0	0
300	1.2870	1.60	1.73	0	0
325	1.6900	1.60	1.56	0	0
350	2.1800	1.60	1.34	0	0

For simplicity, the following formulas are fitted over temperature to estimate S, A_{sp}, A_k, B', and C' conveniently which can be safely applied between 25 ℃ and 300 ℃ unless specified:

$$S = 0.2452\exp(0.002413T) + 7.478\times10^{-7}\exp(0.02277T) \tag{5.56}$$

$$\begin{gathered} A_{sp} = 3.324 - 0.002037T - \frac{363.8}{T} \quad 298\text{ K} \le T \le 398\text{ K (125 ℃)} \\ A_{sp} = 1.60 \quad 398\text{ K} < T \le 573\text{ K (300 ℃)} \end{gathered} \tag{5.57}$$

$$\begin{gathered} A_k = -3.633\times10^{-10}T^4 + 5.969\times10^{-7}T^3 - 3.715\times10^{-4}T^2 + 0.1075T \\ - 11.06 \end{gathered} \tag{5.58}$$

$$\begin{gathered} \mathrm{B}' = -3.552\times10^{-7}T^3 + 3.667\times10^{-4}T^2 - 0.1257T + 14.32 \quad 298\text{ K} \le T \\ \le 323\text{ K (50 ℃)} \end{gathered} \tag{5.59}$$

$$\begin{gathered} \mathrm{B}' = 0 \quad 323\text{ K} < T \le 573\text{ K (300 ℃)} \end{gathered}$$

$$\begin{gathered} \mathrm{C}' = -3.994\times10^{-7}T^2 + 1.436\times10^{-4}T + 0.006143 \quad 298\text{ K} \le T \\ \le 398\text{ K (125 ℃)} \end{gathered} \tag{5.60}$$

$$\mathrm{C}' = 0 \quad 398\text{ K} < T \le 573\text{ K (300 ℃)}$$

As discussed above, in practice, anhydrite scaling occurs when the calcium sulphate supersaturation index exceeds a certain value. However, to the author's knowledge, there is a lack of reported studies on the value of supersaturation required. Hence, it is assumed that $\mathrm{CaSO_4}$ begins to deposit once it becomes supersaturated, i.e. the critical supersaturation index is assumed to be 1. As the solubility of $\mathrm{CaSO_4}$ is known, one can find the maximum concentrations of $\mathrm{Ca^{2+}}$ and $\mathrm{SO_4^{2-}}$ in the solution through the solubility product K_{sp}.

It was proposed by (Hasson and Zahavi 1970) that there are two stages of deposition: the initial deposition of $\mathrm{CaSO_4}$ nuclei to the collector surface, and the later growth of the previously deposited nuclei by crystallization. The two-stage theory is similar to the two-stage assumption with respect to amorphous silica deposition, different in that the anhydrite scale is crystalline whereas the silica scale is in the form of amorphous clusters. As with calcite dissolution, both the mass transfer of reactants and the surface reaction should be considered. In this section, the discussion is limited to surface reaction only. The deposition process can be expressed by:

$$\mathrm{Ca^{2+}} + \mathrm{SO_4^{2-}} \rightarrow \mathrm{CaSO_4(s)} \tag{5.61}$$

The second-order rate law applied to model the kinetics of crystallization for pure salt (Nancollas and Reddy 1971) is:

$$-\frac{d[\mathrm{Ca^{2+}}]}{dt} = -\frac{d[\mathrm{SO_4^{2-}}]}{dt} = k_a\{[\mathrm{Ca^{2+}}][\mathrm{SO_4^{2-}}] - K'_{sp}\} \tag{5.62}$$

where k_a is the reaction rate constant, which can be empirically expressed based on experimental results using the Arrhenius equation, $[\mathrm{Ca^{2+}}]$ and $[\mathrm{SO_4^{2-}}]$ are the average steady-state concentrations of $\mathrm{Ca^{2+}}$ and $\mathrm{SO_4^{2-}}$ respectively, and K'_{sp} is the concentration product of $\mathrm{Ca^{2+}}$ and $\mathrm{SO_4^{2-}}$ at equilibrium, which may be equal to the solubility product K_{sp}, if the assumption of the critical supersaturation index above is acceptable. Equation 5.62 can be alternatively expressed in a logarithmic form:

$$\log(-\frac{d[\mathrm{Ca}^{2+}]}{dt}) = \log(-\frac{d[\mathrm{SO}_4^{2-}]}{dt}) = \log\{[\mathrm{Ca}^{2+}][\mathrm{SO}_4^{2-}] - K'_{sp}\} + \log k_a \qquad (5.63)$$

Theoretically, if the growth of $\mathrm{CaSO_4}$ follows the model above, one can plot $\log(-\frac{d[Ca^{2+}]}{dt})$ vs $\log\{[\mathrm{Ca}^{2+}][\mathrm{SO}_4^{2-}] - K'_{sp}\}$ and obtain a linear correlation with a slope equal to 1 and an intercept equal to $-\log k_a$.

Ideally, if a similar experiment could be done under geothermal conditions, one would be able to obtain a similar empirical expression to predict the $\mathrm{CaSO_4}$ precipitation.

Merdhah and Yassin (2008) experimentally studied the $\mathrm{CaSO_4}$ precipitation by injecting synthetic brines through sandstone samples at the temperatures from 50 to 80 ℃, neutral pH, and under differential pressure from 100 to 200 psig. The effect of pH was not considered, and the ionic strength is approximately 9 to 50 times higher than a typical NZ geothermal fluid. The following Arrhenius equation was fitted:

$$k_a = 3 \times 10^{10}\ \Delta P^{0.354} \exp(-\frac{84296}{8.314T}) \qquad (5.64)$$

where k_a is in $\mathrm{M\ min^{-1}}$, ΔP is the differential pressure in psig, and T is the absolute temperature.

Sheikholeslami and Ng (2001) investigated the thermodynamics and kinetics of $\mathrm{CaSO_4}$ precipitation with and without the presence of $\mathrm{CaCO_3}$ at the temperatures 60 and 70 ℃. The observations are reproduced below:

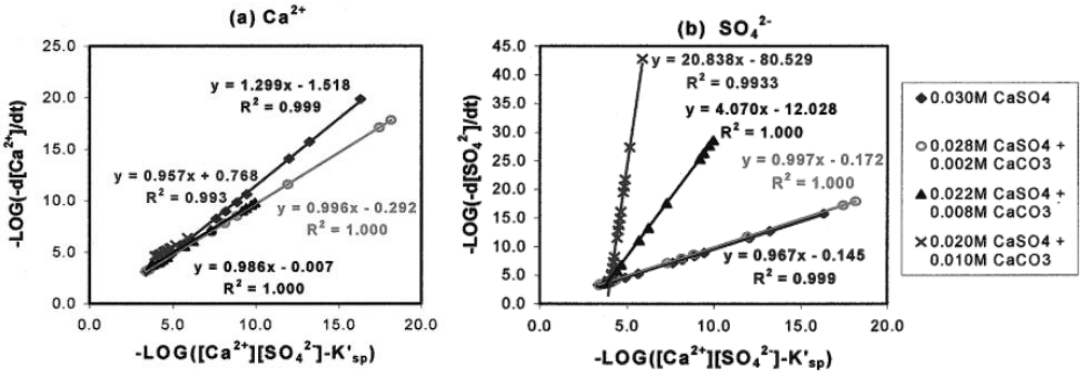

Figure 5.19: Plot of $\log(-\frac{d[\mathrm{Ca}^{2+}]}{dt})$ and $\log(-\frac{d[\mathrm{SO}_4^{2-}]}{dt})$ vs $\log\{[\mathrm{Ca}^{2+}][\mathrm{SO}_4^{2-}] - K'_{sp}\}$ at 60 ℃, reproduced from Sheikholeslami and Ng 2001.

Based on the experimental results, Sheikholeslami and Ng (2001) suggested that the model for the crystallization of pure salt (Equation 5.63 and 5.64) cannot be applied to estimating the precipitation rate of sulphate ion in the presence of dissolved $\mathrm{CaCO_3}$, as the slope of the correlation is not close to 1 for those cases. However, it may not be a problem in the case of geothermal reinjection as, even though the possibility of $\mathrm{CaCO_3}$ precipitation cannot be ignored, the total amount of dissolved $\mathrm{CaCO_3}$ in the injectate may be limited compared to the concentration of dissolved anhydrite. For example, at 160 ℃, by assuming that the supply of sulphuric acid and calcite is unlimited and sulphuric acid is gradually added (allowing $\mathrm{Ca^{2+}}$ and $\mathrm{SO_4^{2-}}$ are equally produced till solubility is reached), there could be ideally as much as $10^{-5.31}$ mol/kg $\mathrm{CaCO_3}$ and $10^{-2.88}$ mol/kg $\mathrm{CaSO_4}$ dissolved.

The experimental results revealing the effect of varying temperatures on the precipitation rate are reproduced below:

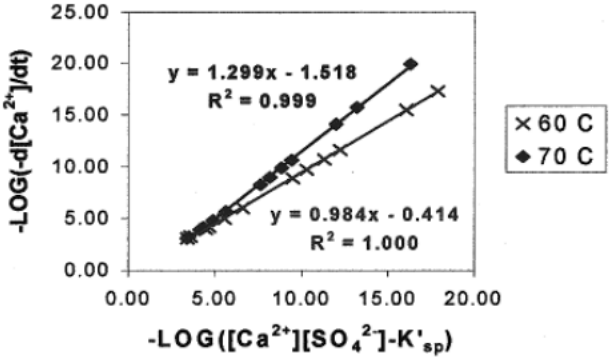

Figure 5.20: Plot of $\log(-\frac{d[Ca^{2+}]}{dt})$ and $\log(-\frac{d[SO_4^{2-}]}{dt})$ vs $\log\{[Ca^{2+}][SO_4^{2-}] - K'_{sp}\}$ in pure 0.03 M $CaSO_4$ solution at 60 and 70 ℃, reproduced from Sheikholeslami and Ng 2001.

As expected, the precipitation rate increased as temperature was increased from 60 to 70 ℃, from 2.5 M^{-1} h^{-1} at 60 ℃ to 32.9 M^{-1} h^{-1} at 70 ℃, which could be extrapolated to higher temperatures using the Arrhenius equation. Despite the narrow temperature range, the biggest problems in applying these experimental data in our work may be caused by the absence of information on the effect of pH, ionic strength, and pressure.

In different geothermal fields, the pressure can vary. Theoretically, the variation of pressure leads to the variation in reaction rate. However, in practice, this usually can be considered as negligible for the reactions occurring in solid or liquid phase. In the present work, the injectate is assumed to be in liquid phase only, and therefore, it may be feasible to assume that all reactive processes of interest are independent of pressure.

The existing theories are useful. However it may not be safe to extrapolate the fitted formula obtained less than 80 ℃ to typical geothermal temperature (say 260 ℃).

Palandri and Kharaka (2004) summarised and evaluated the dissolution rate data for anhydrite based on (Barton and Wilde 1971; Bildstein et al. 2001; Dove and Czank 1995; Jeschke and Dreybrodt 2002). The fitted data is reproduced in Table 5.2. Similar to the method used to calculate the dissolution rate of calcite, the following formula is applied in the present work to find the precipitation rate of anhydrite.

Recall that the solubility product of anhydrite $K_{sp,\mathrm{CaSO_4}}$ is defined by Equation 5.47 and 5.48; and the relationship between the solubility product, the dissolution rate, and precipitation rate is shown in Equation 5.11; the dissolution rate constant $k_{d,\mathrm{CaSO_4}}$ is estimated using Equation 5.10. Therefore, $k_{p,\mathrm{CaSO_4}}$ can be defined by:

$$k_{p,\mathrm{CaSO_4}} = k_{d,\mathrm{CaSO_4}} / K_{sp,\mathrm{CaSO_4}} \tag{5.65}$$

Eventually, by coupling the dissolution of calcite and the precipitation of anhydrite, one can predict the effects of acidified injectate on the surrounding rocks.

5.4 Acidification using weak acid

When the calcite reacts with a strong acid, the reaction (Equation 5.1) is often treated as irreversible and limited by the mass transfer of hydrogen ion from the bulk solution to the calcite

surface. This may not be true for weak acid like acetic acid as, despite the effects of partial dissociation, the dissolution products can also inhibit the reaction. Specifically, the calcite dissolution due to weak acid can be limited by both the transport of hydrogen ion to the surface and the transport of reaction products away from the surface and considered as reversible (Chatelain et al. 1976; Fredd and Fogler 1998).

As a result, it has been reported (Nierode and Williams 1971; Harris 1961) that the calcite dissolution rate in acetic acid is slower than that in a stronger acid like hydrochloric acid or sulphuric acid for the same pH. This was suggested (Fredd and Fogler 1998) to be due to the kinetics of the surface reaction (Nierode and Williams 1971) and the thermodynamics of the reversible reaction (Chatelain et al. 1976) rather than the irreversible reaction seen in strong acids.

Therefore, weak acids could be a better option than strong acids to inhibit silica scaling in the geothermal industry, and would cause less severe corrosion at high temperatures (Abrams et al. 1983; Harris 1961). For example, acetic acid, the simplest stable carboxylic acid, is being applied in the San Jacinto geothermal development in Nicaragua without reported problems (Exler et al. 2014). However, it is much more expensive than sulphuric acid. Also, in some cases enough boric acid may be present in the brine to have a significant buffering effect.

In the present work, acidification using a weak acid is treated quantitatively by modelling the corresponding processes of acetic acid. The dissociation constant of acetic acid $K'_{d,HAc}$ is defined using the equilibrium concentrations by:

$$K'_{d,HAc} = \frac{[\mathrm{H^+}][\mathrm{Ac^-}]}{[\mathrm{HAc}]} \tag{5.66}$$

The dissociation constant of acetic acid in aqueous sodium chloride solutions (0 to 5 M) at high temperatures (0 to 300 ℃) was first measured and reported by Mesmer et al. (1989), which is reproduced in Table 5.6 replotted in Figure 5.21 below:

Table 5.6: Measured dissociation constant of acetic acid $\log K'_{d,HAc}$ as a function of temperature and the concentration of NaCl, reproduced from Mesmer et al. 1989.

$[NaCl](M)$	*0*	*0.1*	*0.5*	*1*	*3*	*5*
T (℃)	$\log K'_{d,HAc}$					
0	-4.78	-4.581	-4.518	-4.548	-4.858	-5.275
25	-4.757	-4.547	-4.469	-4.484	-4.737	-5.086
50	-4.786	-4.564	-4.472	-4.474	-4.675	-4.965
75	-4.848	-4.613	-4.506	-4.494	-4.643	-4.877
100	-4.937	-4.684	-4.56	-4.533	-4.63	-4.811
125	-5.047	-4.774	-4.629	-4.586	-4.628	-4.757
150	-5.18	-4.881	-4.71	-4.647	-4.633	-4.712
175	-5.334	-5.005	-4.802	-4.716	-4.643	-4.673
200	-5.515	-5.147	-4.904	-4.791	-4.653	-4.639
225	-5.727	-5.311	-5.015	-4.868	-4.662	-4.605
250	-5.978	-5.501	-5.136	-4.947	-4.665	-4.571
270	-6.282	-5.725	-5.266	-5.021	-4.653	-4.528
300	-6.664	-5.995	-5.403	-5.081	-4.609	-4.465

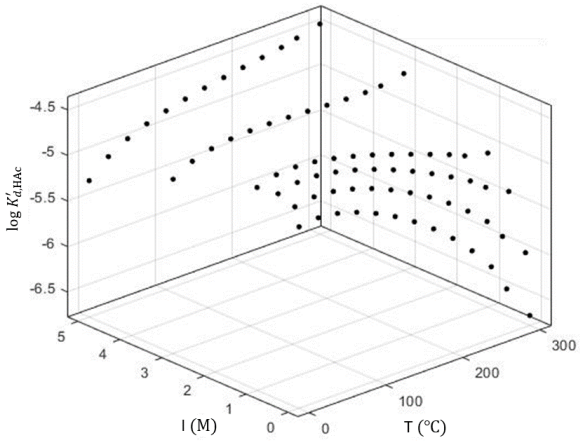

(a)

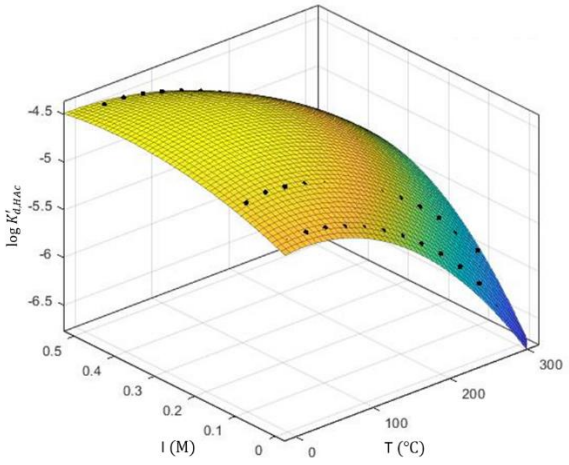

(b)

Figure 5.21: Observed dissociation constant of acetic acid plotted from the data of (Mesmer et al. 1989) on a logarithmic scale up to 300 ℃ (a) in NaCl solutions up to 5 M; (b) in NaCl solutions up to 0.5 M (i.e. a subset of (a)) fitted with Equation 5.67 below.

As the reported data shown in Figure 5.21b already covers typical geothermal conditions (ionic strength is dominated by the concentration of sodium chloride which usually less than 0.1 M and temperature is usually less than 300 ℃), it can be safely used. It can be fitted with a polynomial formula to predict $K'_{d,HAc}$ in the present work:

$$\begin{aligned} K'_{d,HAc} = {} & -6.634 + 0.01305T + 1.236I - 2.272 \times 10^{-5}T^2 - 0.00388TI \\ & + 2.866I^2 + 8.066 \times 10^{-12}T^3 + 2.376 \times 10^{-5}T^2I \\ & - 0.02051TI^2 \end{aligned} \tag{5.67}$$

where T is the absolute temperature.

The surface dissolution rate of calcite due to acetic acid is estimated by using Equation 5.29-5.34 as well, however, the transport of reaction products in this case should be paid special attention.

5.5 Scale removal using hydrofluoric acid

General techniques like injecting acid to reservoir (Arias and Ahmad 1996) have been invented to treat siliceous formations to increase the permeability of porous rocks. In geothermal industries, hydrofluoric acid HF is widely used to remove silica scale for the same reason, as it may be the only effective chemical method for silica scale removal.

Hydrofluoric acid is a weak acid as only a limited portion of it can dissociate in dilute aqueous solutions, but is highly reactive. It is widely accepted that the following reactions occur in dilute solutions ($[\mathrm{HF}] < 1$ M), firstly proposed by Pick (1912):

$$\mathrm{HF} \leftrightarrow \mathrm{H^+} + \mathrm{F^-} \tag{5.68}$$

$$\mathrm{HF} + \mathrm{F^-} \leftrightarrow \mathrm{HF_2^-} \tag{5.69}$$

The equilibrium constants $K_{\mathrm{d,HF}}$ and $K_{2,\mathrm{HF}}$ of the reactions shown in Equation 5.68 and 5.69 are defined below:

$$K_{\mathrm{d,HF}} = \frac{a_{\mathrm{H^+}} a_{\mathrm{F^-}}}{\mathrm{a_{HF}}} = \frac{\gamma_{\mathrm{H^+}}[\mathrm{H^+}]\gamma_{\mathrm{F^-}}[\mathrm{F^-}]}{\gamma_{\mathrm{HF}}[\mathrm{HF}]} \tag{5.70}$$

$$K_{2,\mathrm{HF}} = \frac{a_{\mathrm{HF_2^-}}}{\mathrm{a_{HF}} a_{\mathrm{F^-}}} = \frac{\gamma_{\mathrm{HF_2^-}}[\mathrm{HF_2^-}]}{\gamma_{\mathrm{HF}}[\mathrm{HF}]\gamma_{\mathrm{F^-}}[\mathrm{F^-}]} \tag{5.71}$$

Ellis (1963) measured the equilibrium constants $K_{\mathrm{d,HF}}$ and $K_{2,\mathrm{HF}}$ of the reactions shown in Equation 5.68 and 5.69 in 0.01-0.1 M hydrofluoric acid and 0.002-0.1 M potassium fluoride solutions up to 200 ℃. The reported values are reproduced in Table 5.7 below.

Table 5.7: Observed $K_{\mathrm{d,HF}}$ and $K_{2,\mathrm{HF}}$ against temperature, reproduced from Ellis 1963.

Temperature (℃)	$K_{\mathrm{d,HF}}$ $(\times 10^4)$	$K_{2,\mathrm{HF}}(\times 10^4)$
25	6.60 ± 0.15	3.4 ± 0.5
50	4.0 ± 0.1	4.0 ± 1.0
75	2.3 ± 0.1	4.7 ± 0.8
100	1.40 ± 0.05	4.8 ± 0.8
125	0.82 ± 0.03	4.9 ± 0.8
150	0.46 ± 0.03	5.7 ± 1.5
175	0.26 ± 0.02	5.8 ± 1.5
200	0.13 ± 0.01	8 ± 2

Based on the reported data, Ellis (1963) proposed an empirical expression (shown in Equation 5.72) to predict $K_{\mathrm{d,HF}}$ between 25 and 200 ℃. For convenience, the author proposes another formula (shown in Equation 5.73) to estimate $K_{2,\mathrm{HF}}$, as no expression was given by Ellis (1963) who may have been less confident about the possible linear correlation as shown in Figure 5.22 b. The comparisons between the observation and the empirical expressions are shown in Figure 5.22.

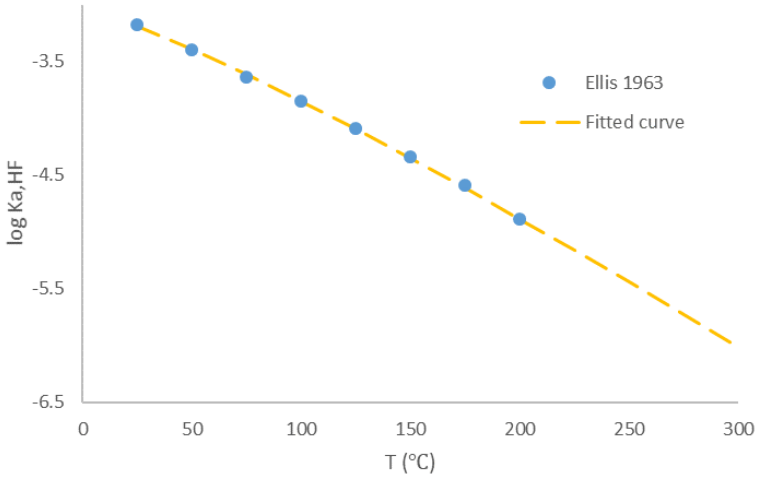

(a)

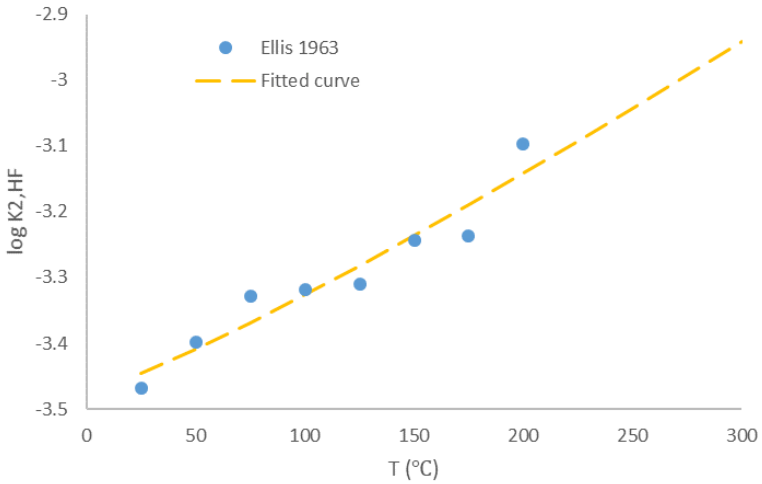

(b)

Figure 5.22: Replotted observed log $K_{d,HF}$ and log $K_{2,HF}$ (dots) against temperature, reproduced from Ellis 1963, fitted with Equation 5.72 and 5.73 (dashed line) below.

$$\log K_{d,HF} = -2.75 - 0.014T - \frac{295}{T} + 1.91 \log T \tag{5.72}$$

$$\log K_{2,HF} = -4.389 + 0.00229T + \frac{77.62}{T} \tag{5.73}$$

where T is the absolute temperature. One may notice the extrapolations of Equation 5.72 and 5.73 shown in Figure 5.22. As the published data goes up to 200°C, both Equation 5.72 and 5.73 are assumed to be applicable up to 300 °C.

Similar to the discussion regarding the dissolution of $CaCO_3$ and the precipitation of $CaSO_4$ in Section 5.3.2, only surface reaction is considered here. It is reasonably assumed that the dissolved amorphous silica is released from the scale surface only in the form of monomeric silica.

Mitra (2008) measured the solubility and dissolution rate of quartz and amorphous silica in acid fluoride solutions. Based on the published results (Kamiya et al. 1974; Knauss and Wolery 1988; Wollast and Chou 1988; Grigsby et al. 1989; Brady and Walther 1990; Mazer and Walther 1994; Worley et al. 1996; Pokrovsky et al. 2006) and Mitra's (2008) own observations, the following expressions were proposed (Mitra 2008) to predict the dissolution rate of quartz J_{qz} and amorphous silica J_{as} in hydrofluoric acid solutions:

$$J_{d,qz} = 10^{-4.53}\, a_{HF}^{1.18}\, a_{H^+}^{-0.39} \exp(-\frac{18932}{RT}) \tag{5.74}$$

$$J_{d,as} = 10^{0.48}\, a_{HF}^{1.50}\, a_{H^+}^{-0.46} \exp(-\frac{34243}{RT}) \tag{5.75}$$

where J_{as} is the dissolution rate of amorphous silica, and a_{HF} and a_{H^+} are the activities of hydrofluoric acid and hydrogen ion. Equation 5.74 is valid in the range of $-5.13 < \log a_{HF} < 1.60$, $-0.28 < \text{pH} < 7.18$, and $298 < \text{T} < 373$ K; Equation 5.75 is valid in the range of $-2.37 < \log a_{HF} < 1.61$, $-0.32 < \text{pH} < 4.76$, and $296 < \text{T} < 343$ K. Based on the fitted empirical correlation, Mitra (2008) interpreted that the mechanism of amorphous silica dissolution could be the attack of hydrofluoric acid (the F end of the molecule, serving as a Lewis base, which is capable of forming a coordinated covalent bond) and hydrogen ion (serving as a Lewis acid, which is capable of obtaining an electron pair) to the $\text{Si} - \text{O}$ bond, which determines the dissolution rate, as reproduced below:

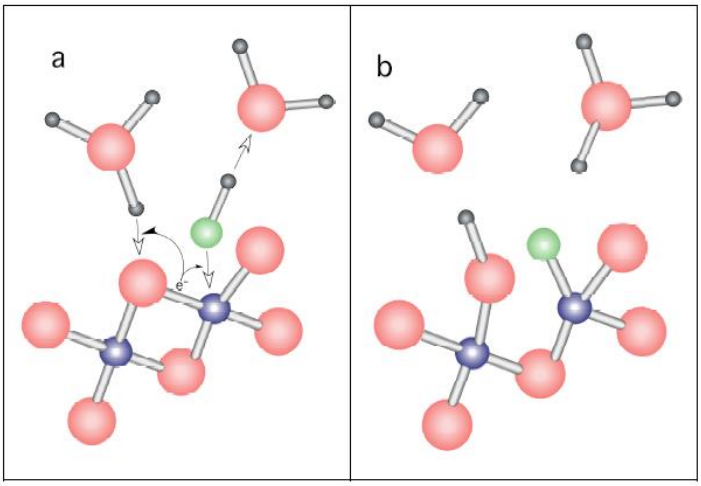

Figure 5.23: Schematic of the HF attack on the Si-O bond: a. a polymerised silica dimer is approaching by a H_3O^+ and a HF molecules, b. the dimer is attacked by a H_3O^+ and a HF molecules and forms a Si-O bond and a O-H bond; reproduced from Mitra 2008.

5.5.1 Possible collateral effects of hydrofluoric acid

When discussing the silica scale removal using hydrofluoric acid, the possible collateral effects, especially on the reservoir formations, must be estimated.

As with other acids stronger than carbonic acid, hydrofluoric acid is able to dissolve calcite. The reaction can be expressed by Equation 5.76 below:

$$\text{CaCO}_3(\text{s}) + \text{HF} \rightarrow \text{CaF}_2 + \text{CO}_2(\text{aq}) + \text{H}_2\text{O} \tag{5.76}$$

The reaction product calcium fluoride (or fluorite) CaF_2 is usually treated as insoluble. Hence, like anhydrite (CaSO_4), the precipitation of CaF_2 may be problematic. However, it is expected

that the precipitation of CaF_2 could hardly damage the geothermal reservoir formations since the molar volume of CaF_2 (25 cm^3/mol) is smaller than that of calcite (37 cm^3/mol).

5.6 Summary of all reactive chemical species

The chemical species discussed in this chapter and their corresponding reactions are briefly summarised in Figure 5.24 below.

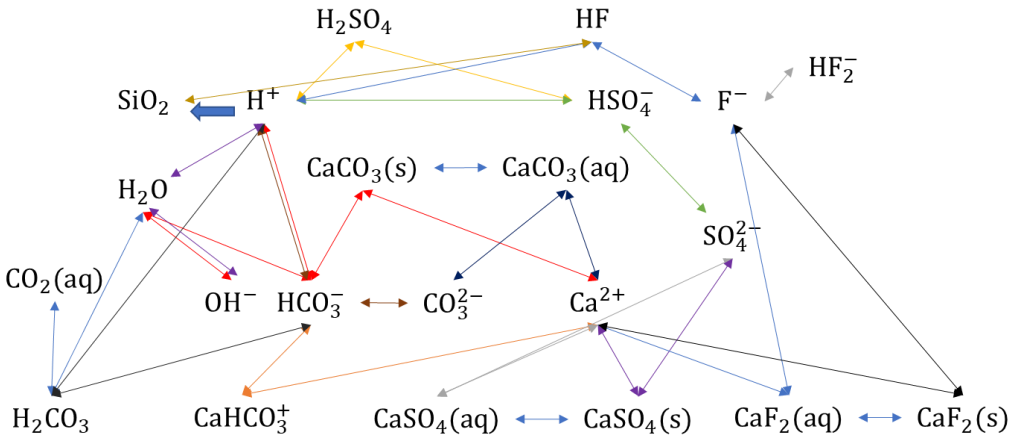

Figure 5.24: Schematic of all reactive chemical species in the present work and their corresponding dependence.

At this stage, the kinetics of all considered reactions can be modelled. The workflow of the chemistry model is reproduced in Figure 5.25 below:

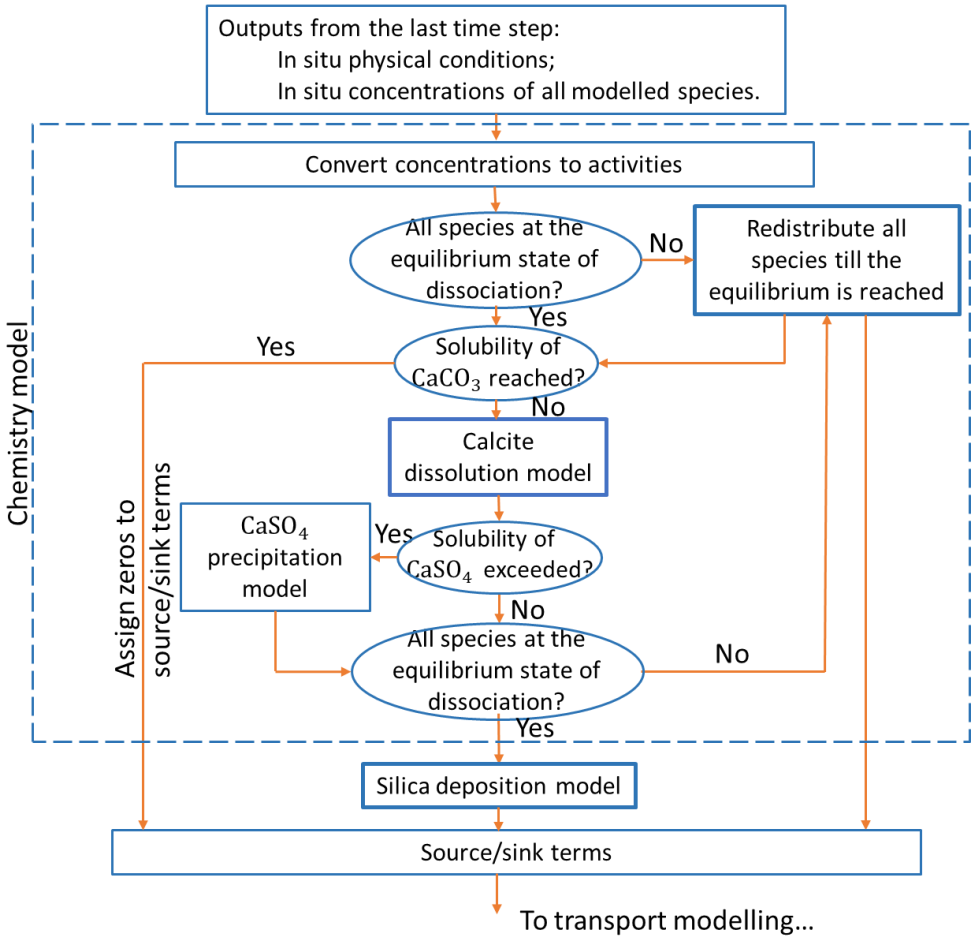

Figure 5.25: Workflow of the chemistry model.

By carefully coupling the formulas of the related reactions, the source or sink terms representing the amount of each species produced or consumed in each time step can be given.

Appendix 1: Activity coefficients

Both the Debye-Hückel equation and the Davies equation are commonly used for estimating the activity coefficient of a certain ion.

The Debye-Hückel equation is originally defined by Debye and Hückel (1923):

$$\log \gamma = -Az^2\sqrt{I} \tag{5.77}$$

where z is the valence of the ion, and A ($\mathrm{mol}^{-1/2}\mathrm{L}^{3/2}$) is determined by the permittivity ϵ, density ρ, and temperature T of the solvent (in this case, water), which can be expressed by (Hamer 1968):

$$A = -\frac{e^2}{18.4\pi\epsilon k_B T}\left(\frac{2e^2 N\rho}{\epsilon k_B T}\right)^{1/2} \tag{5.78}$$

The Debye-Hückel theory estimates the interactions among the ions by assuming that the ion of interest is surrounded by oppositely charged ions to form a spherical ion complex. This assumption limits the validity of the Debye-Hückel equation to very dilute solutions ($I \leq 10^{-2.3}$ M). The discrepancy between the estimated and the measured activity becomes larger

and larger when the concentration increases. Therefore, another form of the extended Debye-Hückel equation was proposed by Robinson and Stokes (1955):

$$\log\gamma = -\frac{Az^2\sqrt{I}}{1+Ba\sqrt{I}} + bI \tag{5.79}$$

where a is the "hydrated ion size" parameter obtained based on experimental results, and b is the second fitting parameter: Truesdell and Jones (1974) fitted and summarised the values of a and b for common ions, which are used in the present work, and B ($\mathrm{m^{-1}mol^{-1/2}L^{3/2}}$) is defined by (Hamer 1968):

$$B = \left(\frac{2e^2N_A\rho}{\epsilon k_B T}\right)^{1/2} \tag{5.80}$$

At 25 ℃, A and B are about 0.51 $\mathrm{mol^{-1/2}L^{3/2}}$ and 3.28 $\mathrm{m^{-1}mol^{-1/2}L^{3/2}}$ for aqueous solutions.

For even more concentrated solutions, the Davies equation (Davies 1962) is commonly used when $I \leq 0.5$ M:

$$\log\gamma = -0.509z^2\left(\frac{\sqrt{I}}{1+\sqrt{I}} - 0.3I\right) \tag{5.81}$$

As the geothermal injectate can be relatively dilute (e.g. the ionic strength of separated geothermal water is approximately 0.034 M at the Sumikawa geothermal station, Japan (Tamura et al. 2018)), the formula above should satisfy the needs in the present work, and it is assumed that the activity of water is fixed to one.

Hence, by substituting the following inputs to Equation 5.79, one can find the activity coefficients for the ions listed below:

Table 5.8: Summary of the input parameters for estimating the activity coefficients

Ion	z	a	b	Reference
$\mathrm{Ca^{2+}}$	+2	5.0	0.165	(MacInnes 1919; Truesdell and Jones 1974)
$\mathrm{HCO_3^-}$	-1	5.4	0	(Walker et al. 1927; Truesdell and Jones 1974)
$\mathrm{CaHCO_3^+}$	+1	5.4	0	(Truesdell and Jones 1974)
$\mathrm{CO_3^{2-}}$	-2	5.4	0	(Walker et al. 1927; Truesdell and Jones 1974)
$\mathrm{H^+/H_3O^+}$	+1	9.0	0	(Robinson and Stokes 1955; Kielland 1937)
$\mathrm{OH^-}$	-1	9.0	0	(Robinson and Stokes 1955; Kielland 1937)
$\mathrm{HSO_4^-}$	-1	0.4	0	(Kielland 1937)
$\mathrm{SO_4^{2-}}$	-2	0.4	0	a is assumed to be equal to that of $\mathrm{HSO_4^-}$
$\mathrm{F^-}$	-1	0.35	0	(Kielland 1937)
$\mathrm{HF_2^-}$	-1	0.35	0	(Kielland 1937; Ellis 1963)
$\mathrm{H_3SiO_4^-}$	-1	0.10	0	(Truesdell and Jones 1974)

The activity of neutral ion pairs is usually considered to be unity. However, Reardon and Langmuir (1975) measured the activity coefficients of $MgCO_3^0$ and $CaSO_4^0$ with ionic strength between 0 and 0.6 M at 25 ℃ and fitted the experimental data with the following limited law form of the Kirkwood equation (Kirkwood 1934; Bateman et al 1940):

$$\log \gamma = -B_k I \tag{5.82}$$

Based on the observations, Reardon and Langmuir (1975) suggested that $B_k = 0.45$ and 0.63 for $CaSO_4^0$ and $MgCO_3^0$ respectively, and $B_k = 0.5$ for other di-divalent ion pairs (i.e. an ion pair made of two divalent ions) at 25 ℃. Therefore, in the present work:

$$\log \gamma_{CaCO_3^0} = -0.5I \tag{5.83}$$

$$\log \gamma_{CaSO_4^0} = -0.45I \tag{5.84}$$

The activity coefficients for other neutral ion pairs that are not mentioned above (e.g. $CO_2(aq)$, HF, etc.) are assumed to be unity.

Chapter 6

Modelling of heat and mass transport

Concentrated geothermal fluid is often injected back underground to maintain reservoir pressure and sequester toxic minerals. The decrement in amorphous silica solubility due to loss of heat and the increment in concentration due to loss of water may cause silica scaling, which plugs the fluid pathways and gradually reduces the injectivity.

There are a few commercial packages like TOUGHREACT (Xu 2008) available for numerically simulating the silica deposition in the case of geothermal production (Xu et al. 2004, Wong et al. 2016), using empirical surface reaction rates to estimate the deposition rate. These can be robust; however, the empirical reaction rate must be predicted for every new set of conditions. A model that predicts it a priori is desired.

6.1 Definition of the problem: silica scaling in reinjection process

To maintain reservoir pressure and sequester toxic minerals, cooled and concentrated geothermal brine (or separated geothermal water, SGW) is often reinjected into the aquifer, as shown in Figure 6.1 below.

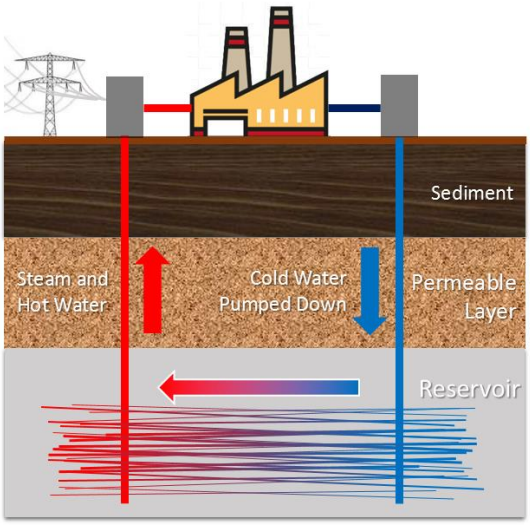

Figure 6.1: Sketch of the geothermal production: the process in red represents geothermal fluid extraction; the process in blue is reinjection (not to scale).

When planning a geothermal reinjection system, the location of reinjection is critical (Kaya et al. 2010). Conventionally, the location of the well can be classified to be either *infield* or *outfield* i.e. in or out of the hot part of the geothermal reservoir (near or far from the production well) respectively. However, these classifications were considered by (Kaya et al. 2010) to lack practical utility as either the definitions themselves are vague or the variables required to determine the which category a location falls into are not always available, especially before drilling. In New Zealand, typical well distances vary from hundreds of metres (Horne 1982; Fossum and Horne 1982) to kilometres (Glover and Scott 2005). As different reinjection strategies are applied in different geothermal power plants, such as total reinjection in the Ngawha geothermal plant (NZ), and partial reinjection in the Wairakei-Tauhara geothermal plant (NZ), the reinjection flow rates can range from hundreds to thousands of tonnes per hour (Kaya et al. 2011). Depending on the geology of the reservoir, other factors such as reinjection well depths and pressures and reservoir volumes vary as well. These are usually less than about two thousand metres, dozens of bars and dozens to hundreds of cubic kilometres respectively (Miyazaki et al. 1990; Glover and Scott 2005; Kaya et al. 2011; Zarrouk and Moon 2013).

In the process of geothermal reinjection, the decrease in amorphous silica solubility due to cooling and loss of steam may cause deposition of silica which blocks the fluid pathways near the reinjection well.

To better understand the reinjection process as a problem of reactive transport, one can visualise a more complex but common case: blood is pumped by the heart though the blood vessels, exchanges mass with surrounding cells while transporting (unloading nutrients and loading waste), and eventually returns to the heart. This forms a closed circulatory system. In a geothermal cycle, the injected fluids containing chemical species are pumped out of the injection well, through the heat-extracting plant, and the cooled fluid (which may also have lost some water to the atmosphere as steam) is pumped back underground. There, it spreads to the surrounding reservoir via fracture networks, exchanges heat and mass, and may be extracted again by the extraction well at the far end to form a partially closed cycle.

To return to the analogy of the blood circulatory system, if blood carries too high concentrations of chemical species that may attach and accumulate on the surfaces of the blood vessels, blockages may form and become fatal. Similarly, for the geothermal reinjection process, the injectate is usually oversaturated with amorphous silica, due to loss of heat and of some water. The amorphous silica may form colloidal silica which may deposit on the surfaces of the fluid pathways in the reservoir. This will gradually increase the hydraulic resistance of the reinjection well. A gradually decline of performance of the re-injector Nag-67 in the Tiwi field, Philippines (Xu et al. 2004, shown in Figure 8.15), is a typical example for this:

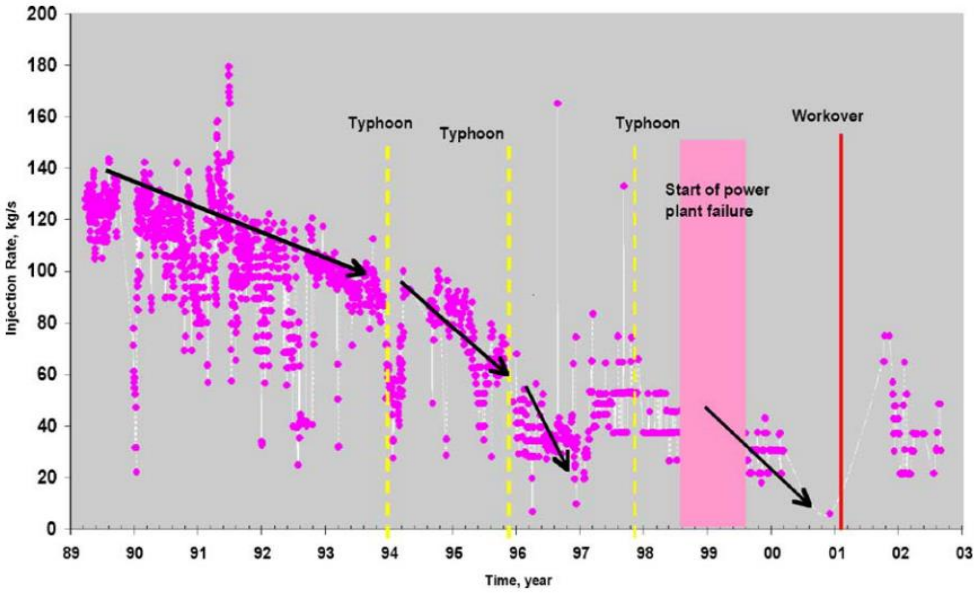

Figure 6.2: Historical records of injection rate decline of the injector Nag-67, reproduced from Xu et al. 2004. However, it should be noted that, depending on the wellhead pressure, a reduction in injection rate does not necessarily mean a reduction in injectivity.

Conventionally, the injectivity index II ($\mathrm{t\,hr^{-1}\,bar^{-1}}$) (Xu et al. 2004; Wong et al. 2016) is used to quantify the ease of geothermal reinjection, defined by:

$$II = \frac{\dot{m}}{P_{\mathrm{inj}} - P_{\mathrm{res}}} \tag{6.1}$$

where $\dot{m}$ is the injection mass flow rate, P_{inj} is the pressure of the injected fluid, and P_{res} is the far-field pressure of the reservoir.

Amorphous silica deposition will lead to an injectivity drop, i.e. it will become more and more difficult to inject fluids to the reservoir. Concretely, either P_{inj} will continuously increase if one attempts to maintain the injection mass flow rate while silica scaling occurs, or the injecting mass flow rate will decrease if P_{inj} is maintained.

It should be noted that when the well reaches some particular value of injectivity (not necessarily zero), the cost of carrying out a workover (physical and/or chemical processes to increase the number or size of fluid pathways near the well) or even drilling a new well will be economically favourable over the cost of upgrading the pumps to increase P_{inj}.

As the pore structure of fractured rock varies over a wide range, e.g. the pore size can vary from nanometres to centimetres, both Darcy's law and the Navier-Stokes equations are used to explain and predict the pressure drop along small pores and large apertures respectively.

6.1.1 Darcy's law: pressure drop along small pores

A widely-used classification of porosity was developed by (Choquette and Pray 1970), as shown in Figure 6.3.

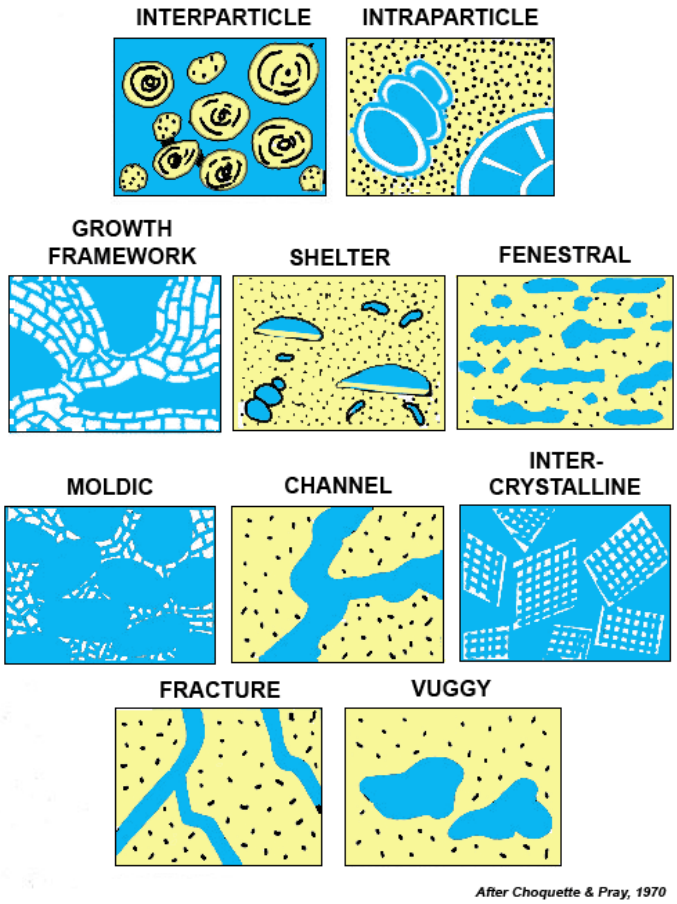

Figure 6.3: Classification of porosity, reproduced from Choquette and Pray 1970.

For porous media with high hydraulic connectivity, five of these types dominate: interparticle, (connected) growth framework, channel, intercrystalline, and fracture. These five types of porosity may not only exist individually but could combine in a heterogeneous system (e.g. fracture-channel).

When "microscopically" studying the reactive transport of the injectate, the Navier-Stokes equations will be used, provided the pores are wide enough (i.e. the Knudsen number is much less than one, which physically means that the mean free path of molecules in the fluid is insignificant compared to the size of the pores). When "macroscopically" considering the injectivity index of the reservoir, Darcy's law will be applied.

Conventionally, for underground fluid transport, flows are commonly classified into three basic types: planar, spherical, and radial.

1. Planar flows

For a line well pattern, which is a common network of extraction and injection wells in petroleum production, the flows among the wells are usually modelled as planar, as shown in Figure 6.4 below:

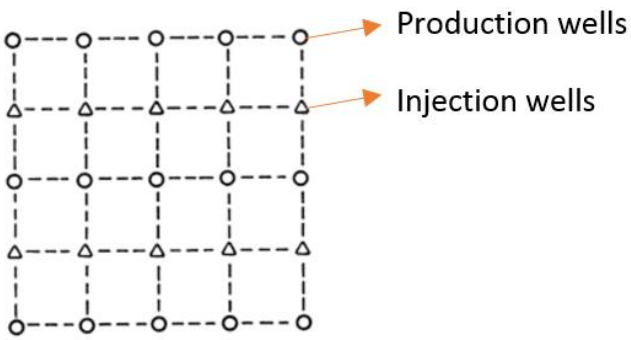

Figure 6.4: Line well pattern in petroleum production.

For planar flow, the pressure drop in the porous reservoir may be modelled by considering, a cylindrical sample of the porous media placed horizontally in a Cartesian coordinate system xyz, as shown in Figure 6.5.

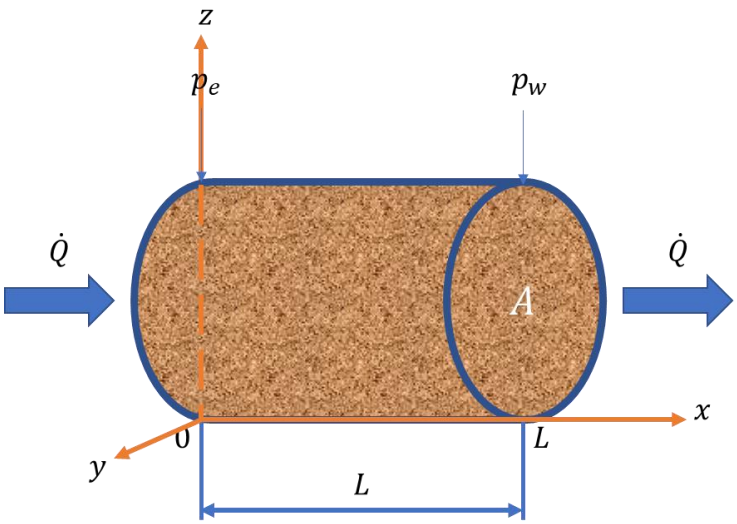

Figure 6.5: A cylinder sample of the porous media placed horizontally.

The length of the test section is L, and the area of cross-section is a constant A. The volumetric flow rate passing through the porous media $\dot{Q}$ is a constant. The boundary conditions at $x = 0$ and $x = L$ are expressed as:

$$p = p_e \quad \text{for} \quad x = 0; \tag{6.2}$$

$$p = p_w \quad \text{for} \quad x = L. \tag{6.3}$$

where p_e and p_w are the pressures at the inflow and outflow boundaries.

Consider a cubic control volume within the cylinder porous sample above, the continuity equation for a steady flow (i.e. $\partial\rho/\partial t = 0$, where ρ is the density of the fluid, and t is time) passing through the control volume can be represented by:

$$\frac{\partial(\rho v_x)}{\partial x} + \frac{\partial(\rho v_y)}{\partial y} + \frac{\partial(\rho v_z)}{\partial z} = 0; \tag{6.4}$$

When "macroscopically" considering the entire reservoir, the flow obeys Darcy's law:

$$v_x = -\frac{K}{\mu}\frac{\partial p}{\partial x}; \tag{6.5}$$

$$v_y = -\frac{K}{\mu}\frac{\partial p}{\partial y}; \tag{6.6}$$

$$v_z = -\frac{K}{\mu}\frac{\partial p}{\partial z}. \tag{6.7}$$

where K is the permeability of the porous media, and μ is the dynamic viscosity.

By combining Equation 6.5, 6.6, and 6.7, the following equation can be obtained:

$$\frac{\partial(-\rho\frac{K}{\mu}\frac{\partial \rho}{\partial x})}{\partial x} + \frac{\partial(-\rho\frac{K}{\mu}\frac{\partial \rho}{\partial y})}{\partial y} + \frac{\partial(-\rho\frac{K}{\mu}\frac{\partial \rho}{\partial z})}{\partial z} = 0; \tag{6.8}$$

By assuming $\rho, K,$ and μ to be constant, the governing equation for pressure can be derived:

$$\frac{\partial^2 p}{\partial x^2} + \frac{\partial^2 p}{\partial y^2} + \frac{\partial^2 p}{\partial z^2} = 0; \tag{6.9}$$

For a planar flow (i.e. $\partial v_y/\partial y = 0$ and $\partial v_z/\partial z = 0$), the governing equation Equation 6.9 can be simplified to:

$$\frac{d^2 p}{dx^2} = 0 \tag{6.10}$$

Using Equation 6.2 and 6.3 as the boundary conditions, the pressure along the axis x can be found by solving Equation 6.10:

$$p = p_e - \frac{p_e - p_w}{L}x \tag{6.11}$$

Therefore, according to Darcy's law, the volumetric flow rate $\dot{Q}$ can be defined as:

$$\dot{Q} = \frac{KA(p_e - p_w)}{\mu L} \tag{6.12}$$

By rearranging Equation 6.12, the pressure drop in a planar flow Δp_{pf} can be derived:

$$\Delta p_{pf} = \frac{\dot{Q}\mu}{KA}L \tag{6.13}$$

From Equation 6.9, 6.10, and 6.13, it can be seen that the pressure gradient is a constant, which is equal to $\frac{\dot{Q}\mu}{KA}$ and the pressure along the porous material is reducing linearly with distance.

2. Spherical flows

When the underground permeable zone (i.e. the reservoir) is partially drilled (see Figure 6.6 below), the injectate will spread spherically.

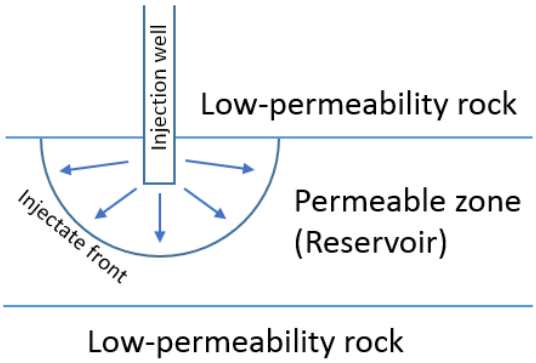

Figure 6.6: Spherical flows developed in the partially drilled reservoir.

Usually, this circumstance is modelled to be a fully drilled reservoir having an equivalent outflow boundary r_{we}, i.e. spherical flows are recognised as equivalent radial flows, which is discussed below. For the flow to be truly spherical, permeability must be constant with depth, and the injectate must be near neutral buoyancy.

3. Radial flows

Radial flows may be the most applicable model for geothermal reinjection (see Figure 6.7 below).

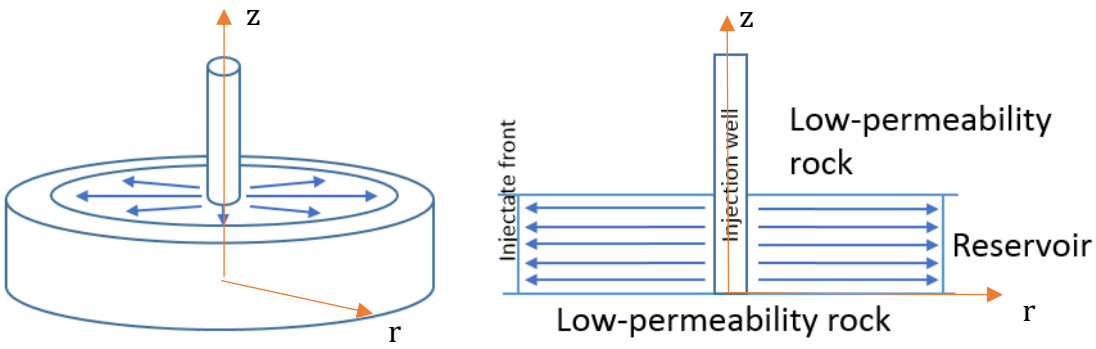

Figure 6.7: Radial flows developed in the fully drilled reservoir.

As the cylindrical coordinate above, the radial axis r starts from the centre of the injection wellbore. The thickness of the disk (i.e. the feedzone thickness) is H. The radial flow assumption allows the effect of impermeable horizontal strata to be modelled.

Consider a control volume ring from r_e to r_w. The boundary conditions can be expressed as:

$$p = p_e \quad \text{for} \quad r = r_e; \tag{6.14}$$

$$p = p_w \quad \text{for} \quad r = r_w. \tag{6.15}$$

Similarly, by coupling the continuity equation and Darcy's law, one can obtain the following governing equation for pressure:

$$\frac{d^2p}{dr^2} + \frac{1}{r}\frac{dp}{dr} = 0 \tag{6.16}$$

By solving Equation 6.16 using the boundary conditions Equation 6.14 and 6.15, the expression for the pressure along the radial axis can be derived:

$$p = p_e - \frac{p_e - p_w}{\ln \frac{r_e}{r_w}} \ln \frac{r_e}{r} \tag{6.17}$$

Therefore, by applying Darcy's law, the volumetric flow rate can be found:

$$\dot{Q} = \frac{2\pi KH(p_e - p_w)}{\mu \ln \frac{r_e}{r_w}} \tag{6.18}$$

By rearranging Equation 6.18, the pressure drop of radial flows Δp_{rf} is:

$$\Delta p_{rf} = \frac{\dot{Q}\mu \ln \frac{r_e}{r_w}}{2\pi KH} \tag{6.19}$$

In the case of spherical flows, the pressure drop of radial flows Δp_{sf} is represented by:

$$\Delta p_{sf} = \frac{\dot{Q}\mu \ln \frac{r_e}{r_{we}}}{2\pi KH} \tag{6.20}$$

With the pressure drop predicted by Darcy's law and the fixed mass flow rate, the injectivity can be easily computed.

According to Equation 6.1, 6.13, and 6.20, if the injecting flow rate and the fluid properties are fixed and the domain is well defined, the permeability K is the only parameter that will be affected by silica scaling through porosity.

6.1.2 Permeability drop due to scale plugging

Silica scaling has direct effects on porosity ($\emptyset$) as the accumulating deposits fill the pores. Porosity $\emptyset$ is defined in Equation 6.21 below:

$$\emptyset = \frac{V_{\text{pore}}}{V} \tag{6.21}$$

where V is the total volume of interested geometry, and V_{pore} is the volume of pores.

The plugging effect will cause a permeability drop due to increasing friction and even complete plugging of some narrower pores, which will lead an increasing pressure drop and eventually an injectivity decline over time.

Unfortunately, the relationship between permeability and porosity is complex as it is determined by many geometric parameters, such as the shapes, the size distribution, and the connectivity of the pores. Therefore, the correlation between permeability and porosity is expected to be site specific.

Vaughan (1985) investigated this problem by conducting a silica redistribution experiment in a granite rock core, and reported that a decrease in porosity of only 8% caused a 96% decline in permeability. Considering that, in this problem, the relative changes of porosity and permeability should be more important than an explicit correlation, Verma and Pruess (1988) studied this problem further based on the conceptual idea proposed by Wyble (1958) and introduced the following empirical expression:

$$\frac{K}{K_0} = (\frac{\emptyset - \emptyset_c}{\emptyset_0 - \emptyset_c})^q \tag{6.22}$$

where K_0 and $\emptyset_0$ are initial permeability and porosity respectively, $\emptyset_c$ is the critical porosity, which represents the porosity when the porous media is completely plugged (i.e. $K = 0$), and q is a power exponent. For different rock types and geothermal fields, different values of $\emptyset_c$ and q will be appropriate to compute the permeability change due to porosity change. For example, Verma and Pruess (1988) suggested that $\emptyset_c$ should be about $0.9\emptyset_0$ for all sandstones. In the work of Wong et al. 2016; Xu et al. (2004) arbitrarily assumed that $\emptyset_c$ ranges between $0.88\emptyset_0$ and $0.92\emptyset_0$, and q ranges between 2 and 13.

6.2 Geometry set up

Before looking into the transport of the silica particles, it is necessary to understand the hydrodynamics of the injecting process first. A simple idealised model is proposed as shown in Figure 6.8 below.

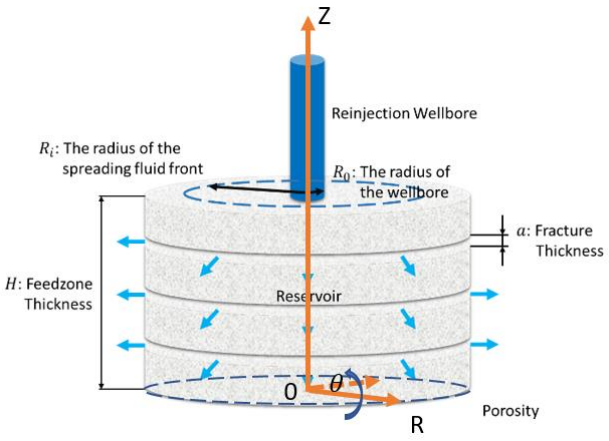

Figure 6.8: Simplified geometry consisting of injection wellbore and geothermal reservoir.

The blue cylinder in Figure 6.8 represents the injection wellbore, which is assumed to fully penetrate the domain. The cooled and separated geothermal fluid is reinjected through the wellbore walls at the mass flow rate $\dot{m}$, and is assumed to uniformly spread along horizontal fracture networks, which are homogeneously distributed (i.e. equally spaced) in the vertical direction. Therefore, the geometry is axis-symmetric with radial distance R from the wellbore. The reservoir is assumed both vertically and horizontally homogeneous, i.e. rock properties are constant over a certain range of depths z between an impermeable basement and cap rock, and do not vary with radial distance R. The model is clearly much simpler than real geothermal reservoirs, but serves to study the evolution of the silica.

In a fracture network, there may be preferential flow paths, which make a large contribution to the permeability despite forming a small fraction of the whole porosity. In the case of reinjection, the horizontal fractures are assumed to be the preferential flow paths, though these may account for a relatively small part of the whole porosity. As the horizontal width of the fracture is larger than the thickness of the aperture by orders of magnitude, the fracture network is treated as equivalent to two parallel flat plates (shown in Figure 6.9 below). Tortuosity of the fractures is neglected. Tortuosity increases pressure drop (Tsang 1984) and increases fracture surface area.

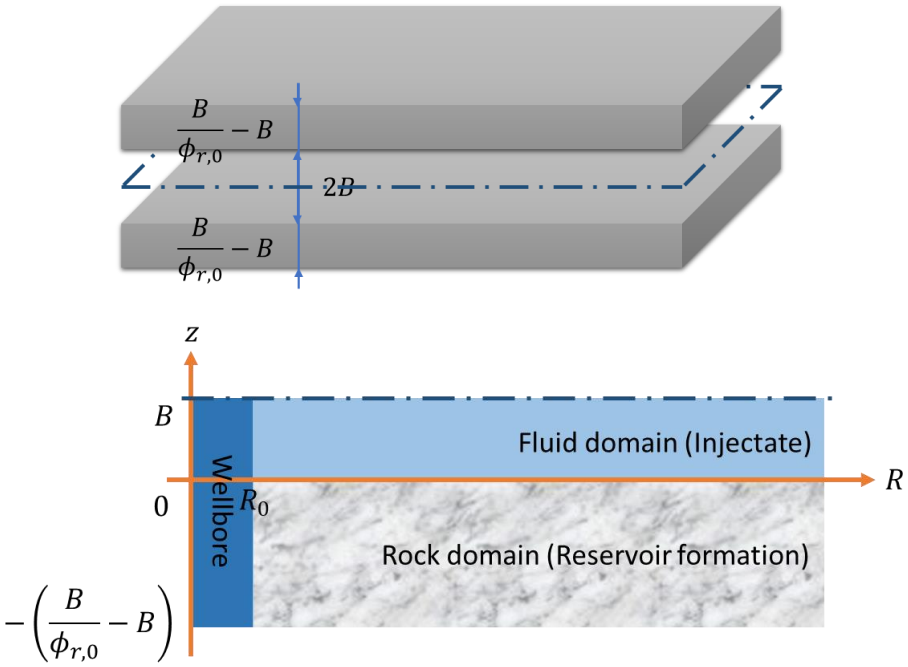

Figure 6.9: Parallel flat plate model showing the radial distance R, the aperture $2B$, and the thickness of one rock plate $\left(\frac{B}{\phi_{r,0}} - B\right)$, where $\phi_{r,0}$ is the initial porosity of the reservoir (not to scale).

Coincidentally, although the geometry shown above was developed independently, the author later found it had already been proposed as a feasible representative for geothermal reservoirs (Bodvarssonn and Tsang 1981).

As shown in Figure 4.2, the initial aperture is $2B$, and the total thickness of two-plate system (including the aperture) is $\frac{2B}{\phi_{r,0}}$. Hence, the thickness of one rock plate is $\left(\frac{B}{\phi_{r,0}} - B\right)$. As the geometry is symmetrical with respect to the centre plane, the rock domain occupies all space in the range of $R_0 \leq R \leq R_{max}$ and $-\left(\frac{B}{\phi_{r,0}} - B\right) \leq z \leq B$.

Theoretically, the reservoir formation may not be rigid and fixed. It could be deformed due to hydraulic pressure or seismic motion. Techniques such as hydraulic fracturing have been developed to increase the reservoir permeability. When injecting fluids into the reservoir, the formation of new fractures and pores may occur, and the pre-existing fluid pathways could become wider. When chemical reactions occur between fluid and rock, the boundary varies. For example, when conditions allow minerals to precipitate, over time, more and more scale can form. As the scale can be considered as a part of the reservoir formation, the interface will grow towards the fluid and the fracture will become narrower. Therefore, the fluid-rock interaction is essentially a moving boundary problem.

To simplify the problem, the reservoir formation is assumed to be static during each timestep. The geometry change due to the fluid-rock interaction is assumed to be negligible. The approach the thesis author selects is to ignore the boundary motion (and the resulting fluid acceleration and pressure terms) during the timestep, but to update the boundary position at the end of each timestep.

To study the problem numerically, the continuous time and space domains must be discretised to the computational grid, i.e. the mesh. Time is uniformly discretized by a constant time step $\mathrm{d}t$.

Since the geometry is quite simple and is assumed to be fixed, and the fluid and rock essentially occupy two adjacent fixed rectangular regions, the mesh is generated by simply discretising along the vertical and radial directions to N_{R} and $(N_{z_r} + N_{z_f})$ cells, where N_{R} is the quantity of the divided cells in the radial direction, and N_{z_r} and N_{z_f} are the quantity of the divided cells in the vertical direction of the rock and the fluid domains respectively. The geometry is therefore divided to $N_{\mathrm{R}}(N_{z_r} + N_{z_f})$ cells.

To minimise the computational cost but maximise the accuracy of the simulation results, the sizes of the cells $\mathrm{d}R$, dz_r, and dz_f may not be constant.

In the vertical direction, the mesh of the fluid domain should be finer near the fluid-rock interface as most of the heat and reactive mass transfer (such as calcite dissolution and colloidal silica deposition) occur near the fracture surface, and the vertical gradients in properties are large here. While the fluid transports between the rock plates, boundary layers form near the plates due to viscosity, which will have effects on the heat and mass transfer. Grids with a uniform z direction spacing may either hinder these effects if the mesh size is too large or waste computational power at the cells far away from the plate, where the effects of the boundary layers are negligible. On the other hand, the closer the silica particle comes to the collector (the rock plate), the more the interaction forces between the collector and the transporting mass (the colloidal silica) vary. Finer mesh near the plates is favoured.

On the other hand, the rock domain can be equally meshed, i.e. dz_r is a constant, as only heat conduction is considered and modelled in the rock domain. The equally meshed grids in the z direction can be safely used to save computational cost.

In the radial direction, while the injected fluids (usually cooler and more concentrated than the reservoir fluid) are spreading, there could be fronts where the gradients of temperature and concentration are maximum, and a higher mesh resolution is often required. These fronts are not fixed and can move further and further from the injection wellbore over time. Adaptive mesh refinement (AMR) may be of interest for this. AMR is a method of adapting higher resolution of mesh where necessary while the solutions are being calculated simultaneously. Applying this can reduce computational cost without affecting accuracy, however it can also significantly complicate the development of the modelling programme. Thus, in the present work the mesh size in the radial direction $\mathrm{d}R$ is kept constant, and $\mathrm{d}R$ is manually adjusted from coarse to fine, and the simulation is iterated till the results converge (i.e. not changing with further mesh refinement). Automatic iterations may be available in a future version of the holistic model.

To conveniently express the time, the spreading distance along the sub-horizontal fractures, and the vertical distance to the bottom plate, the following parameters are defined numerically.

For time:

$$t_k = (k-1)dt, \;\; 0 < k < N_t = \frac{t_{max}}{dt} \tag{6.23}$$

where k is the ordinal number of the present time step.

In the radial direction, recall that dR is constant:

$$R_i = R_{i-1} + dR, \quad 0 < i \leq N_{\mathrm{R}} \tag{6.24}$$

where i is the ordinal number of the present cell (i.e. the control volume) along the radial direction.

In the vertical direction of the rock domain, recall that dz_r is constant:

$$z_j = (j-1)dz_r - \left(\frac{B}{\phi_0^r} - B\right), \quad 0 < j \leq N_{z_r} = \frac{\frac{B}{\phi_0^r} - B}{dz_r} \tag{6.25}$$

where j is the ordinal number of the present cell along the vertical direction.

In the vertical direction of the fluid domain, recall that the mesh is finer near the fluid-rock interface and gradually becomes coarser in the vertical direction until the centre of the fracture is reached:

$$z_j = z_{\min}, \quad j = N_{z_f} \tag{6.26}$$

$$q_{z_f} = \frac{z_j}{z_{j-1}} = \left(\frac{B}{z_{\min}}\right)^{1/(N_{zf}-1)}, \quad N_{z_f} < j \leq (N_{z_r} + N_{z_f}) \tag{6.27}$$

$$z_j = z_{\min}\, q_{z_f}^{\,j-N_{z_f}-1}, \quad N_{z_f} < j \leq (N_{z_r} + N_{z_f}) \tag{6.28}$$

where $z_{\min}$ is the desired minimum cell size, and q_{z_f} is a common ratio.

Thus, by applying Equation 6.26-6.28, the mesh of the fluid domain can be generated. The method used in Equation 6.26-6.28 is commonly called inflation layer meshing.

The mean cross-section area of the fracture at the radial distance R, A_R, can be defined by Equation 6.29 according to the geometry set up shown in Figure 6.8 and Figure 6.9:

$$A_R = 2\pi R H \phi_{r,0} \tag{6.29}$$

At this stage, the geometry is fully defined.

6.3 Hydrodynamics

The hydrodynamics sub-model is used to find the velocity at which the fluid travels away from the wellbore, within the fractures (i.e. only valid in the fluid domain, $R_0 \leq R \leq R_{max}$ and $0 \leq z \leq B$). To study the hydrodynamics, consider the mass continuity equation first:

$$\frac{\partial \rho_f}{\partial t} + \nabla \cdot \boldsymbol{j}_f = 0 \tag{6.30}$$

where ρ_f is the density of the injectate, which is assumed to be equal to that of water under the same physical conditions, $\nabla \cdot$ is the divergence, $\boldsymbol{j}_f$ is the mass flux vector, and the term $\nabla \cdot \boldsymbol{j}_f$ is equal to $\frac{\partial j_{fx}}{\partial x} + \frac{\partial j_{fy}}{\partial y} + \frac{\partial j_{fz}}{\partial z}$ for Cartesian coordinates, $\frac{1}{R}\frac{\partial (R \cdot j_{fR})}{\partial r} + \frac{1}{R}\frac{\partial j_{f\theta}}{\partial \theta} + \frac{\partial j_{fz}}{\partial z}$ for cylindrical coordinates, and $\frac{1}{\mathrm{R}^2}\frac{\partial (\mathrm{R}^2 \cdot j_{fR})}{\partial \mathrm{r}} + \frac{1}{\mathrm{Rsin\theta}}\frac{\partial (\sin\theta \cdot j_{f\theta})}{\partial \theta} + \frac{1}{\mathrm{Rsin\theta}}\frac{\partial j_{f\varphi}}{\partial \varphi}$ for spherical coordinates, where j_f with different subscriptions is the mass flux with respect to the axis named by the subscription (say j_{fx} is the mass flux in the direction of the x-axis in Cartesian coordinates).

As the density of water changes modestly (e.g. decreasing by approximately 15.6% on heating from 952.8 kg m^{-3} at 155 ℃ to 803.7 kg m^{-3} 260 ℃ under 20 MPa (Keenan 1978)), there will be a flux from cell to cell as the water heats up, which can be modelled as a pressure, or as a volume flux due to change in volume. As the later method is more direct and easier to code, it will be used in the present work. This effect is modelled below, after the velocity distribution in the fracture is derived.

Hence, the mass continuity equation can be simplified to Equation 6.31:

$$\nabla \cdot \boldsymbol{j}_f = 0 \tag{6.31}$$

Equation 6.31 is equivalent to the following expression for cylindrical coordinates:

$$\frac{1}{R}\frac{\partial(R \cdot j_{fR})}{\partial R} + \frac{1}{R}\frac{\partial j_{f\theta}}{\partial \theta} + \frac{\partial j_{fz}}{\partial z} = 0 \tag{6.32}$$

Since the permeability of the rock between the adjacent fractures is assumed to be zero, i.e. no fluid can flow through the rock even under the effect of an infinitely high pressure gradient and the gravity effects are neglected, there is no mass transfer of the injectate (chemical species excluded, discussed in Section 6.4.3 and 6.5) in the z-axis, i.e. $j_{fz} = 0$. And since the geometry is axis-symmetrical and the fractures are vertically homogenously distributed, it is reasonable to assume:

$$\frac{\partial j_{f\theta}}{\partial \theta} = 0 \tag{6.33}$$

$$\frac{\partial j_{fz}}{\partial z} = 0 \tag{6.34}$$

Equation 6.32 can be simplified to:

$$\frac{1}{R}\frac{\partial(R \cdot j_{fR})}{\partial R} = 0 \tag{6.35}$$

By integrating Equation 6.35 over an arbitrary control volume i (in the range of $(R - dR/2)$ to $(R + dR/2)$, shown in Figure 6.10), one can find:

$$A_R|_{R=R-0.5dR} \cdot j_{fR}\big|_{R=R-0.5dR} = A_R|_{R=R+0.5dR} \cdot j_{fR}\big|_{R=R+0.5dR} \tag{6.36}$$

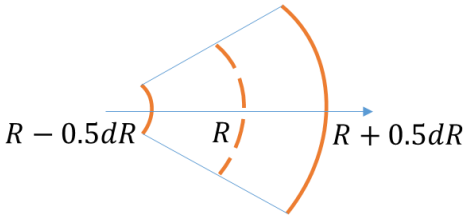

Figure 6.10: An arbitrary control volume of interest. Note: only a part of it is shown here as it is axis-symmetrical.

i.e. $\dot{m}_{out} = \dot{m}_{in} = \dot{m}$.

Since the mean velocity of the injectate can be related to the mass flux $\boldsymbol{j}$:

$$\boldsymbol{j} = \rho_f \boldsymbol{u}_f \tag{6.37}$$

where $\boldsymbol{u}_f$ is the velocity vector of the injectate, and ρ_f is assumed to be fixed in the present set of cells, one can find:

$$\dot{m} = A|_{R=R-0.5dR} \cdot u_{fR}\big|_{R=R-0.5dR} \cdot \rho_f = A|_{R=R+0.5dR} \cdot u_{fR}\big|_{R=R+0.5dR} \cdot \rho_f \tag{6.38}$$

Since R and dR are temporarily arbitrary in Equation 6.38, the formula above can be expressed in general:

$$u_{fRm} A_R \rho_f = \dot{m} \tag{6.39}$$

where A_R is Equation 6.39 in general forms.

Therefore, by coupling Equation 6.29 and 6.39, the spreading velocity (i.e. the mean velocity u_{Rm}) of the injectate in the radial direction can be expressed by:

$$u_{fRm} = \frac{\dot{m}}{A_R \rho_f} = \frac{\dot{m}}{2\pi R \mathrm{H} \phi_{r,0} \rho_f} \tag{6.40}$$

Consider the Reynolds number Re for parallel flat plates:

$$Re = \frac{2 u_{fRm} a_f}{\upsilon} \tag{6.41}$$

where, υ is the kinematic viscosity of the fluid. By comparing Re to the critical Reynolds number for flow in two parallel flate plates $Re_{crit} \approx 1400$, the flow regime in the fracture can be predicted. The present results show the flow to be laminar all along the fracture.

Since the mass and heat transfer under the effects of boundary layers are of interest, and the no-slip boundary condition is applied, so u_R varies in the z-direction.

In the case of the present work, by assuming the flow is fully developed after the inlet of the fracture, one can obtain the only one expression based on the continuity equation:

$$u_{fR} = u_{fR}(z) \tag{6.42}$$

The radial component of the Navier-Stokes momentum equation for the two-dimensional incompressible flow is:

$$\rho \left(u_{fR} \frac{\partial u_{fR}}{\partial R} + u_{fZ} \frac{\partial u_{fz}}{\partial z} \right) = -\frac{\partial p}{\partial R} + \rho_f g_R + \mu \left\{ \frac{\partial}{\partial R} \left[\frac{1}{R} \frac{\partial}{\partial R} \left(R u_{fR} \right) \right] + \frac{\partial^2 u_{fz}}{\partial z^2} \right\} \tag{6.43}$$

where u_{fz} is the velocity of the fluid in the z-axis, $\frac{\partial p}{\partial R}$ is the pressure gradient, which physically drives the flow, g_R is the gravitational acceleration with respect to the radial direction, which is zero, and μ is the dynamic viscosity of the fluid. One should note that this form assumes the Reynolds stresses are zero i.e. the flow is laminar, and that calculations of Re under typical geothermal flows shows the flow will always be laminar.

Since $u_{fz} = 0$ and $g_R = 0$, Equation 6.43 can be simplified to:

$$\mu \frac{\partial^2 u_{fR}}{\partial R^2} = \frac{\partial p}{\partial R} \tag{6.44}$$

According to the no-slip boundary condition: $u_{fR} = 0$ when $R = 0$ and $R = 2B$, the solution to Equation 6.44 can be obtained by integrating with respect to R twice:

$$u_{fR}(z) = -\frac{dp}{dR} \frac{B^2}{2\mu} \left(1 - \frac{(z-B)^2}{B^2} \right) \tag{6.45}$$

The maximum velocity $u_{fRmax} = -\frac{dp}{dx}\frac{B^2}{2\mu}$ occurs when $z = B$.

The average velocity, i.e. $u_m$in Equation 6.40, can be expressed with respect to the maximum velocity u_{fRmax}:

$$u_{fRm} = \frac{\dot{Q}}{A} = \frac{1}{A}\int u_{fR}\, dA = \frac{1}{b(2B)}\int_0^{2B} u_{fRmax}\left(1 - \frac{(z-B)^2}{B^2}\right) b\, dz = \frac{2}{3}u_{fRmax} \tag{6.46}$$

where *b* is the width of the fracture.

Hence, when the no-slip condition applies, the velocity profile can be eventually represented as:

$$u_{fR}(z) = \frac{3}{2}u_{fRm}\left(1 - \frac{(z-B)^2}{B^2}\right), \quad 0 \le z \le B \tag{6.47}$$

$$u_{fR}(z) = 0, \quad -\left(\frac{B}{\phi_{r,0}} - B\right) \le z \le 0 \tag{6.48}$$

Equation 6.47 is the cornerstone in the present work for studying the convective transport of mass and heat.

To handle this unsteady flow problem efficiently, it is assumed that the density change due to heat transfer in each control volume is instantaneous and vertically homogeneous. Therefore, the fluid in each cell is treated as incompressible and there is no mass flux in the z-axis due to the density change. The effects of density change due to heat transfer are discussed below.

One can visualise two sets of cells: one set of cells all at the same radial distance R_i and another set, upstream of and adjacent to the first, and all at the same radial distance R_{i-1}. The corresponding volumetric flow rates at the present and upstream sets of cells are $\dot{Q}_i$ and $\dot{Q}_{i-1}$ respectively. The densities of the injectate transporting from the upstream to the present cells are denoted as $\rho_{f,i-1}$ and $\rho_{f,i} = \rho_{f,i-1} + \Delta\rho_i$ separately, where $\Delta\rho_{f,i}$ is the density variation due to heat transfer (the difference of the average temperature between the upstream and the present cells) at the present cells. In the case of geothermal reinjection, $\Delta\rho_{f,i}$ is usually negative.

According to the conservation of mass, the following expression (Equation 6.49) can be found:

$$\rho_{f,i-1}\dot{Q}_{i-1} = \rho_{f,i}\dot{Q}_i \tag{6.49}$$

Recall Equation 6.46 that the mean fluid velocity $u_{fRm,i}$ at R_i can be defined by:

$$u_{fRm,i} = \dot{Q}_i / A_i \tag{6.50}$$

Thus, the expression for $u_{m,i}$ can be expressed in Equation 6.51 below when the density variation is taken into account:

$$u_{fRm,i} = \frac{\rho_{f,i-1}\dot{Q}_{i-1}}{\rho_{f,i}A_i} \tag{6.51}$$

If the mean cross-section area of the fracture near the present cells is a constant, i.e. $A_{i-1} = A_i$, the following correlations can be derived:

$$u_{fRm,i} = \frac{\rho_{f,i-1}}{\rho_{f,i}} u_{fRm,i-1} \tag{6.52}$$

and:

$$u_{fR,i}(z) = \frac{\rho_{f,i-1}}{\rho_{f,i}} u_{fR,i-1}(z) \tag{6.53}$$

In the case of geothermal reinjection, the fluid usually heats up along the fracture, hence one can find $\rho_{f,i-1} \geq \rho_{f,i}$, i.e. $\frac{\rho_{f,i-1}}{\rho_{f,i}} \geq 1$, $u_{fRm,i} \geq u_{fRm,i-1}$, and $u_{fR,i}(z) \geq \frac{\rho_{f,i-1}}{\rho_{f,i}} u_{fR,i-1}(z)$. The methodology used here suggests an accelerating effect of density drop due to heat transfer on the injectate as shown in Figure 6.11 below:

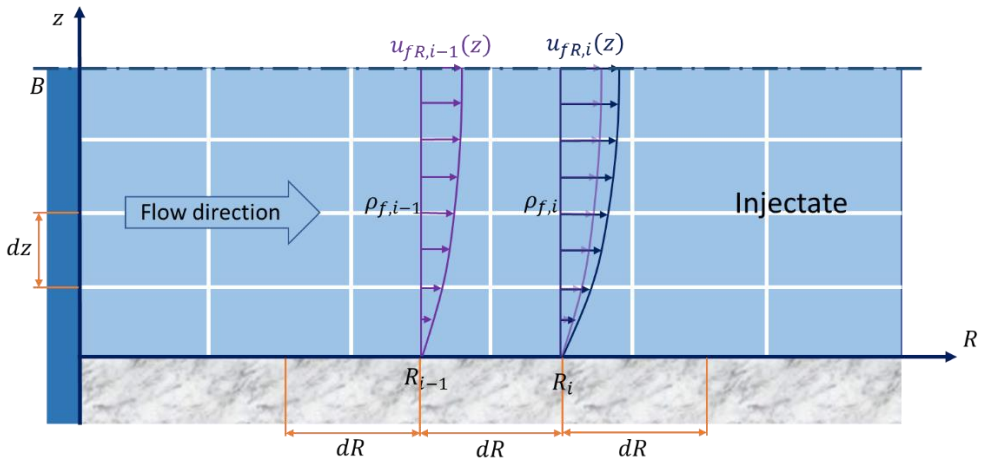

Figure 6.11: The accelerating effect of the density drop due to heat transfer.

Recall that the density change is assumed to be instantaneous. Therefore, the expected acceleration effect on $u_{fR}(z)$ should be instantaneous as well, and $u_{fR}(z)$ and u_{fRm} are treated as fixed in every set of cells.

6.4 Governing partial differential equations (PDEs) and discretisation schemes

The governing equation for the transient convection-diffusion heat and mass transfer is:

$$\frac{\partial(\rho\Phi)}{\partial t} + \nabla \cdot (\rho \boldsymbol{u}\Phi) = \nabla \cdot \Gamma \nabla\Phi + S \tag{6.54}$$

where, ρ is the density of the transferring mass, Φ represents a property such as temperature or species concentration, $\boldsymbol{u}$ is the velocity vector representing the convection induced by the flow, Γ is the diffusion coefficient, and S is a source or sink term. The physical meaning of each term in Equation 6.54 is the varying rate of Φ due to increment of time, convection, diffusion, and external effects, respectively. For the cylindrical coordinates, Equation 6.54 can be expanded in cylindrical coordinates to:

$$\begin{aligned} &\frac{\partial(\rho\Phi)}{\partial t} + \frac{1}{R}\frac{\partial}{\partial R}(Ru_R\Phi) + \frac{1}{R}\frac{\partial}{\partial\theta}(u_\theta\Phi) + \frac{\partial}{\partial z}(u_z\Phi) \\ &\quad = \frac{1}{R}\frac{\partial}{\partial R}\left(\Gamma_R R\frac{\partial\Phi}{\partial R}\right) + \frac{1}{R^2}\frac{\partial}{\partial\theta}\left(\Gamma_\theta\frac{\partial\Phi}{\partial\theta}\right) + \frac{\partial}{\partial z}\left(\Gamma_z\frac{\partial\Phi}{\partial z}\right) + S \end{aligned} \tag{6.55}$$

where u_R, u_θ, and u_z are the velocity components of $\boldsymbol{u}$ in the R, θ, and z directions respectively.

As the fluid is assumed to spread horizontally and homogenously, $\frac{\partial \Phi}{\partial \theta}$ is zero. Therefore, Equation 6.55 can be simplified to the two-dimensional form:

$$\frac{\partial(\rho\Phi)}{\partial t} + \frac{1}{R}\frac{\partial(R\rho\Phi u_R)}{\partial R} = \frac{1}{R}\frac{\partial}{\partial R}\Gamma R\frac{\partial \Phi}{\partial R} + \frac{\partial}{\partial z}\left(\Gamma\frac{\partial \Phi}{\partial z}\right) + S \tag{6.56}$$

The different expressions for each heat and mass transfer are discussed in detail in Section 4.3.1 - 4.3.2. Since the source terms require some detailed study each, these are discussed separately (see Section 6.5).

6.4.1 Heat transfer

In the case of reinjection, there will be convective heat transfer as the injectate is driven from the wellbore to the surrounding rock, and heat conduction between the injectate, the geothermal fluid initially contained in the fractures, and the rock.

Substituting the enthalpy (assuming no change in pressure) $cT = \Phi$, a set of coupled governing equations for heat transfer are obtained:

$$\frac{\partial(\rho cT)}{\partial t} + \frac{\rho c}{R}\frac{\partial(RTu_R)}{\partial R} = \frac{1}{R}\frac{\partial}{\partial R}k_h R\frac{\partial T}{\partial R} + \frac{\partial}{\partial z}\left(k_h\frac{\partial T}{\partial z}\right) + S \tag{6.57}$$

where c and k_h are the heat capacity and the thermal conductivity respectively, $c = c_r$ and $k_h = k_r$ for $-\left(\frac{B}{\phi_0^r} - B\right) \le z \le 0$, and $c = c_f$ and $k_h = k_f$ for $0 < z \le B$. According to Equation 6.48 ($u_R(z) = 0$ for $-\left(\frac{B}{\phi_0^r} - B\right) \le z \le 0$), one can easily find that there is no convective term in the governing equation for intra-rock heat transfer.

To solve Equation 6.57, the following boundary conditions are essential:

$$T|_{R=R_0} = T_{inj} \tag{6.58}$$

$$\frac{\partial T}{\partial R}|_{R=R_{max}} = 0 \tag{6.59}$$

$$\frac{\partial T}{\partial R}|_{z=B} = 0 \tag{6.60}$$

$$\frac{\partial T}{\partial R}|_{z=\frac{B}{\phi_0^r}-B} = 0 \tag{6.61}$$

The boundary condition Equation 6.58 represents the temperature at $R = R_0$ on the surface, which is equal to the temperature on the injection wellbore surface. The boundary condition Equation 6.59 for the far regions of the reservoir is treated as the outlet of the fluid and rock domains. The boundary conditions Equation 6.60 and 6.61 are defined thus as the fluid and rock domains shown in Figure 6.9 are symmetrical with respect to $z_f = B$ and $z_r = \frac{B}{\phi_0^r} - B$ seperately.

By integrating Equation 6.57 over a time step and over a control volume:

$$\int_t^{t+\Delta t}\int_{CV}\rho c\frac{\partial T}{\partial t}dVdt+\int_t^{t+\Delta t}\int_{CV}\frac{\rho c}{R}\frac{\partial(RTu_R)}{\partial R}dVdt$$
$$=\int_t^{t+\Delta t}\int_{CV}\frac{1}{R}\frac{\partial}{\partial R}k_hR\frac{\partial T}{\partial R}dVdt+\int_t^{t+\Delta t}\int_{CV}\frac{\partial}{\partial z}\left(k\frac{\partial T}{\partial z}\right)dVdt \quad (6.62)$$
$$+\int_t^{t+\Delta t}\int_{CV}S\,dVdt$$

For convenience, the arbitrary control volume shown in Figure 6.10 is replotted to Figure 6.12:

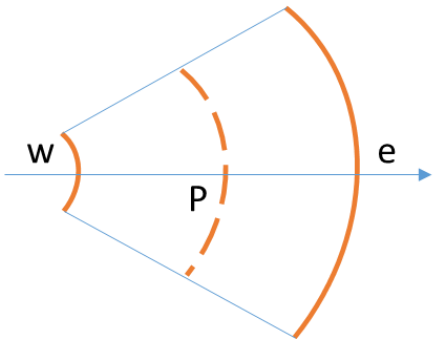

Figure 6.12: An arbitrary control volume, where "w", "P", and "e" in the figure stand for the west boundary at $(R-0.5dR)$, the present node at R, and the east boundary at $(R+0.5dR)$, respectively.

The corresponding properties at the west face, present position, and east face are differentiated with the subscription w, P, and e, respectively. Similarly, the nodes of the adjacent control volumes are marked with the subscription W and E as well.

The five terms in Equation 6.62 are separately derived as follows, and named the first, second, third, fourth and fifth terms, from left to right-hand side:

$$\int_t^{t+\Delta t}\int_{CV}\rho c\frac{\partial T}{\partial t}dVdt=\rho c(T_P-T_P^0)\Delta V\Delta t=\rho c(T_P-T_P^0)A_P\Delta R\Delta t \quad (6.63)$$

$$\int_t^{t+\Delta t}\int_{CV}\frac{\rho c}{R}\frac{\partial(RTu_R)}{\partial R}dVdt=\int_t^{t+\Delta t}[(\rho cu_RAT)_e-(\rho cu_RAT)_w]\,dt$$
$$=\int_t^{t+\Delta t}\rho c[(u_RAT)_e-(u_RAT)_w]\,dt$$
$$=\rho c\{\eta[(u_RAT)_e-(u_RAT)_w]_{t+\Delta t}+(1-\eta)[(u_RAT)_e-(u_RAT)_w]_t\}\Delta t \quad (6.64)$$
$$\xrightarrow{\eta=1,\text{ fully implicit}}$$
$$\rho c[(u_RAT)_e-(u_RAT)_w]\Delta t=\rho c(u_{Re}A_eT_e-u_{Rw}A_wT_w)\Delta t$$

$$\int_t^{t+\Delta t}\int_{CV}\frac{1}{R}\frac{\partial}{\partial R}k_h R\frac{\partial T}{\partial R}dVdt=\int_t^{t+\Delta t}\left[\left(k_hA\frac{\partial T}{\partial R}\right)_e-\left(k_hA\frac{\partial T}{\partial R}\right)_w\right]dt$$

$$=\int_t^{t+\Delta t}\left(k_{h,e}A_e\frac{T_E-T_P}{\delta R_{PE}}-k_{h,w}A_w\frac{T_P-T_W}{\delta R_{WP}}\right)dt \tag{6.65}$$

$$\xrightarrow{\eta=1,\text{ fully implicit}}$$

$$(k_{h,e}A_e\frac{T_E-T_P}{\delta R_{PE}}-k_{h,w}A_w\frac{T_P-T_W}{\delta R_{WP}})\Delta t$$

$$\int_t^{t+\Delta t}\int_{CV}\frac{\partial}{\partial z}\left(k\frac{\partial T}{\partial z}\right)dVdt=\int_t^{t+\Delta t}\left[\left(k_hA\frac{\partial T}{\partial R}\right)_n-\left(k_hA\frac{\partial T}{\partial R}\right)_s\right]dt$$

$$=\int_t^{t+\Delta t}\left(k_{h,n}A_n\frac{T_N-T_P}{\delta z_{PN}}-k_{h,s}A_s\frac{T_P-T_S}{\delta z_{SP}}\right)dt \tag{6.66}$$

$$\xrightarrow{\eta=1,\text{ fully implicit}}$$

$$(k_{h,n}A_n\frac{T_N-T_P}{\delta z_{PN}}-k_{h,s}A_s\frac{T_P-T_S}{\delta z_{SP}})\Delta t$$

$$\int_t^{t+\Delta t}\int_{CV}S\,dVdt=\bar{S}A_P\Delta R\Delta t \tag{6.67}$$

By summing the right-hand sides, one can find:

$$\begin{aligned}\rho c(T_P-T_P^0)A_P\Delta R+\rho c(u_{Re}A_eT_e-u_{Rw}A_wT_w)\Delta t\\ =k\left(A_e\frac{T_E-T_P}{\delta R_{PE}}-A_w\frac{T_P-T_W}{\delta R_{WP}}\right)\Delta t\\ +k\left(A_n\frac{T_N-T_P}{\delta z_{PN}}-A_s\frac{T_P-T_S}{\delta z_{SP}}\right)\Delta t+\bar{S}A_P\Delta R\Delta t\end{aligned} \tag{6.68}$$

where $A_P=2\pi Ra$, $A_e=2\pi R_e a=2\pi(R+\Delta R/2)a$, $A_w=2\pi R_w a=2\pi(R-\Delta R/2)a$, $A_n=A_s=\pi R_e^2-\pi R_w^2=2\pi R\Delta R=\Delta RA_P/a$.

According to the continuity equation, one can obtain $u_{Re}A_e=u_RA_P=u_{Rw}A_w$. Hence, the following correlation can be derived:

$$u_R=u_{Re}A_e/A_P=u_{Rw}A_w/A_P \tag{6.69}$$

By substituting Equation 6.69 to 6.68 and then divided by $A_P\Delta t$, the following formula can be found:

$$\frac{\rho c(T_P - T_P^0)\Delta R}{\Delta t} + \rho c u_R (T_e - T_w) = \frac{k}{\Delta R}\frac{R_e}{R_P}(T_E - T_P) - \frac{k}{\Delta R}\frac{R_w}{R_P}(T_P - T_W) + \frac{k_h}{\Delta z}\frac{\Delta R}{a}(T_N - T_P) - \frac{k_h}{\Delta z}\frac{\Delta R}{a}(T_P - T_S) + \bar{S}\Delta R \tag{6.70}$$

For simplicity, the following coefficients are defined:

$$a_P^0 = \frac{\rho c \Delta R}{\Delta t} \tag{6.71}$$

$$F_e = F_w = \rho c u_R \tag{6.72}$$

$$F_n = F_s = 0 \tag{6.73}$$

$$D_e = \frac{k_h}{\Delta R}\frac{R_e}{R} \tag{6.74}$$

$$D_w = \frac{k_h}{\Delta R}\frac{R_w}{R} \tag{6.75}$$

$$D_n = D_s = \frac{k_h}{\Delta z}\frac{\Delta R}{a} \tag{6.76}$$

Equation 6.70 is simplified to:

$$a_P^0(T_P - T_P^0) + F_e T_e - F_w T_w = D_e(T_E - T_P) - D_w(T_P - T_W) + D_n(T_N - T_P) - D_s(T_P - T_S) + \bar{S}\Delta R \tag{6.77}$$

To solve the formula above, discretisation algorithms that can handle the correlation between the properties at the cell faces and those at the cell nodes must be adopted: for instance, in the case of 2D simulation, there are four parameters at the cell faces: Φ_e, Φ_w, Φ_n, and Φ_s. Fortunately, according to Equation 6.77, only Φ_e and Φ_w (specifically, T_e and T_w in the heat transfer modelling) require attention as the convection only occurs horizontally in the fluid domain. However, this is not true for colloidal silica mass transport, which is discussed in Section 6.6.

6.4.2 Discretisation schemes

Although only T_e and T_w are temporarily of interest, the properties at cell faces in all directions are discussed below. There are several discretisation schemes which may be used to represent T_e, T_w, T_n, and T_s, such as the central differencing scheme, the upwind differencing scheme, the hybrid differencing scheme (Spalding 1970), QUICK scheme (Leonard 1979), and others.

6.4.2.1 The central differencing scheme

For the central differencing scheme, the properties on the boundaries of the cell Φ_e, Φ_w, Φ_n, and Φ_s can be related to the properties of the present node Φ_P and the nodes of the adjacent cells Φ_E, Φ_W, Φ_N, and Φ_S:

$$\Phi_e = \frac{\Phi_P + \Phi_E}{2} \tag{6.78}$$

$$\Phi_w = \frac{\Phi_W + \Phi_P}{2} \tag{6.79}$$

$$\Phi_n = \frac{\Phi_P + \Phi_N}{2} \tag{6.80}$$

$$\Phi_s = \frac{\Phi_S + \Phi_P}{2} \tag{6.81}$$

By combining Equation 6.71-6.81 (Φ_e, Φ_w, Φ_n, and Φ_s in Equation 6.71-6.81 are replaced by T_e, T_w, T_n, and T_s), Equation 6.77 can be rearranged to:

$$a_P T_P = a_W T_W + a_E T_E + a_S T_S + a_N T_N + a_P^0 T_P^0 + S_u \tag{6.82}$$

where $a_P = a_W + a_E + a_S + a_N + a_P^0 + \Delta F - S_P$, $\Delta F = F_e - F_w + F_e - F_w$, and $\bar{S}\Delta R = S_u + S_P T_P$; for the internal nodes (the nodes that are not the first and the last, i.e. the domain boundaries are not the faces of the control volumes): $a_W = D_w + F_w/2$, $a_E = D_e - F_e/2$, $a_N = D_n - F_n/2$, $a_S = D_s + F_s/2$, $S_P = 0$, and $S_u = \bar{S}\Delta R$.

For the cells at the west boundary except for the north-west and south-west corners, since the boundary condition is $T|_{R=R_0} = T_{inj}$:

$$\mathrm{T}_w = \mathrm{T}_{inj} \tag{6.83}$$

Thus, $a_W = 0$, $a_E = D_e - F_e/2$, $a_N = D_n - F_n/2$, $a_S = D_s + F_s/2$, $S_P = -(2D_w + F_w)$, and $S_u = (2D_w + F_w)T_{inj} + \bar{S}\Delta R$.For the cells at the east boundary except for the north-east and south-east corners, since the boundary condition is $\frac{\partial T}{\partial R}|_{R=R_{max}} = 0$, it can be deduced that:

$$\mathrm{T}_e = \mathrm{T}_P \tag{6.84}$$

thus $a_W = D_w + F_w/2$, $a_E = 0$, $a_N = D_n - F_n/2$, $a_S = D_s + F_s/2$, $S_P = 0$, and $S_u = \bar{S}\Delta R$.

For the cells at the north boundary except the north-west and north-east corners, since the boundary condition is $\frac{\partial T}{\partial R}|_{z=B} = 0$, it can be deduced that:

$$\mathrm{T}_n = \mathrm{T}_P \tag{6.85}$$

thus $a_W = D_w + F_w/2$, $a_E = D_e - F_e/2$, $a_N = 0$, $a_S = D_s + F_s/2$, $S_P = 0$, and $S_u = \bar{S}\Delta R$.

For the cells at the south boundary except for the south-west and south-east corners, since the boundary condition is $\frac{\partial T}{\partial R}|_{z=\frac{B}{\phi_0^r}-B} = 0$, it can be deduced that:

$$\mathrm{T}_s = \mathrm{T}_P \tag{6.86}$$

thus $a_W = D_w + F_w/2$, $a_E = D_e - F_e/2$, $a_N = D_n - F_n/2$, $a_S = 0$, $S_P = 0$, and $S_u = \bar{S}\Delta R$.

At the north-east corner, there are two boundary conditions (Equation 6.84 and 6.85) applied to the cell, thus $a_W = D_w + F_w/2$, $a_E = 0$, $a_N = 0$, $a_S = D_s + F_s/2$, $S_P = 0$, and $S_u = \bar{S}\Delta R$.

At the north-west corner, there are two boundary conditions (Equation 6.83 and 6.85) applied to the cell, thus $a_W = 0$, $a_E = D_e - F_e/2$, $a_N = 0$, $a_S = D_s + F_s/2$, $S_P = -(2D_w + F_w)$, and $S_u = (2D_w + F_w)T_{inj} + \bar{S}\Delta R$.

At the south-east corner, there are two boundary conditions (Equation 6.84 and 6.86) applied to the cell, thus $a_W = D_w + F_w/2$, $a_E = 0$, $a_N = D_n - F_n/2$, $a_S = 0$, $S_P = 0$, and $S_u = \bar{S}\Delta R$.

At the south-west corner, there are two boundary conditions (Equation 6.83 and 6.86) applied to the cell, thus $a_W = 0$, $a_E = D_e - F_e/2$, $a_N = D_n - F_n/2$, $a_S = 0$, $S_P = -(2D_w + F_w)$, and $S_u = (2D_w + F_w)T_{inj} + \bar{S}\Delta R$.

6.4.2.2 The upwind differencing scheme

For the upwind differencing scheme, if the present node P is the upstream node of the node E and N, and the node W and S are the upstream nodes of the node P, the correlations are defined by:

$$\Phi_e = \Phi_P \tag{6.87}$$

$$\Phi_w = \Phi_W \tag{6.88}$$

$$\Phi_n = \Phi_P \tag{6.89}$$

$$\Phi_s = \Phi_S \tag{6.90}$$

Otherwise, if the present node P is the upstream node of the node W and S, and the node E and N are the upstream nodes of the node P, the correlations are defined by:

$$\Phi_w = \Phi_P \tag{6.91}$$

$$\Phi_e = \Phi_E \tag{6.92}$$

$$\Phi_s = \Phi_P \tag{6.93}$$

$$\Phi_n = \Phi_N \tag{6.94}$$

If the case of the reverse flow (fluid flows from the node E to the node W, i.e. $u_e < 0$, $u_w < 0$, $u_n < 0$ and $u_s < 0$) is not considered, by combining Equation 6.71 - 6.77, and 6.87-6.90 (Φ_e, Φ_w, Φ_n, and Φ_s in Equation 6.87-6.90 are replaced by T_e, T_w, T_n, and T_s), Equation 6.77 can be rearranged to:

$$a_P T_P = a_W T_W + a_E T_E + a_S T_S + a_N T_N + a_P^0 T_P^0 + S_u \tag{6.95}$$

where $a_P = a_W + a_E + a_S + a_N + a_P^0 + \Delta F - S_P$, $\Delta F = F_e - F_w + F_e - F_w$, and $\bar{S}\Delta R = S_u + S_P T_P$; for the internal nodes: $a_W = D_w + F_w$, $a_E = D_e$, $a_N = D_n + F_n$, $a_S = D_s$, $S_P = 0$, and $S_u = \bar{S}\Delta R$.

Equation 6.83-6.86 are still applicable. Therefore, for the cells at the west domain boundary except for the north-west and south-west corners: $a_W = 0$, $a_E = D_e$, $a_N = D_n + F_n$, $a_S = D_s$, $S_P = -(2D_w + F_w)$, and $S_u = (2D_w + F_w)T_{inj} + \bar{S}\Delta R$;

for the cells at the east domain boundary except the north-east and south-east corners: $a_W = D_w + F_w$, $a_E = 0$, $a_N = D_n + F_n$, $a_S = D_s$, $S_P = 0$, and $S_u = \bar{S}\Delta R$; $a_W = D_w + F_w$, $a_E = D_e$, $a_N = D_n + F_n$, $a_S = D_s$, $S_P = 0$, and $S_u = \bar{S}\Delta R$;

for the cells at the north domain boundary except the north-west and north-east corners: $a_W = D_w + F_w$, $a_E = D_e$, $a_N = 0$, $a_S = D_s$, $S_P = 0$, and $S_u = \bar{S}\Delta R$;

for the cells at the south domain boundary except the south-west and south-east corners: $a_W = D_w + F_w$, $a_E = D_e$, $a_N = D_n + F_n$, $a_S = 0$, $S_P = 0$, and $S_u = \bar{S}\Delta R$;

at the north-east corner: $a_W = D_w + F_w$, $a_E = 0$, $a_N = 0$, $a_S = D_s$, $S_P = 0$, and $S_u = \bar{S}\Delta$;

at the north-west corner: $a_W = 0$, $a_E = D_e$, $a_N = 0$, $a_S = D_s$, $S_P = -(2D_w + F_w)$, and $S_u = (2D_w + F_w)T_{inj} + \bar{S}\Delta R$;

at the south-east corner: $a_W = D_w + F_w$, $a_E = 0$, $a_N = D_n + F_n$, $a_S = 0$, $S_P = 0$, and $S_u = \overline{S}\Delta R$;

and at the south-west corner: $a_W = 0$, $a_E = D_e$, $a_N = D_n + F_n$, $a_S = 0$, $S_P = -(2D_w + F_w)$, and $S_u = (2D_w + F_w)T_{inj} + \overline{S}\Delta R$.

6.4.2.3 The hybrid differencing scheme

The hybrid differencing scheme is a combination of the central differencing scheme and the upwind differencing scheme. To decide which one is applicable, the non-dimensional Peclet number is introduced, which compares the effects of convection and diffusion:

$$Pe = \frac{F}{D} = \frac{\rho u}{\Gamma/\delta x} \tag{6.96}$$

The former applies when $Pe < 2$, and the latter is used and diffusion is ignored (i.e. setting $D_w = D_e = D_n = D_s = 0$) if when $Pe \geq 2$. In applying this scheme, it is not necessary to calculate the Peclet number. The discretisation coefficients a_W, a_E, a_N and a_S can be decided by simply comparing $[\, F_w, \left(D_w + \frac{F_w}{2}\right), 0\,]$, $[\, -F_e, \left(D_e - \frac{F_e}{2}\right), 0\,]$, $[\, -F_n, \left(D_n - \frac{F_n}{2}\right), 0\,]$, and $[F_s, \left(D_s + \frac{F_s}{2}\right), 0]$, and choosing the maximum value among the three as a_W, a_E, a_N and a_S, respectively. The zero for a_W and a_S, $-F_e$ for a_E, and $-F_n$ are set for the case when the reverse flow presents.

Hence, if the case of the reverse flow is not considered, by combining the descriptions above, Equation 6.77 can be rearranged to:

$$a_P T_P = a_W T_W + a_E T_E + a_S T_S + a_N T_N + a_P^0 T_P^0 + S_u \tag{6.97}$$

where $a_P = a_W + a_E + a_S + a_N + a_P^0 + \Delta F - S_P$, $\Delta F = F_e - F_w + F_e - F_w$, and $\overline{S}\Delta R = S_u + S_P T_P$; for the internal nodes: $a_W = \max[F_w, \left(D_w + \frac{F_w}{2}\right)]$, $a_E = \max[\left(D_e - \frac{F_e}{2}\right), 0]$, $a_N = \max[\left(D_n - \frac{F_n}{2}\right), 0]$, $a_S = \max[F_s, \left(D_s + \frac{F_s}{2}\right)]$, $S_P = 0$, and $S_u = \overline{S}\Delta R$.

And, for the first control volume: $a_W = 0$, $a_E = \max[-F_e, \left(D_e - \frac{F_e}{2}\right), 0]$, $S_P = -(2D_w + F_w)$, and $S_u = (2D_w + F_w)T_A + \overline{S}\Delta R$; and for the last control volume: $a_W = \max[F_w, \left(D_w + \frac{F_w}{2}\right), 0]$, $a_E = 0$, $S_P = 0$, and $S_u = \overline{S}\Delta R$.

Still, Equation 6.83-6.86 are applicable. Therefore, for the cells at the west domain boundary except for the north-west and south-west corners: $a_W = 0$, $a_E = \max[-F_e, \left(D_e - \frac{F_e}{2}\right), 0]$, $a_N = \max[\left(D_n - \frac{F_n}{2}\right), 0]$, $a_S = \max[F_s, \left(D_s + \frac{F_s}{2}\right)]$, $S_P = -(2D_w + F_w)$, and $S_u = (2D_w + F_w)T_{inj} + \overline{S}\Delta R$;

for the cells at the east domain boundary except for the north-east and south-east corners: $a_W = \max[F_w, \left(D_w + \frac{F_w}{2}\right)]$, $a_E = 0$, $a_N = \max[\left(D_n - \frac{F_n}{2}\right), 0]$, $a_S = \max[F_s, \left(D_s + \frac{F_s}{2}\right)]$, $S_P = 0$, and $S_u = \overline{S}\Delta R$;

for the cells at the north domain boundary except the north-west and north-east corners: $a_W = \max[F_w, \left(D_w + \frac{F_w}{2}\right)]$, $a_E = \max[\left(D_e - \frac{F_e}{2}\right), 0]$, $a_N = 0$, $a_S = \max[F_s, \left(D_s + \frac{F_s}{2}\right)]$, $S_P = 0$, and $S_u = \overline{S}\Delta R$;

for the cells at the south domain boundary except for the south-west and south-east corners: $a_W = \max[F_w, \left(D_w + \frac{F_w}{2}\right)]$, $a_E = \max[\left(D_e - \frac{F_e}{2}\right), 0]$, $a_N = \max[\left(D_n - \frac{F_n}{2}\right), 0]$, $a_S = 0$, $S_P = 0$, and $S_u = \bar{S}\Delta R$;

at the north-east corner: $a_W = \max[F_w, \left(D_w + \frac{F_w}{2}\right)]$, $a_E = 0$, $a_N = 0$, $a_S = \max[F_s, \left(D_s + \frac{F_s}{2}\right)]$, $S_P = 0$, and $S_u = \bar{S}\Delta R$;

at the north-west corner: $a_W = 0$, $a_E = \max[\left(D_e - \frac{F_e}{2}\right), 0]$, $a_N = 0$, $a_S = \max[F_s, \left(D_s + \frac{F_s}{2}\right)]$, $S_P = -(2D_w + F_w)$, and $S_u = (2D_w + F_w)T_{inj} + \bar{S}\Delta R$;

at the south-east corner: $a_W = \max[F_w, \left(D_w + \frac{F_w}{2}\right)]$, $a_E = 0$, $a_N = \max[\left(D_n - \frac{F_n}{2}\right), 0]$, $a_S = 0$, $S_P = 0$, and $S_u = \bar{S}\Delta R$;

and at the south-west corner: $a_W = 0$, $a_E = \max[\left(D_e - \frac{F_e}{2}\right), 0]$, $a_N = \max[\left(D_n - \frac{F_n}{2}\right), 0]$, $a_S = 0$, $S_P = -(2D_w + F_w)$, and $S_u = (2D_w + F_w)T_{inj} + \bar{S}\Delta R$.

6.4.2.4 The QUICK scheme

The quadratic upstream interpolation for convective kinetics (QUICK) scheme estimates the values at cell faces by using the property at the node of interest Φ_i and the properties at the nearest two upstream nodes Φ_{i-1} and Φ_{i-2}.

If the present node P is the upstream node of the nodes E and N, the nodes W and S are the upstream nodes of the node P, the node WW is the upstream node of the node W, and the node SS is the upstream node of the node S, the correlations are defined by:

$$\Phi_w = \frac{6}{8}\Phi_W + \frac{3}{8}\Phi_P - \frac{1}{8}\Phi_{WW} \tag{6.98}$$

$$\Phi_e = \frac{6}{8}\Phi_P + \frac{3}{8}\Phi_E - \frac{1}{8}\Phi_W \tag{6.99}$$

$$\Phi_s = \frac{6}{8}\Phi_S + \frac{3}{8}\Phi_P - \frac{1}{8}\Phi_{SS} \tag{6.100}$$

$$\Phi_n = \frac{6}{8}\Phi_P + \frac{3}{8}\Phi_N - \frac{1}{8}\Phi_S \tag{6.101}$$

Otherwise, if the present node P is the upstream node of the node W and S, i.e. the case of reverse flow, the nodes E and N is the upstream nodes of the node P, the node EE is the upstream node of the node E, and the node NN is the upstream node of the node N, the correlations are defined by:

$$\Phi_w = \frac{6}{8}\Phi_P + \frac{3}{8}\Phi_W - \frac{1}{8}\Phi_E \tag{6.102}$$

$$\Phi_e = \frac{6}{8}\Phi_E + \frac{3}{8}\Phi_P - \frac{1}{8}\Phi_{EE} \tag{6.103}$$

$$\Phi_s = \frac{6}{8}\Phi_P + \frac{3}{8}\Phi_S - \frac{1}{8}\Phi_N \tag{6.104}$$

$$\Phi_n = \frac{6}{8}\Phi_N + \frac{3}{8}\Phi_P - \frac{1}{8}\Phi_{NN} \tag{6.105}$$

As this scheme involves the upstream nodes Φ_{i-1} and Φ_{i-2}, not only the cells at the boundaries but also the adjacent control volumes shall be treated differently. Therefore, if the case of reverse flow is excluded, by combining Equation 6.71-6.77, and 6.98-6.101 (Φ_e, Φ_w, Φ_n, and Φ_s in Equation 6.98-6.101 are replaced by T_e, T_w, T_n, and T_s), Equation 6.77 can be rearranged to:

$$a_P T_P = a_W T_W + a_E T_E + a_S T_S + a_N T_N + a_P^0 T_P^0 + S_u \tag{6.106}$$

where $a_P = a_W + a_E + a_S + a_N + a_P^0 + \Delta F - S_P$, $\Delta F = F_e - F_w + F_e - F_w$, and $\bar{S}\Delta R = S_u + S_P T_P$; for the internal nodes (the boundary cells and their respective adjacent cells are excluded): $a_W = D_w + F_w$, $a_E = D_e$, $a_S = D_s + F_s$, $a_N = D_n$, $S_P = 0$, and $S_u = \frac{1}{8}F_w(3T_P - 2T_W - T_{WW}) + \frac{1}{8}F_e(T_W - 2T_P - 3T_E) + \frac{1}{8}F_s(3T_P - 2T_S - T_{SS}) + \frac{1}{8}F_n(T_S - 2T_P - 3T_N) + \bar{S}\Delta R$.

For the cells at the west boundaries, the temperature at the east faces T_e can be found by Equation 6.58, but the temperature at the west faces T_w should be treated separately, as the respective upstream nodes T_W do not exist. A linear extrapolation method – the mirror node approach (Leonard 1979) can be used. It is suggested that a linear extrapolation can be defined to create a mirror node outside the domain at the same distance from the boundary node to the domain boundary $\delta x/2$, shown in Figure 6.13 below. The corresponding cell containing the mirror node is usually called the ghost cell.

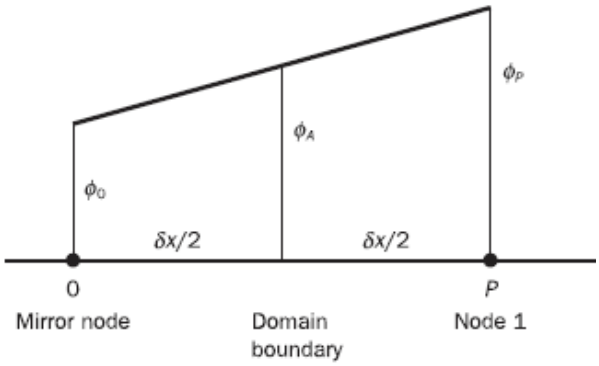

Figure 6.13: Schematic of the mirror node approach, reproduced from Versteeg and Malalasekera 2007.

The property at the mirror node Φ_0 is related to the properties at the first node Φ_1 and at the boundary Φ_A:

$$\Phi_0 = 2\Phi_A - \Phi_P \tag{6.107}$$

By substituting Equation 6.107 to 6.99, the following expression can be found:

$$\Phi_e = \frac{6}{8}\Phi_P + \frac{3}{8}\Phi_E - \frac{1}{8}(2\Phi_A - \Phi_P) = \frac{7}{8}\Phi_P + \frac{3}{8}\Phi_E - \frac{2}{8}\Phi_A \tag{6.108}$$

Similarly, for the south boundary, by considering $\Phi_S = \Phi_P$, the following expression can be found:

$$\Phi_n = \frac{5}{8}\Phi_P + \frac{3}{8}\Phi_N \tag{6.109}$$

For the east and north boundaries, Equation 6.85 and 6.86 are applicable.

As the discussion regarding the relevant cells is complicated, a plot is shown below to sketch all thirteen cases. Regions 1 to 6 may contain multiple cells each. Regions 7 to 15 are each a single cell.

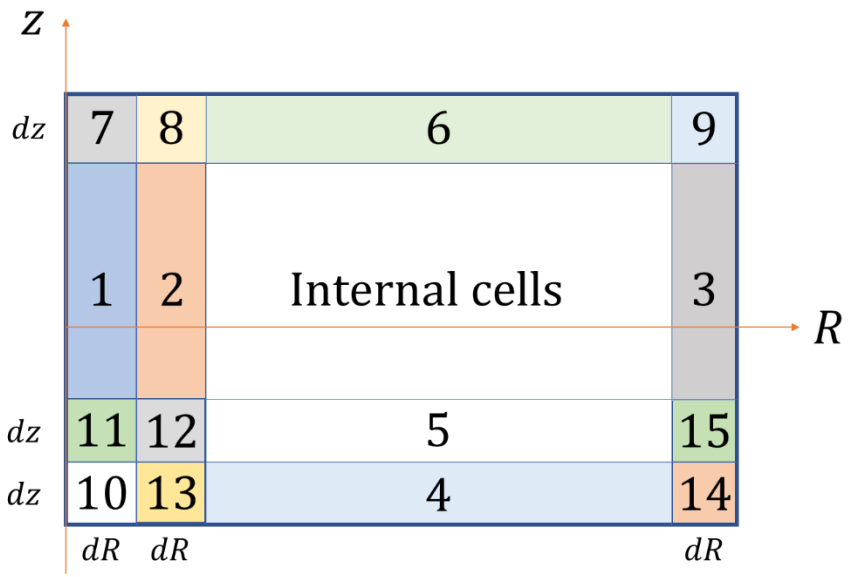

Figure 6.14: Discretised and numbered domain (not to scale).

Therefore, one can obtain:

In region 1, $a_W = 0$, $a_E = D_e + \frac{D_w}{3}$, $a_S = D_s + F_s$, $a_N = D_n$, $S_P = -(\frac{8}{3}D_w + F_w)$, and $S_u = \left(\frac{8}{3}D_w + F_w\right)T_{inj} + \frac{1}{8}F_e(\mathrm{T}_P - 3T_E) + \frac{1}{8}F_s(3T_P - 2T_S - T_{SS}) + \frac{1}{8}F_n(T_S - 2T_P - 3T_N) + \bar{S}\Delta R$;

In region 2: $a_W = D_w + F_w$, $a_E = D_e$, $a_S = D_s + F_s$, $a_N = D_n$, $S_P = 0$, and $S_u = \frac{1}{8}F_w(3T_P - T_W) + \frac{1}{8}F_e(T_W + 2T_P - 3T_E) + \frac{1}{8}F_s(3T_P - 2T_S - T_{SS}) + \frac{1}{8}F_n(T_S - 2T_P - 3T_N) + \bar{S}\Delta R$;

In region 3: $a_W = D_w + F_w$, $a_E = 0$, $a_S = D_s + F_s$, $a_N = D_n$, $S_P = 0$, and $S_u = \frac{1}{8}F_w(3T_P - 2T_W - T_{WW}) + \frac{1}{8}F_s(3T_P - 2T_S - T_{SS}) + \frac{1}{8}F_n(T_S - 2T_P - 3T_N) + \bar{S}\Delta R$;

In region 4: $a_W = D_w + F_w$, $a_E = D_e$, $a_S = 0$, $a_N = D_n + \frac{D_s}{3}$, $S_P = -(\frac{8}{3}D_s + F_s)$, and $S_u = \frac{1}{8}F_w(3T_P - 2T_W - T_{WW}) + \frac{1}{8}F_e(T_W - 2T_P - 3T_E) + \left(\frac{8}{3}D_s + F_s\right)T_P + \frac{1}{8}F_n(\mathrm{T}_P - 3T_N) + \bar{S}\Delta R$;

In region 5: $a_W = D_w + F_w$, $a_E = D_e$, $a_S = D_s + F_s$, $a_N = D_n$, $S_P = 0$, and $S_u = \frac{1}{8}F_w(3T_P - 2T_W - T_{WW}) + \frac{1}{8}F_e(T_W - 2T_P - 3T_E) + \frac{1}{8}F_s(3T_P - T_S) + \frac{1}{8}F_n(T_S + 2T_P - 3T_N) + \bar{S}\Delta R$;

In region 6: $a_W = D_w + F_w$, $a_E = D_e$, $a_S = D_s + F_s$, $a_N = 0$, $S_P = 0$, and $S_u = \frac{1}{8}F_w(3T_P - 2T_W - T_{WW}) + \frac{1}{8}F_e(T_W - 2T_P - 3T_E) + \frac{1}{8}F_s(3T_P - 2T_S - T_{SS}) + \bar{S}\Delta R$;

In region 7: $a_W = 0$, $a_E = D_e + \frac{D_w}{3}$, $a_S = D_s + F_s$, $a_N = 0$, $S_P = -(\frac{8}{3}D_w + F_w)$, and $S_u = \left(\frac{8}{3}D_w + F_w\right)T_{inj} + \frac{1}{8}F_e(\mathrm{T}_P - 3T_E) + \frac{1}{8}F_s(3T_P - 2T_S - T_{SS}) + \bar{S}\Delta R$;

In region 8: $a_W = D_w + F_w$, $a_E = D_e$, $a_S = D_s + F_s$, $a_N = 0$, $S_P = 0$, and $S_u = \frac{1}{8}F_w(3T_P - T_W) + \frac{1}{8}F_e(T_W + 2T_P - 3T_E) + \frac{1}{8}F_s(3T_P - 2T_S - T_{SS}) + \bar{S}\Delta R$;

In region 9: $a_W = D_w + F_w$, $a_E = 0$, $a_S = D_s + F_s$, $a_N = 0$, $S_P = 0$, and $S_u = \frac{1}{8}F_w(3T_P - 2T_W - T_{WW}) + \frac{1}{8}F_s(3T_P - 2T_S - T_{SS}) + \bar{S}\Delta R$;

In region 10: $a_W = 0$, $a_E = D_e + \frac{D_w}{3}$, $a_S = 0$, $a_N = D_n$, $S_P = -(\frac{8}{3}D_w + F_w) - (\frac{8}{3}D_s + F_s)$, and $S_u = \left(\frac{8}{3}D_w + F_w\right)T_{inj} + \frac{1}{8}F_e(\mathrm{T}_P - 3T_E) + \left(\frac{8}{3}D_s + F_s\right)T_P + \frac{1}{8}F_n(\mathrm{T}_P - 3T_N) + \bar{S}\Delta R$;

In region 11: $a_W = 0$, $a_E = D_e + \frac{D_w}{3}$, $a_S = D_s + F_s$, $a_N = D_n$, $S_P = -(\frac{8}{3}D_w + F_w)$, and $S_u = \left(\frac{8}{3}D_w + F_w\right)T_{inj} + \frac{1}{8}F_e(\mathrm{T}_P - 3T_E) + \frac{1}{8}F_s(3T_P - T_S) + \frac{1}{8}F_n(T_S + 2T_P - 3T_N) + \bar{S}\Delta R$;

In region 12: $a_W = D_w + F_w$, $a_E = D_e$, $a_S = D_s + F_s$, $a_N = D_n$, $S_P = 0$, and $S_u = \frac{1}{8}F_w(3T_P - T_W) + \frac{1}{8}F_e(T_W + 2T_P - 3T_E) + + \frac{1}{8}F_s(3T_P - T_S) + \frac{1}{8}F_n(T_S + 2T_P - 3T_N) + \bar{S}\Delta R$;

In region 13: $a_W = D_w + F_w$, $a_E = D_e$, $a_S = 0$, $a_N = D_n + \frac{D_s}{3}$, $S_P = -(\frac{8}{3}D_s + F_s)$, and $S_u = \frac{1}{8}F_w(3T_P - T_W) + \frac{1}{8}F_e(T_W + 2T_P - 3T_E) + \left(\frac{8}{3}D_s + F_s\right)T_P + \frac{1}{8}F_n(\mathrm{T}_P - 3T_N) + \bar{S}\Delta R$;

In region 14: $a_W = D_w + F_w$, $a_E = 0$, $a_S = D_s + F_s$, $a_N = D_n$, $S_P = 0$, and $S_u = \frac{1}{8}F_w(3T_P - 2T_W - T_{WW}) + \frac{1}{8}F_s(3T_P - T_S) + \frac{1}{8}F_n(T_S - 2T_P - 3T_N) + \bar{S}\Delta R$;

In region 15: $a_W = D_w + F_w$, $a_E = 0$, $a_S = 0$, $a_N = D_n$, $S_P = 0$, and $S_u = \frac{1}{8}F_w(3T_P - 2T_W - T_{WW}) + \left(\frac{8}{3}D_s + F_s\right)T_P + \frac{1}{8}F_n(T_S - 2T_P - 3T_N) + \bar{S}\Delta R$.

6.4.2.5 Assessments of the proposed discretisation schemes

At this stage, there are four potential discretisation schemes that can be used. A scheme must have three fundamental properties for the numerical results to be physically realistic: conservativeness, boundedness, and transportiveness.

Conservativeness requires that the flux of the property of interest Φ leaving from a control volume at a specific face is equal to the flux entering the adjacent control volume at the same face to ensure the conservation of the property Φ.

Boundedness requires that the property Φ at internal nodes should be limited by the values on the boundaries if there is no source term. For example, in the case of geothermal reinjection, the temperature of injectate should be in the range of 155 ℃ to 260 ℃ if the initial temperature of the injectate is 155 ℃ and the reservoir is 260 ℃. Boundedness also requires that all coefficients for the discretised equations (Equation 6.71 - 6.77) should be all positive or all negative, which physically means that the increment of the property Φ at one node should cause its increment at the adjacent nodes. The computed results will not converge, or will show large under and overshoots if the requirements of the boundedness are not met.

Transportiveness depends on the influences from the upstream node on the downstream node. For pure diffusion, i.e. $Pe \to 0$: the property at the present node Φ_P spreads equally in all directions (e.g. Φ_E and Φ_W) if the diffusion coefficient is a constant; and for pure convection, i.e. $Pe \to \infty$: the property at the present node Φ_P strongly affects the property at the downstream node Φ_E but is weakly impacted by the property at the upstream node Φ_W.

Based on these three fundamental properties, the discretisation schemes can then be compared and assessed. For simplicity, only one-dimensional parameters are mentioned for defining the properties.

1. For the central differencing scheme:

As the central differencing scheme adopts identical formulas to estimate the fluxes at the faces of the control volumes, the expression of the overall flux balance can be obtained easily. It can be shown that the fluxes moving through the faces cancel out in pairs, and there will be only boundary fluxes entering and leaving the domain, which reveals the conservativeness of the scheme.

Since the east coefficient is defined by $a_E = D_e - F_e/2$, it is possible that a_E becomes negative if F_e is big enough. Concretely, boundedness requires a_E to be positive, i.e. $F_e/D_e = Pe_e < 2$. If Pe_e does not satisfy the requirement, it will lead to unphysical solutions, such as large over- and undershoots.

The scheme considers the effects of all cells adjacent to the present control volume to find the convective and diffusive flux. It fails to deal with the direction of the flow and the strength of the convection flux with respect to diffusion. Therefore, the scheme loses the property of transportiveness once $Pe_e > 2$.

The central differencing scheme is second-order accurate.

Overall, the requirement for positive coefficients suggests that the central differencing scheme is stable only when $Pe_e < 2$, which as defined in Equation 6.96, is a function of density ρ, diffusion coefficient Γ, velocity u, and mesh size δx. If ρ and Γ are fixed, the condition is satisfied only either in low Reynolds number, diffusion dominated flows or when the mesh size is relatively small. Based on these conditions, the central differencing scheme is not appropriate for general fluid simulation.

2. For the upwind differencing scheme:

Similarly, the upwind differencing scheme estimates the fluxes at cell faces using consistent formulas. Thus, it can be easily found that the scheme is conservative.

The discretisation coefficients are positive at all times, which meets the condition of boundedness. The coefficient of the property at the present node becomes $a_P = a_E + a_W$, which leads to a diagonally dominant matrix of coefficients where all elements are positive. This is desirable, and under and overshoot will not be observed.

Since the upwind scheme recognises the direction of the flow, the requirement for transportiveness is met.

This scheme is first-order accurate.

Overall, the upwind differencing scheme is known to be not completely applicable for robust flow simulations. This is due to the inaccurate solutions which arise when the streamlines are not parallel to the mesh grids. It will hinder the transported properties and gives diffusion-like erroneous solutions, which is called false diffusion. This may not be the problem in our case though, as the problem is simplified to one-dimensional.

3. For the hybrid differencing scheme:

Since this scheme is a combination of the central differencing scheme and the upwind differencing scheme, it automatically switches to the latter once the former becomes inaccurate when $\mathrm{Pe} > 2$. Therefore, it inherits the desirable properties of both schemes. It is completely conservative, and unconditionally bounded. It meets the requirement of the transportiveness when convection is dominant.

Highly stable and physical results can be obtained by using the widely applied hybrid scheme, however it is only first-order accurate.

4. For the QUICK scheme:

Like the three schemes above, the QUICK scheme adopts consistent quadratic expressions. The conservativeness property is met.

However, the requirement of boundedness is not satisfied. Although, like an upwind stream, the coefficient of the property at the present node becomes $a_P = a_E + a_W$ when continuity is met (i.e. $\Delta \mathrm{F} = F_e - F_w = 0$), it is possible that the discretisation coefficients a_E and a_W are not positive; and a_{EE} and a_{WW} are negative. When the flow is in the positive direction (from the west to the east), once $F_e/D_e = Pe_e > 8/3$, a_E becomes negative, and unbounded solutions may arise. Hence, the QUICK scheme will be stable only under certain conditions.

The transportiveness is guaranteed as the scheme takes one downstream and two upstream nodes into account.

The QUICK scheme is third-order accurate.

To conveniently compare the advantages and disadvantages of the schemes discussed above, the properties are summarised in the table below:

Table 4.1: Summary of the important properties of the discretisation schemes

Scheme	Conserveness	Boundedness	Transportiveness	Accuracy
Central differencing	Yes	Only when $Pe_e < 2$	Only when $Pe_e < 2$	Second-order
Upwind differencing	Yes	Yes	Yes	First-order
Hybrid differencing	Yes	Yes	Yes	First-order
QUICK	Yes	Only when $Pe_e < 8/3$	Yes	Third-order

Considering that, in the case of geothermal reinjection, the domain will be kilometres in extent, and the simulation should be computationally affordable, it is best to set the mesh size as large as possible. Therefore, since the scheme with highest accuracy allows the larger mesh size, the QUICK scheme is preferred here.

At this stage, the governing equations of heat transfer Equation 6.57 can be solved.

6.4.2.6 Explicit and implicit schemes for unsteady problems

Since the problem is unsteady (i.e. time dependent), the change in the property Φ over one time step Δt can be derived by $\int_t^{t+\Delta t} \Phi \, dt \cong [\eta\Phi + (1-\eta)\Phi^0]\Delta t$, where η is the weighting coefficient, and Φ^0 represents the value of the property Φ at the previous time step.

By substituting $\eta = 0$, the expression above becomes $\int_t^{t+\Delta t} \Phi \, dt \cong \Phi^0 \Delta t$. This gives explicit discretisation. This backwards based scheme is first-order accurate with respect to time. As discussed above, boundedness requires all discretisation coefficients to be either positive or negative. If this backward explicit scheme is adopted, to meet the boundedness requirement, the time step must follow:

$$\Delta t < \frac{\rho c \Delta R^2}{2k} \tag{6.110}$$

Thus, it would be quite computationally expensive to increase the spatial accuracy, as the biggest time step should be reduced by ΔR^2 as well. Therefore, this scheme is not recommended.

The Crank-Nicolson method is obtained if $\eta = 0.5$, i.e. $\int_t^{t+\Delta t} \Phi \, dt \cong [(\Phi + \Phi^0)/2\,]\Delta t$. All schemes setting η in the range of 0.5 to 1 are unconditionally stable for any time step (Fletcher 1991). This scheme is developed based on the central differencing scheme, and hence it is second-order accurate. However, to ensure boundedness, the timestep must obey:

$$\Delta t < \frac{\rho c \Delta R^2}{k} \tag{6.111}$$

Despite a similar disadvantage to the preceding backwards-based scheme, Crank-Nicholson is normally used with the central differencing scheme as the accuracy of the scheme makes it more competitive.

By substituting $\eta = 1$, the fully implicit scheme gives $\int_t^{t+\Delta t} \Phi \, dt \cong \Phi \Delta t$. It is unconditionally stable and guarantees all discretisation coefficients positive. The scheme is only first-order accurate, thus a relatively small timestep is needed. Due to its robustness and stability, the fully implicit scheme is usually recommended for transient simulations as shown in Equation 6.64-6.66.

6.4.3 Mass transfer (colloidal silica excluded)

Depending on the particular case, there are about ten chemical species considered in the reactive mass transfer modelling, as described in Chapter 3. Apart from the importance of knowing the in-situ physical conditions (i.e. the temperature), knowing the in-situ chemical conditions (i.e. the concentrations of the species of interest) over time is critical as well. The concentrations of the species determine the kinetics of the reactive processes. For example, the transport of hydrogen ions (H^+) due to convection and diffusion plus the reaction with the minerals (only calcite being considered in this work) results in a spatial variation of pH. Apart from the temperature, the local pH, the local ionic strength (I), and the local concentration of monomeric silica (dissolved silica, $Si(OH)_4$) dominate the kinetics of silica polymerisation, as they influence the factors such as the surface tension and the degree of dissociation of the silanol groups ($-SiOH$); colloidal silica forms by silica polymerisation, and its surface charge and transport will be affected by the local pH and I as well. Hence, it is essential to model the reactive mass transfer of the chemical species to obtain the chemical conditions before investigating the silica deposition.

Since the transport of colloidal silica plays one of the most important roles in the formation of silica scale, and may be strongly influenced by the interactions between colloidal silica determined by the physical and chemical conditions (discussed in Section 6.4.1 and to be addressed the present section), the transport and the interactions of colloidal silica are separately discussed in Section 6.6.

The mathematical scheme used in mass transfer modelling for non-colloidal species is similar to those in heat transfer described above (Equation 6.57). Substituting $C = \rho\Phi$ into Equation 6.54, the mass transfer governing equation is obtained:

$$\frac{\partial C}{\partial t} + \frac{1}{R}\frac{\partial (RCu_R)}{\partial R} = \frac{1}{R}\frac{\partial}{\partial R}DR\frac{\partial C}{\partial R} + \frac{\partial}{\partial z}\left(D\frac{\partial C}{\partial z}\right) + S \tag{6.112}$$

where C represents the concentration of a species: for instance, hydrogen ion C_{H^+}, sodium ion C_{Na^+}, and dissolved silica C_{ds} (the subscript ds indicates monomeric silica or dissolved silica); D is the diffusion coefficient of the species of interest (such as D_{H^+}, D_{Na^+}, and D_{ds}); and S is the source or sink term of the species (such as S_{H^+}, S_{Na^+}, and S_{ds}).

The diffusion coefficients for ions are calculated from the Nernst formula:

$$D = \frac{RT\lambda}{|z|F^2} \tag{6.113}$$

where, R is gas constant, λ is the conductivity (S m^2 mol^{-1}), z is the valence of the ion (z = 1 for both hydrogen and sodium ions), and $F = 96485.33\ C\ mol^{-1}$ is the Faraday constant.

The conductivity λ can be defined by the following empirical expression (Wright 2007):

$$\lambda = (1.258T - 35.808 + (0.0044T + 0.8841)\,\lambda_0) \times 10^{-4} \tag{6.114}$$

where λ_0 is the reference conductivity of the ion of interest. The specific values are given in Appendix 4 at the end of this chapter.

The diffusion coefficient for other uncharged chemical species (assumed to be spherical) D is estimated by following the Stokes-Einstein equation:

$$D = \frac{k_B T}{6\pi\mu a} \tag{6.115}$$

where, k_B is Boltzmann's constant, μ is the dynamic viscosity of the fluid, and a is the hydrodynamic radius of the particle.

Rebreanu et al. (2008) measured the diffusion coefficient of monomeric silica D_{ds} in 10 mmol L^{-1} and 5 mmol L^{-1} potassium chloride solutions, at temperatures in the range of 275 K to 303 K, and at pH 8.1. A simpler formula (compared to Equation 6.115) was fitted to experimental data (Rebreanu et al. 2008):

$$D_{ds} = 3.33 \times 10^{-12}\frac{T}{10\mu} \tag{6.116}$$

where, the original proposed formula is $D_{ms} = 3.33 \times 10^{-12}T/\mu$ as the dynamic viscosity of the solution μ is in poise P, hence the coefficient 10 in Equation 6.116 is used to multiply μ to transfer the unit from Pa · s to P (1P = 0.1 Pa · s). The ionic strength and pH lie within the ranges found in geothermal aquifers, but the temperature does not since the geothermal temperature would be higher than the room temperature by one order of magnitude in ℃.

Therefore, it is an assumption that the expression above can be safely extrapolated to the geothermal conditions. This seems acceptable as the Stokes-Einstein equation leads one to expect the diffusion coefficient varies only with molecular size a, besides the parameters which appear in Equation 6.116.

The boundary conditions for the reactive mass transfer are set up as follows:

$$C|_{R=R_0} = C_0 \tag{6.117}$$

$$\frac{\partial C}{\partial R}|_{R=R_{max}} = 0 \tag{6.118}$$

$$\frac{\partial C}{\partial R}|_{z=B} = 0 \tag{6.119}$$

$$\frac{\partial C}{\partial R}|_{z=0} = 0 \tag{6.120}$$

By using similar procedures to those employed in Equation 6.62-6.77 for each species of interest and the QUICK scheme, and separately defining the source terms, the governing equations for the mass transfer Equation 6.112 can be solved.

6.5 Definition of source terms for the species involved in fluid-rock interactions

A source (or sink) term can be briefly defined as the net rate of creation (or destruction) of the property Φ within the control volume (Versteeg and Malalasekera 2007). Here, to simplify the problem, source terms are used to model the chemical reactions that create and destroy chemical species in the fluid domain and in the cells adjacent to the interface of the fluid and rock domain.

The kinetics of the reactive processes is covered in Chapter 4 and Chapter 5. A chemistry model was proposed. Figure 3.4 sets out the workflow of the chemistry model.

In each timestep dt, the chemistry model first receives the in situ conditions from either the pre-processed inputs (i.e. the initial conditions in the first timestep) or the outputs from the last timestep. The chemistry model then estimates the variation of in situ concentrations of the consumed and produced species in the present time step, $\mathrm{d}C$; the sink and source terms S_r can be expressed by:

$$S_r = \frac{\mathrm{d}C}{\mathrm{d}t} \tag{6.121}$$

S_r physically represents the rate of the concentration variation. Thus, for species being produced, consumed, and at equilibrium, S_r will be positive, negative, and zero respectively.

As the time scale of the geothermal reinjection can be as long as a decade, and computational power is limited, the timestep could be very long (say days), however, the time scale for most of the considered reactions to reach equilibrium can be as short as dozens of minutes. Therefore, when programming, it is very important to ensure that the source terms can still reasonably represent the reactions no matter how long the timestep is. This is done by following the method below:

Recall that the chemistry model outputs the variation of in situ concentrations $\mathrm{d}C$ in one timestep $\mathrm{d}t$ (say from $t = t_0$ to $t = t_0 + dt$). $\mathrm{d}C$ can be expressed by:

$$\mathrm{d}C = C|_{t=t_0+dt} - C|_{t=t_0} \tag{6.122}$$

$\mathrm{d}C$ is obtained by modelling the reaction occurring in each cell in the chemistry model numerically. At the end of each computational loop, the concentrations are checked if the equilibrium is reached. This allows $C|_{t=t_0+dt}$ to be obtained properly by either finishing the loop (i.e. the timestep dt is shorter than the time needed for the reactions to reach the equilibrium) or terminating the loop once the equilibrium is reached (i.e. the timestep dt is longer than the time needed for the reactions to reach the equilibrium). Hence, a suitable value of S_r can be obtained as well, no matter how long the timestep is.

As the source/sink terms representing the chemical reactions are obtained from the values in the present timestep and will be applied in the next timestep, the stability of the numerical scheme might be a problem. However, in the present work, to limit the computational cost, the defined time steps are usually much longer than the time required for the reactions to reach the equilibriums. The sink and the source terms hardly change between timesteps. Therefore, the calculation rarely experiences stability issues.

Equation 6.121 is capable of defining the source or sink terms for all reactive processes in the holistic model, except for those involved with silica, which are defined in the next section. At this stage, the in situ concentrations of all species (dissolved and colloidal silica excluded) can be predicted. The models above predict the chemical conditions so that the reactive processes of silica can be simulated.

6.6 Silica polymerisation, particle formation, transport, and deposition

6.6.1 Source term for silica polymerisation and molecular deposition

In Section 4.1.1, Weres et al.'s (1980) model (i.e. SILNUC) is reproduced and adopted to model silica polymerisation and predict the molecular deposition rate J_{md}.

The transient convection-diffusion transport of dissolved silica is modelled by following the methodologies shown in Section 6.4.3. Based on SILNUC (Section 4.1.1) and similar to other species described in Section 6.5, the sink and source terms for the concentrations of dissolved and polymerised (i.e. colloidal) silica (S_{ds} and S_{ps}) respectively can be defined using Equation 6.121. Therefore, the following correlation can be defined:

$$S_{\mathrm{ds}} = \frac{\mathrm{d}C_{ds}}{\mathrm{d}t} = -S_{\mathrm{ps}} \leq 0 \tag{6.123}$$

$S_{\mathrm{ds}} \leq 0$ physically means the decrement rate of dissolved silica concentration due to silica polymerisation, and $S_{\mathrm{ps}} \geq 0$ physically represents the increment rate of polymerised silica (i.e. colloidal silica) due to the same reason.

As the molecular deposition rate J_{md} can be predicted by SILNUC, in one timestep dt and one control volume dV, the sink term for the molecular deposition of dissolved silica S_{md} can be defined as:

$$S_{\mathrm{md}} = -\frac{J_{\mathrm{md}}\, A_r}{dV\, dt} \leq 0 \tag{6.124}$$

where A_r is the surface area available for molecular deposition. Therefore, for the control volumes next to the fluid-rock interface, A_r is assumed to be equal to the fracture surface area, whereas for the rest of the fluid domain, A_r is assumed to be zero. The upper and lower surfaces of a fracture are assumed to be equally available.

$S_{\mathrm{md}} \leq 0$ physically stands for the decrement rate of dissolved silica concentration due to monomeric (or molecular) silica deposition. Therefore, the total decrement rate (i.e. the sink term) of dissolved silica concentration is the sum of S_{ds} and S_{md}:

$$S_{\mathrm{ds,total}} = S_{\mathrm{ds}} + S_{\mathrm{md}} = S_{\mathrm{ds}} - \frac{J_{\mathrm{md}}\, A_r}{dV\, dt} \tag{6.125}$$

At this stage, the in situ concentrations of dissolved silica can be found. By incorporating this source term into the mass transfer governing equation, the model considers (1) convection, (2) diffusion, (3) concentration decrement due to silica polymerisation, and (4) concentration decrement due to molecular deposition.

6.6.2 Formation of silica particles

In the present work, the formation of silica nanoparticles is discussed in Section 4.1.2. The silica particle growth model predicts the in situ average silica particle size. In each timestep dt, the source term for the concentration of colloidal silica S_{ps} is given by Equation 6.125 above.

6.6.3 Transport and deposition of silica particle

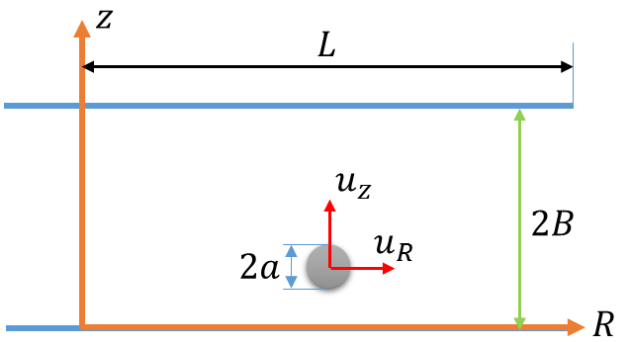

Figure 6.15: Coordinate set up. The flow is assumed to be fully developed for $R \geq 0$.

As described in Section 6.3, by coupling the continuity equation and the Navier-Stokes equations, a parabolic (Poiseuille) velocity profile of the flow in the R direction, u_{fR}, can be found (see Equation 6.47).

It is reasonable to assume the velocities of the flow in the both θ and z direction are zero, i.e. $u_{f\theta} = 0$ and $u_{fz} = 0$.

It is desired to predict particle transport from fluid to collector under the influence of external forces $F_R, F_\theta,$ and F_z. Hence, by coupling the continuity and the transport equations, one can obtain the governing equation for particle transport:

$$\frac{\partial C_{ps}}{\partial t}+\frac{1}{R}\frac{\partial}{\partial R}\left(Ru_R C_{ps}\right)+\frac{1}{R}\frac{\partial}{\partial \theta}\left(u_\theta C_{ps}\right)+\frac{\partial}{\partial z}\left(u_z C_{ps}\right) = \frac{1}{R}\frac{\partial}{\partial R}\left(D_R R\frac{\partial C_{ps}}{\partial R}\right)+\frac{1}{R^2}\frac{\partial}{\partial \theta}\left(D_\theta \frac{\partial C_{ps}}{\partial \theta}\right)+\frac{\partial}{\partial z}\left(D_z \frac{\partial C_{ps}}{\partial z}\right) + S_{\mathrm{cd}} \quad (6.126)$$

where C_{ps} is the concentration of the particles of interest (the subscript ps stands for "polymerised silica"); R, θ, and z are the spatial coordinates of the centre of the particles; u_R, u_θ, and u_z are the particle transport velocities induced by the fluid, $D_R, D_\theta,$ and D_z are the diffusion tensors of the particles, and S is the source or sink term, representing the quantity of particles generated or lost in one control volume.

The mesh shown in Equation 6.23, 6.24, and 6.26-6.28 is reused here.

To obtain a simplified geothermal reinjection model, the following assumptions may be made to simply the problem.

By assuming the particle velocities induced by flow in the R, θ, and z directions are equal to the fluid velocity:

$$u_R = u_{fR} = \frac{3}{2}u_m(1-\frac{(z-B)^2}{B^2}) \quad (6.127)$$

$$u_\theta = u_{f\theta} = 0 \quad (6.128)$$

$$u_z = u_{fz} = 0 \quad (6.129)$$

This may be feasible as particles travelling at such a small Stokes number (usually far less than one) quickly equilibrate their velocity with the fluid.

By assuming the diffusion tensors of the particles in the R, θ, and z directions are equal and can be expressed using the Stokes-Einstein equation (Equation 6.115):

$$D_R = D_\theta = D_z = D = \frac{k_B T}{6\pi\mu a} \quad (6.130)$$

As there is no known reason for unbalanced forces to appear in the R and z directions, it is assumed that there is no external force acting on the particles in the R and z directions:

$$F_R = 0 \quad (6.131)$$

$$F_\theta = 0 \quad (6.132)$$

By assuming there is no concentration gradient of the particles in the θ directions as the model is axis-symmetrical:

$$\frac{\partial C}{\partial \theta} = 0 \quad (6.133)$$

Therefore, the governing equation Equation 6.126 can be simplified to:

$$\frac{\partial C_{ps}}{\partial t}+\frac{1}{R}\frac{\partial}{\partial R}\left(Ru_R C_{ps}\right)=\frac{1}{R}\frac{\partial}{\partial R}\left(DR\frac{\partial C_{ps}}{\partial R}\right)+\frac{\partial}{\partial z}\left(D\frac{\partial C_{ps}}{\partial z}\right)+S_{\text{ps,total}} \qquad (6.134)$$

In Section 6.4.3, the domain for the chemical species transport modelling is $R_0 \le R \le R_{max}$ and $0 \le z \le B$. In this case, the domain is slightly different as the coordinate represents the centre of the particle. The minimum z is no longer equal to zero but equal to the radius of the silica particle, i.e. $z = a$, which can be obtained when the particle touches the plate. Hence, the domain for the colloidal silica transport is $R_0 \le R \le R_{max}$ and $a \le z \le B$.

Similar to those described in Section 6.4.3, the boundary conditions in the radial direction for polymerised silica transport can be defined by:

$$C_{ps}|_{R=R_0} = c_{\text{inj}}^{\text{ps}} \qquad (6.135)$$

$$\frac{\partial C_{ps}}{\partial R}|_{R=R_{max}} = 0 \qquad (6.136)$$

In the z direction, the boundary conditions are more complex. The boundary condition at $z = B$ does not change as the model is symmetrical with respect to that boundary:

$$\frac{\partial C_{ps}}{\partial R}|_{z=B} = 0 \qquad (6.137)$$

Since the conditions near the rock surface (or, to use a more general term, the 'collector') are still not well understood, assumptions must be made. The following two models consider two different possible assumptions: the perfect-sink model and the non-penetration model.

6.6.3.1 Perfect-sink model

The perfect-sink model assumes that the particles immediately deposit and irreversibly disappear from the system once they reach the rock surface. Therefore, the following boundary condition can be expressed:

$$C_{ps}|_{z=a} = 0 \qquad (6.138)$$

Hence, the diffusion mass flux at the boundary $z = a$ is:

$$j_z|_{z=a} = -D\frac{\partial C_{ps}}{\partial R}|_{z=a} = -D\frac{2C_{ps}\big|_{z=\frac{\delta z}{2}+a}}{\delta z} \qquad (6.139)$$

The perfect-sink model does not consider the scale formation on the rock surface as an independent phase controlled by the chemical reactions and physical forces between the particles and the deposited scale.

As the investigations of the minerals' surface properties are not included in the present work, it is assumed that the reservoir formation neither attract nor repulse the silica particles, i.e. the interactions between silica and the rock surface are assumed to be negligible.

Therefore, in the vertical direction, diffusion is considered as the dominant transport mechanism in the perfect-sink model as the concentration gradient near the wall is very high, and any particle reaching the wall deposits and 'disappears'.

The perfect-sink model may not be valid for the most of time of geothermal reinjection modelling, but may still hold to be true in the initial attachment between the particles and "clean" rock surfaces, if the assumption above is valid.

6.6.3.2 Non-penetration model

The non-penetration model (Adamczyk and van de Ven 1984) considers that the normal mass flux of particles near the rock surface converges over z to zero and a source term is added to the governing equations to model the processes that cannot be expressed explicitly yet, i.e.:

$$j_z|_{z=a} = 0 \tag{6.140}$$

which is equivalent to:

$$\frac{\partial C_{ps}}{\partial R}|_{z=a} = 0 \tag{6.141}$$

To apply this method, the sink or source term $S_{\text{ps,total}}$ should be defined to represent the kinetics of particle formation, accumulation, immobilization, and removal at the surface of the plates

In principle, on the surface of the plate, as the deposition is treated as the binding of newly arrived particles to previously deposited particles, one can derive:

$$J_{\text{cd}} = k_{dep} C_{ps}^{n}\big|_{z=\frac{\delta z}{2}} \tag{6.142}$$

where k_{dep} is the reaction constant of deposition, $C_{ps}\big|_{z=\frac{\delta z}{2}}$ is the concentration of colloidal silica at the nodes of the cells adjacent to the fracture surface, and n is the power exponent. Since the collisions of interest occur between suspended and deposited particles, and three-body collisions are ignored (being only important at a high number density of particles), it is considered that the deposition at the surface is of the first order, i.e. $n = 1$. Equation 6.142 physically means that, in a stationary or quasi-stationary state, the reactant supply rate is equal to the reaction rate.

As discussed in Section 4.2.2, for two suspended particles with the same size, if there is no repulsion and the effective capture distance is the centre-to-centre distance (i.e. $2a$), the collision rate constant is $\frac{8k_BT}{3\mu}$, which is equal to the aggregation rate constant if the collision efficiency is unity, i.e. $\alpha = 1$. Therefore, $\frac{8k_BT}{3\mu}$ is the maximum aggregation rate constant for homogenous colloidal suspensions. In the case of deposition, since one particle is considered to be fixed on the collector, the maximum collision rate is $\frac{4k_BT}{3\mu}$. Therefore, the maximum the reaction constant of deposition,

$$k_{dep}^{0} = \frac{4k_BT}{3\mu A_r} \tag{6.143}$$

where A_r is the reaction surface area. Note, the superscript 0 represents the simplest aggregation model in which the repulsion is not considered. When repulsion is taken into account, the real aggregation rate is $\frac{4k_BT}{3\mu W}$, where W is the stability, and the reaction constant of deposition is:

$$k_{dep} = \frac{k_{dep}^0}{W} = \frac{4k_B T}{3\mu W A_r} \tag{6.144}$$

Therefore, the sink term representing the effect of colloidal deposition S_{cd} can be expressed as:

$$S_{\text{cd}} = -\frac{J_{\text{cd}}\, A_r}{dV\, dt} = -\frac{4k_B T A_r}{3\mu W A_r\, dV\, dt} C_{ps}\Big|_{z=\frac{\delta z}{2}} \tag{6.145}$$

The total source or sink term is:

$$S_{\text{ps,total}} = S_{\text{ps}} + S_{\text{cd}} \tag{6.146}$$

where S_{ps} is obtained using Equation 6.123 shown in Section 6.6.1 and SILNUC shown in Section 4.1.1.

At this stage, the heat and the reactive mass transfer can be modelled. By coupling the sub-models described in Chapter 4-Chapter 6, a holistic model can be assembled and tested.

6.6.4 External forces applied on silica particle

This section describes the method used to estimate the external forces which may act on the silica colloids. In the holistic model developed in this thesis, those forces which have a significant effect on colloid behaviour are included implicitly, using the Eulerian method in the form of interactive potentials taken into account in S_{cd} (Equation 6.145). An explicit formulation, as presented below, may be still useful in future modelling using the Lagrangian method.

When silica particles are formed in the fluids, in the z direction, there are five external forces applied on the particles: gravity, buoyancy, Saffman lift force, London-van der Waals' force, and electrostatic force, shown in the figure below.

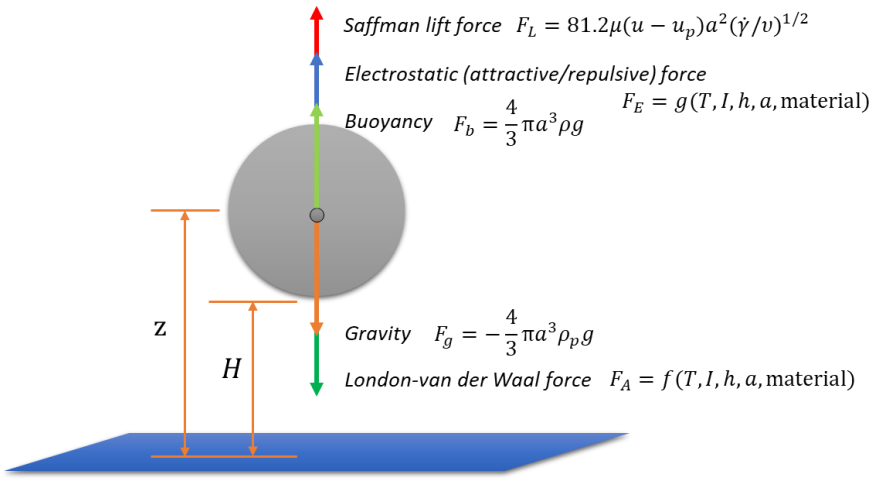

Figure 6.16: five external forces of interest applied on the colloidal silica particle.

6.6.4.1 Net gravity force

By coupling the expressions for gravity and buoyancy, the net gravity F_g can be described as:

$$F_g = -\frac{4}{3}\pi a^3(\rho_p - \rho)g \tag{6.147}$$

where ρ_p is the density of amorphous silica, and g is the gravitational acceleration.

6.6.4.2 Saffman lift force

The Saffman lift force, F_L, is a lift force experienced by a sphere transporting through a viscous liquid perpendicular to the flow direction due to the velocity difference (Saffman 1965; 1968). It can be defined by:

$$F_L = 81.2\mu(u_{fR} - u_R)a^2(\dot{\gamma}/v)^{1/2} \tag{6.148}$$

where $(u_{fR} - u_R)$ represents the velocity difference between the flow and the particle of interest, i.e. the relative velocity, and $\dot{\gamma} = \frac{\partial u}{\partial z} = -3u_m\frac{(z-B)}{B^2}$ is the shear rate. There are four requirements to meet when applying Equation 6.148:

$$Re_s = \frac{|u_{fR} - u_R|a}{\nu} \ll 1 \tag{6.149}$$

$$Re_\Omega = \frac{\Omega a^2}{\nu} \ll 1 \tag{6.150}$$

$$Re_G = \frac{\dot{\gamma}a^2}{\nu} \ll 1 \tag{6.151}$$

$$Re_s \ll Re_G^{1/2} \tag{6.152}$$

where Re_s, Re_Ω, and Re_G are Reynolds numbers defined in terms of the slip velocity, the rotational speed of the spherical particle Ω, and the velocity gradient (i.e. the shear rate). McLaughlin (1989; 1991) performed a direct numerical simulation (DNS) of the transport of aerosol in a channel under turbulent flow conditions and found that the last condition (Equation 6.152) was not satisfied. McLaughlin (1989; 1991) and Wong and Squires (1996) reported that deposition rates were overestimated over the particle relaxation time under turbulent flow conditions when the Saffman lift force was considered. Hence, the Saffman formula may not be accurate near solid boundaries especially under turbulent flow conditions. Further studies on the shear-induced lift force on a particle have found more general forms of Equation 6.148 and corrections for when solid boundaries are present (Vasseur and Cox 1977; Cox and Hsu 1977; McLaughlin 1991; 1993 and Cherukat and McLaughlin 1994).

Considering that the flow considered in the present work is always laminar, Equation 6.148 may be safe to apply; however as particles travelling at such small Stokes number (usually far less than one), their velocity should quickly equilibrate with the fluid, i.e. $u_{fR} - u_R = 0$. Therefore, the Saffman lift force vanishes.

6.6.4.3 London-van der Waals' force

As mentioned in Section 4.2.2, the attractive potential energy, V_A, is expressed in Equation 4.60. The London-van der Waals' force, F_A can be derived:

$$F_A = \frac{dV_A}{dH} \tag{6.153}$$

6.6.4.4 Electrostatic force

Similarly, the electrostatic potential energy, V_E, is expressed in Equation 4.62 (classic) and Equation 4.104 (the soft-particle model). The electrostatic force, F_E can be derived:

$$F_E = \frac{dV_E}{dH} \tag{6.154}$$

The magnitudes of the external forces applied on a single 7.84 nm silica nanoparticle at the condition of 80 ℃, 0.043 M ionic strength, pH 5.69 are plotted in Figure 6.17 below:

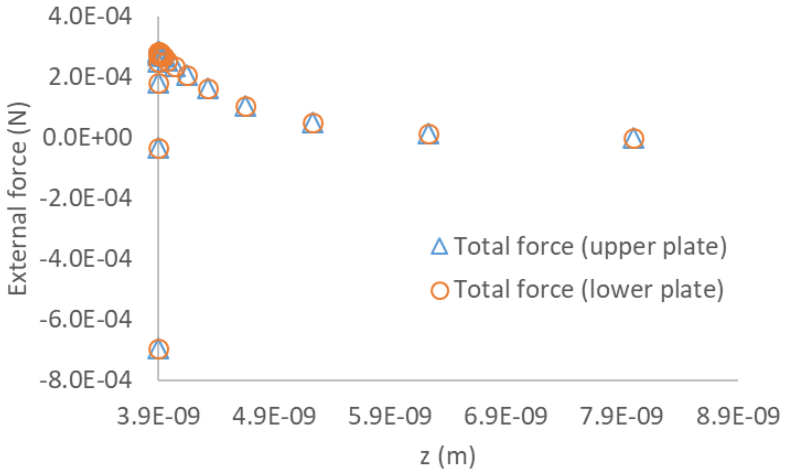

(a)

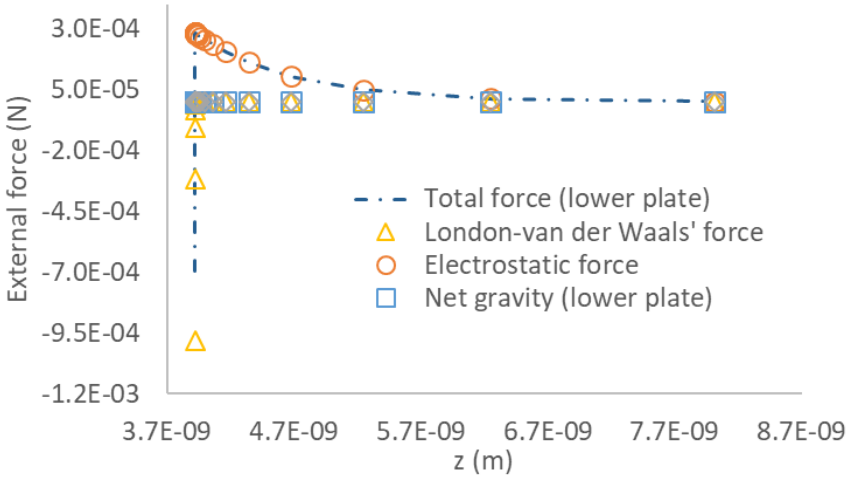

(b)

Figure 6.17: External forces applied on a single silica particle: (a) comparison between the total forces with respect to the upper and lower plates; (b) comparison among the external forces (the Saffman lift force is zero and excluded for clarity).

The results shown in Figure 6.17 (a) indicate that the effect of the net gravity and the London-van der Waals forces on the transport of silica particle is negligible. Therefore, the problem becomes fully symmetrical with respect to $z = B$. Figure 6.17 (b) also suggests that the electrostatic force determines the interactions between the suspended particles and the silica coated fracture surface, especially in the short range of the separation distance, and therefore is the only force significant in controlling the rate of colloidal deposition.

Appendix 2: Summary of reference conductivity values

The reference conductivities of species of interest are summarised in Table 6.1 below:

Table 6.1: Summary of the reference conductivity

Ion	Valency	λ_0 (S cm^{-2} mol^{-1})
Na^+	+1	50.11
H^+	+1	349.8
OH^-	-1	197.8
Cl^-	-1	76.34
SO_4^{2-}	-2	160.0
Ac^-	-1	40.90
HSO_4^-	-1	52.00
Ca^{2+}	+2	119.0
HCO_3^-	-1	44.50
CO_3^{2-}	-2	138.6
$CaHCO_3^+$	+1	19.00
F^-	-1	55.40
HF_2^-	-1	75.00
SiF_6^{2-}	-2	160.0

Chapter 7

Documentation for *GEOREPR* — the user guide

7.1 Introduction

The code: *GEOREPR* (GEOthermal Reinjection lifetime Prediction model) is an original code that integrates all sub-models described previously, such as the idealised geothermal reservoir, hydrodynamics of injectate, heat and reactive mass transfer (including the deposition of $CaSO_4$ due to the dissolution of $CaCO_3$ caused by sulphuric acid), silica polymerisation and particle growth, transport of silica particles, prediction of colloidal silica stability, estimation of deposition rate and ultimately the injectivity. The work flow is shown in Figure 5.1 below:

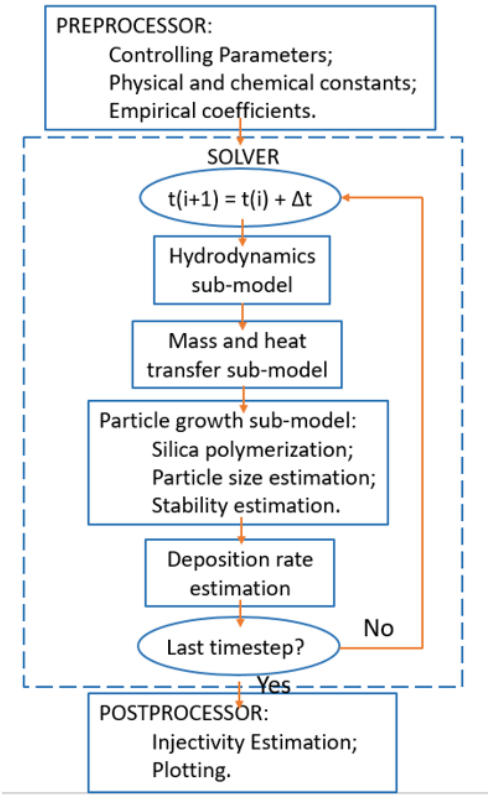

Figure 7.1: Workflow of *GEOREPR*.

This model is developed to predict geothermal reinjection lifetime under user-defined geothermal conditions at an acceptable computational cost. The inputs and the outputs are described in Section 7.2 and 23 respectively.

GEOREPR has been developed in MATLAB 2018b and is offered as a free open-source code under the GNU (General Public License) from 2019, and may be developed further in the future or reprogrammed in a more open and free alternative language such as Python. The user can use, modify, and redistribute the code for commercial or non-commercial proposes.

7.2 Control of the user definable parameters

7.2.1 Basic controlling inputs

The controlling inputs are classified into the following eight types:

1. Initial conditions of the injectate and the pre-existing fluid in the reservoir

The initial physical conditions and the initial quantities of silica dissolved or suspended in the injectate and the pre-existing fluid in the reservoir are defined here, which are temperature `Tinj` and `Tres` (℃), pH `pHinj` and `pHres` (equivalent pH at the room temperature), the concentrations of the dissolved silica `cDSinjppm` and `cDSresppm` (ppm) and the pre-existing polymerised silica `cPSinjppm` and `cPSresppm` (ppm), respectively.

For example, to separately define the injectate and the pre-existing fluid which are initially dissolved with 1200 and 0 ppm amorphous slica, and 0 and 0 ppm polymerised silica at pH 4.5 and 7 and 160 and 260 ℃:

```
1. [Tinj, pHinj, cDSinjppm, cPSinjppm] = deal(160, 7, 1272, 0);
2. [Tres, pHres, cDSresppm, cPSresppm] = deal(260, 7, 0, 0);
```

where `deal` is a MATLAB command to distribute the inputs to the outputs, i.e. assign the values in the right-hand side to the varibles in the left-hand side.

2. Reinjection operating conditions

The function `massflowrateSI(x1, x2, Tinj)` is used to define the injecting flow rate, where `x1` represents the value of the injecting flow rate, `x2` indicates the unit (e.g. `x2` = 'kg/s' for the SI unit kg/s), and `Tinj` is used to estimate the density of the injectate. For the convenience of users, the function can convert values in non-SI units to values in SI units kg/s. There are eighteen optional units used to describe the injecting flow rate: `'kg/s'`, `'g/s'`, `'t/s'`, `'kg/min'`, `'g/min'`, `'t/min'`, `'kg/h'`, `'g/h'`, `'t/h'`, `'m3/s'`, `'dm3/s'`, `'cm3/s'`, `'m3/min'`, `'dm3/min'`, `'cm3/min'`, `'m3/h'`, `'dm3/h'`, `'cm3/h'`, where `'kg'`, `'g'`, and `'t'` represent kilogram, gram, and tonne; `'m3'`, `'dm3'`, and `'cm3'` stand for cubic metre, cubic decimetre, and cubic centimetre; `'s'`, `'min'`, `'h'` means second, min, and hour, respectively.

For example, to define the injecting mass flow rate as 60 kg/s:

```
3. mDot = massflowrateSI(60, 'kg/s', Tinj);
```

3. Ageing

GEOREPR considers the effects of ageing on the silica. The ageing time can be defined by inputting a preferred value to the variable `tAgeing`.

For convenience, the function `timeSI(x1, x2)` is used to convert the unit of the inputted time from non-SI to SI, where `x1` represents the value of the time, and `x2` indicates the unit of the input. There are five optional units that can be used in the function: `'s'`, `'min'`, `'h'`, `'d'`, and `'a'`, where `'d'` and `'a'` represent day and year, respectively.

For example, to define the ageing time as 0.5 hr:

```
4. tAgeing = timeSI(0.5, 'h');
```

If there is no ageing process before reinjection, one can simply input 0 for `x1`.

4. Timescale of interest

The user can determine the preferred maximum reinjection time by defining `tmax`. The function `timeSI(x1, x2)` is used again for converting the unit.

For example, to define a maximum reinjection time of 12 years:

```
5. tmax = timeSI(12, 'a');
```

5. Spatial mesh and timestep

The meshing quality can be controlled by the user to minimise the computational cost while keeping the simulation results as physical as possible. The user can define the desired quantities of discretised cells in the radial and vertical direction and timesteps separately by giving `Nx`, `Nz`, and `Nt`.

For example, to discretise the reservoir geometry into 50×50 cells and the 12-year reinjection time into 25 timesteps:

```
5. [Nx, Nz, Nt] = deal(50, 50, 25);
```

6. Reservoir geometry

There are five variables used to define the geometry of the idealised reservoir: the radius of the injection wellbore `R0` (m), the feedzone thickness `H` (m), the initial idealised fracture aperture `a0mm` (mm), the initial porosity of the reservoir `phiR0`, and the initial permeability of the fracture `Kf0` (m^{-2}). The number of fractures `Nf` can be obtained by following Equation 8.1 shown below:

$$\mathrm{Nf} = \frac{\mathrm{H\ phiR0}}{0.001\mathrm{a0mm}} \tag{8.1}$$

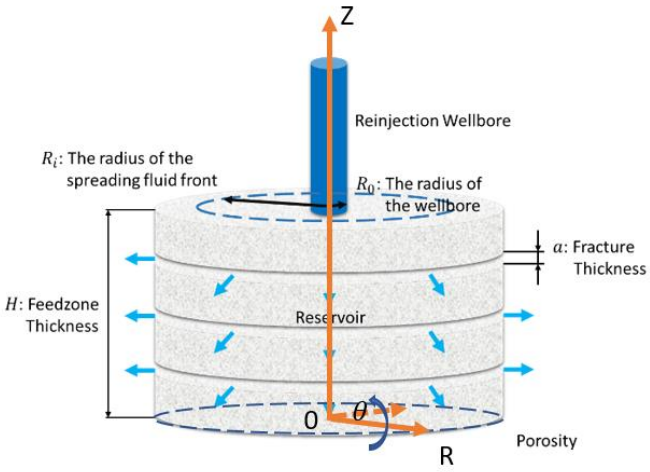

Figure 7.2: Simplified geometry consisting of injection wellbore and geothermal reservoir.

For example, to define a reservoir, where the initial porosity and permeability are 0.01 and 5×10^{-12} m^{-2} respectively, with a 9 5/8 inch (0.122 m in radius) injection wellbore, a 120 m (in depth) feedzone, 2 mm thick idealised fractures:

```
7. [R0, H, a0mm, phiR0, Kf0] = deal(0.122, 120, 2, 0.01, 5e-12);
```

7. Composition of the reservoir formation

The reservoir formation is modelled as a binary mixture: calcium carbonate, and all other minerals (which are assumed inert) lumped together. The composition of the reservoir formation is defined by the percentage of the reaction surface area of a certain mineral.

For example, to define a reservoir made from 40% calcium carbonate and 60% other inert minerals:

```
8. sCaCO3 = 0.4;
```

8. Initial compositions of the injectate and the pre-existing fluid in the reservoir

The initial compositions (the chemical conditions) of the injectate and the pre-existing fluid in the reservoir are defined here. Unless otherwise specified, the unit of the variables mentioned in this section is always mol/kg.

(1) `cNaClinj` and `cNaClres`: the initial concentrations of sodium chloride in the injectate and the pre-existing fluid, e.g. to define an injectate and a pre-existing fluid dissolved with 0.09 and 0.07 mol/kg sodium chloride respectively:

```
9. [aHinj, cNaClinj] = deal(10^-pHinj, 0.09);
10.[aHres, cNaClres] = deal(10^-pHres, 0.07);
```

where `aHinj` and `aHres` are the activities of hydrogen ion in the injectate and the pre-existing fluid and equal to `10^-pHinj` and `10^-pHres`.

(2) `cCainj`, `cCaCO30inj`, `cCaHCO3inj`, `cH2CO3inj`, `cHCO3inj`, `cCO3inj`: the initial concentrations of Ca^{2+}, ion pair $CaCO_3^0$, $CaHCO_3^+$, H_2CO_3, HCO_3^-, CO_3^{2-} in the injectate respectively. Similarly, in the pre-existing fluid, there are `cCares`, `cCaCO30res`, `cCaHCO3res`, `cH2CO3res`, `cHCO3res`, `cCO3res`, e.g. to define an injectate and a pre-existing fluid dissolved without any species mentioned here:

```
11.[cCainj, cCaCO30inj, cCaHCO3inj] = deal(0, 0, 0);
12.[cH2CO3inj, cHCO3inj, cCO3inj] = deal(0, 0, 0);
13.[cCares, cCaCO30res, cCaHCO3res] = deal(0, 0, 0);
14.[cH2CO3res, cHCO3res, cCO3res] = deal(0, 0, 0);
```

(3) `cH2SO4inj`, `cHSO4inj`, `cSO4inj`: the initial concentrations of H_2SO_4, HSO_4^-, and SO_4^{2-} in the injectate respectively. Similarly, in the pre-existing fluid, there are `cH2SO4res`, `cHSO4res`, `cSO4res`, e.g. to define an injectate acidified by 10^{-4} mol/kg H_2SO_4 and no naturally dissolved HSO_4^- and SO_4^{2-}, and a pre-existing fluid dissolved without any species mentioned here:

```
15.[cH2SO4inj, cHSO4inj, cSO4inj] = deal(1e-4, 0, 0);
16.[cH2SO4res, cHSO4res, cSO4res] = deal(0, 0, 0);
```

Note that the concentrations of species such as H_2SO_4, HSO_4^-, and SO_4^{2-} is not necessarily given at equilibrium state here but can be defined at the user's convenience. The concentration distribution will be pre-processed and updated in the chemistry model.

(4) `cHFinj`, `cFinj`, `cSiF6inj`: the initial concentrations of HF, F^-, and SiF_6^{2-} in the injectate respectively. Similarly, in the pre-existing fluid, there are `cHFres`, `cFres`, `cSiF6res`, e.g. to define an injectate added with 10^{-2} mol/kg HF and no naturally dissolved F^- and SiF_6^{2-}, and a pre-existing fluid dissolved without any species mentioned here:

```
17.[cHFinj, cFinj, cSiF6inj] = deal(1e-2, 0, 0);
18.[cHFres, cFres, cSiF6res] = deal(0, 0, 0);
```

By defining `cHFinj`, the user enables the optional module to simulate reservoir stimulation by injecting hydrofluoric acid, which will dissolve the deposited amorphous silica. To conveniently define the quantity of deposited silica, it is assumed that the fracture surface has been completely coated with an amorphous silica layer. Therefore, the quantity of deposited silica can be expressed in the form of the thickness of silica layer `aSilica`. A function `lengthSI(x1, x2)` to convert common units of length to SI units is used, where `x1` is the value of the input, and `x2` indicates the unit of the input: `'km'`, `'m'`, `'mm'`, `'um'`, and `'nm'` representing km, m, mm, μm, and nm, respectively.

For example, to a 10-μm-thick silica scale layer:

```
19.aSilica = lengthSI(10, 'um');
```

If the duration of acid dosing `tmax` is long enough, the silica scale may be fully removed. The model monitors `aSilica`: if `aSilica` becomes zero, the modelling will be stopped as the composition and the dissolution kinetics of different forms of silica in reservoir formation are out of the scope in the present work but may be included in the future.

(5) `cHAcinj, cAcinj`: the initial concentrations of HAc (acetic acid) and Ac^- in the injectate respectively. Similarly, in the pre-existing fluid, there are `cHAcres, cAcres`, e.g. to define an injectate added with 10^{-4} mol/kg HAc and no naturally dissolved F^- and SiF_6^{2-}, and a pre-existing fluid dissolved without any species mentioned here:

```
[cHAcinj, cAcinj] = deal(1e-4, 0);
[cHAcres, cAcres] = deal(0, 0);
```

7.2.2 Advanced user-definable inputs

An optional model to empirically describe the reaction rates has been described in Chapter 5 (Equation 5.10), which can be enabled to simulate the precipitation/dissolution of chemical species of interest.

There are several inputs that shall be addressed. As with the initial conditions of injectate and pre-existing reservoir fluid, the initial concentrations and the percentage of reactive surface area of the interested chemical species N ($N = 1, 2, 3$ ...) shall be defined as well, represented by `cNinj`, `cNres`, and `sN` respectively.

Since three mechanisms (named the a, b, and c mechanisms for simplicity) are supported, the user will need to define the Arrhenius pre-exponential factor (`AaN`, `AbN`, `AcN`, in $\mathrm{mol\ m^{-2}\ s^{-1}}$), log rate constant at 25 ℃ (`logkaN`, `logkbN`, `logkcN`, in $\log(\mathrm{mol\ m^{-2}\ s^{-1}})$), the Arrhenius activation energy (`EaN`, `EbN`, `EcN`, in $\mathrm{kJ\ mol^{-1}}$ the reaction order (`naN`, `nbN`, `ncN`), and the chemical affinity parameters (`paN`, `qaN`, `pbN`, `qbN`, `pcN`, `qcN`). Data for common water-mineral reactions can be found in (Palandri and Kharaka 2004).

For example, if the user wants to model the dissolution of the two minerals albite and andesine, which make up 10% and 5% in the reactive surface area separately and have been initially dissolved in the injectate and reservoir fluid at 120 and 40 ppm and 80 and 20 ppm respectively, one can define the following inputs:

```
optMinerals = 2;  % quantity of interested minerals types
% for Mineral 1
[c1inj, c1res, s1] = deal(120, 40, 0.1);
[Aa1, logka1, Ea1, na1, pa1, qa1] = deal(1, -10.16, 65.0, 0.457, 1, 1);
[Ab1, logkb1, Eb1, nb1, pb1, qb1] = deal(1, -12.56, 69.8, 1, 1, 1) ;
[Ac1, logkc1, Ec1, nc1, pc1, qc1] = deal(1, -15.60, 71.0, -0.572, 1, 1);
% for Mineral 2
[c2inj, c2res, s2] = deal(80, 20, 0.05) ;
[Aa2, logka2, Ea2, na2, pa2, qa2] = deal(1, -8.88, 53.5, 0.541, 1, 1);
[Ab2, logkb2, Eb2, nb2, pb2, qb2] = deal(1, -11.47, 57.4, 1, 1, 1);
```

7.3 Summary of outputs

For simplicity, there are two default main outputs: the in situ amorphous silica deposition rate and the injectivity as a function of time; and four default plots to monitor if the modelling is working correctly. The sample plots are shown in Figure 7.3 below; for specific modelling results, one can refer to Chapter 6.

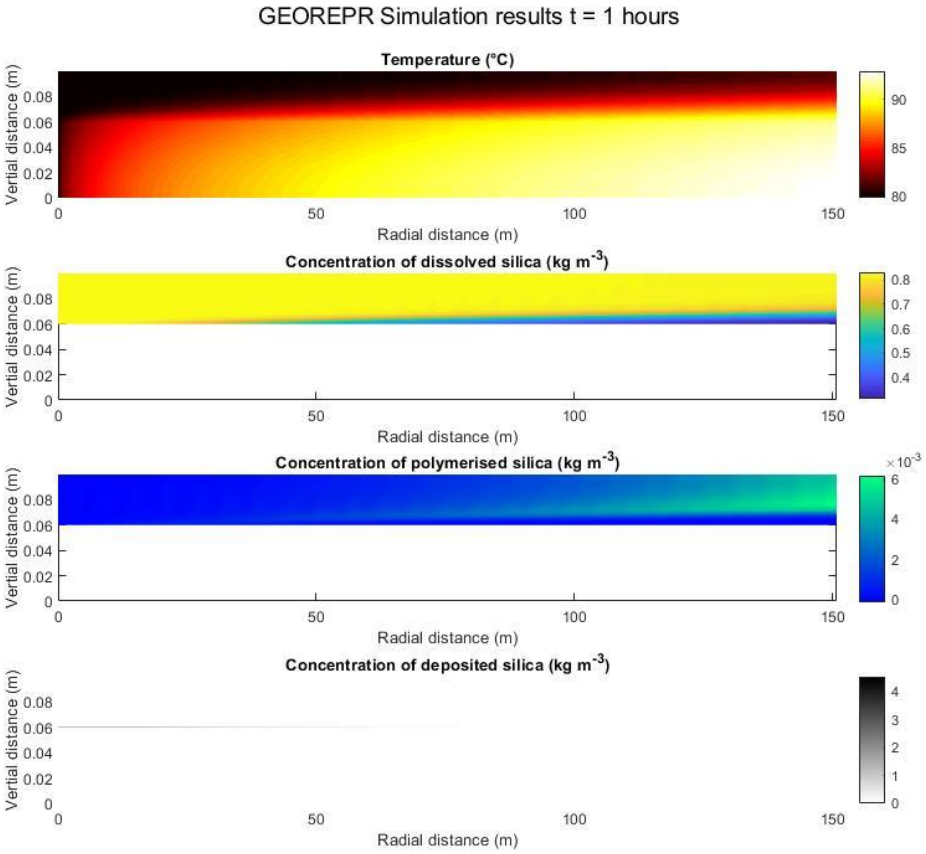
GEOREPR Simulation results t = 1 hours
Temperature (°C)
Vertial distance (m)
Radial distance (m)
Concentration of dissolved silica (kg m-3)
Concentration of polymerised silica (kg m-3)
Concentration of deposited silica (kg m-3)

(a)

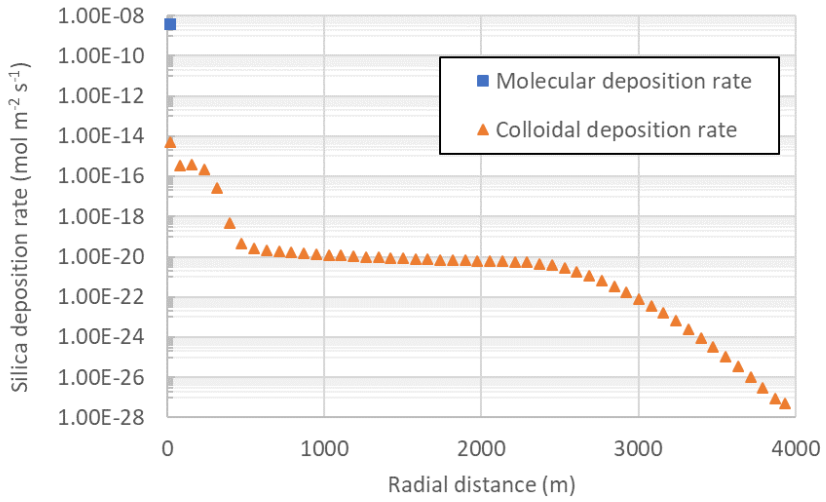
Molecular deposition rate
Colloidal deposition rate
Silica deposition rate (mol m-2 s-1)
Radial distance (m)

(b)

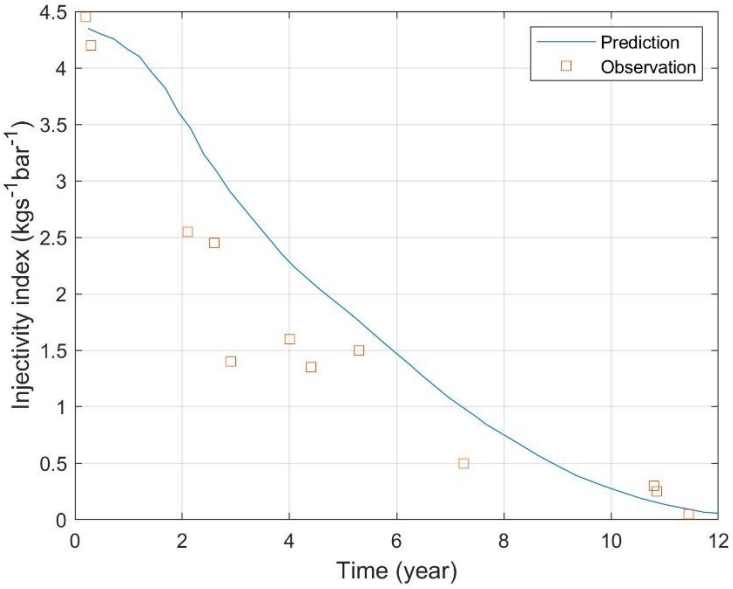

(c)

Figure 7.3: Default plots of sample outputs: (a) temperature and concentrations of dissolved, polymerised, and deposited silica over vertical and radial directions, (b) silica deposition rate over vertical and radial directions, and (c) injectivity over time.

Other simulated spatially resolved results in the sub-models can be plotted if required: the average velocity and temperature of injectate, the concentration of default and user-defined chemical species of interest (e.g. default: $CaSO_4$, dissolved silica, etc., defined: $MgCO_3$), the silica particle size, the stability of colloidal silica, and the permeability as a function of time.

7.4 Basic functions and algorithms

Once all inputs are properly defined, the simulation can be proceeded.

Firstly, the controlling parameters will be pre-processed to find the factors that can be directly used in the solver. For example, from the temperature of the injectate, the pre-processor will estimate the physical properties such as density, viscosity of fluid; by defining the initial conditions, the solubility of the amorphous silica and the tendency of silica polymerisation will be predicted.

Once all parameters have been pre-processed, input data is fed to each of the sub-models of the solver. The hydrodynamics sub-model will solve the Navier-Stokes equations to find the velocity at which the fluid travels away from the wellbore, within the idealised fractures. The heat transfer sub-model will solve the transient convection-diffusion heat transport equations to predict the in situ temperature. The reactive mass transfer sub-model will solve the transient convection-diffusion mass transport equations to estimate the in situ concentrations, dissolution rate, and deposition rate of the interested chemical species. Afterwards, the outputs from the sub-models will be gathered and post-processed to assess the effects of these heat and mass transfers on the reservoir porosity, permeability, and injectivity. At this point the reinjection simulation for one time step is complete.

By evolving the system over the desired number of time steps, one can finally obtain the time-dependent simulation results, i.e. the injectivity as a function of time.

7.5 Assumptions review

The assumptions used in GEOREPR are briefly summarised as follows for the user's reference.

General assumptions

1. Idealisations of geothermal reservoirs and fractures, which include:
   (1) the reservoir formation is vertically and horizontally homogeneous;
   (2) The permeability of the rock between the adjacent fractures is zero, i.e. no fluid can flow through the rock even under the effect of an infinitely high pressure gradient.
   (3) the horizontal fractures are the only flow paths;
   (4) the fracture is equivalent to two parallel flat plates;
   (5) tortuosity of the fractures is negligible.
2. The reservoir formation is static during one timestep, i.e. the geometry change due to the fluid-rock interaction is assumed to be negligible within one timestep.
3. The permeability of the idealised fractures is a constant until modified by silica deposition.
4. The reservoir formation is composed of only calcite and inert minerals.
5. Injection mass flow rate is a constant.
6. Pressure has no effect on reaction rates.
7. The injectate is in the liquid phase, i.e. no gas bubbles.

The assumptions for the hydrodynamic sub-model are:

1. The injectate is incompressible (i.e. the density is a constant) in each single control volume but may be slightly and instantaneously varied while the fluid transports from one cell to another, and is subject to a change in temperature.
2. The density change due to heat transfer in each control volume is instantaneous and vertically homogeneous.
3. The velocity profile is fully developed once it enters fractures.
4. The velocity difference between the flow and the silica nanoparticle is negligible.
5. The velocity of the fluid in the horizontal tangential (i.e. θ) and vertical (i.e. z) direction is fixed and zero.
6. Physical properties (density, viscosity, heat capacity, and thermal conductivity) of the injectate are equal to those of water under the same physical conditions.

Assumptions for the heat transfer

1. Heat capacity and thermal conductivity of the injectate and the reservoir formation are constants.

Assumptions for the reactive mass transfer

1. When conditions favour the formation of silica particles, compared to the timescale of the entire particle growth, the formation of silica nuclei is instantaneous.
2. If aggregation is not considered, the final silica particle size only depends on temperature.
3. In each control volume, the particle size distribution is strictly homogenous, i.e. all particles have the same size $\bar{R}$.

4. The unique interactions of colloidal silica are caused by the ion-penetrable and swellable silicone hairy layer under varying chemical conditions.
5. The thickness of the silicone hairy layer is a function of pH and ionic strength only.
6. Under fixed background conditions, the charge density of the hairy layers is a constant, i.e. the dissociated silanol groups in the hairy layers are uniformly distributed.
7. The permittivity of the hairy layer and the background solution are equal.
8. The surface of the silica particle core is uncharged.
9. Aggregation occurs once the hairy layers from two particles touch each other.
10. The dissociation and association reactions are instantaneous processes.
11. Certain reaction model parameters, fitted to room temperature data, are valid at geothermal temperatures (extrapolation), where noted in the text.
12. The possible reasons for the discrepancies among the reported dissolution rates of calcite such as surface conditions (roughness, defects), impurities, and grain size are negligible.
13. $CaSO_4$ begins to deposit once it becomes supersaturated, i.e. the critical supersaturation index is 1.
14. $CaSO_4$ only precipitates in the form of insoluble anhydrite.
15. The activity of water is fixed to one.
16. The activity coefficients of neutral ion pairs are unity, unless specified otherwise in Appendix 3.
17. In the modelling of workover using hydrofluoric acid, unless specified, the silica scale is uniformly and equally distributed over the top and bottom surfaces of a fracture.
18. The dissolved amorphous silica released from the scale surface will be in the form of monomeric silica only.
19. The Stokes-Einstein equation is valid to estimate the diffusivity of silicic acid molecules.
20. There are no reactions generating or consuming sodium chloride.
21. All species that are not modelled are treated as per sodium chloride. The ionic strengths of the two cases are defined to be equal, which can give a pseudo concentration of sodium chloride.
22. The particle velocities induced by flow in the R, θ, and z directions are equal to the fluid velocity.
23. The diffusion tensors of the silica particles in the R, θ, and z directions are equal and can be expressed using the Stokes-Einstein equation.
24. There is no external force acting on the silica particles in the R and z directions.
25. There is no concentration gradient of the silica particles in the θ directions as the model is axis-symmetrical.
26. The silica deposition is a two-step process: the first step is the initial attachment between the silica and the "clean" rock surface (i.e. no silica scale formed on the surface yet), and the second is the subsequent attachment between the silica in the fluids and the deposited silica on the surface.
27. The preliminary deposition of silica to at least one molecule thick on the "clean" fracture surface (i.e. the first step) is assumed to be instantaneous.
28. The surface area available for silica deposition is equal to the fracture surface area.
29. Thermophoresis of silica particles is negligible.

Chapter 8

Case studies and sensitivity analysis

To evaluate the performance of the models developed previously, simulation results and real-world experiences published by other workers are reproduced in Section 8.1-8.7 and compared with the outputs of *GEOREPR* under similar input conditions. A sensitivity analysis is presented in Section 8.8, to study the effects of the controlling parameters on the lifetime of reinjection. This is the basis for the study of silica scaling inhibition strategies in Chapter 9.

8.1 Heat transfer

As the reinjected, cooled geothermal wastewater spreads in the geothermal reservoir, it may eventually arrive at the production well, and if the injected fluids have not gained enough heat, the enthalpy of the produced fluid will be decreased. This phenomenon is called thermal breakthrough and is deleterious to energy extraction. Therefore, the heat transfer in the reservoir due to reinjection is of great interest.

Bödvarsson and Tsang (1982) proposed a model, shown in Figure 8.1 below, to simulate the underground heat transfer in a fractured reservoir formation. The geometry is similar to that used in the present thesis however Bödvarsson and Tsang (1982) considered only one dimension (i.e. the heat transfer along the radial axis).

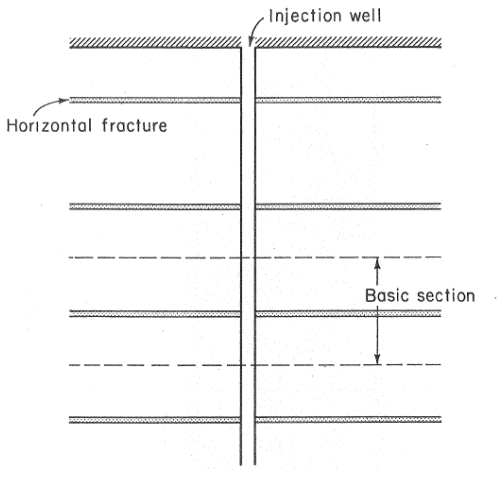

(a)

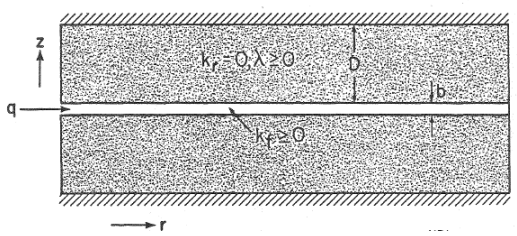

(b)

Figure 8.1: Geometry used in the work of Bödvarsson and Tsang (1982).

If the heat conduction can be considered to be isotropic in the fluids and the reservoir formation separately and the reservoir temperature is constant before reinjection, the thermal front is where the fluid temperature is equal to the average temperature of the injectate and the reservoir before reinjection, i.e. $T|_{r=\text{thermal front}} = 0.5(T_{\text{inj}} + T_{\text{res}})$. If the location of thermal front at any given time can be predicted, the thermal breakthrough can be forecast as well.

The boundary conditions and assumptions used by Bödvarsson and Tsang are similar to the present work and are described in Section 6.4.1 of the current work and in Section 3.1 of Bödvarsson and Tsang 1982. The differences are that Bödvarsson and Tsang (1982) treated the problem as one dimensional, and no non-linearities were allowed, which means that parameters such as density, heat capacity, and thermal conductivity are constant; also, the flow is steady. Hence, Bödvarsson and Tsang (1982) were able to solve the governing equation using the Laplace transformation. The analytical solutions for thermal breakthrough time t_{tb} as a function of radial distance r are described in Equation 8.1-8.3 below:

For $r \leq \left(\frac{\dot{Q}}{4.396\pi 2B}\frac{\rho_f^2 c_f^2}{\rho_r c_r k_r}\right)^{0.5}$:

$$t_{\text{tb}} = \frac{\pi a_f}{\dot{Q}} \tag{8.1}$$

For $\left(\frac{\dot{Q}}{4.396\pi 2B}\frac{\rho_f^2 c_f^2}{\rho_r c_r k_r}\right)^{0.5} < r \leq \left[\frac{\rho_f c_f \dot{Q} a_r}{4.396\pi k_r}(2 + \frac{\rho_f c_f a_f}{\rho_r c_r a_r})\right]^{0.5}$:

$$t_{\text{tb}} = \frac{4.396 k_r \rho_r c_r}{\rho_f^2 c_f^2}\left(\frac{\pi r^2}{\dot{Q}}\right)^2 \tag{8.2}$$

For $r > \left[\frac{\rho_f c_f \dot{Q} a_r}{4.396\pi k_r}(2 + \frac{\rho_f c_f a_f}{\rho_r c_r a_r})\right]^{0.5}$:

$$t_{\text{tb}} = \frac{\pi\left(2\rho_r c_r a_r + \rho_f c_f a_f\right)}{\rho_f c_f \dot{Q}} \tag{8.3}$$

where a_r is half the thickness of rock matrix, $\dot{Q}$ is the volumetric flow rate, a_f is the fracture aperture, ρ_r, c_r and ρ_f, c_f are the density and the heat capacity of rock and fluid respectively, and k_r is the thermal conductivity of rock matrix. Physically, Equation 8.1-8.3 mean that, near the thermal front, the heat conduction between the fluid and the rock is negligible at the early stage (Equation 8.1); the injected fluids start to obtain heat from the rock in the intermediate stage (Equation 8.2); and no heat transfer between the rock and the fluids occurs at the later stage (Equation 8.3). Bödvarsson and Tsang (1982) presented the modelling results shown in Figure 8.2 (b) when the inputs shown in Figure 8.2 (a) were used.

Flowrate q, (kg/s):	10.0
Thermal conductivity λ(J/m·s·°C):	2.0
Fluid density ρ_w(kg/m^3):	1000
Fluid specific heat, c_w(J/kg·°C):	4000
Rock density ρ_r:	2500
Rock specific heat c_r(J/kg·°C):	1000
Fracture porosity, ϕ (-):	1.0
Fracture aperture, b(m):	1 x 10^{-4}

(a)

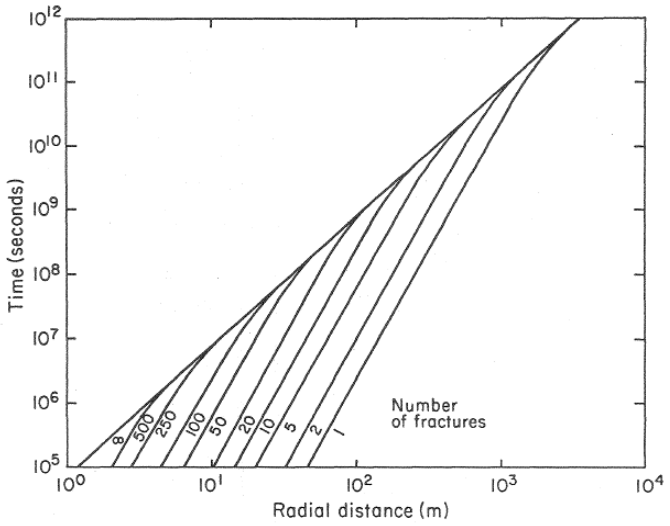

(b)

Figure 8.2: Modelling example in the work of Bödvarsson and Tsang: (a) summary of the inputs (b) modelling results, reproduced from Bödvarsson and Tsang 1982.

Inputting the values shown in Figure 8.2 (a) to the model developed in this thesis yields the square dots in Figure 8.3. These match the modelling results of Bödvarsson and Tsang for an infinite number of fractures. Only the case when the number of fractures is much greater than 500 (say 10000) is plotted in Figure 8.3 below for clarity. Normally a reinjection feedzone will have a large number of fractures. Therefore, the heat transfer sub-model in the present work is equivalent to a very large (>500) number of fractures due to the use of a distributed porosity, instead of discrete fractures. With a small number (<500) of discrete fractures, the time taken for the rock separating the fractures to reach equilibrium temperature is significant compared to the timescale of the simulation.

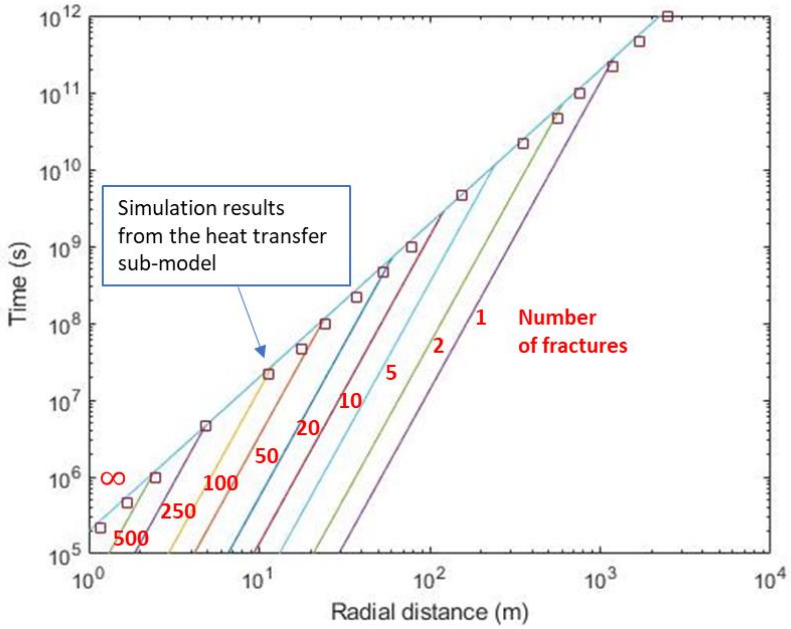

Figure 8.3: Heat transfer modelling results in the form of Figure 8.2b when the inputs shown in Figure 8.2a are used. For simplicity, only the results of one example: number of fractures is much higher than 500 is plotted.

The agreement with the work of Bödvarsson and Tsang (1982) shown in Figure 8.3 suggests that the heat transfer sub-model can be accepted if a high concentration of fractures is assumed, which is reasonable in energy-producing geothermal reservoirs.

8.2 Acid-calcite interaction

As described earlier, before looking into the behaviour of amorphous silica, it is necessary to obtain the transient chemical conditions in situ. Therefore, it is important to make sure that the geochemistry sub-model can produce reasonable results first.

The sub-model of acid-calcite interaction is developed by strictly following the theories such as Plummer et al. (1978) shown in Chapter 4 and it describes an idealised case: the reaction is controlled by the surface reaction only -- the transport of chemical species is assumed to be sufficiently fast that the transport mechanisms do not affect the reaction rate. This is because the sub-model serves as the sink/source term in the transport equation (e.g. the term S in Equation 6.112 in Section 6.4.3) describing the surface reaction at the bottom of the boundary layer (i.e. $z = 0$). Therefore, it is expected that the predicted overall reaction rate will always be greater than or equal to measured values, which do include transport effects.

Huminicki and Rimstidt (2007) experimentally measured the dissolution rate of crushed calcite having a specific surface area $A_{sp} = 0.015\ m^2/g$ in 0, 0.1, 0.3, and 1.0 M Na_2SO_4 aqueous solutions in the initial pH range of 1.5-3.5 acidified using nitric acid (HNO_3) at 22 ℃. The reaction vessels are open to the atmosphere, which suggests that the measured reaction rates are expected to be lower than the predictions as the sub-model considers that all produced CO_2 is trapped in the fluids in the form of H_2CO_3 and increasing concentration of H_2CO_3 boosts calcite dissolution.

Comparison of the observations of (Huminicki and Rimstidt 2007) and predictions of the present model confirms these expectations, as shown in Figure 8.4 below:

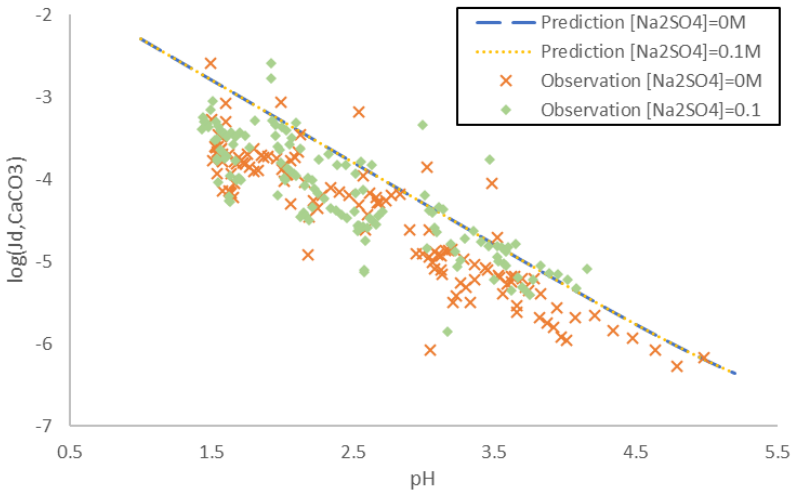

Figure 8.4: Comparison of observed calcite dissolution rates reproduced from Huminicki and Rimstidt 2007 and predicted rates (from the geochemistry sub-model developed in this work, assuming the reaction area is fixed at all times).

It should be noted that: (a) considering that the concentration of sulphate ion (SO_4^{2-}) in geothermal brines in New Zealand is usually less than 0.001 M (~ 100 ppm), measurements in 0.3 and 1.0 M Na_2SO_4 aqueous solutions are out of the range of interest and are not shown in Figure 8.4 above; (b) the predictions shown in Figure 8.4 are the "initial" dissolution rates on the mineral surface at varying pH (i.e. no reaction products e.g. Ca^{2+}, CO_3^{2-} etc., which may have decelerating effects on the dissolution rates, are considered), however, the observed dissolution rates as a function of pH were obtained by measuring the quantity of calcium dissolved over a set period of time, and the corresponding increment of pH. This may be the reason for why most of the observations are slightly lower than the predictions.

8.3 Silica nanoparticle growth in geothermal brine at the Sumikawa geothermal station, Japan

Tamura et al. (2018) measured the time-resolved silica nanoparticle growth in samples of geothermal brine at pH 6.6 and 8, and in diluted brines. The temperature of the samples was maintained at 90 ℃ during the experiments. The chemical composition of the original geothermal brines is reproduced in Table 8.1 below.

Table 8.1: pH and composition of geothermal brine from the Sumikawa geothermal station, Japan, reproduced form Tamura et al. 2019.

pH at 25 ℃	**6.6**
Component	**Concentration (ppm)**
Na^+	650
K^+	110
Ca^{2+}	5.1
Mg^{2+}	< 0.1
Fe^{2+}	< 0.1
Fe^{3+}	< 0.1
Al^{3+}	0.5
B	430

Cl^-	1100
SO_4^{2-}	120
HCO_3^-	16
SiO_2	1130

Calculated ionic strength: 0.034 M

8.3.1 Results and discussion

The comparison between the concentration dissolved silica in these observations, and predictions made by Weres et al. (1981)'s model, which is adopted in this work, is shown in Figure 8.5 below:

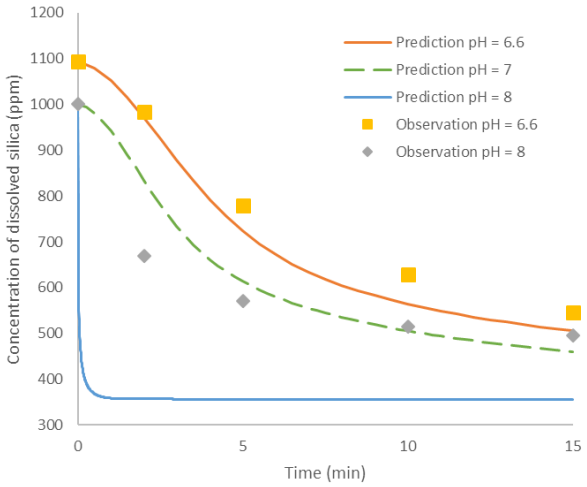

(a)

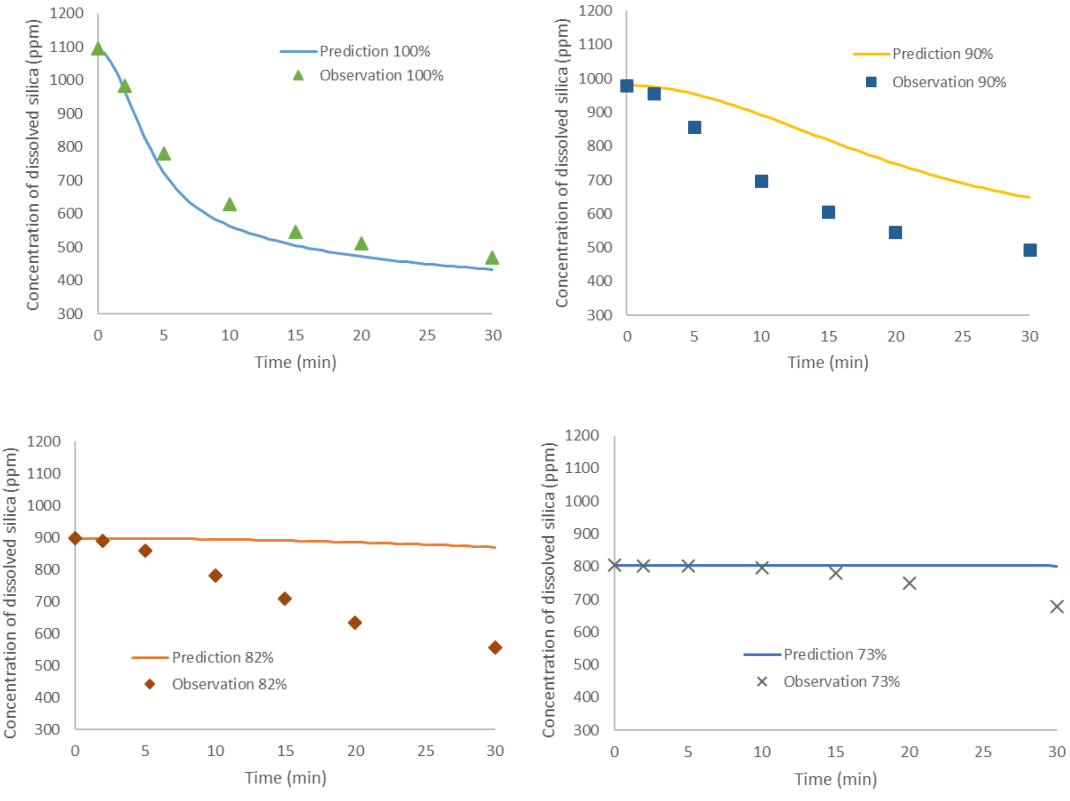

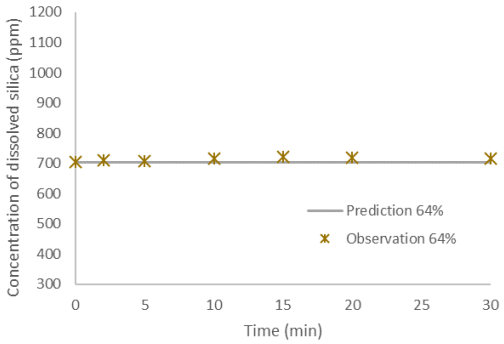

(b)

Figure 8.5: Comparison of predicted and observed concentration of dissolved silica as a function of time at 90 ℃ under the initial conditions: (a) [SiO_2] = 1094 ppm, pH = 6.6, 7, and 8.8, I = 0.034 M; (b) [SiO_2] = 1094, 980, 898, 804, and 704 ppm, pH ≈ 6.6, I = 0.034, 0.031, 0.025, 0.018, and 0.012 M (i.e. 100%, 90%, 82%, 73%, and 64% of the original brines, where the percentages are the dilution ratios and 100% means the natural extracted geothermal fluids without dilution).

Discrepancies exist. It is possible that ageing of the samples after transport and pre-processing (such as adjusting pH and diluting) might be responsible for the discrepancies. Other factors which may have effects are discussed below.

As it is suggested (Weres et al. 1981) that the silica polymerisation model should not be relied on very much when pH is above 8, the discrepancy shown in Figure 8.5 (a) may be understandable. As a comparison, however, the predictions at pH 7 agree with the observations at pH 8 reasonably well. Also, as the surface tension drops with increasing temperature and pH, the critical nuclei become very small, and SILNUC can overestimate the rate of nucleation. Furthermore, the quantity of boron contained in the geothermal fluids at Sumikawa are about 16 times higher than at the Wairakei geothermal station, New Zealand (Carroll et al. 1998). The inhibition effects of trivalent boron on silica polymerisation are known and increase with increasing pH as boron has chemical properties similar to aluminium (Iler 1979; Weres et al. 1981), which may explain the observed persistence of dissolved silica at pH=8, in Figure 8.5 (a), where the model, without the effects of trivalent ions, shows a rapid decline.

In Figure 8.5 (b), the silica polymerisation predicted by the model is, in the first three plots, slower than the observations in varying degrees. This may be caused by the presence of salts other than sodium chloride. The silica polymerisation model of Weres et al. (1981) takes the effects of sodium chloride into account, but not other ions e.g. Mg^{2+}, Al^{3+}, Br^{-}, SO_4^{2-}, which are expected to be present in the trials. Weres et al. (1981) discuss the accelerating effects of larger anions on silica polymerisation qualitatively. The disagreement could also be explained by the fact that SILNUC ignores heterogeneous nucleation, and, under these conditions, the rate of homogeneous nucleation is relatively low.

As shown in Figure 8.5 (a) and the first plot of Figure 8.5 (b), only the observations in the case of the natural geothermal fluids without dilution at its original pH can be reasonably well explained by the model. Hence, only the historical particle growth data in the undiluted brine at its original pH is used here for comparison.

The comparison between observed and predicted silica particle size is shown in Figure 8.6 below:

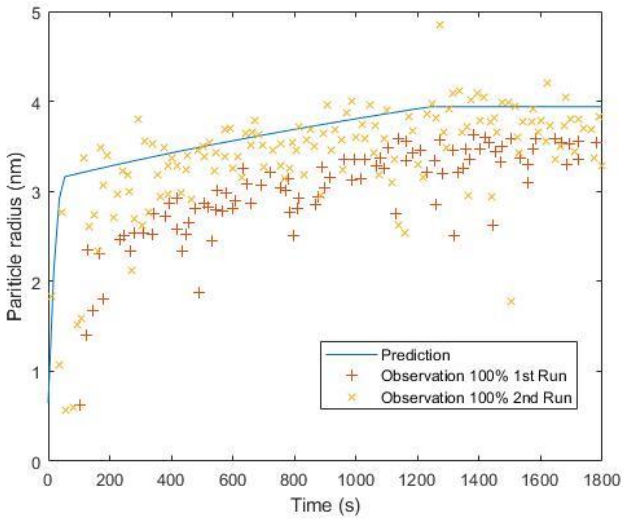

Figure 8.6: Comparison of predicted and observed silica particle size as a function of time at 90 ℃ under the initial conditions: [SiO_2] = 1094 ppm, pH = 6.6, I = 0.034 M (i.e. the original geothermal fluids). Historical particle growth data is reproduced from Tamura et al. 2018.

Tamura et al. (2018) measured the growth of silica nanoparticles twice under the same conditions. In Figure 8.6, one may notice that the mean particle size in the second measurement is slightly larger than that in the first measurement and, overall, agrees with the predictions reasonably well.

On the other hand, the particle growth seems to be delayed by an "induction" time, which, however, is not apparent in the curve of observed concentration of dissolved silica (the first plot of Figure 8.5 (b)). The thesis author replots the simulated results by adding 100 seconds as the "induction" time for the particle formation, as shown in Figure 8.7 below:

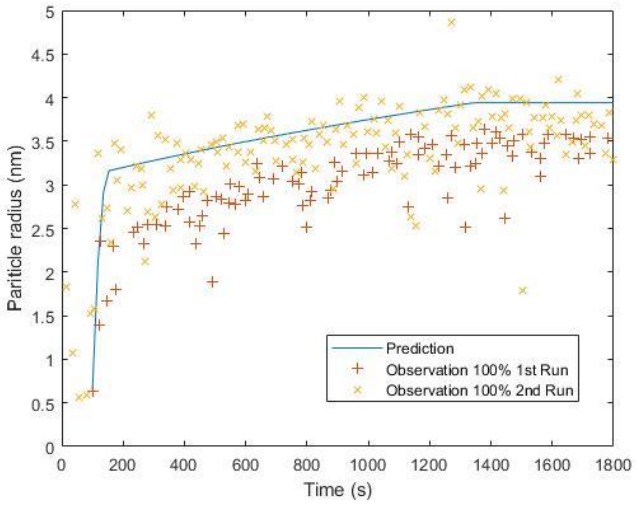

Figure 8.7: Comparison of predicted (a pseudo induction time of 100 seconds is included) and observed silica particle size as a function of time at 90 ℃ under the initial conditions: [SiO_2] = 1094 ppm, pH = 6.6, I = 0.034 M (i.e. the original geothermal fluids). Historical particle growth data is reproduced from Tamura et al. 2018.

Adding this induction time appears to improve the prediction of the time at which the change in slope (1300 s in Figure 8.7) occurs, though it is difficult to be certain.

8.3.2 Summary

The comparison above suggests that the models of silica polymerisation (Weres et al. 1981) and silica particle growth can be used to simulate the formation of colloidal silica in geothermal fluids during the process of reinjection. However, care must be taken when pH is above 8 and/or the concentrations of chemical impurities such as boron, aluminium, etc. are not negligible relatively high. Also, the performance of the model regarding the first and the second stages may be improved when more time-resolved observations are available, especially under the conditions which are not covered in the fittings previously shown in Section 4.1.2.3.

8.4 Silica precipitation under field conditions

Carroll et al. (1998) measured the precipitation rate of amorphous silica in ~0.1 M sodium chloride aqueous solution and in geothermal water samples from Wairakei, New Zealand under the conditions of pH 7.73-8.08 and 58-117 ℃ in field experiments.

8.4.1 Inputs

The conditions of the experiments (Carroll et al. (1998)) are rearranged in the form of inputs for the current model, and the silica supersaturation indices are estimated for reference, shown in Table 8.2 below:

Table 8.2: Summary of input parameters, reproduced from Carroll et al. 1998.

EXP. ID	pH	Ionic Strength (M)	Temperature (℃)	Initial $[SiO_2]$ (ppm)	SSI
3/07/1995	7.86	~0.07	89	493.4	1.43
4/07/1995	7.86	~0.07	88	513.0	1.51
5/07/1995	7.95	~0.07	74	490.4	1.75
10/07/1995	8.08	~0.07	58	477.5	2.18
11/07/1995	7.82	~0.07	97	512.5	1.34
12/07/1995	7.98	~0.07	71	490.4	1.83
13/07/1995	7.82	~0.07	97	509.5	1.33
28/09/1995	7.92	~0.07	79	488.9	1.63
28/09/1995	7.92	~0.07	79	490.0	1.63
28/09/1995	7.91	~0.07	80	493.0	1.62
28/09/1995	7.93	~0.07	78	483.0	1.63
29/09/1995	7.82	~0.07	96	519.0	1.37
29/09/1995	7.89	~0.07	84	496.0	1.54
29/09/1995	7.99	~0.07	69	458.0	1.76
2/10/1995	7.84	~0.07	92	517.0	1.44
2/10/1995	7.95	~0.07	75	480.5	1.69
2/10/1995	8.05	~0.07	61	435.9	1.90
3/10/1995	7.84	~0.07	93	519.5	1.43
3/10/1995	7.80	~0.07	100	522.0	1.31
3/10/1995	7.89	~0.07	83	502.4	1.58
4/10/1995	7.94	~0.07	76	483.9	1.68
4/10/1995	7.98	~0.07	70	478.5	1.81
5/10/1995	8.05	~0.07	61	458.0	1.99
5/10/1995	8.01	~0.07	67	478.5	1.89
6/10/1995	7.75	~0.07	112	521.4	1.13
6/10/1995	7.74	~0.07	115	522.5	1.10

6/10/1995	7.78	~0.07	104	522.9	1.25
9/10/1995	7.79	~0.07	102	519.9	1.28
9/10/1995	7.73	~0.07	117	522.9	1.07
9/10/1995	7.77	~0.07	107	521.4	1.20
10/10/1995	7.80	~0.07	101	519.9	1.29
10/10/1995	7.77	~0.07	106	524.0	1.23

The geometries of Carroll et al.'s experiments and the model developed in the current work are different: a 50 mm in diameter x 3 m in length pipe-like fluidised bed reactor (FBR) filled with quartz sand (mean diameter 0.2 mm, estimated pore diameter ~0.1 mm, initial surface area 0.8 $m^2\ g^{-1}$, estimated total surface reaction area 3150 m^2) was used in the field experiments; whereas in the current model, axis-symmetric parallel flat plates as shown in Section 6.2 are adopted. However, the observations and the predictions can still be compared by matching the pore size (hence concentration gradients), the residence times, and the surface reaction areas.

As it is claimed (Carroll et al. 1998) that the quartz sand and the silica gel are comparable in the experiments serving as the substrate for silica to precipitate, no new particles should form. This is represented in the model by manually disabling the modules describing the relevant particle formation processes.

No ageing or induction period before the laboratory and field experiments was reported by (Carroll et al. 1998). Hence, it is assumed that, before the experiments began, all silica contained in the solutions is in the form of monomer, i.e. no silica polymerisation occurs before the measured residence time begins.

8.4.2 Results and discussion

8.4.2.1 Field observations

Before comparing the observations and the modelling results, the experimental results are briefly summarised in this section. The observed values are reproduced in Table 8.3 in the next section.

As mentioned previously, it is noted that no new silica particles should form in the field experiments due to the pre-existing quartz sand. Therefore, molecular deposition of silica should be the dominant scaling mechanism. Under the typical field conditions of Wairakei, New Zealand, the measured silica deposition rates are in the range of $10^{-11} - 10^{-12}$ mol $m^{-2}\ s^{-1}$. Carroll et al. (1998) suggested that the most uncertainty in the experiments may be induced by the chemical impurities such as aluminium. Quantitatively, it was reported (Carroll et al. 1998) that, in the field experiments, the aluminium contained in the silica scale was four orders of magnitude more concentrated than in the geothermal brines (about 10^4 ppm vs. < 1 ppm). Aluminium could have accelerating or decelerating effects on silica polymerisation depending on pH (Yokoyama et al. 1989; 1991).

When comparing the deposition, it should be noted that the effects of chemical impurities such as aluminium other than modifying the ionic strength are not considered in the present work, which was suggested (Carroll et al. 1998) to play an important role in silica precipitation.

8.4.2.2 Prediction vs. observation

By using the inputs listed in Table 8.2, the predicted silica deposition rate in each field experiment can be found, represented in Table 8.3 below:

Table 8.3: Comparison between the predictions made in the current work and the observations in field experiments reported in Carroll et al. 1998.

EXP. ID	Residence Time (s)	Observed total deposition rate (10^{-10} mol m^{-2} s^{-1})	Predicted deposition rate (10^{-10} mol m^{-2} s^{-1})	Orders of discrepancy
3/07/1995	252.3	11.4	13.03	0.1
4/07/1995	109.4	5.83	17.68	0.5
5/07/1995	163.0	13.8	16.96	0.1
10/07/1995	245.4	17.1	17.50	0.0
11/07/1995	184.2	5.73	13.70	0.4
12/07/1995	141.3	16.7	17.69	0.0
13/07/1995	235.5	6.5	13.08	0.3
28/09/1995	171.0	11.8	15.28	0.1
28/09/1995	159.2	13.3	15.49	0.1
28/09/1995	141.5	12.5	15.85	0.1
28/09/1995	204.4	12.6	14.33	0.1
29/09/1995	85.3	3.98	15.66	0.6
29/09/1995	239.8	7.93	15.22	0.3
29/09/1995	279.5	13.8	11.89	0.1
2/10/1995	201.0	4.52	16.98	0.6
2/10/1995	216.2	12.9	14.61	0.1
2/10/1995	242.6	17.3	9.82	0.2
3/10/1995	170.9	4.65	17.09	0.6
3/10/1995	185.4	4.26	14.40	0.5
3/10/1995	193.6	9.23	17.01	0.3
4/10/1995	179.2	13.8	15.08	0.0
4/10/1995	184.1	15.2	15.41	0.0
5/10/1995	176.4	19.2	13.25	0.2
5/10/1995	178.6	16.1	16.02	0.0
6/10/1995	230.8	1.78	7.56	0.6
6/10/1995	230.3	1.78	5.83	0.5
6/10/1995	247.2	2.28	12.53	0.7
9/10/1995	171.2	2.42	12.94	0.7
9/10/1995	178.8	1.87	4.61	0.4
9/10/1995	192.3	2.73	10.53	0.6
10/10/1995	189.9	2.38	13.38	0.7
10/10/1995	189.3	1.98	11.65	0.8

As shown in Table 8.3, all discrepancies are within one order of magnitude. The deposition mechanisms in the field experiments are expected to be more complicated than those in the carefully controlled laboratory experiments, mainly due to the presence of other species.

Therefore, the thesis author considers the discrepancy may be introduced due to the model is lack of ability to estimate the effects of chemical impurities on the silica polymerisation and hence the deposition rate, which is one of the limitations of the present work.

While the comparison looks promising, the higher predicted rates comparing the observed values in Table 8.3 may not be explained as due to ignoring heterogenous nucleation in the

model. Comparing Tables 8.2 and 8.3, it appears that (a) the disagreement is greater at higher *T*, while (b) pH is higher at lower *T*. This suggests that the problem may be originated in how the measured pH shown in Table 8.2 was correlated with the pH used in the modelling.

It is worth noting that, initially, the physical and chemical conditions determine the molecular silica deposition rate and the decrement of the concentration of dissolved silica along with the reactive surface area (i.e. the surface of silica gel in the laboratory experiment and quartz sand in the field experiment) in one timestep. Specifically, when the molecular deposition rate is fixed, the larger the reactive surface area is, the greater the decrement of the concentration of the dissolved silica within one timestep is, and therefore the lower the molecular silica deposition rate in the next timestep is.

8.4.3 Summary

The comparisons shown in Table 8.3 suggest that the model can be relied on to make orders of magnitude estimates of silica deposition rates under field conditions in Wairakei, New Zealand. Considering that the observed silica deposition rates were dominated by the rates of molecular deposition, the unreliability under alkaline conditions could play a role in the discrepancy as well as a possible failure of the nucleation submodel, leading to give unreliable predictions of the decrement of monomeric silica concentration.

8.5 Ohaaki geothermal fields, New Zealand

Mroczek et al. (2013; 2017) experimentally studied the silica scaling potential of cooled geothermal water saturated with amorphous silica at the Wairakei and Ohaaki fields, New Zealand. Small-scale field experiments at the Wairakei field, had shown a low silica scaling rate after brine (containing 730 ppm silica) was cooled to 30 ℃ and aged for several days before reinjection. Due to this success, the first major large-scale injection of cold (30 ℃) geothermal water in New Zealand was carried out at the Wairakei field. Mroczek et al. (2017) reported that, after a 10-month trial, there was no evidence of any loss of injectivity due to silica scaling. However, in a similar small-scale field investigation at Ohaaki, silica deposition was observed in a rapidly cooled, but only briefly aged (30 min at 80 ℃) brine containing 840 ppm dissolved and polymerised silica. Hence no large-scale field trial at Ohaaki was proposed.

Although the idealised geothermal reservoir defined in the present work (see Section 6.2) differs in geometry from Mroczek et al.'s scaling rig (reproduced in Figure 8.8 below), it is still possible, by matching residence times, to make comparisons to test whether the model proposed in the present work can reasonably estimate the silica deposition rate under known conditions, and predict the possible results of any future field trial.

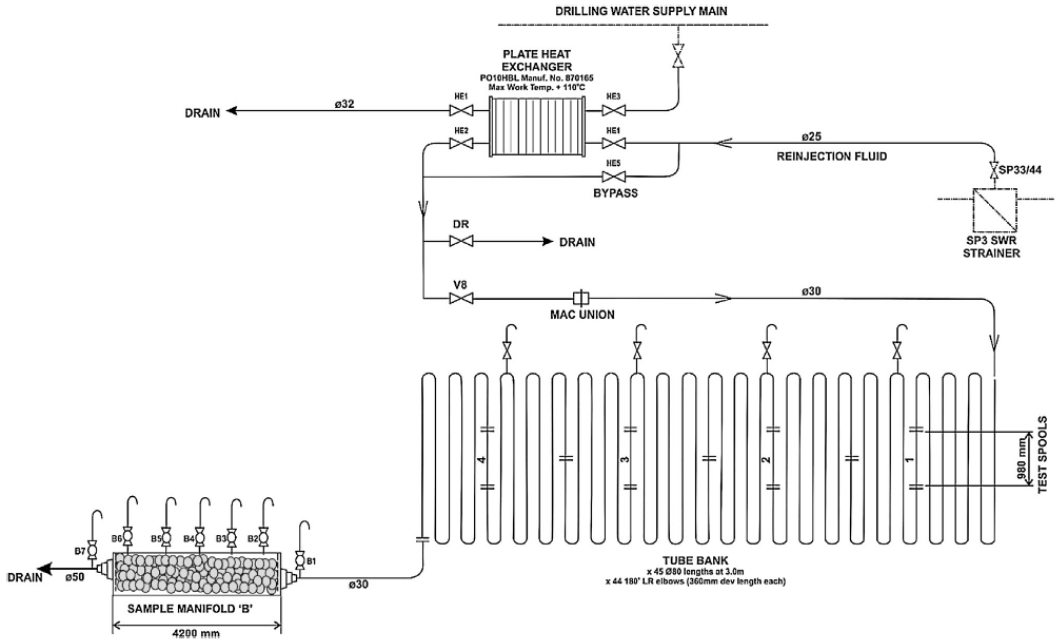

Figure 8.8: Silica scaling rig at Ohaaki geothermal field, reproduced from Mroczek et al. 2017.

8.5.1 Inputs

Based on the descriptions and Table 1-3 of Mroczek et al. 2017, the inputs required for the present work are summarised in Table 8.4 below:

Table 8.4: Summary of input parameters

Input parameter	*In Mroczek et al. 2017*	*In the present work*
Radius of injection wellbore	-	0.122 m
Thickness of feedzone	-	120 m
Initial fracture aperture	80 mm	80 mm
Initial reservoir porosity	-	0.01
Initial fracture porosity	-	1
Initial permeability of fractures	-	5.0×10^{-12} m^2
Injecting mass flow rate	27 L/min	270 t/hr
Temperature	~80 ℃	80 ℃
pH	5.69	5.69
Ionic strength	~0.043 M	0.043 M
Initial concentration of dissolved silica	849 ppm	849 ppm
Injection time	46 days	40 minutes

8.5.2 Results and discussion

To compare the model predictions to Mroczek et al.'s (2017) small-scale field experiment at Ohaaki, results are compared at points in the model which have the same residence time (i.e. how long it takes the injectate to transport from the inlet to a point of interest), as the sampling points T1, T2, T3, T4, B2, and B6 in Mroczek et al.'s trial. For example, the residence time 6.3 minutes at R=366.23 m in the present model is equal to that of T1 in Mroczek et al. 2017.

Since (1) the given maximum residence time of the sampling points in the Ohaaki small-scale field experiment is about 30 minutes at B6, (2) only the estimation of the deposition rates are of interest in the present work, and (3) the effects of decreasing injectivity on the fluid flow are not taken into consideration in the model, a relatively short injection time of 40 minutes, which covers the residence times of all measurements, is used.

8.5.2.1 Perfect-sink model vs. non-penetration model

A boundary condition for the silica concentration at the collector surface (rock) must be chosen. The perfect-sink model (i.e. the concentration of the interested species is fixed to zero on the collector surface, $C|_{z=\text{boundary}} = 0$) was tested, but predicted a deposition rate at least 12 orders of magnitude higher than the observations. The non-penetration model (i.e. the concentration gradient of the interested species is fixed to zero on the collector surface, $\frac{\partial C}{\partial z}|_{z=\text{boundary}} = 0$) predicted a deposition rate of the correct order of magnitude, so was used for all the results shown below.

8.5.2.2 In situ concentration of dissolved silica

The concentration distribution of the dissolved silica is shown in Figure 8.9 below:

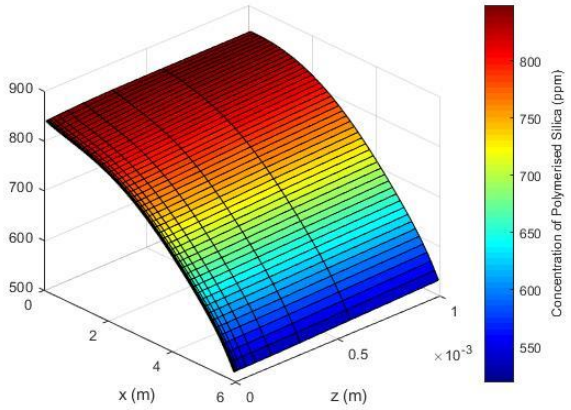

Figure 8.9: Dissolved silica concentration distribution, where $x = R - R_0$ (i.e. the injection wellbore is not included in the domain, as the modelled experiment does not have a wellbore). Note the *x* and *z* axes have different scales.

The concentration of the dissolved silica is expected to drop along with both the radial and the vertical directions due to polymerisation and molecular deposition. According to the Figure 8.9 above, the decrease near the fracture surface is much smaller than the decline along the fluid pathway, suggesting that the silica polymerisation into particles which remain suspended is the main reason for the loss of dissolved silica.

The comparison between the observed and predicted dissolved silica concentration at the sampling points is shown in Figure 8.10 below:

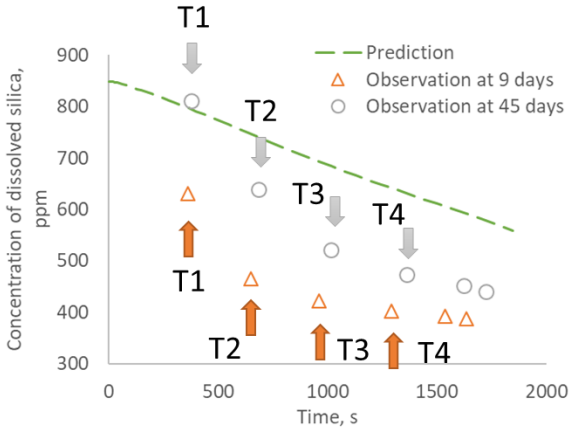

Figure 8.10: Comparison between the observed (reproduced from Mroczek et al. 2017) and the predicted in situ concentration of the dissolved silica, where T1-T4 are the sampling points and the horizontal axis is residence time.

The model predicts a reduction in the dissolved silica concentration of the correct order of magnitude, and is in closer agreement with the 45-day observations than the 9-day observations. The predictions have a lower rate of decline (slope) than the 45-day observations by a factor of approximately two. It was reported that mild steel pipes were used in the experiment which could introduce chemical impurities such as iron ions to the brines, especially in the early stage. These multivalent ions can ultimately accelerate the decreasing rate of the dissolved silica concentration. In the later stage of the experiment, as the pipeline walls might be gradually covered by the silica scale, less and less chemical impurities could be released to the brines. Hence, the 45-day observations would be expected to be closer to the predictions produced by SILNUC, in which heterogenous nucleation is ignored and the effects of multivalent ions are also not taken into account.

As mentioned before, the surface area available for molecular deposition determines the decrement of the concentration of dissolved silica in one timestep. In the reproduced SILNUC model, an additional variable of specific area ($m^2\ m^{-3}$) is defined to represent this effect. In the case of pipe, the specific area is four over the diameter of the pipe, i.e. 50 $m^2\ m^{-3}$ in the Ohaaki field experiment. However, compared to the surface area of the formed silica particles ($\sim 5.08 \times 10^4\ m^2\ m^{-3}$, calculated from the surface area of formed $\sim 7.90 \times 10^{21}\ m^{-3}$ nuclei at the critical radius 7.15×10^{-10} m), the effect of molecular deposition on the concentration drop of dissolved silica in the early stage is expected to be negligible; it could be negligible in the later stage as well if the scale does not increase the specific area significantly.

Therefore, the thesis author suspects that the chemical impurities may be the dominant reason for the discrepancy shown in Figure 8.10. These impurities can act like pre-existing nuclei allowing silica to deposit on their surface and the introduced specific area is usually large, but also chemically affect the kinetics of silica polymerisation. The reproduced SILNUC model takes the effects of sodium chloride into account, but not other ions e.g. Mg^{2+}, Al^{3+}, Br^-, SO_4^{2-}, which are expected to be present in the trials. Weres et al. (1981) qualitatively reported the accelerating effects of larger anions on silica polymerisation. To the author's knowledge, there is no published work which quantifies these effects.

8.5.2.3 In situ silica particle size

Mroczek et al. (2017) reported that, at sampling points T4 (~22.1 min after injection) and B2 (~26.3 min after injection), the average radius of the formed silica nanoparticles was 4-4.5 nm. The predicted particle size over the residence time under same conditions is shown in Figure 8.11 below:

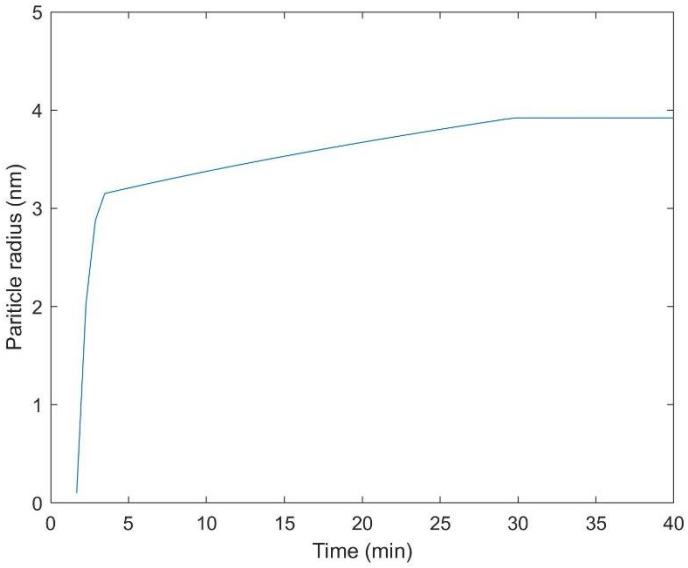

Figure 8.11: Predicted particle radius as a function of residence time under the condition shown in Table 8.4.

The proposed model predicts 7.84 nm at the same residence time. This suggests that the silica particle growth sub-model might be useful in predicting the in situ particle size. Reliable prediction of the particle size is essential for predictions of subsequent growth, aggregation and deposition.

8.5.2.4 In situ concentration of polymerised silica and deposition rate

To differentiate the roles of the molecular and colloidal deposition mechanisms, the concentration distribution of the polymerised (i.e. particulate) and deposited silica due to the molecular and colloidal deposition after 40 minutes of residence time is separately shown in Figure 8.12 (a) and (b) below:

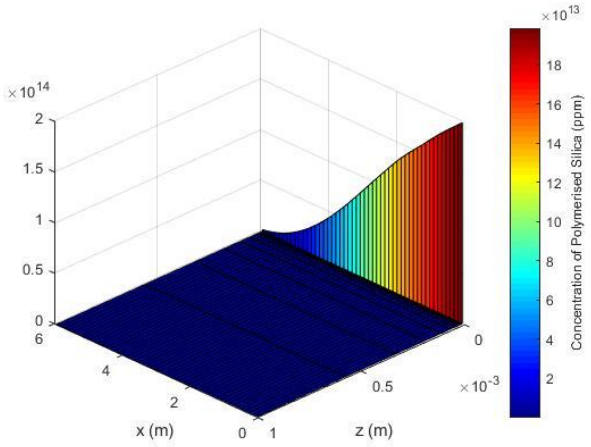

(a)

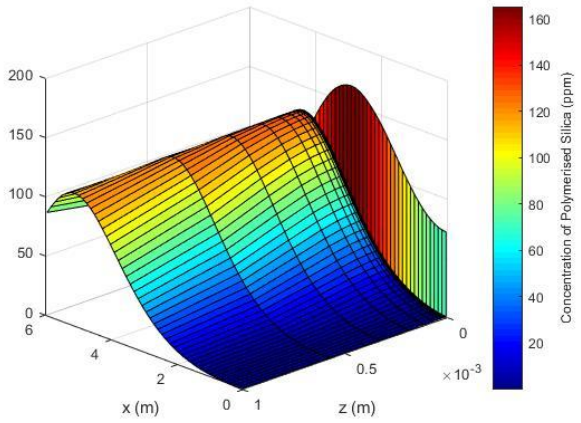

(b)

Figure 8.12: Concentration distribution of (a) polymerised and deposited silica (molecular and colloidal), (b) polymerised and deposited silica (colloidal only) after 40 minutes of reinjection. The discontinuous values at $z = a \approx 0$ represent the immobilised (deposited) silica scale. Note that the concentration of the suspended silica particles shown in (a) is outnumbered by the accumulating silica scale at the wall $z = a \approx 0$ and therefore hard to read.

Based on the results shown in Figure 8.12 above, the comparison between the observed and predicted deposition rates at the sampling points is summarised in Table 8.5 and Figure 8.13 below:

Table 8.5: Comparison between the observed (at 46 days) and the predicted in situ silica deposition rate (kg m^{-2} s^{-1})

Deposition rate at	In Mroczek et al. 2017	Model predictions	Model predictions (colloidal deposition only)
T1	5.07×10^{-9}	5.04×10^{-8}	2.00×10^{-14}
T2	5.23×10^{-8}	3.12×10^{-8}	2.72×10^{-17}
T3	2.38×10^{-8}	1.67×10^{-8}	5.58×10^{-19}
T4	3.17×10^{-9}	5.07×10^{-9}	1.76×10^{-21}

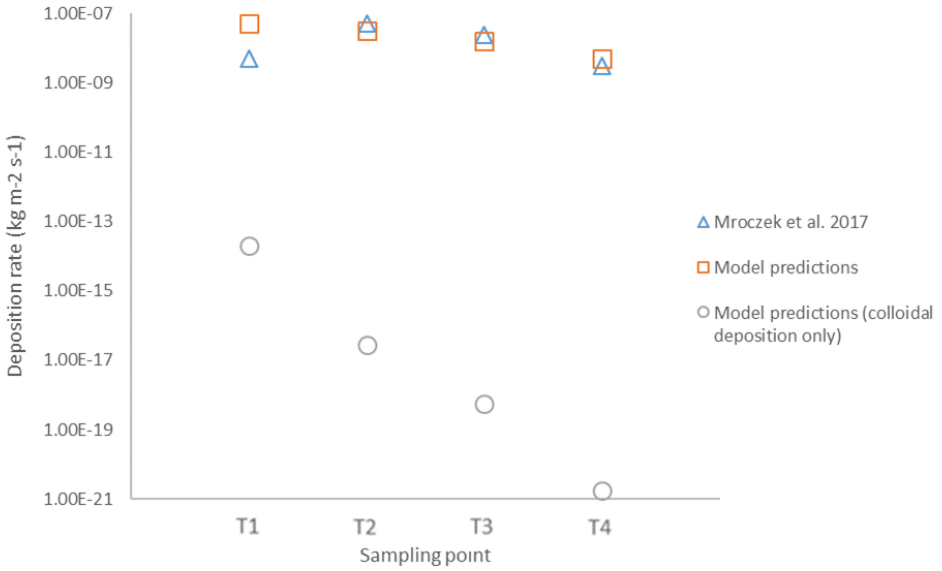

Figure 8.13: Comparison between the observed (at 46 days) and the predicted in situ silica deposition rate (kg m^{-2} s^{-1})

For comparison, the deposition rates of colloidal silica alone (excluding molecular deposition) are shown in the last column of Table 8.5, which suggests that the molecular deposition is the dominant silica scaling mechanism. Under the conditions summarised in Table 8.4, the predictions in the third column of Table 8.5 match the observations to at least one order of magnitude, and usually better. The exception is at T1, where the experimental observations show a rapid rise in deposition rate from T1 to T2. In the model, while the molecular deposition rate constantly decreases from the inlet, the colloidal deposition rate varies very slightly near the inlet and begins to drop near T2.

Since the effects of ions other than Na^+ and Cl^- on the interactions of colloidal silica are not included in the proposed model yet, the deposition of flocculated (aggregated) colloidal silica due to iron corrosion which was observed by Mroczek et al. 2017 is not modelled in the present work. This may have a role in explaining the discrepancy of one order of magnitude between the observation and the prediction at T1. Also, as mentioned before, the effects of multivalent ions such as Al^{3+} are included only in the form of ionic strength, which is a major simplification and source of errors as well. Due to this, colloidal stability may be overestimated and colloidal deposition rate may be underestimated. The (perhaps unfeasibly large) size of the difference between the predicted molecular and colloidal deposition rates could be a consequence of this.

Despite the discrepancy, the modelling results suggest that the dominant mechanism for silica scaling should be the molecular deposition, and the deposition of colloidal silica in these aged brines may be negligible, which is consistent with Mroczek et al.'s (2017) conclusion, and indeed the aim of their tests was to suppress colloidal deposition.

The low colloidal deposition rate may be due to, on one hand, the relatively small particle size (compared to unaged brines) which leads to a weaker attractive London-van der Waals' force and hence it becomes more difficult for the suspended particles to overcome the repulsive electrostatic force to reach the fracture surface (i.e. deposit), resulting in a negligible deposition rate of colloidal silica in this case. On the other hand, although a considerable amount of the dissolved silica has been consumed rapidly to form silica nanoparticles near the inlet of the

fluid pathway, the remaining concentration of dissolved silica is still high enough to yield a considerable molecular deposition rate.

8.5.3 Summary

The comparison shown Table 8.5 and Figure 8.13 suggests that the model is capable to reproduce the real world experience in the Ohaaki field, New Zealand, in the correct order. The silica deposition is predicted to be controlled by the molecular deposition, which is in agreement with Mroczek et al. (2017). The non-penetration model is considered to be a valid boundary condition at wall when modelling the transport of silica particles. The colloidal deposition in the timescale of the experiment is expected to be negligible.

8.6 Hellisheiði geothermal power plant, SW-Iceland

Van den Heuvel et al. (2018) reported the first ever industrial-scale and time-resolved (up to 10 weeks) field silica scaling investigation in the Hellisheiði geothermal power plant, Iceland. By using S316 stainless steel plates ($5.4 \times 2 - 2.5$ cm) mounted in the working pipelines for transporting geothermal fluids and having their surfaces aligned to the direction of the flow, Van den Heuvel et al. (2018) measured the silica scaling rates and investigated the morphologies of the scales to identify the deposition mechanisms. The silica scales were observed as two major forms: a botryoidal dense silica precipitate layer and a fan or ridge-shaped 3D structured silica aggregate. These observations suggested (Van den Heuvel et al. 2018) that the silica deposition mechanisms are (1) heterogeneous nucleation on the wall and the subsequent growth due to fast deposition of monomeric silica; (2) homogeneous nucleation and the subsequent growth, aggregation, and cementation with coagulation agents such as Al^{3+} and Fe^{3+} involved. As mentioned previously, the former mechanism is treated as pure monomeric deposition (i.e. the "clean" collector surface is coated instantaneously with silica once submerged in the fluids supersaturated with silica), the later one is treated as the interactions between suspended silica nanoparticles and the silica-coated plates, and the effects of multivalent cations are reflected by using the ionic strength only (i.e. the effects of coagulation agents are modelled indirectly through ionic strength).

8.6.1 Inputs

During the field experiments, Van den Heuvel et al. (2018) constantly monitored the physical and chemical conditions of the geothermal fluids, which brought convenience for comparison. Unfortunately, a few inputs that are used in previous sections are missing, such as the dimension of the pipe, the exact locations and the corresponding residence time of the sampling points. However, the in situ concentrations of the dissolved and polymerised silica were measured and reported. Therefore, in this section, the experiments are modelled by four simulations. In each simulation, the geothermal fluids flow over a 5.4×2.25 cm plate under similar conditions in the experiments, which are summarised in Table 8.6 below. Considering that the flow rate is relatively large ($\sim 282 - 430$ L s^{-1}) and no significant change of the silica concentration should occur along the plate, the residence time is set to be ten seconds, which is an arbitrary value that serves to guarantee the conditions are relatively steady within the residence time.

Table 8.6: Summary of the input parameters, derived from Van den Heuvel et al. 2018.

	Location 1	Location 2	Location 3	Location 4

Temperature (℃)	117.8 ± 0.4	56.6 ± 1.6	58.0 ± 5.3	72 ± 11.2
Assumed pH (explained below)	9.4 ± 0.2	9.4 ± 0.2	9.4 ± 0.2	9.1 ± 0.3
Lowered pH	8.0	8.0	8.0	8.0
Ionic strength (estimated, M)	0.0082	0.0082	0.0083	0.0057
Monomeric [SiO_2] (ppm)	681.70	652.01	599.47	471.90
Polymerised [SiO_2] (ppm)	120.30	148.99	194.53	78.10

However, at 117.8 ℃, the solubility of amorphous silica predicted by the formula (Equation 2.7, valid till pH 9.5) proposed by Henley (1983) can increase from 507.5 ppm at pH 8 to 1969.3 ppm at pH 9.4, as shown in Figure 8.14 below.

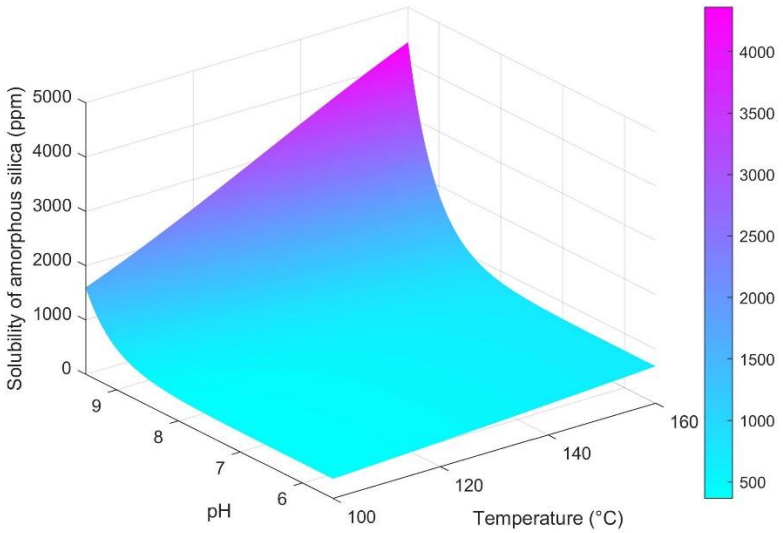

Figure 8.14: Estimated solubility of amorphous silica as a function of pH and temperature.

This is problematic, as, predictably, the solution becomes undersaturated with amorphous and no silica deposition is expected. This suggests that either the solubility formula may not be very reliable when pH is greater than 8 at relatively higher temperatures, or possibly that the effect of chemical impurities on the solubility under these conditions may be significant. Therefore, to compare the results, an assumed lowered pH, 8 is used.

8.6.2 Results and discussion

By using the inputs listed in Table 8.6, the predicted silica deposition rate in each experiment can be found, given in Table 8.7 below:

Table 8.7: Comparison between the predictions made in the current work and the observations reported in Van den Heuvel et al. 2018. The unit of deposition rate is kg m^{-2} s^{-1}.

	Observed silica deposition	Predicted total silica	Predicted colloidal silica	Predicted total silica	Predicted colloidal silica

		rates (at measured pH)	deposition rates (at assumed pH)	deposition rates (at assumed pH)	deposition rates (at measured pH)	deposition rates (at measured pH)
Location 1	1 day	1.19×10^{-8}	4.01×10^{-9}	7.92×10^{-13}	-	-
	3 days	8.89×10^{-9}	4.01×10^{-9}	7.92×10^{-13}	-	-
	1 week	8.87×10^{-9}	4.01×10^{-9}	7.92×10^{-13}	-	-
Location 2	1 day	1.30×10^{-8}	7.14×10^{-9}	1.02×10^{-12}	2.70×10^{-10}	1.10×10^{-12}
	3 days	8.75×10^{-9}	7.14×10^{-9}	1.02×10^{-12}	2.70×10^{-10}	1.10×10^{-12}
	1 week	8.30×10^{-9}	7.14×10^{-9}	1.02×10^{-12}	2.70×10^{-10}	1.10×10^{-12}
Location 3	1 day	9.29×10^{-9}	4.50×10^{-9}	1.33×10^{-12}	1.21×10^{-10}	1.45×10^{-12}
	3 days	9.06×10^{-9}	4.50×10^{-9}	1.33×10^{-12}	1.21×10^{-10}	1.45×10^{-12}
	1 week	7.67×10^{-9}	4.50×10^{-9}	1.33×10^{-12}	1.21×10^{-10}	1.45×10^{-12}
Location 4	1 day	3.65×10^{-9}	9.29×10^{-10}	5.29×10^{-13}	5.72×10^{-10}	5.29×10^{-13}
	3 days	9.49×10^{-10}	9.29×10^{-10}	5.29×10^{-13}	5.72×10^{-10}	5.29×10^{-13}
	1 week	2.19×10^{-9}	9.29×10^{-10}	5.29×10^{-13}	5.72×10^{-10}	5.29×10^{-13}

According to the comparison, apart from Location 1 where the silica deposition rate is expected to be zero as the geothermal fluids are predicted to be undersaturated, the discrepancy is less than two orders of magnitude; however, once the pH is lowered to 8 in the model, the predictions match the observations better as the discrepancy becomes within one order of magnitude. Therefore, it is considered that the discrepancy could be due to the unreliability of the solubility formula used in the modelling when pH > 8 at relatively high temperature or the possible effect of chemical impurities on the solubility is significant under these conditions.

Colloidal silica deposition is predicted to be less important than monomeric silica deposition and varies little with position, i.e. the molecular deposition mechanism dominates in all cases. This agrees with the conclusion of Van den Heuvel et al. It was also reported (Van den Heuvel et al. 2018) that the thickness of the silica scale layers on the top face, the bottom face, and edges of the plate have no difference. Van den Heuvel et al. (2018) suggested that it indicates the gravity has no or negligible effect on monomeric silica deposition, which supports the author's findings described in Section 6.6.4. Similar to the predictions, deposited colloidal silica was observed in all sampling locations.

It is worth noting that platy alumosilicates were observed by Van den Heuvel et al. (2018) using FEG-SEM (Field Emission Gun Scanning Electron Microscopy), which is not modelled in the current work.

8.6.3 Summary

The comparison shown Table 8.7 suggests that the model is capable to reproduce the real world experience in the Hellisheiði field, Iceland, in the correct order. The estimated deposition rate is shown to be not sensitive to the residence time, whereas, in the experiment, it can vary up to

one order of magnitude. Still, the predictions at pH > 8 may or may not accurate, especially at higher temperatures. The negligible effect of net gravity on silica deposition is confirmed.

8.7 Tiwi geothermal field, Philippines

The injector Nag-67 in Tiwi geothermal field, Philippines experienced severe scaling problems with the injection rate declining from approximately 140 to almost 5 kg s^{-1} (i.e. from 4.6 to 0 kg s^{-1} bar^{-1}) over 12 years. In this section, the observed injectivity drop in Tiwi geothermal field is reproduced using the developed holistic model.

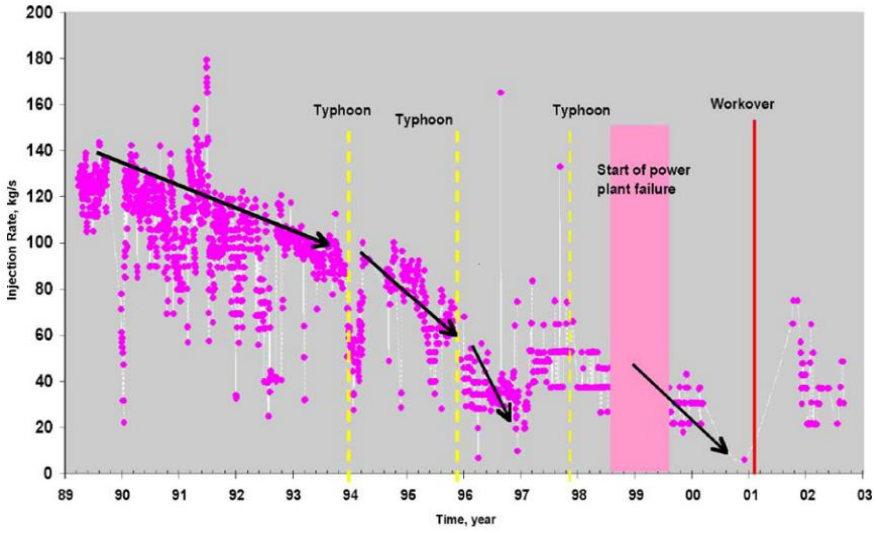

Figure 8.15: Historical records of injection rate decline of the injector Nag-67, reproduced from Xu et al. 2004. However, it should be noted that, depending on the wellhead pressure, a reduction in injection rate does not necessarily mean a reduction in injectivity.

8.7.1 Inputs

The controlling parameters and typical values used for simulations are summarised in Table 8.8. The values below are reproduced from Xu et al. 2004, where injectivity drop is reported at Tiwi field, Philippines. The unreported data are highlighted and replaced with typical assumed values typical of fields in the New Zealand Taupo Volcanic Zone.

Table 8.8 Summary of input parameters for the case of reinjection in Tiwi geothermal field

Notation	Value used	Explanation	Notation	Value used	Explanation
t_{max}	12 year	Time after injection begins	pH_{inj}	7	Initial pH of injected fluid[a]
t_{ageing}	35 min	Ageing time before reinjection[c]	pH_{res}	7	Initial pH of reservoir fluid[a]
R_0	0.122 m	Radius of injection wellbore	I_{inj}	0.09 mol/kg	Initial ionic strength of injected fluid[b]
H	120 m	Thickness of feedzone	I_{res}	0.07 mol/kg	Initial ionic strength of reservoir fluid[b]
a_0	15.4 mm	Initial fracture aperture	c_0^{SiO2}	1272 ppm	Initial concentration of monomeric silica in geothermal fluid
ϕ_0^r	0.01	Initial reservoir porosity	c_{inj}^{SiO2}	705 ppm	Concentration of monomeric silica in geothermal fluid before injection[c]

ϕ_0^f	1	Initial fracture porosity	c_{res}^{SiO2}	620 ppm	Initial concentration of monomeric silica in reservoir fluid
k_0^f	5.0×10^{-12} m^2	Initial permeability of fractures	c_{inj}^{cp}	567 ppm	Initial concentration of polymerised silica in injected fluid
$\dot{m}$	60 kg/s	Injecting mass flow rate	c_{res}^{cp}	0 ppm	Initial concentration of polymerised silica in reservoir fluid[d]
T_{inj}	160 ℃	Initial temperature of injected fluid	n	4	Power exponent of Equation 8.2
T_{res}	260 ℃	Initial temperature of reservoir			

Notes: a: equivalent pH at the room temperature; b: sodium chloride is assumed to be the only electrolyte in the injected brine; c: as the injectate is reported to be containing both dissolved and polymerised silica, the initial concentration of dissolved silica c_0^{SiO2} are assumed to model the ageing process to match the concentration of dissolved silica $c_{\mathrm{inj}}^{\mathrm{SiO2}}$ at the end of the ageing and the beginning of the injection; d: it is assumed that before the reinjection (i.e. $t < 0$) there is no polymerised silica in reservoir fluid.

8.7.2 Results and discussion

The predicted silica deposition rates are shown in Figure 7.1 below:

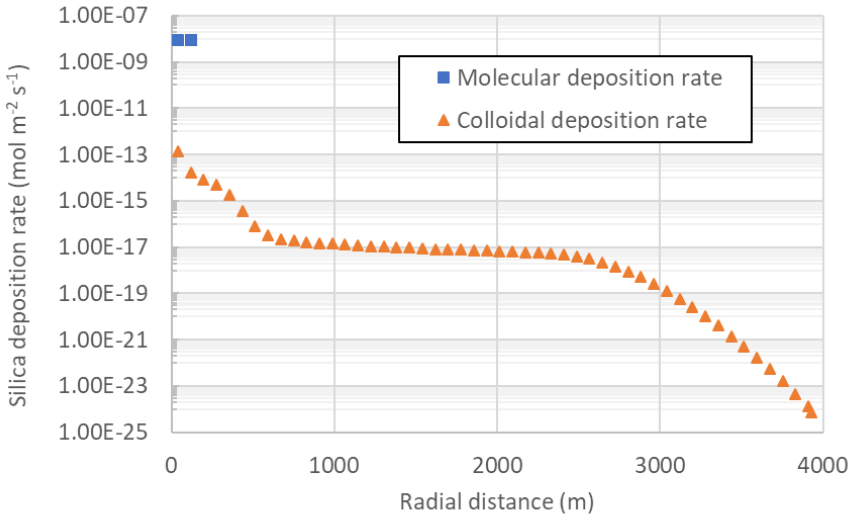

Figure 8.16: Expected silica scaling rate (kg m^{-2} s^{-1}) at the 12th year of geothermal reinjection at Tiwi field, Philippines.

The simulation results above suggest that the silica scaling mainly occurs near the injection wellbore, which agrees with the conclusion of Xu et al. (2004). Under the conditions described in Table 8.8, the molecular deposition rate is predicted to be 3.79×10^{-9} kg m^{-2} s^{-1} in the control volume that is the nearest to the wellbore (i.e. the fracture entrance) and drop to a negligible value in the rest of reservoir where the colloidal silica deposition dominates. In the aspect of depositing area, the area of molecular deposition is a lot more concentrated than that of colloidal deposition. In this case, in the radial direction, only the area from wellbore to less than 40 metres (i.e. the first cell in the computational mesh) is affected by molecular deposition, whereas, colloidal deposition is predicted out to 4000 metres.

This may be due to the ageing process, in which the concentration of dissolved silica decreases due to polymerisation and molecular deposition. Recall that, in the holistic model, no molecular deposition on the collector surfaces (e.g. pipeline and pond surfaces) is considered in the ageing process, i.e. the dissolved silica is consumed only by the formation of silica particles. Therefore, the total concentration of silica in the injectate is fixed before reinjection.

To find the injectivity II, recall that II is defined by:

$$II = \frac{\dot{m}}{P_{inj} - P_{res}} \tag{8.1}$$

where $\dot{m}$ is the injection mass flow rate, P_{inj} is the pressure of the injected fluid, and P_{res} is the far-field pressure of the reservoir.

Accumulating the deposition over time gives the change in fracture porosity directly. A correlation between porosity and permeability is given by Verma and Pruess 1988:

$$\frac{k^f}{k_0^f} = \left(\frac{\emptyset^f - \emptyset_c^f}{\emptyset_0^f - \emptyset_c^f}\right)^n \tag{8.2}$$

where, $\emptyset_c^f$ is the critical porosity, and n is the power law exponent.

Based on Darcy's law, the following expression can be derived for the horizontal radial flow:

$$\dot{Q} = \frac{\dot{m}}{\rho} = \frac{2\pi k^f a_0 (P_{inj} - P_{res})}{\mu \ln \frac{R_{max}}{R_0}} \tag{8.3}$$

where, R_{max} represents the radius of the domain. By coupling Equation 8.1, 8.2, and 8.3, the goal of the holistic model, the injectivity over time, can be computed.

The computed injectivity as a function of time is shown in Figure 8.17 below:

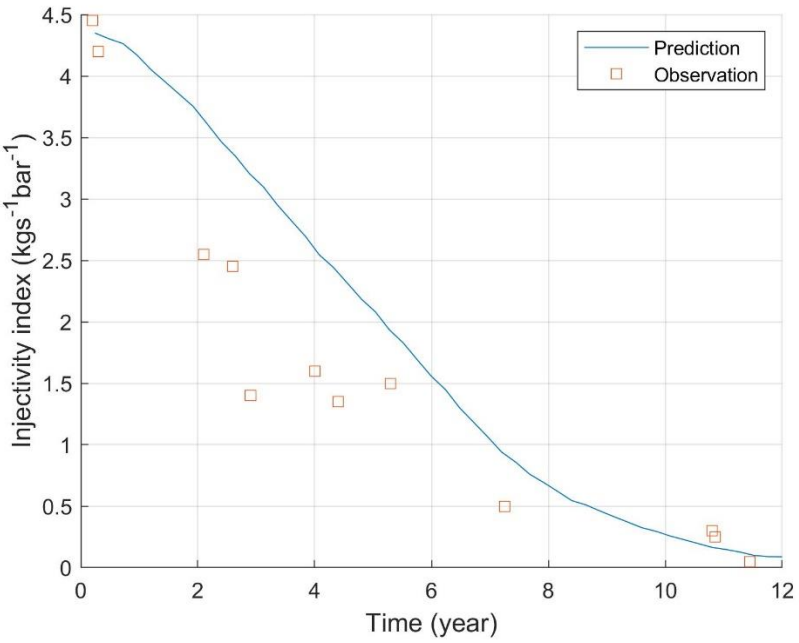

Figure 8.17: Expected injectivity curve after 12-year geothermal reinjection vs. observations reproduced from Xu et al. 2004.

The injectivity curve shows a decline, at decreasing rate, in line with the modelling results of Xu et al. 2004. The discrepancy may be due to different reservoir geometries, e.g. fracture dimensions, permeable zone thickness etc.

8.7.3 Summary

The comparison shown Figure 8.17 suggests that the model is capable to reproduce the historical injectivity data in the Tiwi field, Philippines, in the correct order. At this stage, it may be reasonable to conclude that the model can be useful in making predictions of injection lifetime under these conditions, and some limitations should be noted, such as the lack of ability to estimate the effects of chemical impurities such as multivalent ions and the less reliability of the model when pH is greater than 8. In the case of the Tiwi field, compared to the other cases discussed in this chapter, no significant concentration of trivalent ions such as Al^{3+} is reported. Therefore, as the model does not include their effects, it may give better predictions for Tiwi field than for other fields where trivalent ions are present in higher concentrations.

8.8 Sensitivity analysis

A sensitivity analysis is conducted on the following six controlling parameters in this section to qualitatively study how the parameters affect the predicted injectivity.

For the ease of comparison, the inputs shown in Table 8.8 to model the injectivity drop observed in Tiwi geothermal field, Philippines are reused here.

8.8.1 Effects of injection temperature

The injection temperature dominates the solubility of amorphous silica. Generally, it is expected that, with a fixed initial concentration of dissolved silica and other conditions, the lower the injection temperature is, the higher the rate of silica scaling.

However, once the ageing process is taken into account, the results can be different from the expectations. When the separated geothermal water is not fully aged and injected at a certain temperature, as the solution does not reach its equilibrium state (i.e. the silica supersaturation index (*SSI*) is close to, but still greater than one, it results in a non-zero molecular deposition rate near the injection wellbore and the possible formation and growth of silica particles still. If the temperature can be lowered, as the initial *SSI* is higher and then the silica polymerisation is more rapid, the geothermal brine will reach its equilibrium in a shorter period. The ageing, while previously insufficient, can become sufficient. This leads to zero molecular deposition rate and no silica particles newly formed (growth via Ostwald ripening or aggregation is still possible).

When the ageing process is believed to be insufficient at the present injection temperature, lower temperature may result in faster consumption of dissolved silica in the ageing process and could have positive effects on extending the reinjection lifetime by minimising the possibility of molecular silica deposition in the reservoir formation.

For example, by decreasing the injection temperature T_{inj} from 160 ℃ to 140 and 110 ℃, the predicted deposition rates and the estimated injectivities over time is shown in Figure 8.18.

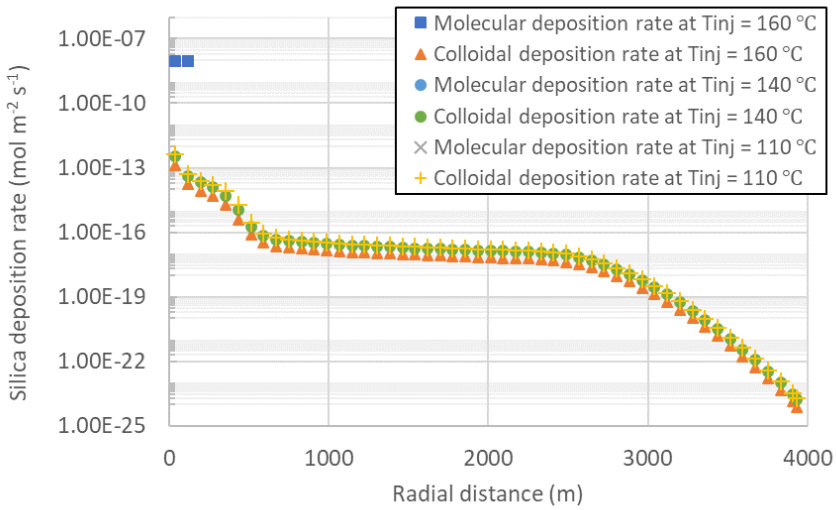

(a)

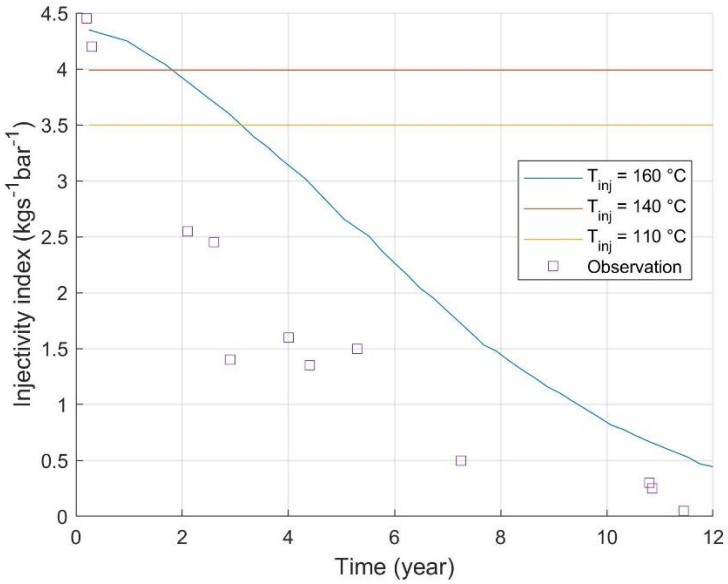

(b)

Figure 8.18: Comparison of (a) silica scaling rates (b) injectivities at different injection temperatures. Note that the molecular rates shown in (a) are zero for 140 and 110 ℃.

As shown in Figure 8.18 (a), the molecular deposition rate at 110 ℃ is predicted to be smaller by two orders of magnitude than that at 160 ℃, and the lifetime of injection is significantly extended. As the colloidal deposition rate only slightly increases, the decrement of the molecular deposition rate can be the reason for the extended reinjection lifetime. When the injection temperature T_{inj} is decreased, the drop of the initial injectivity (i.e. II at $t = 0$) is due to the viscosity μ being increased.

8.8.2 Effects of injection mass flow rate

The injection mass flow rate determines the convection rate in the radial direction. The result of adjusting the injection mass flow rate from 60 kg/s to 90 kg/s, is shown in Figure 8.19 below:

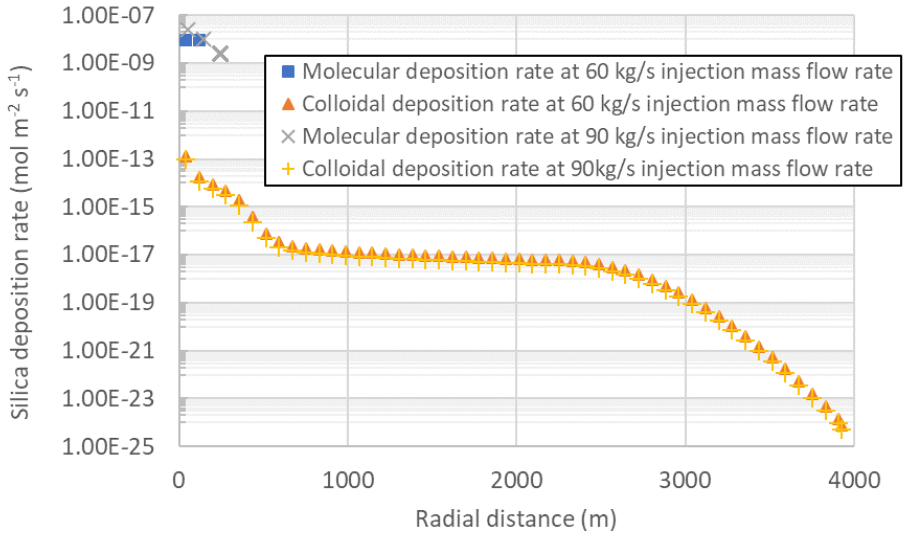

(a)

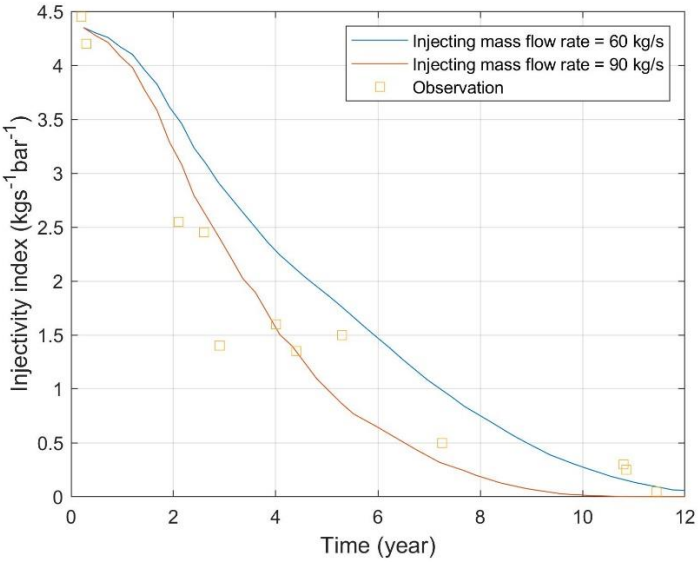

(b)

Figure 8.19: Comparison of (a) silica scaling rates (b) injectivities at different injection mass flow rates.

The comparison shows moderate changes due to the higher injection flow rate. Within a unit time, at a higher injection flow rate, more silica that could potentially deposit and damage the reservoir formation would be injected. This is reflected in the deposition rates and the injectivity curve (Figure 8.19 (a) and (b)): the molecular deposition rate only varies within one order of magnitude, but the area affected by deposition increases by about three times, which causes a more rapid injectivity drop.

8.8.3 Effects of acidification

As described previously, acidification is frequently used in the industry to inhibit the formation of colloidal silica, and therefore the silica scaling. It can be effective, but risk still exists when carbonate minerals (e.g. calcite) are abundant in the reservoir formations. Also, it should be noted that the inhibition is a kinetic effect and the silica will polymerise eventually.

While silica scaling is occurring, the reactive surface may be gradually covered up. Unfortunately, to the best of author's knowledge, there appears to be no well-recognized theory to predict the variation of the reactive surface area due to silica scaling. Considering that the variation of the reactive surface is very complex to describe, especially for the systems of multimineral (Xu et al. 2007), the relevant models such as TOUGHREACT (Xu et al. 2006) assume the reactive surface area to be independent of time. Here, to expose the risk of reservoir formation damage due to silica scaling as much as possible, the reactive surface area is treated as fixed as well.

By adjusting pH of the injectate from neutral to 4.5 and setting the percentage of the reaction surface area of calcite to 100% (to maximise the negative effects of calcite on acidification), the simulation results are shown in Figure 8.20 below:

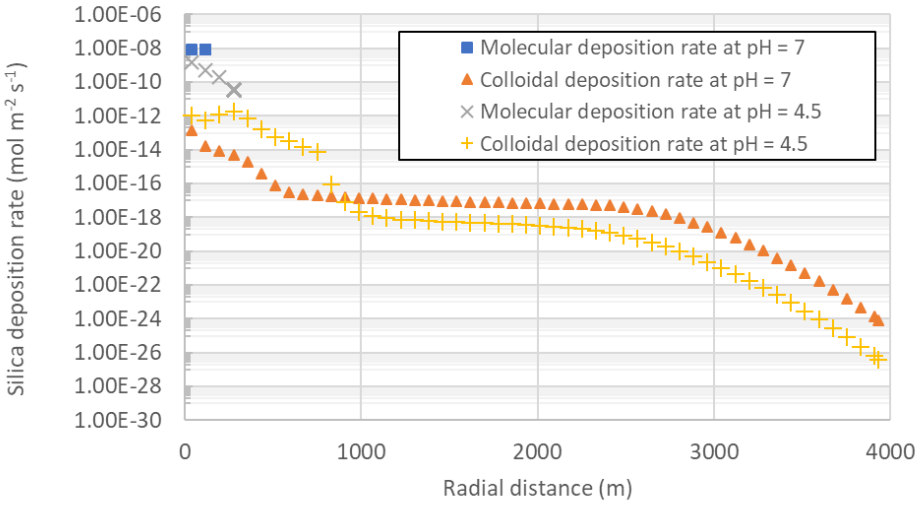

(a)

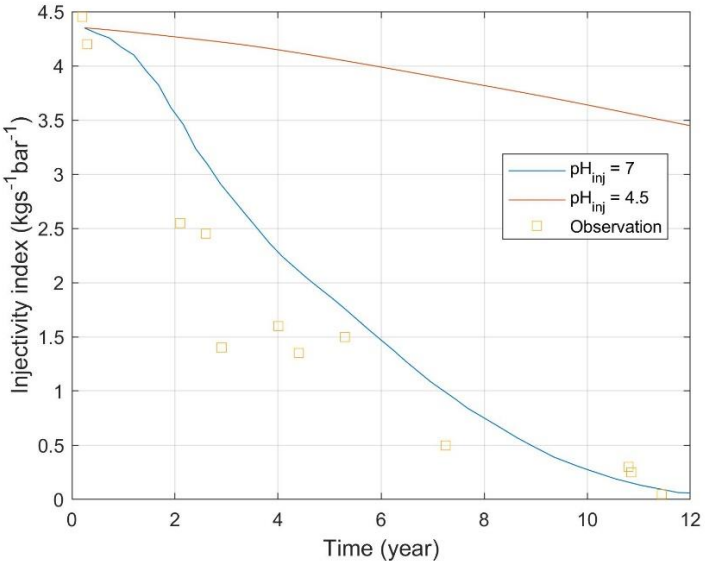

(b)

Figure 8.20: Comparison of (a) silica scaling rates (b) injectivities at different pH.

Similar to the case of higher injection mass flow rate, the area of molecular deposition increases by a factor of two, but the rate of deposition is lower. This is expected as the formation of silica nanoparticles is limited at lower pH in the ageing process, and more dissolved silica "survived" from it, i.e. more dissolved silica is available for deposition in the later stage. Despite the concentration of colloidal silica being limited when pH is relatively low, the predicted magnitude of colloidal silica deposition rate does not change much. This could be explained by the relatively low stability of silica nanoparticles at lower pH, i.e. it is easier for colloidal silica to attach at lower pH. In the later stage, the acid is neutralised by the dissolution of calcite, and then pH rises again. This triggers the formation of colloidal silica. Therefore, the expanded area of colloidal deposition can be observed in the modelling results.

The estimated lifetime of reinjection extends when acidification is applied. This is mainly due to the lowered molecular deposition rate near the fracture entrance. However, the decrement is still obvious, which suggests that, theoretically, the risk of silica scaling may still exist as (1) the holistic model does not consider the effect of ions other than sodium and chloride ions and coagulation agents (such as aluminium and iron ions) will accelerate the molecular and colloidal deposition rates respectively; (2) other parameters reflecting the properties of reservoir such as the critical porosity and power exponent may change the injectivity as well, as discussed in Section 8.8.4.

The risk of anhydrite precipitation is monitored by tracking the activity product of calcium and sulphate ions. The holistic model suggests that the risk can be negligible if the amount of sulphuric acid used is carefully controlled and not exceeding the current typical value (approximately 10^{-5} M). This conclusion agrees with Wong et al. 2015.

One should note that, to expose the risk of the acidified injectate being neutralised, what is modelled in this section is an extreme case, i.e. the percentage of the reaction surface area of calcite is 100%. This case could be extremely rare in real world. Commonly, the typical value would be a maximum of 5%. Therefore, in practice, acidification is still an effective method to inhibit silica scaling during the geothermal reinjection.

8.8.4 Effects of critical porosity and power exponent

As shown in Equation 8.1, 8.2, and 8.3, the critical porosity $\emptyset_c$ and the power exponent n have direct effects on the estimated injectivity. By adjusting the two parameters, the computed results are shown in Figure 8.21 below:

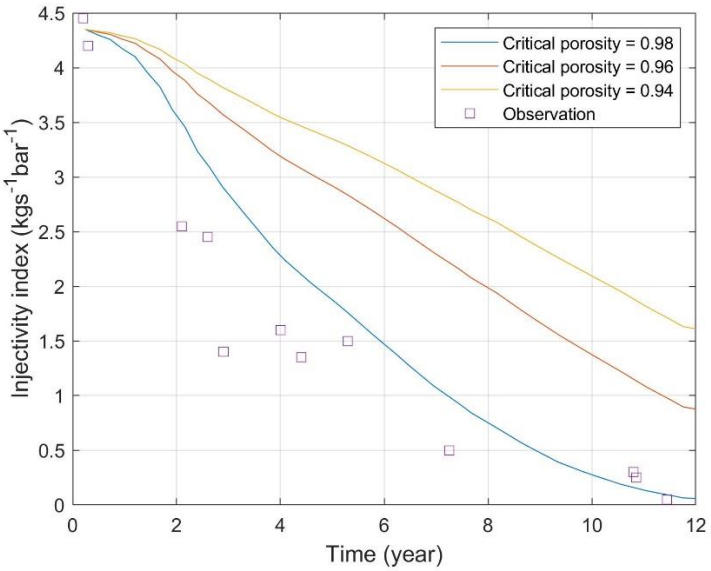

(a)

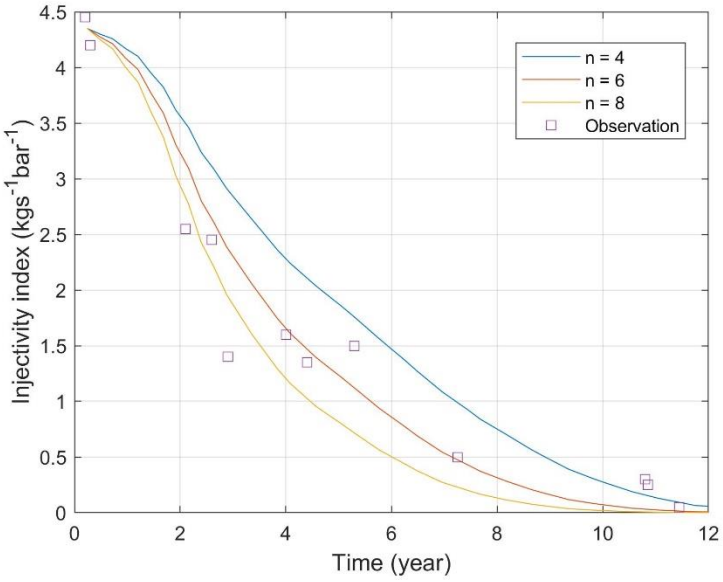

(b)

Figure 8.21: Comparison of injectivities at different (a) critical porosities $\emptyset_c$ and (b) power exponents n.

The comparison suggests that the critical porosity $\emptyset_c$ and the power exponent n share similar effects on the estimated injectivity: higher $\emptyset_c$ and n leads to faster decreasing rate, and lower $\emptyset_c$ and n result in slower decreasing rate.

8.8.5 Effects of feedzone thickness

The effects of a varying feedzone thickness *H* are expected to have similar effects with injection mass flow rate: the effects of a smaller feedzone thickness (or porosity) should be qualitatively equivalent to higher mass flow rate; the effects of a larger feedzone thickness (or porosity) should be qualitatively equivalent to lower mass flow rate. By adjusting the feedzone thickness, the simulation results are shown in Figure 8.22 below:

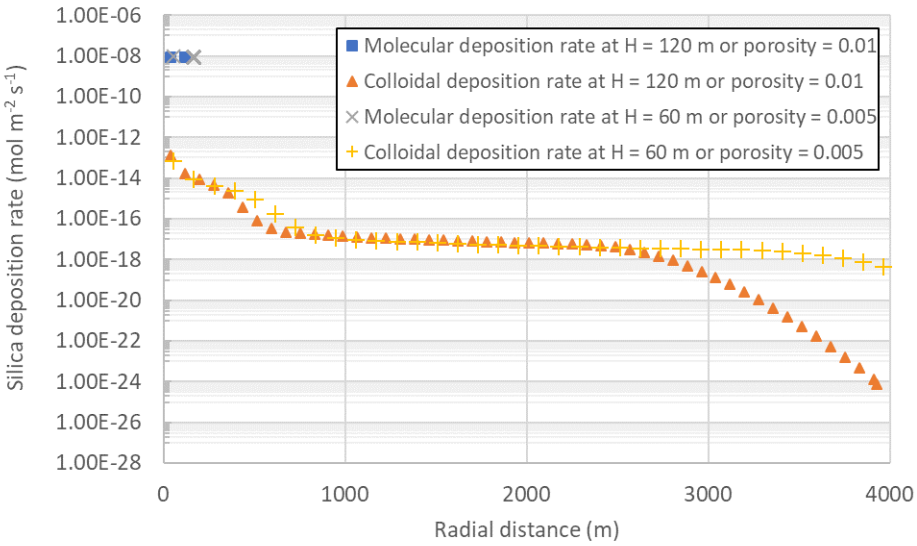

(a)

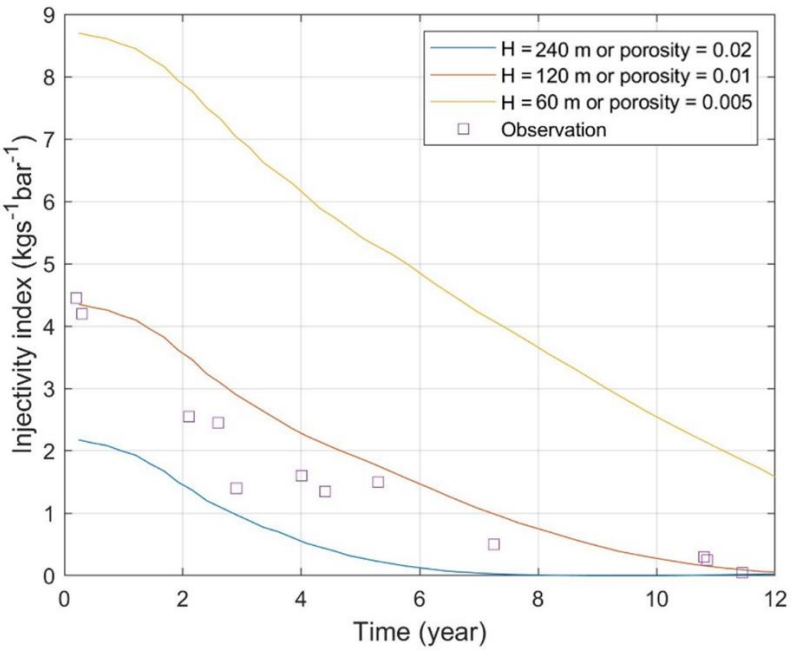

(b)

Figure 8.22: Comparison of (a) silica scaling rates (b) injectivities at different feedzone thickness *H*.

Note that Figure 8.22 (a) only shows two cases for clarity. The comparisons agree with the expectations. The larger feedzone thickness (equivalent to higher porosity) leads to the lower

mass flow rate, which results in lower initial injectivity, slower injectivity drop rate, and more concentrated depositing area.

8.8.6 Effects of fracture aperture

The fracture aperture a_0 is expected to have a direct effect on the injectivity, as, for the same deposition rate, the injectivity drop will be slow when the aperture is larger, but rapid for narrower fractures.

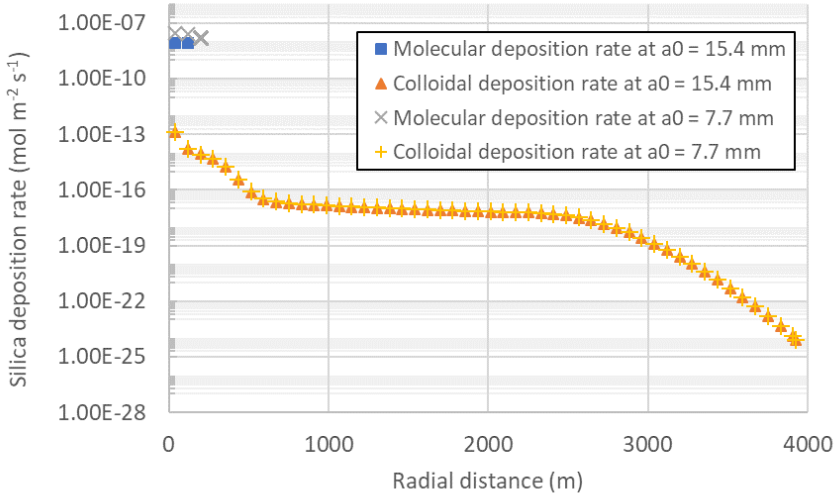

(a)

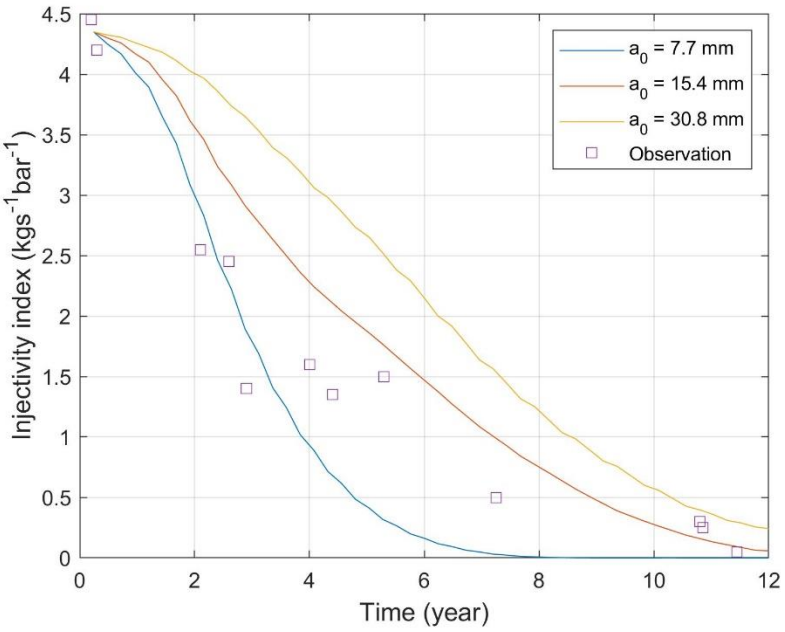

(b)

Figure 8.23: Comparison of (a) silica scaling rates (b) injectivities at different feedzone thickness a_0.

Note that Figure 8.23 (a) only shows two cases for clarity. The results shown in Figure 8.23 (a) suggest that the deposition rate varies negligibly and the injectivity shown in Figure 8.23 (b) drops as expected.

8.8.7 Summary of sensitivity analysis

The findings in the sensitivity analysis are summarised here.

When the ageing process is insufficient at the present injection temperature, lower temperature may result in faster consumption of dissolved silica in the ageing process and could have positive effects on extending the reinjection lifetime.

Despite the presence of carbonate minerals which could neutralise the acid and cancel the inhibiting effect on silica scaling, in practice, acidification is still an effective method to inhibit silica scaling during the geothermal reinjection. The risk of anhydrite precipitation is usually negligible if the amount of sulphuric acid used is carefully controlled. Also, when the estimation shows an immediate anhydrite oversaturation (e.g. Salton Sea), hydrogen chloride acid instead of sulphuric acid can be used to avoid anhydrite deposition.

A higher mass flow rate could moderately shorten reinjection lifetime essentially due to more silica available to deposit is injected to the reservoir formation per unit of time. Similarly, the larger feedzone thickness (equivalent to higher porosity) leads to the lower mass flow rate in each fracture, which results in lower initial injectivity, slower injectivity drop rate, but more concentrated depositing area.

When estimating the injectivity, the critical porosity $\emptyset_c$ and the power exponent n share similar effects: higher $\emptyset_c$ and n leads to a faster decreasing rate of injectivity and therefore a shorter lifetime of reinjection, and lower $\emptyset_c$ and n result in slower decreasing rate and therefore a longer lifetime of reinjection. The fracture aperture a_0 can have a direct effect on the injectivity, as, for the same deposition rate, the injectivity drop will be slow when the aperture is larger, but rapid for narrower fractures.

8.9 Summary

In this chapter, the holistic model is shown to be capable of predicting the in situ silica deposition rate and the time-resolved injectivity drop due to silica scaling. The discrepancies can be within one order of magnitude or better. Overall, the deposition rate is expected at its maximum near the fracture entrance and gradually decreases.

In all cases studied, under typical reinjection conditions, molecular silica deposition is shown to play a very important role in determining the lifetime. Once it can be inhibited or even eliminated, the lifetime of reinjection is expected to extend significantly. The colloidal deposition rate is dependent on the variables that determine the interactions between silica such as pH, ionic strength, and the average size of the formed particles. Specifically, lower pH and ionic strength, and smaller particles usually results in lower estimated colloidal deposition rates.

Presence of chemical impurities such as multivalent ions can strongly affect deposition rates and needs further work (needs in fact further experimental data) to be modelled. The performance of the holistic model is also limited when pH is above than 8.

Based the sensitivity analysis of the holistic model summarised in detail in Section 8.8.7, there are several findings that may be useful for extending the reinjection lifetime, such as:

moderately lowering the injection temperature if ageing is insufficient; acidifying the injectate despite the acid can be neutralised by carbonate minerals; decreasing the mass flow rate in each fracture by decreasing the total injection mass flow rate or deepening the feedzone thickness if possible.

Chapter 9

Stimulation of geothermal injection

In this chapter, some concepts for increasing injectivity are modelled using the holistic model. To ease the injection, three targets are of interest: the reservoir, the formation of scale, and the deposited mass. Therefore, the discussions of the potential techniques in the following sections focus on dissolution of calcite, control of silica polymerisation and particle formation, removal of silica from injectate, and dissolution of deposited silica.

9.1 Ageing

Recall the simulation results shown in Section 8.8.1: a proper ageing process may allow the geothermal fluids to be cooled to a relatively low temperature without shortening the lifetime of injection. This is similar to the findings of Mroczek et al. (2017): the injectate can be as low as 30 ℃ without causing any notable scaling problem.

The reason behind this is that at such temperatures, both molecular deposition rate and homogenous nucleation rate are very high. For example, at 30 ℃, the predicted initial silica molecular deposition rate of the geothermal brines dissolved with 1200 ppm silica at pH 7, 0.09 M can be as high as 1.12×10^{-9} kg m^{-2} s^{-1}, and the predicted initial homogenous nucleation rate is 3.52×10^{22} m^{-3} s^{-1}. This means that, within 30 minutes, the concentration of dissolved silica can rapidly drop from 1200 ppm to about 173 ppm, i.e. more than 85% of dissolved silica polymerises and forms silica nanoparticles in a fairly short period of time. At this stage, the silica molecular deposition rate drops by three orders of magnitude to 1.64×10^{-12} kg m^{-2} s^{-1}. As suggested in Section 4.1.2 and 4.2.2, the average diameter of the formed silica particles is less than 8 nm, and more importantly, the smaller particles usually have a higher stability ratio W than the larger particles, i.e. deposit at lower rates. Thus, the risk of silica scaling reduces as the brine is aged and cooled.

However, as uncertainties like the effects of multivalent ions still exist, field experiments are necessary to fully understand how best to use ageing.

9.2 Silica extraction

Essentially, the silica can be removed from geothermal fluids in the form of either solid scale or filtered colloids.

As mentioned previously, in the ageing process, the silica molecular rate can be high. A portion of dissolved silica may easily and rapidly deposit monomerically on the surfaces of interest such as walls of pipeline and ageing pond. A dense scale forms due to this and usually is very hard to remove. On the other hand, the colloidal silica forms via silica polymerisation. Under specific conditions, such as a high ionic strength, the existence of multivalent ions, etc., silica colloids can attach to surfaces quickly. A porous scale forms due to this. As the former (monomeric) deposition mechanism is commonly dominant in the early stage of silica scaling, dense silica scales have frequently observed in pipelines, ageing ponds, and even wellbore surfaces. Therefore, the silica deposition may be lowered by allowing silica deposition to occur in a favoured location, where the dense silica scale shall be conveniently removed, such as a fluidised bed reactor (FBR) filled with amorphous silica grains. For instance, for the separated geothermal water dissolved with 800 ppm silica under the condition of 80 ℃, pH 7, and ionic strength of 0.07 M, approximately 25% of total dissolved silica can be removed within a day by ageing in a container having the reactive surface area of 400 m^2/m^3 (estimated using SILNUC described in Section 4.1.1).

This method could extend the injection lifetime, but may not be easy to apply in practice, as it requires large surface areas to deposit and may not be capable of avoiding the formation of colloidal silica, therefore the risk of colloidal deposition still remains. Further investigation is needed.

To remove the suspended silica colloids, one can either accelerate the colloidal deposition in a favoured location by adding chemicals like coagulation agents or using other innovative techniques such as Electrocoagulation (EC), electroflotation (EF), or electrocoagulation/flotation (ECF). EC, EF, and ECF are found to be useful for pollutants (e.g. inorganic contaminants, pathogens) removal from water and wastewater (Joffe and Knieper 2000; Emamjomeh and Sivakumar 2008). EC is a technique to destabilise the pollutants by introducing an electric current, as the metal "sacrificial electrodes" produce destabilisation agents (e.g. Al^{3+} and Fe^{3+}) that will neutralise the surface charge of the contaminates and lead to coagulation; EF introduces the hydrogen gas bubbles generated at the cathode that may adhere to the coagulated clusters of pollutants and float these to the water surface; and ECF is a combination of EC and EF (Emamjomeh and Sivakumar 2008). Mroczek et al. (2006) experimentally studied whether electrocoagulation treatment is effective on silica removal from separated geothermal water. It was reported that, in laboratory scale, both silica and arsenic were rapidly removed from the aged geothermal water by this technique resulting in floc that is easy to settle out. Providing that EC is a cost-effective technique as well, Mroczek et al. (2006) suggested that it can be a promising method of silica removal for geothermal industries.

For the suspended silica particles that are difficult to settle out such as smaller particles, application of filtration, or even ultrafiltration (UF) for the nanoparticles in downstream may be necessary for silica removal. Brown and Bacon (2000) experimentally investigated this further. Considering that utilising the unwanted silica to produce silica product (e.g. silica sols) could compensate the cost of geothermal energy production and even be profitable, (Brown and Bacon 2000) conducted experiments using the separated geothermal water collected from the Wairakei field, New Zealand. Promising results were observed and suggested that commercial level silica sols product can be produced using the separated geothermal water, however, Brown and Bacon (2000) also mentioned that it is difficult to conclude if the full-scale production in the field is possible as the replacement of ultrafilters can be expensive and the large ageing containers could occupy a large area. The later may be a common problem for all methods discussed in this section. Geo40 (2019) claim to be the world's first company to commercially

produce high purity and quality colloidal silica from natural geothermal brines. The first achievement was a Geo40 pilot plant operated from February 2014 to September 2015 at the Contact Energy Wairakei, New Zealand. The trial productions were successful. The company reported that the colloidal silica products performed as well as or better than the other products currently used by the potential customers (Geo40 2019).

9.3 Dosage of antiscalant

Antiscalant is widely applied for suppressing the formation of scale from dissolved solids in water (Hasson et al. 2011). The inhibition effect is due to the active growth sites of the formed scale becoming unavailable when the antiscalant is adsorbed (Weijnen and Van Rosmalen 1986; Amjad 1996; Hasson 1999; Reddy and Hoch 2001; Tang et al. 1996). This process is usually not a chemical reaction but controlled by physical mechanisms. It is suggested (Hansson et al. 2011) that small amounts of antiscalant (say less than 10 ppm) can effectively suppress the formation of scale when used properly. Common inorganic antiscalants are sodium hexametaphosphate ($Na_6P_6O_{18}$), sodium polyphosphate ($(NaPO_3)_n$), sodium pyrophosphate ($Na_4P_2O_7$), etc; common organic antiscalants are organophosphate (also called phosphate esters (OPEs)) and phosphonates. Due to the instability of these mentioned antiscalants in water, more stable alternatives such as polyacrylic acid ($(C_3H_4O_2)_n$) and polymaleic acid ($(C_4H_2O_4)_n$) are applied for scaling suppression as well.

In practice, the inhibitor is usually a formulation of several antiscalants to maximise the desired effects. For instance, in the case of silica scaling suppression, inhibitors like Geogard SX marketed by BWA Water Additives is essentially an aqueous solution of phosphinocarboxylic acid copolymer but also include components such as phosphonic acids, phosphonates, acrylate polymers, etc. It was reported (Gallup 2001) that, when dosing properly (typical dosage is about 1-1.5 ppm), an average of approximately 70% of silica scale can be suppressed; however, when the inhibitor is overdosed, the deposition rate can be even accelerated. Gallup (2001) suggested that this could be due to flocculation of colloidal silica caused by the overdosage. Also, it was reported that (Gallup 2001) the performance of inhibitors usually could not outperform acidification or simply injecting at higher temperatures.

Similar to other polymers, these antiscalants can also persist in the environment for many years. Many environmental problems, such as eutrification (or hypertrophication, extravagant growth of algae due to excessive amount of minerals and nutrients contained in water), are believed to be caused by the antiscalant, especially phosphorus-based ones. Environmentally friendly scale inhibitors are demanded. Polyaspartic acid ($(C_4H_5NO_3)_n$) is suggested (Hasson et al. 2011) to be the most promising "green" antiscalant due to its biodegradability.

9.4 Reservoir stimulation

Reservoir stimulation includes any technology developed to maintain or improve the transport of fluids underground. Applications include but are not limited to enhancement of well productivity (e.g. oil and natural gas) and injectivity, storage, environmental remediation (e.g. nuclear waste disposal by injecting small waste solid particles of waste with a carrier fluid such as water into underground), exploration of underground resources in tight sands and unconventional reservoirs, etc. (Economides and Nolte 1989). In the early stage of development, mechanical stimulation (e.g. fracturing) by injecting fluids or using even nuclear explosives, were proposed. In the 1960s, chemical treatments such as introducing acid were proposed (Economides and Nolte 1989).

Only reservoir stimulation by injecting acid is briefly discussed in this section. For convenience, the case of the Tiwi field is used as an example below.

Before the injection was initiated, the reservoir was stimulated to improve injectivity by acidizing as the drilling mud damaged the reservoir formation near the wellbore (Xu et al. 2004). It is assumed here that the reservoir formation consists of calcite plus other inert minerals, so only the dissolution of calcite is assumed to be able to contribute to the improvement of injectivity. However, such a model may still manage to represent how acidizing stimulates the reservoir.

As described before, sulphuric acid is often used in the industry to minimise the cost of acidizing. Hence, the injection of sulphuric acid having a pH of 4.5 is modelled, and it is assumed that there is no silica (no deposition) and no pre-existing carbon dioxide. The inputs used are summarised in Table 9.1 below:

Table 9.1 Summary of input parameters for the case of injecting brines acidified using sulphuric acid

Notation	Value used	Explanation	Notation	Value used	Explanation
t_{max}	7 days	Time after injection begins	$c_{inj}^{H_2SO_4}$	1.6×10^{-5} mol/kg	Initial concentration of added sulphuric acid in injected fluid (before dissociation)
t_{ageing}	0 min	Ageing time before reinjection	$c_{res}^{H_2SO_4}$	0	Initial concentration of sulphuric acid in pre-existing reservoir fluid (before dissociation)
R_0	0.122 m	Radius of injection wellbore	I_{inj}	0.09 mol/kg	Initial ionic strength of injected fluid
H	120 m	Thickness of feedzone	I_{res}	0.07 mol/kg	Initial ionic strength of pre-existing reservoir fluid
a_0	15.4 mm	Initial fracture aperture	c_0^{SiO2}	0 ppm	Initial concentration of monomeric silica in injected fluid (before any ageing process)
ϕ_0^r	0.01	Initial reservoir porosity	c_{inj}^{SiO2}	0 ppm	Concentration of monomeric silica silica in injected fluid before injection (after any ageing process)
ϕ_0^f	1	Initial fracture porosity	c_{res}^{SiO2}	0 ppm	Initial concentration of monomeric silica in pre-existing reservoir fluid
k_0^f	5.0×10^{-12} m^2	Initial permeability of fractures	c_{inj}^{cp}	0 ppm	Initial concentration of polymerised silica in injected fluid
$\dot{m}$	60 kg/s	Injecting mass flow rate	c_{res}^{cp}	0 ppm	Initial concentration of polymerised silica in pre-existing reservoir fluid
T_{inj}	160 ℃	Initial temperature of injected fluid	n	4	Power exponent of Equation 8.2
T_{res}	260 ℃	Initial temperature of reservoir	s_{CaCO_3}	100%	The percentage of the reaction surface area of calcite
pH_{res}	7	Initial pH of pre-existing geothermal fluid			

Note that, to expose the effect of reservoir stimulation by injecting acid, the percentage of the reaction surface area of calcite is defined as 100%. The predicted injectivity over time and the expected dissolved volume of calcite are shown in Figure 9.1 below:

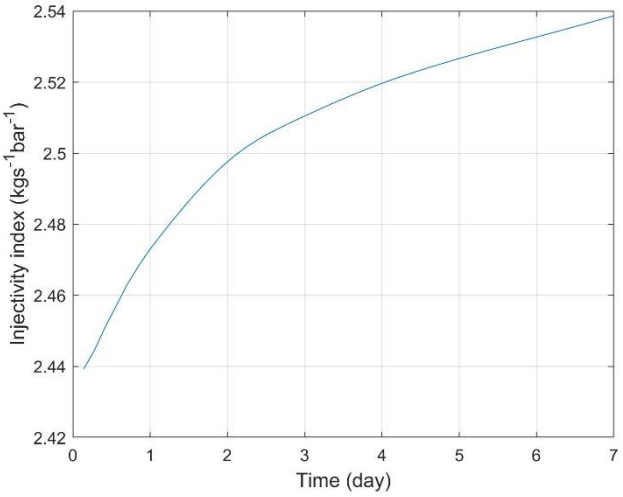

(a)

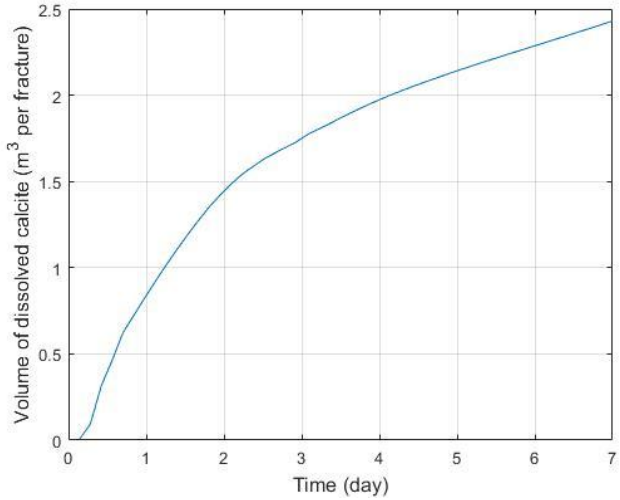

(b)

Figure 9.1: Simulation results of the reservoir stimulation by injecting sulphuric acid at 60 kg/s, pH 4.5, and 25 ℃ for 7 days: (a) injectivity and (b) volume of dissolved calcite per fracture over time.

According to the simulation results, a 4.1% injectivity increment is observed after a one-week reservoir stimulation using sulphuric acid. 2.4 m^3 of calcite per fracture (187.2 m^3 in total) is predicted to be dissolved. One may notice that the initial injectivity in this scenario is about 2.44 kg s^{-1} bar^{-1} as shown in Figure 9.1 (a) and is different from that in the stimulation of the Tiwi injector, which is about 4.50 kg s^{-1} bar^{-1} as shown in Figure 6.15. This is mainly caused by the lowered injection temperature (25 ℃ in this case comparing to 160 ℃), as the viscosity increases from approximately 1.71×10^{-4} Pa s at 160 ℃ to 8.90×10^{-4} Pa s at 25 ℃, at 20 bar. While the modelling results seem to be promising, it is worth noting that the geometry of fractures and the texture of the formation rock will have a large effect upon the effectiveness of acid stimulation. Therefore, shortfalls are possible.

As described in Section 5.3.2, the risk of anhydrite ($CaSO_4$) deposition may exist due to sulphate ion (SO_4^{2-}) introduced by sulphuric acid. According to the modelling results, the maximum activity product of Ca^{2+} and SO_4^{2-} (i.e. $a_{Ca^{2+}}a_{SO_4^{2-}}$) is about 3.70×10^{-8}. The activity product

at naturally existing concentrations of Ca^{2+} and SO_4^{2-} in geothermal fluids is typically of the same order of magnitude as well (e.g. 5.19×10^{-8}, reported by Carroll et al. 1998). Both values are less than the solubility constant of anhydrite under the conditions mentioned above: $K_{sp,CaSO_4} = 4.25 \times 10^{-4}$. Therefore, the deposition of anhydrite should not occur.

9.5 Acidification using weak acid

As discussed in Section 5.4, weak acids could be a better option than strong acids to inhibit silica scaling in the geothermal industry, and would cause less severe corrosion at high temperatures (Abrams et al. 1983; Harris 1961). In this section, one weak acid (acetic acid) is used for preliminary modelling to explore the effects of weak acid on silica deposition rates and injectivity. It is expected that at the same pH, all acids essentially have identical effects on solubility of amorphous silica, monomeric silica deposition, silica polymerization, and interactions between silica as discussed in Section 2.2.2, 4.1.1, 4.2.2, and 8.8.3, however, since the calcite dissolution rate in weak acid is slower than that in a stronger acid for the same pH due to the kinetics of the surface reaction (Nierode and Williams 1971) and the thermodynamics of the reversible reactions (Chatelian et al. 1976), the acid could be consumed more slowly and therefore the effects of the weak acid may significantly last longer than that of strong acid.

To compare the results conveniently, the same injection pH of 4.5 is used. The used inputs are summarised in Table 9.2 below:

Table 9.2 Summary of input parameters for the cases of injecting separated geothermal water acidified using sulphuric acid or acetic acid

Notation	Value used	Explanation	Notation	Value used	Explanation
t_{max}	12 years	Time after injection begins	$c_{inj}^{H_2SO_4}$	1.6×10^{-5} mol/kg	Initial concentration of added sulphuric acid in injected fluid (before dissociation)
t_{ageing}	35 min	Ageing time before reinjection	$c_{res}^{H_2SO_4}$	0	Initial concentration of sulphuric acid in pre-existing reservoir fluid (before dissociation)
R_0	0.122 m	Radius of injection wellbore	c_{inj}^{HAc}	6.8×10^{-5} mol/kg	Initial concentration of added acetic acid in injected fluid (before dissociation)
H	120 m	Thickness of feedzone	c_{res}^{HAc}	0	Initial concentration of acetic acid in pre-existing reservoir fluid (before dissociation)
a_0	15.4 mm	Initial fracture aperture	I_{inj}	0.09 mol/kg	Initial ionic strength of injected fluid
ϕ_0^r	0.01	Initial reservoir porosity	I_{res}	0.07 mol/kg	Initial ionic strength of pre-existing reservoir fluid
ϕ_0^f	1	Initial fracture porosity	c_0^{SiO2}	1272 ppm	Initial concentration of monomeric silica in injected fluid (before any ageing process)
k_0^f	5.0×10^{-12} m^2	Initial permeability of fractures	c_{inj}^{SiO2}	705 ppm	Concentration of monomeric silica silica in injected fluid before injection (after any ageing process)
$\dot{m}$	60 kg/s	Injecting mass flow rate	c_{res}^{SiO2}	620 ppm	Initial concentration of monomeric silica in pre-existing reservoir fluid

T_{inj}	160 ℃	Initial temperature of injected fluid	c_{inj}^{cp}	567 ppm	Initial concentration of polymerised silica in injected fluid
T_{res}	260 ℃	Initial temperature of reservoir	c_{res}^{cp}	0 ppm	Initial concentration of polymerised silica in pre-existing reservoir fluid
pH_{res}	7	Initial pH of pre-existing geothermal fluid	n	4	Power exponent of Equation 8.2

The modelling results are shown in Figure 9.2 below:

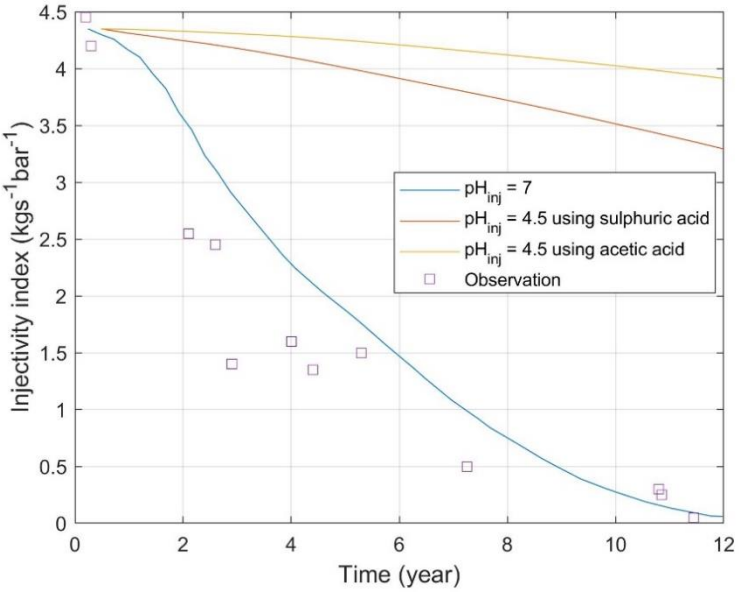

(a)

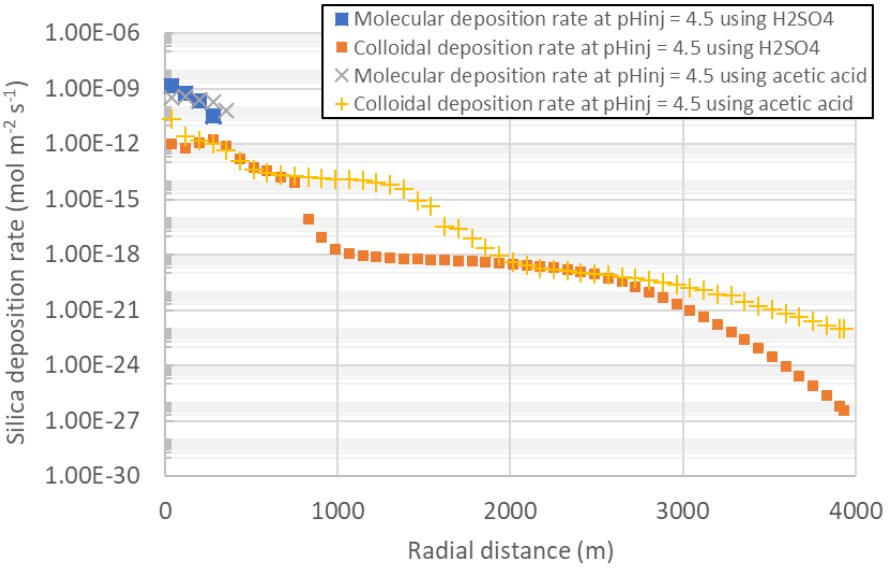

(b)

Figure 9.2: Comparison of the effects of acidification using sulphuric acid and acetic acid on (a) injectivity and (b) deposition rate.

As expected, it can be clearly seen that the effects of acetic acid last longer than that of sulphuric acid. In fact, as sulphuric acid is a diprotic acid (i.e. one mole of sulphuric acid molecules can offer two moles of hydrogen ion), the difference between acetic acid and monobasic acid like hydrochloric acid is expected to be even greater

However, the high expense of acetic acid compared to sulphuric acid may make it less practical. For example, at the similar purity (98-99%), the price of sulphuric acid listed on alibaba.com is approximately US$230-250 per tonne (i.e. US$0.011-0.012 per molar of introduced H^+), whereas the price of industry grade acetic acid can be as high as US$500-650 per tonne (i.e. US$0.025-0.032 per molar of introduced H^+).

9.6 Reservoir recovery

As shown in Section 8.7.2, silica scaling can severely damage the reservoir formation. Mechanical techniques like workover may be useful, however, considering that this can be one of the most expensive well operations and the scale can exist in the reservoir formation from dozens to thousands of metres along the radial direction, it may not always be a cost-effective method for reservoir recovery. As described in Section 5.5, silica is soluble in hydrofluoric acid (HF), which suggests that the injection of hydrofluoric acid could be effective. Hence, the injection of 2.5 mol/kg hydrofluoric acid without any other chemical impurities such as suspended or dissolved silica, carbon dioxide, etc. for 24 hours is modelled, and it is assumed that the volume of deposited silica is 252 m^3 per fracture (19656 m^3 in total, obtained in the modelling of the Tiwi field, shown in Section 8.7).

Table 9.3 Summary of input parameters for the case of injecting hydrofluoric acid

Notation	Value used	Explanation	Notation	Value used	Explanation
t_{max}	24 hours	Time after injection begins	c_{inj}^{HF}	2.5 mol/kg	Initial concentration of added hydrofluoric acid in injected fluid (before dissociation)
t_{ageing}	0 min	Ageing time before reinjection	c_{res}^{HF}	0	Initial concentration of hydrofluoric acid in pre-existing reservoir fluid (before dissociation)
R_0	0.122 m	Radius of injection wellbore	I_{inj}	0.09 mol/kg	Initial ionic strength of injected fluid
H	120 m	Thickness of feedzone	I_{res}	0.07 mol/kg	Initial ionic strength of pre-existing reservoir fluid
a_0	15.4 mm	Initial fracture aperture	c_0^{SiO2}	0 ppm	Initial concentration of monomeric silica in injected fluid (before any ageing process)
ϕ_0^r	0.01	Initial reservoir porosity	c_{inj}^{SiO2}	0 ppm	Concentration of monomeric silica silica in injected fluid before injection (after any ageing process)
ϕ_0^f	1	Initial fracture porosity	c_{res}^{SiO2}	0 ppm	Initial concentration of monomeric silica in pre-existing reservoir fluid
k_0^f	5.0×10^{-12} m^2	Initial permeability of fractures	c_{inj}^{cp}	0 ppm	Initial concentration of polymerised silica in injected fluid
$\dot{m}$	60 kg/s	Injecting mass flow rate	c_{res}^{cp}	0 ppm	Initial concentration of polymerised silica in pre-existing reservoir fluid
T_{inj}	160 ℃	Initial temperature of injected fluid	n	4	Power exponent of Equation 8.2

T_{res}	260 ℃	Initial temperature of reservoir	V_{SiO_2}	19656 m³	Total volume of pre-deposited silica
pH_{res}	7	Initial pH of pre-existing geothermal fluid			

The predicted volume of deposited silica and the expected injectivity over time are shown in Figure 9.3 below:

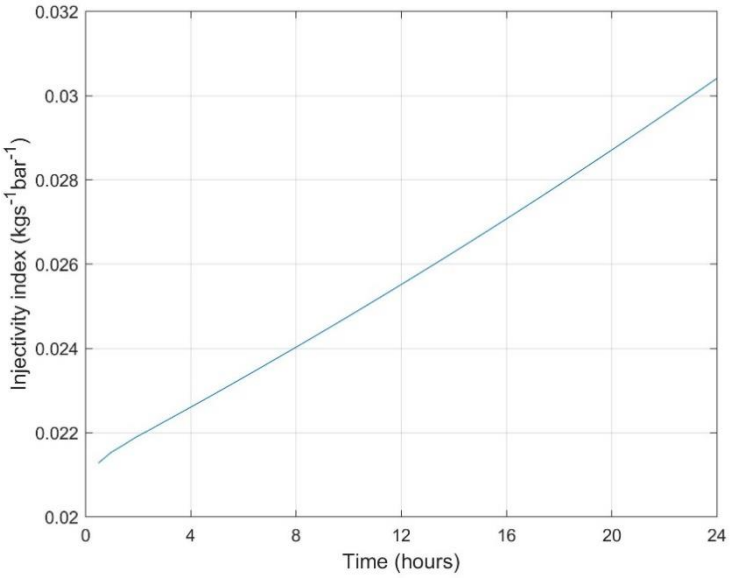

(a)

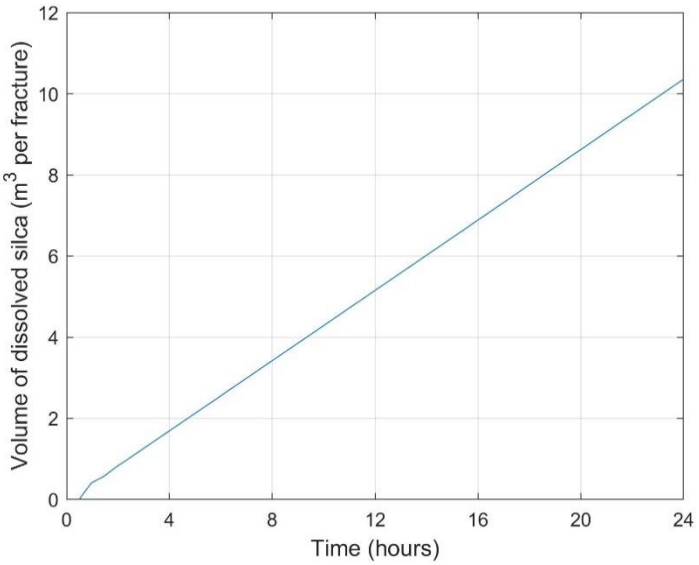

(b)

Figure 9.3: Simulation results of the reservoir stimulation by injecting 2.5 mol/kg hydrofluoric acid at 60 kg/s and 25 ℃ for 24 hours: (a) injectivity and (b) volume of dissolved silica per fracture over time.

One may note that the injectivity and the dissolved volume look like linear functions of time. This is due to the short time scale in this case and therefore the limited effects of the axis symmetric geometry on the spreading speed.

As discussed in Section 5.5.1, when using hydrofluoric acid for reservoir recovery, there should be a negligible chance of damaging the reservoir formation. Therefore, compared to sulphuric acid, a higher concentration of the injected acid could be used to maximise the dissolution rate of deposited silica. According to the simulation results, 4% of a 12 year accumulation of deposited silica can be removed in 24 hours, and an increment of injectivity from less than 0.022 to over 0.03 $\mathrm{kg\,s^{-1}\,bar^{-1}}$ can be observed. This suggests that the injection of hydrofluoric acid is an effective technique for reservoir recovery.

Theoretically, it seems that the continuous injection of hydrofluoric acid may be able to remove 100% of deposited silica, however, as suggested by Xu et al. (2004), the recovery cannot achieve this due to the deposited albite-low ($\mathrm{NaAlSi_3O_8}$), which is not modelled in the holistic model.

9.7 Summary

Silica scaling can be suppressed by any of the six techniques discussed in the previous sections, however, no method mentioned before is perfect. There are drawbacks such as: the risk of silica scaling cannot be fully eliminated by ageing as colloidal silica can still form; silica removal or extraction at commercial intensities requires capital and time investment, which can be significant; the performance of inhibitors usually could not outperform acidification or simply injecting at higher temperatures (Gallup 2001); etc. Hence, a combination of the inhibition methods, such as combining acidification and dosage of inhibitors (Harrar 1980), may achieve even better results.

All methods discussed before can extend the lifetime of geothermal reinjection. The composition of the separated geothermal water and the characteristics of reservoirs can vary a lot in different fields. The compositions and conditions of the injectate must be known to identify the best methods of extending the reinjection lifetime.

Chapter 10

Conclusions and future work

The findings in the present work are summarised in this chapter.

10.1 Chemistry of silica

The chemistry of silica is discussed in Section 2.2 and Chapter 4 in detail.

10.1.1 Prediction of average silica particle size

In Section 4.1.2, a semi-empirical three-stage silica particle growth model is developed. Ostwald ripening is considered as the dominant mechanism in the later stage of particle growth. The model is proved to be able to predict the silica particle size as a function of time when input conditions are given.

Discrepancies with measured data are usually less than 50% of the final particle size and are most likely to be observed in the first and the second stages. While such discrepancies are not ideal, there is no more accurate method at present, and order of magnitude estimates are sufficient to predict which particle transport mechanisms dominate. Discrepancies of more than 50% in the first two stages could be seen when the initial silica supersaturation index (SSI) is relatively low (e.g. less than 2.5), which may be corrected after an induction time is introduced as shown in Section 8.3. The induction time is known to delay the start of particle formation. Depending on SSI, the induction time can vary from seconds to dozens of minutes (Iler 1979; Weres et al. 1981; Tamura et al. 2018). It could potentially be a key variable to include in the model, and further investigations may be of interest.

10.1.2 The validity of the soft particle model

The classic DLVO theory is discussed in Section 4.2.2.1. It can quantitatively describe the interactions of colloids of a range of chemical compositions with reasonable accuracy. However, based on observations reported in the literature and by comparing the predictions made by the DLVO theory and the observations (Škvarla 2013), the discrepancy in stability can be as much as over 40 orders of magnitude (shown in Figure 4.38 (j)). Therefore, the DLVO theory is shown to be inapplicable to colloidal silica.

The application of the soft particle model (Ohshima 2015) is discussed in Section 4.2.2.2-4.2.2.4. Compared to the DLVO theory, the soft particle model is shown to be able to explain

the unexpected interaction behaviours at pH = 4, 6, and 8 and $c_{\mathrm{KCl}} = 0.001 - 1\mathrm{M}$ at ambient temperature, which may offer a better understanding of the mechanisms for the aggregation and the deposition of colloidal silica. Further studies may be of interest to experimentally investigate the interactions between colloidal silica at high temperatures and compare the results with the predictions made by the soft particle model.

10.1.3 Stability prediction using the soft particle model

The variation in the hairy layer thickness d_0 is the key variable in the soft particle model and dominated by pH and the concentration of KCl (or ionic strength of the background electrolyte if the effects of varying the salt species are negligible). Particle size has minor effects and is assumed to have a negligible effect. By fitting the values of d_0 to experimental data, an expression of pH and ionic strength is developed to predict d_0, completing the soft particle model and giving it a predictive capability. Hence, when given a set of conditions, it becomes possible to find the stability (a variable to reveal the interaction behaviours of silica) and eventually the deposition rate of colloidal silica.

10.2 Development of the holistic model

The model: *GEOREPR* (*GEOthermal REinjection lifetime PRediction model*) is an original work that integrates all sub-models described in the previous chapters, such as the sub-models of hydrodynamics, heat transfer, fluid-rock interaction (i.e. the chemistry sub-model), silica polymerisation and monomeric silica deposition (i.e. SILNUC), colloidal silica deposition (based on the soft particle model and the non-penetration model), dissolution of silica in hydrofluoric acid, and injectivity estimation. One can refer to Chapter 5 as the user guide.

10.2.1 The validity of the non-penetration model

Compared to the perfect-sink model (i.e. the concentration of the interested species is fixed to zero on the collector surface, $C|_{z=\mathrm{boundary}} = 0$) which gives the predicted deposition rate at wrong orders of magnitude, the non-penetration model (i.e. the concentration gradient of the interested species is fixed to zero on the collector surface, $\frac{\partial C}{\partial z}|_{z=\mathrm{boundary}} = 0$) predicted a deposition rate of the correct order of magnitude, so was used in the present work.

10.2.2 The validity of the simple idealised geometry used to represent the reservoir formation

A simple idealised model (described in Section 6.2) is proposed to represent the reservoir formation. Based on the relatively good comparison results shown in Chapter 8, the idealised geometry is considered as a useful representation of the reservoir formation in geothermal reinjection.

10.2.3 The validity of the heat transfer and the chemistry model

The physical and chemical conditions (i.e. the temperature and the concentrations of the chemical species discussed in Chapter 5, such as H^+ and Na^+) are shown to dominate the kinetics of all reactive processes considered in the present work.

To obtain the conditions of interest, two models are developed. A heat transfer model (see Section 6.4.1) is developed and shown to be useful in predicting the in situ temperature over time (Bödvarsson and Tsang 1982). A chemistry model (see Chapter 5 and Section 6.5) is proposed and proved to be capable of estimating the in situ concentrations of considered species over time physically (Huminicki and Rimstidt 2007).

10.2.4 Prediction of silica deposition rate and injectivity

A first-order colloidal silica deposition model (see Section 6.6.3) is developed to estimate the deposition rate of colloidal silica considering the interaction potentials between silica in the form of stability. Among the five external forces acting on the silica nanoparticles, London-van der Waals's force and electrostatic force are shown to determine the kinetics of colloidal silica deposition, whereas net gravity (including gravity and buoyancy) and Saffman lift force are negligible (see Section 6.6.4,). The deposition rate of dissolved silica is predicted by adopting SILNUC (see Section 4.1.1 and 6.6.1; Weres et al. 1981). By combining the two, the total silica deposition rate may be found. According to the good agreements (usually within the same order of magnitude) between the modelling results and the observations shown in Chapter 8, the silica deposition model is shown to be able to physically simulate the silica scaling process in geothermal reinjection. The discrepancy of more than one order of magnitude is expected to be caused by the chemical impurities such as multivalent ions. The model as stands is most reliable when multivalent ions are present only in negligible concentrations. More observations of the effects of multivalent ions on silica polymerisation and aggregation will allow functions to be added to the model to improve its performance still further.

The deposition of silica is expected to be the dominant reason for the decrease of porosity, resulting in the subsequent decrement of permeability and injectivity over time. The predicted injectivity shows a decline, at a decreasing rate, in line with the observed historical injectivity data (Xu et al. 2004). The comparison and the sensitivity analysis shown in Chapter 8 suggest that the holistic model is able to physically predict the variation of injectivity as a function of time due to the fluid-rock interactions.

10.3 Interactions between injectate and rock matrix

10.3.1 Effects of calcite dissolution

The effects of calcite dissolution are shown in Section 8.8.3. Acidized injectate can be rapidly neutralised by the dissolution of carbonate minerals, and the inhibition effects on silica scaling would be cancelled.

Based on the modelling results, when the rapid neutralisation of acid due to the dissolution of carbonate minerals is considered, the estimated lifetime of reinjection still increases mainly due to the lowered molecular deposition rate near the fracture entrance while the concentration of colloidal silica is still relatively low. However, the decrement is still obvious if the timescale of interest is long enough, which suggests that the risk of silica scaling still cannot be ignored.

10.3.2 Risk of anhydrite precipitation

In the holistic model, the risk of anhydrite precipitation is monitored by tracking the activity product of calcium and sulphate ions. The holistic model suggests that the risk can be negligible

if the amount of sulphuric acid used is carefully controlled and does not exceed the current typical value (approximately 10^{-5} M). This conclusion agrees with Wong et al. 2015.

10.3.3 Effects of acidification using weak acid

As discussed in Section 5.4 and 8.8.3, overall, sulphuric acid and acetic acid share similar effects on silica scaling suppression, but acetic acid would cause less severe corrosion at high temperatures (Abrams et al. 1983; Harris 1961); furthermore, according to the modelling results shown in Section 9.5, the effects of acetic acid are found to last longer than that of sulphuric acid as the weak acid could be consumed more slowly by the dissolution of carbonate. In fact, as sulphuric acid is a diprotic acid (i.e. one mole of sulphuric acid molecules can offer two moles of hydrogen ion), the difference can be even more obvious between acetic acid and monobasic acid like hydrochloric acid. However, this is usually considered to be less practical due to the high expense of acetic acid relative to sulphuric acid.

10.3.4 Effects of hydrofluoric acid on reservoir recovery

The simulation results suggest that the injection of hydrofluoric acid can be effective for removing the silica scale in the reservoir formation. According to the simulation results, by injecting separated geothermal water dosed with 2.5 M hydrofluoric acid, 4% of a 12-year accumulation of deposited silica can be removed in 24 hours. However, full recovery may not be achievable due to the formation of scale minerals that do not dissolve or dissolve very slowly in hydrofluoric acid (e.g. albite-low, $NaAlSi_3O_8$, Xu et al. 2004).

10.4 Conceptual ideas for extending reinjection lifetime

Based on the discussion and the modelling results of geothermal reinjection, six possible methods (such as ageing, silica extraction, dosage of antiscalant, reservoir stimulation using acid, acidification, and reservoir recovery using hydrofluoric acid) that may be of use to extend the reinjection lifetime are discussed in Chapter 9. All of these methods are believed to have positive effects to some extent. Further field investigations may be of interest to quantify the effects.

10.5 Future work

Research opportunities are briefly summarised but not limited to the list below:

1. Iterations of the current model *GEOREPR*:
    a. reprogramming using more open and easily accessible languages such as Python;
    b. fixing the possible bugs discovered in the future;
    c. adding the function of automatic convergence check;
    d. adding the module of any work finished in the future, especially the effect of multivalent ions on particle growth and aggregation;
2. Future experimental work on the effects of chemical impurities such as multivalent ions on silica polymerization and aggregation, leading to models of the same, which can be incorporated into the modelling framework established in the present work.
3. Modelling of naturally fractured reservoir:
    a. modelling of unsteady fluid transport in natural fractures, including tortuosity, roughness, and the pressure loss at the intersection of fractures;
    b. modelling of interactions between injected fluids and natural fracture surface;

4. Modelling of the changes in fracture roughness due to the modified boundary and its corresponding effects;
5. Modelling of thermophoretic transport of colloidal silica;
6. Modelling of silica deposition near fracture throats;
7. Modelling of heat and reactive mass transfer in the other processes of geothermal energy production (such as the transport of separated geothermal water in pipelines) where the fluid flow is usually turbulent;
8. Modelling of silica removal using electrocoagulation treatment;
9. Modelling of supercritical geothermal systems (in excess of 374 °C and 221 bar), e.g. Taupo Volcanic Zone (TVZ), New Zealand; Krafla, Iceland; etc.
10. Experimental investigations to check the models at temperatures, pressures and ionic strengths spanning the range seen in geothermal systems (such as the interactions between colloidal silica from ambient to higher temperatures (say over 100 ℃); and the time-resolved silica particle size over a range of SSI (say from 1 to 5) at higher temperatures).

References

Abraham, F. (2012). Homogeneous nucleation theory: the pretransition theory of vapor condensation, Elsevier.

Abrams, A., et al. (1983). "Higher-pH acid stimulation systems." Journal of Petroleum Technology 35(12): 2,175-172,184.

Adamczyk, Z., et al. (1984). "Kinetics of particle accumulation at collector surfaces. II. Exact numerical solutions." Journal of Colloid and Interface Science 97(1): 91-104.

Adamczyk, Z. and T. Van de Ven (1984). "Kinetics of particle accumulation at collector surfaces. I. Approximate analytical solutions." Journal of Colloid and Interface Science 97(1): 68-90.

Adamczyk, Z. and P. Weroński (1999). "Application of the DLVO theory for particle deposition problems." Advances in colloid and interface science 83(1-3): 137-226.

Addison, S. J., et al. (2015). Brine Silica Management at Mighty River Power, New Zealand. Proceedings.

Alexander, G. B. and J. R. McWhorter (1958). Concentrating silica sols without particle growth, Google Patents.

Allen, L. H. and E. Matijević (1969). "Stability of colloidal silica: I. Effect of simple electrolytes." Journal of Colloid and Interface Science 31(3): 287-296.

Aneke, M., et al. (2011). "Performance analysis of the Chena binary geothermal power plant." Applied Thermal Engineering 31(10): 1825-1832.

Arias, G. F. D. L. and A. J. Ahmad (1996). Acid treatment method for siliceous formations, Google Patents.

Arnorsson, S. (1981). "Mineral deposition from Icelandic geothermal waters: environmental and utilization problems." Journal of Petroleum Technology 33(01): 181-187.

Arvidson, R. S., et al. (2003). "Variation in calcite dissolution rates: A fundamental problem?" Geochimica et cosmochimica acta 67(9): 1623-1634.

Aubert, C. and D. S. Cannell (1986). "Restructuring of colloidal silica aggregates." Physical review letters 56(7): 738.

Aubert, C. and D. S. Cannell (1986). "Restructuring of colloidal silica aggregates." Physical review letters 56(7): 738-741.

Avrami, M. (1939). "Kinetics of phase change. I General theory." The Journal of Chemical Physics 7(12): 1103-1112.

Azimi, G., et al. (2007). "Modelling of calcium sulphate solubility in concentrated multi-component sulphate solutions." Fluid Phase Equilibria 260(2): 300-315.

Barton, A. and N. Wilde (1971). "Dissolution rates of polycrystalline samples of gypsum and orthorhombic forms of calcium sulphate by a rotating disc method." Transactions of the Faraday Society 67: 3590-3597.

Bateman, L. C., et al. (1940). "188. Mechanism of substitution at a saturated carbon atom. Part XXIII. A kinetic demonstration of the unimolecular solvolysis of alkyl halides.(Section E) a general discussion." Journal of the Chemical Society (Resumed): 979-1011.

Baucke, F. G., et al. (1968). "Rotating Disk System for the Study of Metal Deposition from Nonaqueous Solvents." Review of Scientific Instruments 39(11): 1753-1754.

Bénézeth, P., et al. (2013). "Mineral solubility and aqueous speciation under hydrothermal conditions to 300 C–the carbonate system as an example." Reviews in Mineralogy and Geochemistry 76(1): 81-133.

Bergna, H. E. (2005). Colloid chemistry of silica: an overview. Colloidal Silica, CRC Press: 32-58.

Bergna, H. E. and W. O. Roberts (2005). Colloidal silica: fundamentals and applications, CRC Press.

Berner, R. A. (1976). "Solubility of calcite and aragonite in seawater at atmospheric pressure and 34. 5% salinity." Am. J. Sci.;(United States) 276(6).

Berner, R. A. and J. W. Morse (1974). "Dissolution kinetics of calcium carbonate in sea water; IV, Theory of calcite dissolution." American journal of science 274(2): 108-134.

Bertani, R. (2012). "Geothermal power generation in the world 2005–2010 update report." Geothermics 41: 1-29.

Bildstein, O., et al. (2001). "Assessment of anhydrite dissolution as the rate-limiting step during thermochemical sulfate reduction." Chemical geology 176(1-4): 173-189.

Birol, F. (2017). "Key world energy statistics." International Energy Agency.

Blounot, C. and F. Dickson (1969). "The solubility of anhydrite (CaSO4) in NaCl-H2O from 100 to 450 C and 1 to 1000 bars." Geochimica et cosmochimica acta 33(2): 227-245.

Blount, C. W. and F. W. Dickson (1973). "Gypsum-anhydrite equilibria in systems CaSO4-H2O and CaCO4-NaCl-H2O." American Mineralogist: Journal of Earth and Planetary Materials 58(3-4_Part_1): 323-331.

Bödvarsson, G. S. and C. F. Tsang (1982). "Injection and thermal breakthrough in fractured geothermal reservoirs." Journal of Geophysical Research: Solid Earth 87(B2): 1031-1048.

Brady, P. V. and J. V. Walther (1990). "Kinetics of quartz dissolution at low temperatures." Chemical geology 82: 253-264.

Breck, D. W. and Z. M. Sieves (1974). "Structure, chemistry and use." Zeolite Molecular Sieves. Wiley, New York.

Brinker, C. J. and G. Scherer (1990). "Sol-gel sciences." The Processing and the Chemistry of Sol-Gel Processing.

Brown, K. (2011). Thermodynamics and kinetics of silica scaling. International Workshop on Mineral Scaling.

Brown, K. (2011). Thermodynamics and kinetics of silica scaling. Proceedings of International Workshop on Mineral Scaling.

Brown, K. and M. Dunstall (2000). Silica scaling under controlled hydrodynamic conditions. Proceedings World Geothermal Congress, Citeseer.

Browne, P. (1978). "Hydrothermal alteration in active geothermal fields." Annual review of earth and planetary sciences 6(1): 229-248.

Carman, P. (1940). "Constitution of colloidal silica." Transactions of the Faraday Society 36: 964-973.

Carroll, S., et al. (1998). "Amorphous silica precipitation (60 to 120 C): Comparison of laboratory and field rates." Geochimica et cosmochimica acta 62(8): 1379-1396.

Chatelain, J., et al. (1976). "Thermodynamic Limitations in Organic-Acid/Carbonate Systems." Society of Petroleum Engineers Journal 16(04): 189-195.

Chauhan, V., et al. (2018). Silica deposition in superheated geothermal systems. Proceedings 43rd Workshop on Geothermal Reservoir Engineering.

Chen, S., et al. (2017). A model of silica colloid growth, stability and transport used to predict geothermal reinjection lifetime. New Zealand Geothermal Workshop 2017, Rotorua, New Zealand.

Chen, S., et al. (2018). An explanation for the unexpected interactions of silica nanoparticles using the soft particle model. Proceedings 40th New Zealand Geothermal Workshop.

Chen, S., et al. (2018). Modelling of in situ silica particle growth and deposition under geothermal conditions. Proceedings 40th New Zealand Geothermal Workshop.

Chen, S., et al. (2018). Predictions of average silica particle size over time under geothermal conditions. Proceedings 40th New Zealand Geothermal Workshop.

Cherukat, P. and J. B. McLaughlin (1994). "The inertial lift on a rigid sphere in a linear shear flow field near a flat wall." Journal of Fluid Mechanics 263: 1-18.

Choquette, P. W. and L. C. Pray (1970). "Geologic nomenclature and classification of porosity in sedimentary carbonates." AAPG bulletin 54(2): 207-250.

Cox, R. and S. Hsu (1977). "The lateral migration of solid particles in a laminar flow near a plane." International Journal of Multiphase Flow 3(3): 201-222.

Crowe, C. T., et al. (1977). "The particle-source-in cell (PSI-CELL) model for gas-droplet flows." Journal of fluids engineering 99(2): 325-332.

Davies, C. and I. Association (1962). Butterworths, London.

Davies, C. W. and T. Shedlovsky (1964). "Ion association." Journal of The Electrochemical Society 111(3): 85C-86C.

De Gennes, P. (1987). "Polymers at an interface; a simplified view." Advances in colloid and interface science 27(3-4): 189-209.

Debye, P. and E. Hückel (1923). "Zur theorie der elektrolyte. II." Phys. Zft 24: 305-325.

Depasse, J. and A. Watillon (1970). "The stability of amorphous colloidal silica." Journal of Colloid and Interface Science 33(3): 430-438.

Deraguin, B. and L. Landau (1941). "Theory of the stability of strongly charged lyophobic sols and of the adhesion of strongly charged particles in solution of electrolytes." Acta Physicochim: USSR 14: 633-662.

Derjaguin, B. (1940). "On the repulsive forces between charged colloid particles and on the theory of slow coagulation and stability of lyophobe sols." Transactions of the Faraday Society 35: 203-215.

Dickson, M. and M. Fanelli (2004). What is geothermal energy? International geothermal association.

Dove, P. M. and C. A. Czank (1995). "Crystal chemical controls on the dissolution kinetics of the isostructural sulfates: Celestite, anglesite, and barite." Geochimica et cosmochimica acta 59(10): 1907-1915.

Dunstall, M. and K. Brown (1998). Silica scaling under controlled hydrodynamic conditions: vertical flat plate and vertical cylinder tests. Proceedings of the 23rd Workshop on Geothermal Reservoir Engineering, Stanford University Stanford, CA, USA.

Dunstall, M., et al. (2000). The onset of silica scaling around circular cylinders. CD-ROM Proceedings World Geothermal Congress, Kyushu-Tokohu, Japan.

Dutrizac, J. (2002). "Calcium sulphate solubilities in simulated zinc processing solutions." Hydrometallurgy 65(2-3): 109-135.

El-Ashry, M. (2010). "Renewables 2010 global status report." Paris: REN21 Secretariat). Copyright Deutsche (GTZ) GmbH: 2010.

Elimelech, M., et al. (2013). Particle deposition and aggregation: measurement, modelling and simulation, Butterworth-Heinemann.

Ellis, A. (1963). "823. The effect of temperature on the ionization of hydrofluoric acid." Journal of the Chemical Society (Resumed): 4300-4304.

Ellis, A. (1963). "The solubility of calcite in sodium chloride solutions at high temperatures." American journal of science 261(3): 259-267.

Ellison, B. T. and I. Cornet (1971). "Mass transfer to a rotating disk." Journal of The Electrochemical Society 118(1): 68-72.

Exler, V. A., et al. (2014). Hybrid matrix acidizing techniques successfully stimulate geothermal wells in Latin America. SPE International Symposium and Exhibition on Formation Damage Control, Society of Petroleum Engineers.

Fleming, B. A. (1986). "Kinetics of reaction between silicic acid and amorphous silica surfaces in NaCl solutions." Journal of Colloid and Interface Science 110(1): 40-64.

Fletcher, C. A. (2012). Computational techniques for fluid dynamics 2: Specific techniques for different flow categories, Springer Science & Business Media.

Fossum, M. and R. N. Horne (1982). "Interpretation of tracer return profiles at Wairakei geothermal field using fracture analysis." Trans.-Geotherm. Resour. Counc.;(United States) 6.

Fournier, R. O. and J. J. Rowe (1977). "The solubility of amorphous silica in water at high temperatures and high pressures." American Mineralogist 62(9-10): 1052-1056.

Frank-Kamenetskii, D. A. b. (1969). Diffusion and heat transfer in chemical kinetics, Plenum Press.

Fredd, C. N. and H. S. Fogler (1998). "Influence of transport and reaction on wormhole formation in porous media." AIChE journal 44(9): 1933-1949.

Fredd, C. N. and H. S. Fogler (1998). "The kinetics of calcite dissolution in acetic acid solutions." Chemical engineering science 53(22): 3863-3874.

Fuchs, N. (1934). "Zur theorie der koagulation." Zeitschrift für Physikalische Chemie 171(1): 199-208.

Gallup, D. L. (1997). Inhibition of silica precipitation, Google Patents.

Garibaldi, F. and D. Freeston (1981). Effect of hydrodynamic flow conditions on silica deposition. Third New Zealand Geothermal Workshop. University of Auckland, Auckland, New Zealand.

Gibbs, J. W. (1961). The Scientific Papers, Vol I: Thermodynamics, Dover Publications.

Gledhill, D. K. and J. W. Morse (2006). "Calcite solubility in Na–Ca–Mg–Cl brines." Chemical geology 233(3-4): 249-256.

Glover, R. B. and T. M. Scott (2005). Geochemical monitoring before and during six years of power generation at Ngawha, New Zealand. Proceedings of the World Geothermal Congress, Antalya, Turkey.

Grigsby, C. O., et al. (1989). "Rock-water interactions in the Fenton Hill, New Mexico, hot dry rock geothermal systems I. Fluid mixing and chemical geothermometry." Geothermics 18(5-6): 629-656.

Gunnarsson, I. and S. Arnórsson (2000). "Amorphous silica solubility and the thermodynamic properties of H4SiO°4 in the range of 0° to 350°C at Psat." Geochimica et cosmochimica acta 64(13): 2295-2307.

Gunnarsson, I., et al. (2010). Reducing silica deposition potential in waste waters from Nesjavellir and Hellisheiði Power Plants, Iceland. Proceedings World Geothermal Congress 2010 Bali, Indonesia, 25-29 April 2010.

Gupta, H. and S. Roy (2007). "Worldwide status of geothermal resource utilization." Geotherm Energy: 199-229.

Haddon, C. and M. Brown (1924). "Calcium Sulphate Cement." Soc. Chem. Ind 43: 11-16T.

Hamaker, H. (1937). "The London—van der Waals attraction between spherical particles." physica 4(10): 1058-1072.

Hamer, W. J. (1968). "Theoretical mean activity coefficients of strong electrolytes in aqueous solutions from 0 to 100 C."

Harris, F. (1961). "Applications of acetic acid to well completion, stimulation and reconditioning." Journal of Petroleum Technology 13(07): 637-639.

Hasson, D. and J. Zahavi (1970). "Mechanism of calcium sulfate scale deposition on heat transfer surfaces." Industrial & Engineering Chemistry Fundamentals 9(1): 1-10.

Healy, T. W. (1994). "Stability of aqueous silica sols." Advances in Chemistry Series 234: 147-147.

Hofmann, U., et al. (1934). "Röntgenographische und kolloidchemische Untersuchungen über Ton." Angewandte Chemie 47(30): 539-547.

Holdmann, G. and K. List (2007). "The Chena Hot Springs 400kW geothermal power plant: experience gained during the first year of operation." Geothermal Resources Council Transactions 31: 515-519.

Honig, E., et al. (1971). "Effect of hydrodynamic interaction on the coagulation rate of hydrophobic colloids." Journal of Colloid and Interface Science 36(1): 97-109.

Hori, K. and S. Matsumoto (2010). "Bacterial adhesion: from mechanism to control." Biochemical Engineering Journal 48(3): 424-434.

Horne, R. N. (1982). "Geothermal reinjection experience in Japan." Journal of Petroleum Technology 34(03): 495-503.

Hulbert, S. (1969). "Models for Solid-state Reactions." J. Brit. Ceram. Soc 6: 11-20.

Huminicki, D. and J. Rimstidt (2007). "Anoxic limestone drain (ALD) design: Role of calcite dissolution kinetics and gypsum coatings." Applied Geochemistry 23: 148-165.

Hunter, R. J. (1993). Introduction to modern colloid science, Oxford University Press Oxford.

Ibrahim, R., F. A. Fauzi., and Suryadarma (2005). The Progress of Geothermal Energy Resources Activities in Indonesia. Proceedings.

Iler, R. (1971). "Relation of particle size of colloidal silica to the amount of a cationic polymer required for flocculation and surface coverage." Journal of Colloid and Interface Science 37(2): 364-373.

Iler, R. K. (1979). "Chemistry of Silica--Solubility, Polymerization, Colloid and Surface Properties, and Biochemistry."

Jacobson, R. L. and D. Langmuir (1974). "Dissociation constants of calcite and CaHC03+ from 0 to 50 C." Geochimica et cosmochimica acta 38(2): 301-318.

Jeschke, A. A. and W. Dreybrodt (2002). "Pitfalls in the determination of empirical dissolution rate equations of minerals from experimental data and a way out: an iterative procedure to find valid rate equations, applied to Ca-carbonates and-sulphates." Chemical geology 192(3-4): 183-194.

Kamiya, H., et al. (1974). "Dissolution rate of powdered quartz in acid solution." Geochemical Journal 8(1): 21-26.

Karásek, P., et al. (2013). "Solubility of fused silica in sub-and supercritical water: Estimation from a thermodynamic model." The Journal of Supercritical Fluids 83: 72-77.

Kashpura, V. and V. Potapov (2000). Study of the amorphous silica scales formation at the Mutnovskoe hydrothermal field (Russia). Proceedings of the 25th Stanford Workshop on Geothermal reservoir engineering, Stanford, USA.

Kaya, E. and M. O'Sullivan (2010). Reinjection at Wairakei Tauhara Geothermal Field. Proceedings of 17th Australasian Fluid Mechanics Conference.

Kaya, E., et al. (2011). "Reinjection in geothermal fields: a review of worldwide experience." Renewable and sustainable energy reviews 15(1): 47-68.

Keenan, J. H. (1978). Steam tables: thermodynamic properties of water including vapour, liquid, and solid phases (International system of units - S.I.). N.Y, Wiley.

Kielland, J. (1937). "Individual activity coefficients of ions in aqueous solutions." Journal of the American Chemical Society 59(9): 1675-1678.

Kirkwood, J. G. (1934). "On the theory of strong electrolyte solutions." The Journal of Chemical Physics 2(11): 767-781.

Knauss, K. G. and T. J. Wolery (1988). "The dissolution kinetics of quartz as a function of pH and time at 70 C." Geochimica et cosmochimica acta 52(1): 43-53.

Kobayashi, M., et al. (2005). "Aggregation and charging of colloidal silica particles: effect of particle size." Langmuir 21(13): 5761-5769.

Laidler, K. J. and M. C. King (1983). "Development of transition-state theory." The Journal of Physical Chemistry 87(15): 2657-2664.

Lasaga, A. C. (1984). "Chemical kinetics of water‐rock interactions." Journal of Geophysical Research: Solid Earth 89(B6): 4009-4025.

Lasaga, A. C. (1995). "Fundamental approaches in describing mineral dissolution and precipitation rates." Chemical weathering rates of silicate minerals: 23-86.

Lasaga, A. C. and R. A. Berner (1998). "Fundamental aspects of quantitative models for geochemical cycles." Chemical geology 145(3-4): 161-175.

Lebron, I. and D. Suarez (1996). "Calcite nucleation and precipitation kinetics as affected by dissolved organic matter at 25 C and pH> 7.5." Geochimica et cosmochimica acta 60(15): 2765-2776.

Leonard, B. P. (1979). "A stable and accurate convective modelling procedure based on quadratic upstream interpolation." Computer methods in applied mechanics and engineering 19(1): 59-98.

Levich, V. G. (1962). "Physicochemical hydrodynamics."

Lifshitz, I. M. and V. V. Slyozov (1961). "The kinetics of precipitation from supersaturated solid solutions." Journal of physics and chemistry of solids 19(1-2): 35-50.

Lin, M., et al. (1989). "Universality in colloid aggregation." Nature 339(6223): 360.

Ling, Y. and G. P. Demopoulos (2004). "Solubility of Calcium Sulfate Hydrates in (0 to 3.5) mol·kg^{-1} Sulfuric Acid Solutions at 100 °C." Journal of Chemical & Engineering Data 49(5): 1263-1268.

Litt, M. and G. Serad (1964). "Chemical reactions on a rotating disk." Chemical engineering science 19(11): 867-884.

London, F. (1937). "The general theory of molecular forces." Transactions of the Faraday Society 33: 8b-26.

MacInnes, D. A. (1919). "The activities of the ions of strong electrolytes." Journal of the American Chemical Society 41(7): 1086-1092.

Makrides, A. C., Turner, M., & Slaughter, J. (1980). "Condensation of silica from supersaturated silicic acid solutions. " Journal of Colloid and Interface Science, 73(2), 345-367.

Mandelbrot, B. B. (1989). Multifractal measures, especially for the geophysicist. Fractals in geophysics, Springer: 5-42.

Markusson, S. H. and T. Hauksson (2015). Utilization of the hottest well in the world, IDDP-1 in Krafla. Proceedings World Geothermal Congress.

Marshall, W. L. and R. Slusher (1966). "Thermodynamics of Calcium Sulfate Dihydrate in Aqueous Sodium Chloride Solutions, 0-110° 1, 2." The Journal of Physical Chemistry 70(12): 4015-4027.

Mazer, J. J. and J. V. Walther (1994). "Dissolution kinetics of silica glass as a function of pH between 40 and 85 C." Journal of non-crystalline solids 170(1): 32-45.

MBIE (2015). Energy in New Zealand 2015. Ministry of Business, Innovation and Employment, New Zealand.

MBIE (2017). Energy in New Zealand 2017. Ministry of Business, Innovation and Employment, New Zealand.

McLaughlin, J. (1994). "Numerical computation of particles-turbulence interaction." International Journal of Multiphase Flow 20: 211-232.

McLaughlin, J. B. (1989). "Aerosol particle deposition in numerically simulated channel flow." Physics of Fluids A: Fluid Dynamics 1(7): 1211-1224.

McLaughlin, J. B. (1991). "Inertial migration of a small sphere in linear shear flows." Journal of Fluid Mechanics 224: 261-274.

McLaughlin, J. B. (1993). "The lift on a small sphere in wall-bounded linear shear flows." Journal of Fluid Mechanics 246: 249-265.

McLin, K. S., et al. (2006). Mineral characterization of scale deposits in injection wells; Coso and Salton Sea geothermal fields, CA. Thirty-First Workshop on Geothermal Reservoir Engineering, Stanford University, Stanford, California.

McWhorter, J. M., et al. (1976). "Posterior cervical fusion in children." Journal of neurosurgery 45(2): 211-215.

Mehrbach, C., et al. (1973). "Measurement of the apparent dissociation constants of carbonic acid in seawater at atmospheric pressure 1." Limnology and Oceanography 18(6): 897-907.

Merdhah, A. B. B. and A. A. M. Yassin (2008). "Laboratory study and prediction of calcium sulphate at high-salinity formation water." the Open Petroleum Engineering Journal 1(1).

Mesmer, R. E., et al. (1989). "Ionization of acetic acid in aq. sodium chloride media: a potentiometric study to 573 K and 130 bar." The Journal of Physical Chemistry 93(21): 7483-7490.

Mitra, A. (2008). Silica dissolution at low pH in the presence and absence of fluoride, Virginia Tech.

Mitra, A. and J. D. Rimstidt (2009). "Solubility and dissolution rate of silica in acid fluoride solutions." Geochimica et cosmochimica acta 73(23): 7045-7059.

Miyazaki, Y., et al. (1991). "Assessment of geothermal resources of Japan-1990." National Geothermal Resource Evaluation Study: 17-43.

Morales, J., et al. (2012). "A nanoscopic approach to the kinetics of anhydrite (100) surface growth in the range of temperatures between 60 and 120 C." American Mineralogist 97(5-6): 995-998.

Mott, R. L., et al. (2006). "Applied fluid mechanics."

Mroczek, E. (1994). The effect of colloidal silica on silica scaling from geothermal fluid. Proc. 16th New Zealand Geothermal Workshop.

Mroczek, E., et al. (2017). "Silica scaling in cooled silica saturated geothermal water: Comparison between Wairakei and Ohaaki geothermal fields, New Zealand." Geothermics 69: 145-152.

Mroczek, E., et al. (2013). Silica Scaling Trial and Injection of Cold Separated Geothermal Water At Wairakei, New Zealand. 35th New Zealand Geothermal Workshop, number November.

Mroczek, E. and G. McDowell (1990). "Silica scaling field experiments." Ratio 1: 1-6.

Nancollas, G. and M. Reddy (1971). "The crystallization of calcium carbonate. II. Calcite growth mechanism." Journal of Colloid and Interface Science 37(4): 824-830.

Narasimhan, T. and P. Witherspoon (1976). "An integrated finite difference method for analyzing fluid flow in porous media." Water Resources Research 12(1): 57-64.

Newman, J. (1966). "Schmidt number correction for the rotating disk." The Journal of Physical Chemistry 70(4): 1327-1328.

Newton, Claire J., et al. "ALUMINIUM-RICH SILICA SCALING: SAN JACINTO-TIZATE GEOTHERMAL ENERGY PROJECT, NICARAGUA." Proceedings 40th New Zealand Geothermal Workshop. Vol. 14. 2018.

Nielsen, A. E. (1964). Kinetics of precipitation, Pergamon Press Oxford.

Nierode, D. and B. Williams (1971). "Characteristics of acid reaction in limestone formations." Society of Petroleum Engineers Journal 11(04): 406-418.

Nishimori, H., et al. (1997). "Growth mechanism of large monodispersed silica particles prepared from tetraethoxysilane in the presence of sodium dodecyl sulfate." Journal of Sol-Gel Science and Technology 9(1): 25-31.

Nordeng, S. H. and D. F. Sibley (1994). "Dolomite stoichiometry and Ostwald's step rule." Geochimica et cosmochimica acta 58(1): 191-196.

Normand, C., et al. (2002). "Hydrothermal alteration of olivine in a flow-through autoclave: Nucleation and growth of serpentine phases." American Mineralogist 87(11-12): 1699-1709.

Ohshima, H. (2015). "Electrostatic interaction of soft particles." Advances in colloid and interface science 226: 2-16.

Palandri, J. L. and Y. K. Kharaka (2004). A compilation of rate parameters of water-mineral interaction kinetics for application to geochemical modeling, Geological Survey Menlo Park CA.

Partridge, E. P. and A. H. White (1929). "The solubility of calcium sulfate from 0 to 200." Journal of the American Chemical Society 51(2): 360-370.

Pauling, L. (1960). The Nature of the Chemical Bond, Cornell university press Ithaca, NY.

Perry, C. C. and T. Keeling-Tucker (2000). "Model studies of the precipitation of silica in the presence of aluminium; implications for biology and industry." Journal of Inorganic Biochemistry 78(4): 331-339.

Pick, H. (1912). "Nernst Festschrift." Z. Phys. Chem. 360.

Plummer, L., et al. (1978). "The kinetics of calcite dissolution in CO_2-water systems at 5 °C to 60 °C and 0.0 to 1.0 atm CO_2." American journal of science 278(2): 179-216.

Plummer, L. N. and E. Busenberg (1982). "The solubilities of calcite, aragonite and vaterite in CO_2-H_2O solutions between 0 and 90 °C, and an evaluation of the aqueous model for the system $CaCO_3$-CO_2-H_2O." Geochimica et cosmochimica acta 46(6): 1011-1040.

Pokrovsky, O. S., et al. (2006). "Kinetic evidences of the existence of positively charged species at the quartz-aqueous solution interface." Journal of Colloid and Interface Science 296(1): 189-194.

Pott, J., et al. (1996). Numerical simulation of silica scaling. Proceedings 18th NZ Geothermal Workshop.

Pribush, A., et al. (2007). "The mechanism of the dextran-induced red blood cell aggregation." European Biophysics Journal 36(2): 85-94.

Pruess, K., et al. (1999). TOUGH2 user's guide version 2, Lawrence Berkeley National Lab.(LBNL), Berkeley, CA (United States).

Pusey, P., et al. (1989). "Structure of crystals of hard colloidal spheres." Physical review letters 63(25): 2753.

Reardon, E. J. and D. Langmuir (1976). "Activity coefficients of $MgCO_3^0$ and $CaSO_4^0$ ion pairs as a function of ionic strength." Geochimica et cosmochimica acta 40(5): 549-554.

Rebreanu, L., et al. (2008). "The diffusion coefficient of dissolved silica revisited." Marine chemistry 112(3-4): 230-233.

Reddy, M. M. (1949). "Effect of magnesium ion on calcium carbonate nucleation and crystal growth in dilute aqueous solutions at 25 °C." Studies in Digenesis, US Geological Survey Bulletin 1578: 169-182.

Reeder, R. J. (2018). Carbonates: mineralogy and chemistry, Walter de Gruyter GmbH & Co KG.

Robinson, R. A. and R. H. Stokes (1955). Electrolytil Solutions: The Measurement and Interpretation of Conductance, Chemical Potential and Diffusion in Solutions of Simple Electrolytes, Butterworths.

Rumble, J. and CHEMnetBASE (2017). CRC Handbook of Chemistry and Physics, 98th Edition. Boca Raton Florence, CRC Press LLC Taylor & Francis Group Distributor: 1 online resource.

Saffman, P. (1964). "The amplification of a weak magnetic field by turbulent motion of a fluid of large conductivity." Journal of Fluid Mechanics 18(3): 449-465.

Saffman, P. (1968). "The lift on a small aphere in a slow shear flow." Corrigendum 31: 624.

Sass, E., et al. (1983). "Dependence of the values of calcite and aragonite thermodynamic solubility products on ionic models." American journal of science 283(3): 218-229.

Schoonen, M. and H. Barnes (1991). "Reactions forming pyrite and marcasite from solution: II. Via FeS precursors below 100 °C." Geochimica et cosmochimica acta 55(6): 1505-1514.

Segnit, E., et al. (1962). "The solubility of calcite in aqueous solutions—I the solubility of calcite in water between 75 and 200 at CO_2 pressures up to 60 atm." Geochimica et cosmochimica acta 26(12): 1301-1331.

Sheikholeslami, R. and M. Ng (2001). "Calcium sulfate precipitation in the presence of nondominant calcium carbonate: thermodynamics and kinetics." Industrial & engineering chemistry research 40(16): 3570-3578.

Shiraki, R. and S. L. Brantley (1995). "Kinetics of near-equilibrium calcite precipitation at 100 °C: An evaluation of elementary reaction-based and affinity-based rate laws." Geochimica et cosmochimica acta 59(8): 1457-1471.

Sibley, D. F., et al. (1987). "Kinetics of dolomitization." Geology 15(12): 1112-1114.

Singurindy, O. and B. Berkowitz (2004). "Competition among flow, dissolution, and precipitation in fractured carbonate rocks." DYNAMICS OF FLUIDS IN FRACTURED ROCK: 81.

Singurindy, O. and B. Berkowitz (2004). "The role of fractures on coupled precipitation and dissolution patterns in carbonate rocks." Adv. Water Resour.

Sjöberg, E. L. and D. Rickard (1983). "The influence of experimental design on the rate of calcite dissolution." Geochimica et cosmochimica acta 47(12): 2281-2285.

Škvarla, J. i. (2013). "Quantitative interpretation of anomalous coagulation behavior of colloidal silica using a swellable polyelectrolyte gel model of electrical double layer." Langmuir 29(28): 8809-8824.

Škvarla, J., and Škvarla, J. (2017). "An identification of the soft polyelectrolyte gel-like layer on silica colloids using atomic force and electron microscopy. " Ultramicroscopy, 181, 97-106.

Sonnefeld, J. (1995). "Surface charge density on spherical silica particles in aqueous alkali chloride solutions." Colloid and polymer science 273(10): 932-938.

Spalding, D. B. (1972). "A novel finite difference formulation for differential expressions involving both first and second derivatives." International Journal for Numerical Methods in Engineering 4(4): 551-559.

Steefel, C. I. and P. Van Cappellen (1990). "A new kinetic approach to modeling water-rock interaction: The role of nucleation, precursors, and Ostwald ripening." Geochimica et cosmochimica acta 54(10): 2657-2677.

Talman, S., et al. (1990). "Dissolution kinetics of calcite in the H_2O–CO_2 system along the steam saturation curve to 210 °C." Fluid-Mineral Interactions: A Tribute to HP Eugster: 41-55.

Tamura, R., et al. (2019). "In situ observations of silica nanoparticle growth in geothermal brine at the Sumikawa geothermal station, Japan, by dynamic light scattering." Geothermics 77: 304-312.

Tobler, D. J. and L. G. Benning (2013). "In situ and time resolved nucleation and growth of silica nanoparticles forming under simulated geothermal conditions." Geochimica et cosmochimica acta 114: 156-168.

Tobler, D. J., et al. (2009). "Quantification of initial steps of nucleation and growth of silica nanoparticles: An in-situ SAXS and DLS study." Geochimica et cosmochimica acta 73(18): 5377-5393.

Tolman, R. C. (1925). "The principle of microscopic reversibility." Proceedings of the National Academy of Sciences of the United States of America 11(7): 436.

Truesdell, A. H. and B. F. Jones (1974). "WATEQ, a computer program for calculating chemical equilibria of natural waters." J. Res. US Geol. Surv 2(2): 233-248.

Tsang, Y. (1984). "The effect of tortuosity on fluid flow through a single fracture." Water Resources Research 20(9): 1209-1215.

Unger, K. K. (1979). Porous silica, Elsevier.

van den Heuvel, D. B., et al. (2018). "Understanding amorphous silica scaling under well-constrained conditions inside geothermal pipelines." Geothermics 76: 231-241.

Vasseur, P. and R. Cox (1977). "The lateral migration of spherical particles sedimenting in a stagnant bounded fluid." Journal of Fluid Mechanics 80(3): 561-591.

Verma, A. and K. Pruess (1988). "Thermohydrological conditions and silica redistribution near high - level nuclear wastes emplaced in saturated geological formations." Journal of Geophysical Research: Solid Earth 93(B2): 1159-1173.

Versteeg, H. K. and W. Malalasekera (2007). An introduction to computational fluid dynamics: the finite volume method, Pearson education.

Verwey, E. J. W. and J. T. G. Overbeek (1955). "Theory of the stability of lyophobic colloids." Journal of Colloid Science 10(2): 224-225.

Verwey, E. J. W., et al. (1999). Theory of the stability of lyophobic colloids, Courier Corporation.

Vysotskii, Z. and D. Strazhesko (1974). Adsorption and Adsorbents, Wiley, New York.

Vysotskii, Z. and D. Strazhesko (1974). The role of polymerization and depolymerization reactions of silicic acid, etc, Wiley New York: pp. 55-75.

Wagner, C. (1961). "Ostwald ripening theory." Ber. Bunsenges. Phys. Chem 65: 581-591.

Walker, A. C., et al. (1927). "Equilibrium in solutions of alkali carbonates." Journal of the American Chemical Society 49(5): 1235-1256.

Wang, Q. and K. Squires (1996). "Large eddy simulation of particle deposition in a vertical turbulent channel flow." International Journal of Multiphase Flow 22(4): 667-683.

Weres, O., et al. (1981). "Kinetics of silica polymerization." Journal of Colloid and Interface Science 84(2): 379-402.

Weres, O., and L. Tsao. "Chemistry of silica in Cerro Prieto brines." Geothermics 10.3-4 (1981): 255-276.

White, F. M. (2003). "Fluid mechanics, chapter 6." McGraw-Hill, New York, NY 10020: 366-376.

Williams, R., et al. (1985). "Preparation and properties of spherical zinc sulfide particles." Journal of Colloid and Interface Science 106(2): 388-398.

Wollast, R. and L. Chou (1988). Rate control of weathering of silicate minerals at room temperature and pressure. Physical and Chemical Weathering in Geochemical Cycles, Springer: 11-32.

Wong, C., et al. (2016). Reactive transport modelling of injection fluid-reservoir rock interaction. New Zealand Geothermal Workshop 2016, Auckland, New Zealand.

Worley, W., et al. (1996). "Quartz dissolution kinetics from 100–200 C as a function of pH and ionic strength." AIChE journal 42(12): 3442-3457.

Wright, M. R. (2007). An introduction to aqueous electrolyte solutions, John Wiley & Sons.

Xu, T. (2008). "TOUGHREACT user's guide: A simulation program for non-isothermal multiphase reactive geochemical transport in variably saturated geologic media, V1. 2.1." Lawrence Berkeley National Laboratory.

Xu, T., et al. (2004). "Reactive transport modeling of injection well scaling and acidizing at Tiwi field, Philippines." Geothermics 33(4): 477-491.

Xu, T. and K. Pruess (2001). "Modeling multiphase non-isothermal fluid flow and reactive geochemical transport in variably saturated fractured rocks: 1. Methodology." American journal of science 301(1): 16-33.

Xu, T., et al. (2004). TOUGHREACT user's guide: a simulation program for non-isothermal multiphase reactive geochemical transport in variable saturated geologic media, Lawrence Berkeley National Lab.(LBNL), Berkeley, CA (United States).

Xu, T., et al. (2006). "TOUGHREACT—a simulation program for non-isothermal multiphase reactive geochemical transport in variably saturated geologic media: applications to geothermal injectivity and CO2 geological sequestration." Computers & Geosciences 32(2): 145-165.

Xu, T., et al. (2011). "TOUGHREACT Version 2.0: A simulator for subsurface reactive transport under non-isothermal multiphase flow conditions." Computers & Geosciences 37(6): 763-774.

Yokoyama, T., et al. (1991). "Retarding and accelerating effects of aluminum on the growth of polysilicic acid particles." Journal of Colloid and Interface Science 141(2): 559-563.

Yokoyama, T., et al. (1989). "Effect of aluminium on the polymerization silicic acid in aqueous solution and the deposition of silica of silica." Geothermics 18(1-2): 321-326.

Zarrouk, S. J. and H. Moon (2014). "Efficiency of geothermal power plants: A worldwide review." Geothermics 51: 142-153.

Zdanovskii, A. and G. Vlasov (1968). "Determination of the boundaries of the reciprocal transformation of CaSO4. 2H2O and γ-CaSO4 in H2SO4 solutions." Russian Journal of Inorganic Chemistry 13: 1318-1319.

Zhdanov, S. and A. Kiselev (1957). "The chemical structure of quartz and silica gel surfaces and their hydration." Zhurnal Fizicheskoi Khimii 31(10): 2213-2223.

Zhuravlev, L. (1993). "Surface characterization of amorphous silica—a review of work from the former USSR." Colloids and Surfaces A: Physicochemical and Engineering Aspects 74(1): 71-90.

翟云芳 (2003). "渗流力学." 北京: 石油工业出版社.